HAL
open science

Coherent Transport of Matter Waves in Disordered Optical Potentials

Kuhn Robert

To cite this version:

Kuhn Robert. Coherent Transport of Matter Waves in Disordered Optical Potentials. Quantum Gases [cond-mat.quant-gas]. Université Nice Sophia Antipolis, 2007. English. NNT : . tel-00717232

HAL Id: tel-00717232

https://theses.hal.science/tel-00717232v1

Submitted on 12 Jul 2012

HAL is a multi-disciplinary open access archive for the deposit and dissemination of scientific research documents, whether they are published or not. The documents may come from teaching and research institutions in France or abroad, or from public or private research centers.

L'archive ouverte pluridisciplinaire **HAL**, est destinée au dépôt et à la diffusion de documents scientifiques de niveau recherche, publiés ou non, émanant des établissements d'enseignement et de recherche français ou étrangers, des laboratoires publics ou privés.

Binationale Dissertation
der Fakultät für Mathematik, Physik und Informatik
der Universität Bayreuth
&
der Université de Nice Sophia–Antipolis
École doctorale : Sciences Fondamentales et Appliquées

Thèse
présentée pour obtenir le titre de
Docteur en Sciences
Spécialité : Physique

Coherent Transport of Matter Waves in Disordered Optical Potentials

Robert Kuhn

Prof. Dr. C. A. Müller	:	Codirecteur de thèse
Dr. C. Miniatura	:	Codirecteur de thèse
Dr. B. A. van Tiggelen	:	Examinateur
Prof. Dr. A. Seilmeier	:	Président du jury

Coherent Transport of Matter Waves in Disordered Optical Potentials

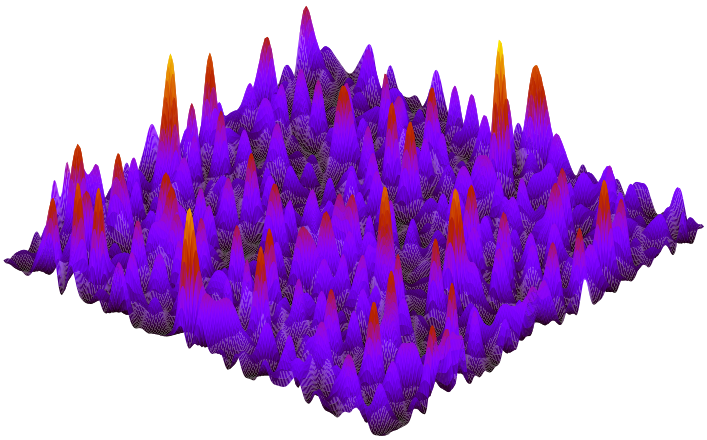

Kurzfassung

Mit der Entwicklung moderner Techniken zur Kühlung und zur Manipulation von Atomen in den letzten Jahren und der Möglichkeit, Bose-Einstein-Kondensate und entartete Fermi-Gase zu erzeugen und in regelmäßige optische Gitter oder in ungeordnete optische Potentiale zu laden, ist das Interesse an der Lokalisierung von ultrakalten Atomen neu entfacht worden. Die vorliegenden Arbeit untersucht die Transporteigenschaften von Materiewellen in ungeordneten Lichtpotentialen, die auch als Speckle-Interferenzmuster bekannt sind. Zunächst haben wir die Auswirkung der korrelierten Unordnung auf die Lokalisierung im Rahmen des Anderson-Modells numerisch untersucht. Mit Hilfe der diagrammatischen Störungstheorie können die relevanten Transportgrößen im Konfigurationsmittel über viele Speckle-Realisierungen in zwei und in drei Dimensionen schließlich analytisch bestimmt und damit Vorhersagen für eine mögliche experimentelle Umsetzung getroffen werden. Für die Beschreibung der Transporteigenschaften kommt der räumlichen Korrelation der Speckle-Fluktuationen dabei eine besondere Bedeutung zu, da sie für den anisotropen Charakter der Streuprozesse im effektiven Medium verantwortlich ist. Durch kohärente Vielfachsteuung kommt es zu Interferenzeffekten, die eine Korrektur der Diffusionskonstanten im Vergleich zur klassischen Beschreibung bewirken. Diese sogenannte schwache Lokalisierung der Materiewellen gilt als Ursache für den durch den Grad der Unordnung gesteuerten Übergang zur Anderson-Lokalisierung und ist ebenfalls Gegenstand der vorliegenden Arbeit.

Résumé

Le développement de techniques modernes pour le refroidissement et le piégeage d'atomes et la possibilité de charger des réseaux optiques ou des potentiels désordonnés avec des condensats de Bose ou des gaz de Fermi dégénérés a déclenché un intérêt nouveau pour la localisation des atomes ultra-froids. Dans le présent travail théorique nous étudions le transport cohérent des ondes de matière dans des potentiels lumineux désordonnés, ou échantillons de tavelures (speckle). L'influence du désordre corrélé est d'abord étudié numériquement dans le cadre du modèle d'Anderson. Un calcul auto-consistante diagrammatique permet finalement de déterminer analytiquement les paramètres fondamentaux de transport dans le régime de faible désordre. Une importance cruciale pour le calcul analytique revient à la fonction de corrélation spatiale des fluctuations du potentiel désordonné qui détermine le degré d'anisotropie d'un événément de collision. Nous considérons en particulier la transition du régime de la localisation faible à celui de la localisation forte. Dans ce cas la constante de diffusion des ondes de matière diminue et tend vers zéro au seuil de la localisation forte, ce qui décrit la transition d'Anderson. Dans le présent travail on calcule la renormalisation de la constante de diffusion due a l'interférence cohérente des ondes de matière en tenant compte explicitement de la correlation des fluctuations du potentiel désordonné.

Contents

List of Figures **xi**

1 Introduction **1**
1.1 Electron Transport and Localization in Disordered Systems . . . 2
1.1.1 Weak Localization . . . 3
1.1.2 Metal-Insulator Transition . . . 4
1.1.3 Scaling Theory . . . 5
1.1.4 Electron Transport Experiments . . . 8
1.2 Ultra-cold Atoms in Disordered Systems . . . 10
1.2.1 Bose-Hubbard Model . . . 11
1.2.2 Quasicrystals, Superlattices, and Speckle Potentials . . . 13
1.2.3 Alternative Concepts . . . 15

2 Speckle Theory and Numerical Implementation **17**
2.1 Speckle Statistics . . . 18
2.1.1 Probability Distribution . . . 19
2.1.2 Correlation Functions . . . 19
2.1.3 2D Speckle . . . 21
2.1.4 3D Speckle . . . 25
2.2 Numerical Implementation of a Speckle Pattern . . . 25
2.3 Summary . . . 28

3 Numerical Study of the Anderson Model **31**
3.1 The Tight-Binding Model . . . 32
3.1.1 Exact Diagonalization . . . 34
3.1.2 The Lanczos Algorithm . . . 38
3.1.3 Correlated On-Site Energies . . . 40
3.2 Summary . . . 44

4 Matter Waves in Disordered Optical Potentials **45**
4.1 Atomic Hamiltonian Dynamics . . . 45
4.2 Effective Medium . . . 48
4.2.1 Retarded and Advanced Propagator . . . 48
4.3 Spectral Function and Density of States . . . 51
4.4 Diagrammatic Representation of the Self-Energy . . . 54
4.5 Identification of the Perturbation Parameter . . . 55
4.6 Weak-Scattering Approximation . . . 58
4.6.1 Weak-Scattering Parameter . . . 58
4.6.2 Weak-Scattering Energy . . . 60
4.7 Scattering Mean Free Path . . . 60
4.7.1 2D Speckle . . . 62

4.7.2 3D Speckle . . . 63
4.8 Summary . . . 64

5 Diffusive Transport **65**
5.1 Probability Transport . . . 65
5.2 Quantum Kinetic Equation . . . 68
5.2.1 Diffusion Approximation . . . 70
5.2.2 Solution in the Kubo Limit and for Weak Disorder . . . 72
5.3 Diagrammatic Representation of the Scattering Vertex . . . 74
5.4 Boltzmann Transport . . . 75
5.4.1 The Diffuson . . . 76
5.5 Comparison to Isotropic Scattering . . . 77
5.6 Transport Mean Free Path . . . 79
5.6.1 2D Speckle . . . 79
5.6.2 3D Speckle . . . 80
5.7 Summary . . . 81

6 Coherent Multiple Scattering **83**
6.1 Weak-Localization Correction . . . 84
6.1.1 The Cooperon . . . 84
6.1.2 Discussion of the Cooperon and the Hikami Function . . . 88
6.1.3 Comparison to the Kubo Theory . . . 90
6.2 Anisotropic Hikami Contributions . . . 91
6.2.1 Correlated Hikami Diagrams . . . 92
6.3 Self-Consistent Renormalization of the Scattering Vertex . . . 96
6.4 Localization Length and Critical Exponents . . . 99
6.5 Possible Experimental Observation of Localization . . . 102
6.5.1 2D Speckle . . . 103
6.5.2 3D Speckle . . . 106
6.6 Influence of the Initial Wigner Distribution . . . 108
6.7 Summary . . . 114

7 Conclusions and Outlook **117**

A Chebyshev Polynomials **121**

B Optical Bloch Equations **123**

C Multidimensional Fourier Transform **125**
C.1 2D Fourier Bessel Transform . . . 125
C.2 3D Fourier Transform . . . 125

Bibliography **I**

Acknowledgements – Danksagung – Remerciements **IX**

List of Figures

1.1 Transport diagrams . . . 3
1.2 Mobility edge . . . 5
1.3 Scaling function . . . 6
1.4 Experimental evidence for weak localization . . . 9
1.5 Bose-Hubbard phase plot . . . 12
1.6 Optical quasicrystal . . . 14

2.1 Granular speckle pattern . . . 17
2.2 Creation of a speckle interference pattern . . . 18
2.3 Two-dimensional speckle geometry . . . 22
2.4 Numerically generated speckle pattern . . . 26
2.5 Intensity distribution . . . 27
2.6 Numerical correlation function . . . 28

3.1 Anderson matrix . . . 33
3.2 Localized states . . . 35
3.3 Average density of states . . . 36
3.4 Inverse participation number . . . 37
3.5 Dependence of the IPN on the system size . . . 39
3.6 Speckle eigenvalue histograms . . . 40
3.7 Rayleigh eigenvalue histograms . . . 41
3.8 Correlated vs. effectively uncorrelated potential . . . 41
3.9 Average density of states & inverse participation number . . . 42
3.10 Average density of states & inverse participation number . . . 43

4.1 Potential barrier analogy . . . 60
4.2 Polar plot of the 2D phase function . . . 61
4.3 Disorder parameter $k\ell_s$ in 2D . . . 62
4.4 Polar plot of the 3D phase function . . . 63
4.5 Disorder parameter $k\ell_s$ in 3D . . . 63

5.1 ℓ_s and ℓ_B & anisotropy function . . . 80

6.1 Cooperon vs. Hikami diagrams . . . 89
6.2 Dressed cooperon vs. Hikami diagrams . . . 95
6.3 Nested loop diagram . . . 97
6.4 2D: Weak-localization correction . . . 103
6.5 2D: Critical wavenumber & phase diagram . . . 104
6.6 2D: Localization length . . . 105
6.7 3D: Weak-localization correction . . . 106
6.8 3D: Critical wavenumber & phase diagram . . . 107

6.9 3D: Localization length 108
6.10 Ratio $\mathcal{D}^*/\mathcal{D}_B$ in 2D and 3D 111
6.11 Ratio $\mathcal{D}^*/\mathcal{D}_B$ for $\sigma_k = 0$ in 2D and 3D 112
6.12 Ratio $\mathcal{D}^*/\mathcal{D}_B$ for $k_0 = 0$ in 2D and 3D 112
6.13 Diffusion coefficient $\mathcal{D}^*$ in 2D and 3D 113

A.1 Chebyshev polynomials 122

Chapter 1

Introduction

In nature in general, disorder is much more common than order. Almost all natural media vary randomly in time and space. These variations also enforce a random propagation of particles or waves that are interacting with the disordered medium. Often the effect of disorder is undesirable and ingenious methods have been devised to reduce disorder and to create perfectly ordered systems. However, disorder itself can have interesting properties and reveal surprising physical phenomena. Maybe the most prominent example is the fact that waves, which usually extend to infinity, can become localized in a disordered environment.

Originally, this concept of localization has been devised to explain the metal-insulator transition in electronic systems [1, 2]. However, the fascinating idea that disorder can produce localized structures has since then attracted attention in various fields of physics far from its original domain. Quite naturally, its impact has spread for example to the field of radiative transfer theory and atomic physics where it has developed new branches like coherent backscattering, weak localization of waves, Bose or Anderson glasses and many more.

In this thesis we address the question of matter-wave transport in disordered optical potentials, which are commonly referred to as speckle patterns. Speckle patterns are known since the operation of the first Helium-Neon laser in 1960, when it was realized that objects, which are illuminated by the coherent light of a laser acquire a peculiar granular appearance [3]. The speckle pattern is created via the interference of many coherent partial waves with random amplitudes and phases, that are reflected from the microscopically rough surface of the object.

A speckle pattern can easily be generated in an experiment and probed by a cloud of cold atoms, for which it constitutes a disordered potential landscape due to the atom-light interaction. Atomic matter waves propagating in this disordered landscape are multiply scattered by the random intensity fluctuations of the speckle pattern. Our aim is to describe the transport properties of the atomic matter waves in the effective medium given by the statistical average over many speckle configurations. This can be achieved in the framework of the diagrammatic perturbation theory [4–7], which is well-known from electron transport in condensed matter physics.

Our work has been motivated by several recent developments in the field of atom optics. Since the first observation in 1995 of a gaseous Bose-Einstein condensate [8, 9] and a few years later of the first ultra-cold Fermi gas [10], rapid progress has been made in this field.

Current cooling and trapping techniques for ultra-cold atomic gases have reached a high degree of control and are nowadays routinely used in experiments.

Loading ultra-cold atomic gases [11–14] into optical lattices [15, 16] has opened fascinating new possibilities to probe condensed matter phenomena. The investigation of the influence of disorder on optically confined atoms presents a natural evolution in this domain. Several experiments have recently been performed for ultra-cold atoms and Bose-Einstein condensates in disordered optical potentials [17–24]. However, these experiments have been carried out for one-dimensional disordered optical potentials in the interaction-dominated regime, where wave localization phenomena are difficult to observe.

In our work we focus on the influence of disorder in the independent-particle regime and discard the atom-atom interactions. Experimentally, the interaction-free regime could be achieved, if the ultra-cold atomic gas is given time to expand, such that its spatial density decreases, before switching on the speckle potential. A more elaborate way would be to tune the two-body interactions by using a Feshbach resonance [25, 26]. In this case, by scanning a magnetic field, one can continuously go from the strongly interacting regime to the independent-particle regime, where weak localization of atomic matter waves does become important.

In this thesis we present a theoretical description of matter-wave transport in disordered optical potentials, which allows to determine the relevant transport parameters in the weak scattering regime. Special attention is drawn to the weak localization effect due to quantum interference corrections. In particular we calculate the renormalized diffusion constant for anisotropic multiple scattering. The anisotropy is a consequence of the spatial correlations of the potential fluctuations and one of the main differences of the transport of matter-waves in optical potentials in comparison with electron scattering due to uncorrelated impurities in a solid. In addition we derive a general expression for the probability density and discuss the influence of a finite initial Wigner distribution of the atoms. For the special case of a separable Wigner function given by the product of two Gaussian wave packets, this approach provides a criterion for the detectability of weak localization in the experiment. Some results of this thesis have been published in [27] and [28].

1.1 Electron Transport and Localization in Disordered Systems

Some of the most important results of localization theory have been obtained for electron transport in solids [29–31]. Two milestones in this respect are the scaling theory of localization [32] inspired by the renormalization theory of statistical physics, and the diagrammatic perturbation theory [4–7] adopted from quantum field theory. Since the diagrammatic perturbation theory is indispensable for the most important results presented in this work, I would like give a brief review of the theoretical predictions and the experimental evidence in

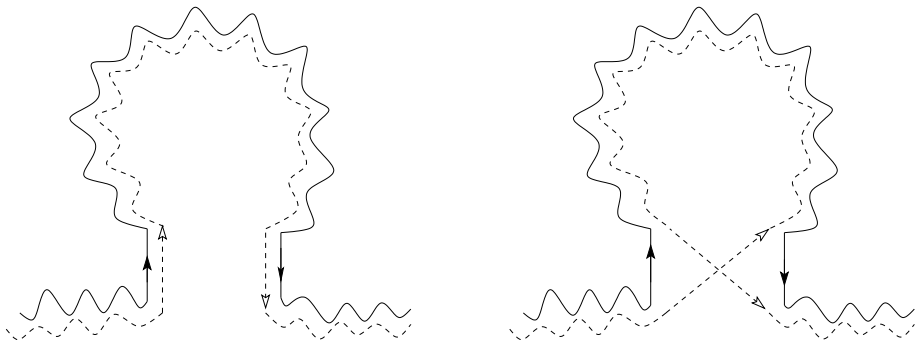

(a) diffuson contribution (b) cooperon contribution

Figure 1.1:
Schematic transport diagrams: The solid line describes the scattering path for the partial wave ψ_p, whereas the dotted line describe the scattering path for the conjugated wave $\psi^*_{p'}$. (a) Classical (diffuson) contribution ($p' = p$). (b) Quantum interference (cooperon) contribution ($p' = p_{\text{rev}}$).

the case of electron transport.

Disorder in solids can appear in the form of impurities, vacancies or dislocations in otherwise ideal crystal lattices. Introducing disorder in a perfect crystal has striking implications for its physical properties. Classically, the conductivity of a metal with impurities is given by the Drude-Boltzmann formula [7, 33]

$$\sigma_B = \frac{ne^2\tau_s}{m} \tag{1.1}$$

where e is the elementary charge of the electrons, n is the electron density and τ_s is the elastic scattering time during which an electron of mass m and velocity v travels along the elastic scattering mean free path $\ell_s = v\tau_s$. However, close to zero temperature, $T = 0$, the wave nature of the electrons becomes important. The classical result is then reduced due to wave interference effects; the actual conductivity becomes $\sigma = \sigma_B - \delta\sigma$. This reduction of the conductivity is known as the weak-localization phenomenon.

1.1.1 Weak Localization

Weak localization arises from the constructive interference of multiply scattered counter-propagating waves in a random medium. This interference survives the statistical average over many configurations of disorder and has to be taken into account for a correct description of the average conductivity.

To understand the origin of the weak-localization phenomenon, it might be helpful to study the average probability of an electronic wave to return to a given point after it has undergone a series of scattering events. The resulting wave at the point of origin is given by the sum over all possible partial waves ψ_p, each associated to a different loop-like scattering path. The return probability averaged over many realizations of disorder can be written as

the sum of two terms [34]

$$P = \overline{\left|\sum_p \psi_p\right|^2} = \sum_p \overline{|\psi_p|^2} + \sum_{p,\,p'\neq p} \overline{\psi_p \psi_{p'}^*} \tag{1.2}$$

where $\overline{(\dots)}$ denotes the disorder (or configurational) average. The first term on the right hand side counts all contributions where the partial wave ψ_p and the conjugated wave ψ_p^* have encountered exactly the same series of scattering events in the same order. For classical waves, this term is sometimes called the incoherent intensity. It is also known as the diffuson, since it describes the classical diffusion of electrons in a disordered system.

The second term comprises all contributions where ψ_p and $\psi_{p'}$ each belong to a series of different scattering events. One could expect that the interference term $\sum_{p,\,p'\neq p} \overline{\psi_p \psi_{p'}^*}$ vanishes with the configurational average. However, it does give a non-vanishing contribution, which stems from the constructive interference of ψ_p and $\psi_{p'}$, if $p' = p_{\mathrm{rev}}$ is the reverse scattering path of p

$$\sum_{p,\,p'\neq p} \overline{\psi_p \psi_{p'}^*} = \sum_p \overline{\psi_p \psi_{p_{\mathrm{rev}}}^*} + \sum_{p,\,p'\notin\{p,p_{\mathrm{rev}}\}} \overline{\psi_p \psi_{p'}^*} \tag{1.3}$$

Only the last term on the right hand side averages to zero. If $\psi_{p_{\mathrm{rev}}}^*$ does not display a phase difference compared to ψ_p, the first term on the right hand side in (1.3), also known as the cooperon contribution, is identical to the diffuson term in (1.2). The importance of the cooperon contribution was first realized by J. S. Langer and T. Neal [35]. For this reason, the corresponding diagrams within the Kubo formalism have also been named Langer-Neal graphs by G. Bergmann [30]. Including the cooperon contribution the average quantum return probability thus reaches twice its classical value. This phenomenon is also responsible for the coherent backscattering effect, which describes the enhancement by a factor of 2 of the average intensity of light that is reflected from a disordered medium in the exact backscattering direction. A direct observation of this effect was first achieved for visible light by P. Wolf and G. Maret [36] and M. P. van Albada and A. Lagendijk [37] in 1985.

The same phenomenon affects the conductivity of a solid, since an enhancement of the return probability means that the conducting electrons have a tendency to rest at one point. This contribution is not included in the Drude-Boltzmann formula (1.1), where the electrons are regarded as classical particles. Alongside the described enhancement of the return probability, the cooperon contribution thus slows down the classical diffusion and leads to a reduced conductivity $\sigma = \sigma_B - \delta\sigma$. The diffuson contribution and the cooperon contribution are depicted schematically in Fig. **1.1(a)** and Fig. **1.1(b)**.

1.1.2 Metal-Insulator Transition

In principle, the conductivity can be zero, if the weak-localization correction $\delta\sigma$, which arises from the cooperon contribution, reaches a value similar to the Drude-Boltzmann conductivity σ_B itself. This corresponds to the regime of Anderson (or strong) localization, where the

electronic states are exponentially localized. The creation of exponentially localized electronic states is probably the most significant consequence of the presence of disorder in a solid.

The concept of localization has first been formulated by Anderson in 1958 [1]. Ten years later, Mott [2] pointed out its relevance for the metal-insulator transition and introduced the mobility edge as the energy that separates localized and extended states energetically as shown in Fig. **1.2**. The conductivity of a solid is influenced by the nature of the states available to the conduction electrons at the Fermi level. If only localized states are available, the solid is an insulator. On the other hand, if the Fermi level lies inside an energy region that belongs to extended states, the conduction electrons can move freely inside the solid, which then becomes a metal. The presence of disorder as the origin of exponentially localized states thus triggers the transition between the insulating and the metallic states of matter.

1.1.3 Scaling Theory

As a fundamental prediction of the scaling theory [32], localized electronic states can in principle be found in all one- and two-dimensional disordered quantum systems, whereas in three-dimensional systems they only exist, if the amount of disorder is sufficiently strong. In one or two dimensions the observation of localized states may not be possible, if the size of the system or the typical distance for coherent transport is smaller than the localization length, i. e. the characteristic length over which the electronic wavefunction decays. Even though these electronic states are exponentially localized on a large scale, they appear extended on the smaller length scale accessible to the observer. In two dimensions, where the localization length grows exponentially with decreasing disorder, this effect may be very strong. In this sense, two-dimensional systems establish a marginal case between systems with a true Anderson transition and systems where such a transition does not exist.

The scaling theory is based on the idea that only one scaling variable is sufficient to describe the critical behaviour of the conductivity in the metallic regime and the critical behaviour

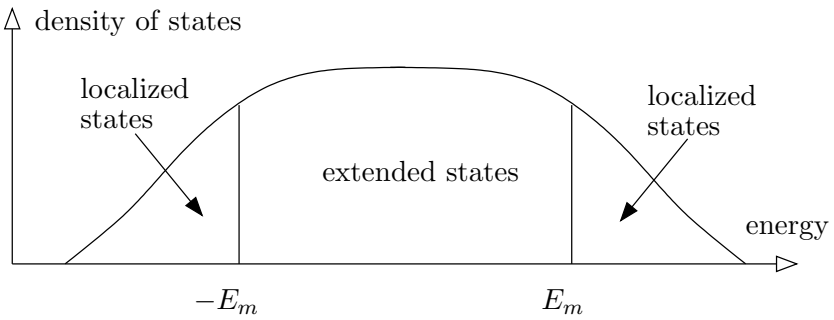

Figure 1.2:
Schematic representation of the mobility edge (cf. [2]) for the Anderson model of a cubic solid. Extended states at the band centre and localized states at the band edges are separated energetically by the mobility edge $|E_m|$. The density of states for higher disorder always has the described form, and the localized states are concentrated at the band edges (cf. Fig. **3.3** and Fig. **3.4** in section 3.1).

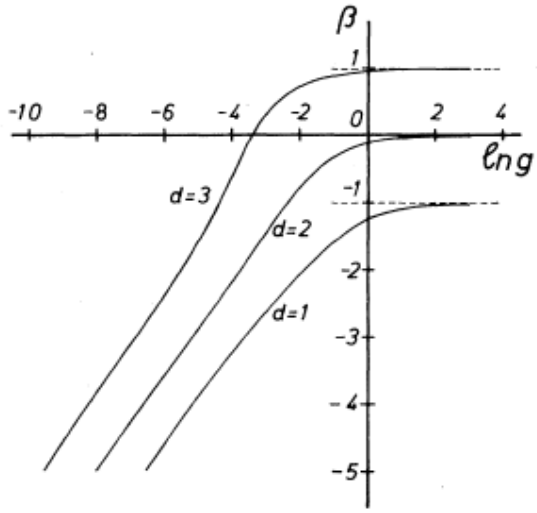

Figure 1.3:
The scaling function (1.6) for a d-dimensional sample under the influence of a homogeneous electric field, from [38]. $\beta(g)$ is positive in the metallic regime and negative in the localized regime. For $d = 1$ and $d = 2$ $\beta(g)$ is always negative, i. e. there is no true metallic state in 1D and in 2D.

of the localization length in the insulating regime. The role of the scaling parameter for a d-dimensional hypercube of length L is embodied by the dimensionless conductance [4]

$$g(L) = L^{d-2}\sigma(L)\hbar/e^2 \tag{1.4}$$

where $\sigma(L)$ is the conductivity of the system. The one-parameter scaling hypothesis [4] states that if n^d identical hypercubes are assembled to a larger hypercube of length nL, the conductance for the larger hypercube is given as a function of the conductance of the building block alone, and does not depend separately on the extension of the system or the amount of disorder

$$g(nL) = f\big(n, g(L)\big) \tag{1.5}$$

If the one parameter scaling hypothesis holds, the scaling function [4]

$$\beta(g(L)) = \frac{d\ln\big(g(L)\big)}{d\ln L} = \frac{L}{g(L)}\frac{dg(L)}{dL} = \frac{L}{g(L)}\frac{dg(nL)}{d(nL)}\Big|_{n=1} = \frac{1}{g(L)}\frac{df\big(n, g(L)\big)}{dn}\Big|_{n=1} \tag{1.6}$$

can also be written as a function of the conductance of the building block alone. Two limiting cases may be distinguished:

Weak Disorder – Metallic Regime: In the metallic regime the conductance is large ($g \gg 1$) and can be described by Ohm's law: $g_B(L) = L^{d-2}\sigma_B\hbar/e^2$, where σ_B denotes the

classical conductivity. In this case the scaling function must be

$$\beta(g) = d - 2 \tag{1.7}$$

which can be directly obtained form (1.4). In particular, the scaling function in the metallic regime depends only on the dimension of the system.

Strong Disorder – Insulating Regime: In the insulating regime ($g \ll 1$), although this is not directly obvious from (1.4), one expects the conductance to decrease exponentially, $g(L) \propto \exp[-L/\xi_{\text{loc}}]$, where ξ_{loc} is the localization length [4]. In this case, one finds a logarithmic dependence of the scaling function on the conductance

$$\beta(g) = \ln g + c \tag{1.8}$$

where c is a constant. This asymptotic behaviour of the scaling function has been verified by Vollhardt and Wölfle [38] for a d-dimensional sample of length L under the influence of a homogeneous electric field. The two asymptotic limits (1.7) and (1.8) may be connected by a continuous function.

Fig. **1.3** shows the result for the scaling function as obtained by Vollhardt and Wölfle [38] for all three dimensions $d = 1, 2, 3$. In particular, Fig. **1.3** confirms the two limiting cases (1.7) and (1.8).

The transition occurs at a critical value for the conductance where the scaling function is zero ($\beta(g_c) = 0$). The scaling function is positive in the metallic regime and negative in the localized regime. For a three-dimensional sample with a conductance larger than the critical value ($g > g_c$, $\beta > 0$) the conductance increases further with the size of the system until it reaches the state of a pure metal with a constant conductivity σ_B (1.7). In one and two dimensions the scaling function is always negative, and hence the system never reaches the metallic regime.

Vollhardt's and Wölfle's result [38] has been obtained through a quantitative extrapolation from the weak-disorder limit using diagrammatic perturbation techniques. However, it reproduces entirely the predictions made by Abrahams et al. [32] concerning the scaling behaviour of the conductance. This remarkable result indicates the strength of the diagrammatic perturbation theory even beyond the weak-localization regime.

The scaling theory predicts a continuous metal-insulator transition in 3D. In analogy to second-order phase transitions the conductivity and the localization length at the mobility edge exhibit the following critical behaviour (E_m denotes the mobility edge) [29]

$$\xi_{\text{loc}} \propto (E_m - E)^{-\nu} \tag{1.9a}$$

$$\sigma \propto (E - E_m)^s \tag{1.9b}$$

with the predicted numerical values $s = \nu = 1$ [38]. These values have been verified experimentally for amorphous materials like $Al_xGa_{1-x}As$ and compensated semiconductors [29]. The critical exponents s and ν obey the scaling relation [29]

$$s = (d-2)\,\nu \tag{1.10}$$

From the definition of the critical exponents (1.9) and the scaling relation (1.10) one can directly obtain the relation $\xi_{\text{loc}} \propto \sigma^{-1/(d-2)}$ between the localization length and the conductivity.

1.1.4 Electron Transport Experiments

Experimental evidence about localization phenomena can be gained indirectly through the study of phase-breaking mechanisms. At this point a new length scale has to be considered, which is known as the phase coherence length L_ϕ. It describes the average distance over which coherent multiple scattering can occur, or in other words, the average distance after which phase-breaking mechanisms become important. Changing for example the temperature or the strength of an external magnetic field, allows a direct control of this characteristic length scale. An increase of either of these external parameters entails a higher conductivity (or a lower resistivity), since it alters the phase coherence of the interfering waves inside the quantum loops in Fig. **1.1**. This change in the conductivity can then be compared to the phase-coherent measurement.

Phase-breaking mechanisms are always connected to the presence of additional degrees of freedom. In general, the phase-breaking mechanism results in an exponential decay of the probability density with time on a characteristic time scale τ_ϕ. If more than one phase-breaking mechanism is present, each contributes a new time scale, and if the associated degrees of freedom are not coupled to each other, these contributions can be treated independently. According to Matthiessen's rule [7], the sum of all inverse dephasing or decoherence times then results in a new total inverse time scale.

Temperature Dependence

The finite conductivity of electrons in a metal is entirely due to deviations from the perfect periodicity of the lattice. At room temperature the dominant deviation effect is given by thermal vibrations of the ions. Above the Debye temperature Θ_D the conductivity is inversely proportional to the temperature ($\sigma \propto T^{-1}$ for $T \gg \Theta_D$) [33]. For temperatures below the Debye temperature one encounters Bloch's T^5 law for the resistivity (i. e. $\sigma \propto T^{-5}$ for $T \ll \Theta_D$) [33]. As the temperature decreases further, the thermal motion of the ions freezes out and eventually impurity and defect scattering dominates.

In two dimensions the diagrammatic perturbation theory predicts in this case a logarithmic

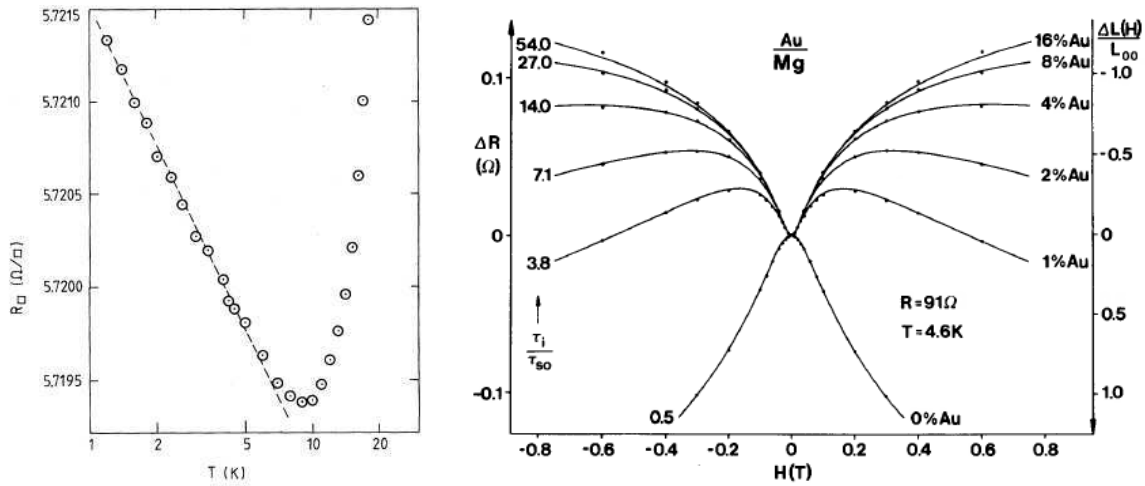

(a) Temperature dependence of the resistance

(b) Magnetic field dependence of the resistance

Figure 1.4:
Experimental evidence for weak localization. (a) Temperature dependence of the resistance of a thin Cu-film, from [39]. (b) Magnetic field dependence of the resistance of a thin Mg-film for different concentrations of Au-impurities, from [30]. A higher concentration of gold atoms increases the spin orbit scattering such that the negative magneto-resistance becomes positive again.

correction $g = g_B - \delta g$ to the Drude-Boltzmann conductance g_B with [7]

$$\delta g \propto \ln(L_\phi/\ell_s) \tag{1.11}$$

The phase coherence length associated with the temperature is proportional to T^{-p}, where T denotes the temperature. In 2D, the exponent p is given by $p = 3/2$ for electron-phonon interactions, and by $p = 1/2$ for electron-electron interactions [7].

One thus expects a logarithmic increase of the conductance (decrease of the resistance) with increasing temperature. This is indeed what has been found in a series of experiments with two-dimensional thin films as described in [30]. Fig. **1.4(a)** shows the result of one of these experiments by L. van den Dries [39] on two-dimensional Cu-films.

Magnetic Field Dependence

It turned out that a logarithmic temperature dependence of the conductance as expected for weak localization (cf. (1.11)) can also be attributed to a different physical effect. Altshuler et al. showed that in disordered systems a modification of the Coulomb interaction leads to the same conductance anomaly [30]. For an unambiguous proof of the predictions of the scaling theory and the diagrammatic perturbation theory one has to resort to a different phase-breaking mechanism that is induced by the application of an external magnetic field perpendicular to the two-dimensional film. In this case the classical conductivity, which takes

into account the bending of the electron trajectories due to the Lorentz force, reads [7]

$$\sigma(B) = \frac{\sigma(0)}{1 + \omega_c^2(B)\tau_s^2} \tag{1.12}$$

Here, $\omega_c(B) = eB/m$ is the cyclotron frequency. For small enough magnetic fields $\omega\tau_s \ll 1$, (1.12) reduces to the Drude-Boltzmann conductivity (1.1).

Nevertheless, the magnetic field has a significant impact on the interference of electronic waves in the loop-like interferometers of Fig. **1.1**. Each of these loops can be seen as a little Aharonov-Bohm ring. The magnetic flux $\phi = BA$ through a loop which encloses the area A results in a phase shift $2\pi\phi/\phi_0$ for the associated wave. $\phi_0 = h/e$ denotes the elementary flux quantum. While Fig. **1.1(a)** remains unaffected since the phase change is the same for both waves, Fig. **1.1(b)** acquires the phase difference $e^{-i\,4\pi BA/(h/e)}$. If the magnetic field B is larger than the characteristic field $B_\phi = \phi_0/(4\pi L_\phi^2)$, the weak-localization correction disappears.

The application of a magnetic field thus increases the conductance and decreases the resistance. This effect is known as negative magneto-resistance. It is shown in Fig. **1.4(b)** for a pure magnesium film without gold impurities. Since the Coulomb interaction gives a positive magneto-resistance, magnetic field experiments on thin films, in contrast to the temperature measurements, can be considered as an unambiguous proof of weak localization. Most interestingly, the coupling to the magnetic field can result in another peculiar effect known as weak anti-localization (cf. Fig. **1.4(b)** for finite Au-concentrations). This increase of the resistance with an increasing magnetic field at low temperature, is due to spin-orbit coupling [30].

1.2 Ultra-cold Atoms in Disordered Systems

Even more than by the theoretical and experimental results on electron transport, which have been reviewed in the preceding section, our work is motivated by the current ongoing research in the field of atomic transport in the presence of disorder. In the following, I would like to give an overview of present experimental and numerical studies of Bose-Einstein condensates in disordered quantum systems. Special attention is given, on the one hand, to the Bose-Hubbard model for interacting many-boson systems, and the occurrence of quantum phase transitions within this model and, on the other hand, to recent experiments with ultra-cold atoms subjected to different kinds of disordered and quasi-disordered optical potentials.

Disorder in condensed-matter systems is an intrinsic feature of the considered sample. The study of different isolated kinds of disorder requires the preparation of different samples. Moreover, several kinds of disorder might be present simultaneously, which makes it difficult to study the effect of one single kind of disorder independently from the others. In electronic systems one encounters the additional difficulty that electrons interact via the long-range Coulomb interaction. It can therefore be desirable to study disordered atomic systems as a model for the more complicated condensed matter systems [11]. In atomic systems, disorder

can be introduced in a controlled way using optical potentials. Almost any kind of potential can be realized in this way. Moreover, the method of superlattices allows to add different optical lattices on top of each other. State of the art laser cooling and evaporative cooling techniques allow to control the temperature of atomic systems reaching temperatures in the nano-Kelvin range, far below the condensation temperature for bosonic systems.

Optical lattices are rigid structures with the particular advantage that one does not have to deal with lattice phonons. A perfectly symmetric optical lattice provides an ideal optical crystal without any lattice defects or dislocations. The single-particle energy spectrum in this case consists of Bloch bands and the eigenstates are Bloch functions reflecting the periodicity of the optical potential just like in solid state physics for an ideal crystal [33]. If the excitation energy to the upper bands is high compared to the kinetic energy of the atoms, only the lowest energy band needs to be considered, where the Bloch functions can be expanded into Wannier functions that are localized at each lattice site.

1.2.1 Bose-Hubbard Model

A bosonic many-body system with an interaction range that is small compared to the lattice spacing can be very accurately described by the Bose-Hubbard Hamiltonian [40] by taking into account the on-site interaction and the hopping (or tunnelling) between neighbouring sites. The Bose-Hubbard Hamiltonian reads [41]

$$H = -J \sum_{\langle i,j \rangle} a_i^\dagger a_j + \sum_i (\epsilon_i - \mu) n_i + \tfrac{1}{2} U \sum_i n_i (n_i - 1) \tag{1.13}$$

Here, $a_i^\dagger$ and a_i are the creation and annihilation operators for a boson on the ith lattice site and $n_i = a_i^\dagger a_i$ is the occupation number operator. The index $\langle i, j \rangle$ indicates the sum over nearest neighbours. The hopping energy is given by $J = -\int \mathrm{d}\boldsymbol{r}\; w(\boldsymbol{r} - \boldsymbol{r}_i)(-\hbar^2 \nabla^2 / 2m + V_{\text{lat}}(\boldsymbol{r})) w(\boldsymbol{r} - \boldsymbol{r}_j)$ with the single-particle Wannier function $w(\boldsymbol{r} - \boldsymbol{r}_i)$ at the ith site, and the lattice potential $V_{\text{lat}}(\boldsymbol{r})$. m is the atomic mass. The second term describes the energy offset $\epsilon_i = V_{\text{ext}}(\boldsymbol{r}_i)$ on the ith site due to an external confinement or a superimposed disordered potential. μ is the chemical potential. The third term in (1.13) describes the on-site interaction. The interaction energy is given by $U = (4\pi\hbar^2 a/m) \int \mathrm{d}\boldsymbol{r}\;\; |w(\boldsymbol{r})|^4$ where a is the scattering length. The on-site interactions can be controlled by a modification of the scattering length under the influence of an external magnetic field close to a Feshbach resonance [25, 26].

Quantum Phases: One important feature of the Bose-Hubbard model is the fact that it displays a quantum phase transition at zero temperature between three possible ground states: the Mott-insulator state, the Bose-glass phase and the superfluid phase. The phase transition between the Mott-insulator and the superfluid phase in the absence of disorder was first observed experimentally by M. Greiner et al. [42]. The existence of a gap-less Bose-glass phase with non-zero compressibility between the superfluid phase and the Mott-

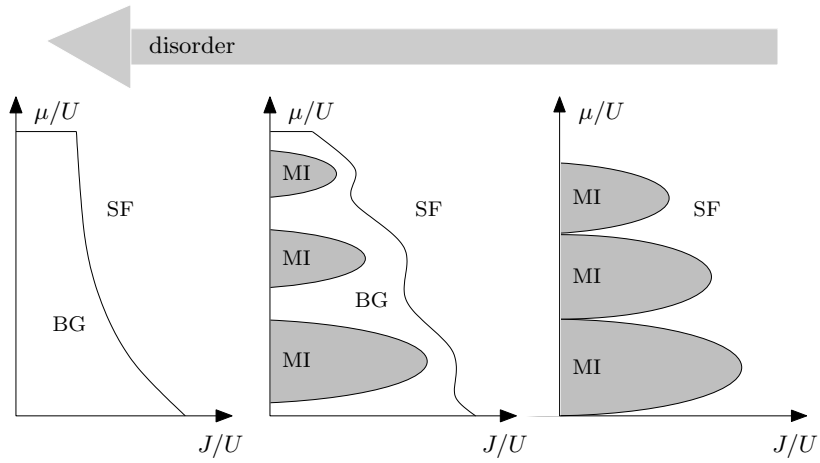

Figure 1.5:
Schematic phase plot for the Bose-Hubbard model at $T = 0$, depending on the ratio J/U and the ratio μ/U with the hopping energy J, the interaction energy U and the chemical potential μ. For zero disorder the phase transition occurs between the Mott-insulator phase (MI) and the superfluid phase (SF). For increasing disorder the Bose glass phase (BG) appears in-between the Mott-insulator phase and the superfluid phase, whereas for disorder strengths larger than the interaction energy, only the Bose-glass phase and the superfluid phase are present (This plot is based on [45]).

insulating phase in the presence of a random external potential was predicted by M. P. A. Fisher et al. [43]. Even long-range dipolar interactions [11] can be included in the Bose-Hubbard Hamiltonian (1.13), which can lead to new quantum phases in addition to the ones mentioned above like supersolid, checkerboard and collapse phases [44].

An exact numerical solution of the Bose-Hubbard model for a two-colour superlattice[1] with a sinusoidal modulation of the potential wells has been performed by R. Roth and K. Burnett [46]. Such an exact diagonalization is only possible for very small systems as the dimension of the Bose-Hubbard Hilbert space grows according to $(M + N - 1)!/(M!(N - 1)!)$, where N denotes the number of sites and M denotes the number of atoms in the lattice. For a relatively small system of $N = 8$ sites and $M = 8$ atoms the solution of the eigenvalue problem already requires the diagonalization of a 6435×6435 matrix [47].

A numerical analysis of the Bose-Hubbard model with a purely random potential has been performed by B. Damski et al. [48] and compared to the quasi-disordered superlattice. For both cases a dynamical phase transition from the Bose-glass phase to the superfluid phase was found. In the same paper a direct diagonalization of the 1D Anderson Hamiltonian for both potentials revealed a phase transition from the superfluid phase to the Anderson-glass phase as a function of the strength of the potential. In the quasi-disordered case, the periodicity of the superimposed lattice in the quasi-disordered case was reflected in a periodical structure of the localized domains.

[1]Two-colour superlattices are formed by the superposition of two standing-wave lattices with comparable amplitudes but different wavelengths. These superlattices, however, only provide a form of quasi disorder, not a truly disordered potential like a speckle pattern.

The first experimental evidence of the phase transition between the Mott-insulating phase and the Bose-glass phase has been found by L. Fallani et al. [45] for a bichromatic optical lattice superimposed on a perfect 1D lattice. The combination of time-of-flight measurements for different heights of the quasi-disordered potential, and the excitation spectra were seen as an indication that the system went from a Mott-insulator state over to a Bose-glass state with vanishing long-range order and a flat density of excitations.

1.2.2 Experiments with Optical Quasicrystals, Superlattices and Speckle Potentials

One possible realization of random optical potentials are optical quasicrystals [49]. Even though these potentials display long-range order they are not translation invariant, similar to the Penrose tiling [50]. The first experiment on atomic diffusion in an optical quasicrystal with five-fold symmetry was performed by L. Guidoni et al. [51] in 1999. A special configuration of five laser beams with an angular distance of 72° between the beams was used to create an optical quasicrystal with 5-fold symmetry (cf. Fig. **1.6**) in order to cool and trap the atoms. The time evolution of the variance was measured in the quasicrystal plane and in the perpendicular plane, where the atoms evolved in a periodic potential. In both cases a linear increase of the variance with time was observed as expected for a diffusive expansion of the atomic cloud. In addition, the experiment by L. Guidoni et al. clearly revealed a slower expansion in the quasicrystal plane with a reduced diffusion constant given by the slope of the variance. Suppression of diffusion was also observed by L. Sanchez-Palencia and L. Santos [17] in a numerical study of the Gross-Pitaevskii equation for the BEC wavefunction in a similar quasicrystal configuration with 5-fold symmetry.

The first experiment with a quasi one-dimensional Bose-Einstein condensate in a harmonic trap, subjected to a purely random speckle potential, was performed by J. E. Lye et al. [18]. In this experiment a strong damping of dipole and quadrupole oscillations [12] of the condensate in the presence of the optical potential was observed and analysed theoretically (cf. also [52]). Later work by the same group included measurements of the spatial variance and the centre-of-mass motion of the condensate, without the confining trapping potential, as a function of time, which clearly revealed a reduced expansion due to the disordered potential [19]. Recently J. E. Lye et al. [53] studied damped dipole oscillations of a Bose-Einstein condensate in a 1D incommensurate bichromatic lattice. A numerical study of an effective 1D Gross-Pitaevskii equation for a condensate in a similar bichromatic lattice revealed a strong destructive influence of the atom-atom interactions (controlled by a variation of the number of atoms for a fixed disorder strength) on initially localized states [53].

The same screening of Anderson localization by interactions for a condensate in an optical lattice with a superimposed disordered potential (both for a speckle and a pseudorandom potential) had been observed beforehand by T. Schulte et al. [20] (cf. also [24]). The experiment [20] also revealed a fragmentation of the initially immobile condensate in the

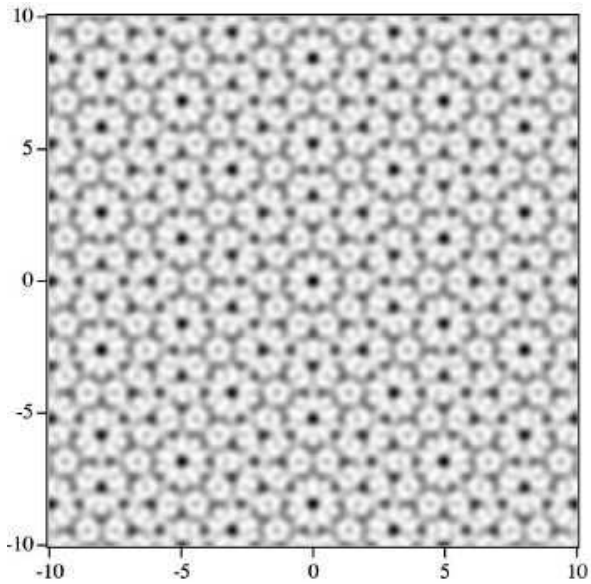

Figure 1.6:
Two-dimensional optical quasicrystal as obtained by the interference of five laser beams with an angular distance of 72° (from [51]).

presence of the disordered speckle potential. Similar observations of the fragmentation of the condensate have been reported in [18]. The fragmentation was attributed to the distribution of atoms in the wells of the disordered potential.

A detailed study of the suppression of transport of a quasi one-dimensional Bose-Einstein condensate in a random potential was carried out by D. Clément et al. [21] and in later experiments by the same group [22, 23]. These experiments showed a strong suppression of the expansion of the Bose-Einstein condensate in the presence of disorder, which was attributed to disorder-induced trapping of the Bose-Einstein condensate between two high peaks of the random potential. The authors distinguished between two different regions, namely the centre of the condensate, where interaction effects are very strong and the wings of the condensate, which are populated by almost free particles. The relevant length scale for this distinction is the healing length [12], $\xi_{\mathrm{h}} = (8\pi na)^{-1/2}$ (here, n is the density of atoms and a is the scattering length). The healing length defines the typical distance, below which spatial variations of the condensate wavefunction contribute significantly to the energy of the Bose-Einstein condensate [54]. At the centre of the condensate the density is high and ξ_{h} is small compared to the correlation length of speckle potential and the condensate can be described in the Thomas-Fermi regime [21]. In the wings of the condensate, the atomic density is low and ξ_{h} reaches the same order of magnitude as the correlation length [21]. In this region, where the interaction energy between the atoms becomes less important, Anderson localization effects are expected.

1.2.3 Alternative Concepts

Alternative concepts for the study of Bose-Einstein condensates in disordered optical potentials include evanescent wave mirrors, where the disordered potential for the condensate is created by the evanescent wave above a rough dielectric surface [55–57], the scattering of ultra-cold atoms on atomic impurities of a different atomic species in an optical lattice [58, 59], effective potential variations due to fermionic impurities for bosonic atoms [60], random magnetic potentials [61] on atom chips [62], and random on-site interactions on atom chips close to a Feshbach resonance [63]. A very promising new field are Fermi-Bose mixtures [11, 60, 64, 65]. A detailed numerical analysis of the transmission of a Bose-Einstein condensate through a one-dimensional random magnetic potential of an atom chip with a rough surface was performed by T. Paul et al. [66]. For small interactions a stationary flow was observed, displaying an exponential decay of the transmission, whereas for strong interactions the system displayed a time-dependent flow with an algebraic decay of the time-averaged transmission. The exponential decay of the transmission is a clear signature of localization, which is destroyed for strong interactions.

Most of the presented results in this section have been obtained for 1D systems in the interaction-dominated regime. Localization effects in this regime are screened by the interactions. However, in the non-interacting case, Anderson localization effects are expected to become important. In the following, we will consider non-interacting particles subjected to a truly random speckle potential in two and in three dimensions.

Chapter 2

Speckle Theory and Numerical Implementation

When an atom is exposed to electromagnetic radiation, it is polarized, and its energy levels are shifted. In the dipolar approximation these light shifts are proportional to the field intensity evaluated at the centre of mass of the atom [67]. If the field intensity is space dependent, a moving atom experiences dipolar forces, due to the field-dependent light shifts, which alter its trajectory.

In the case of a speckle potential, the intensity varies randomly in space and assumes a different shape for each realization of the speckle potential. Generic transport properties of the atomic matter wave inside the speckle potential can only be obtained via statistical averages over different realizations. We will therefore need to take a closer look at the statistical properties of speckle potentials. The present chapter gives an introduction into the basic theory of speckle statistics following the review by J. W. Goodman [3].

A typical example of the granular intensity pattern, which is generally known as a speckle interference pattern, is shown in Fig. **2.1**. This speckle pattern has been created numerically

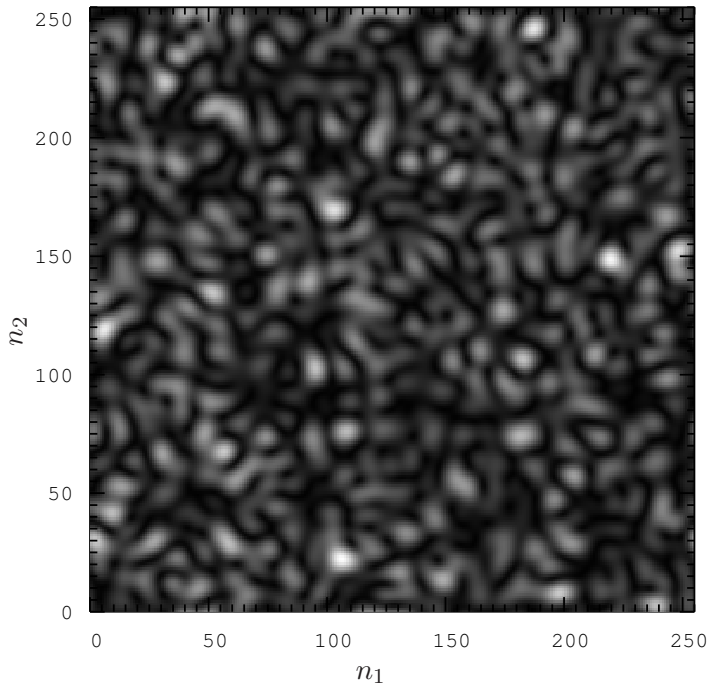

Figure 2.1: Contour plot of a numerically generated two-dimensional speckle pattern.

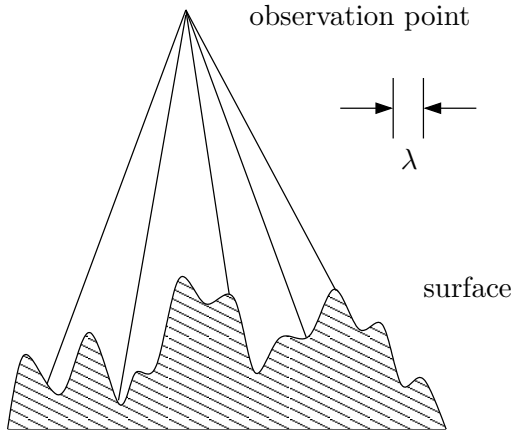

Figure 2.2:
Schematic representation of different coherent components to the speckle intensity pattern at the observation point, arising from different scattering regions on a surface that is rough on the scale of the optical wavelength λ. This plot is based on the description in [3]. Due to the large surface roughness, the phase difference between the different coherent components can be very large. For this reason a uniform phase distribution over the interval $[0, 2\pi]$ can be assumed.

on a 256×256 lattice as described in section (2.2). A real speckle pattern is obtained by the interference of many coherent partial waves with uniformly distributed random phases, originating from different regions of a disordered surface, which is illuminated by the coherent light of a laser. A schematic view of these coherent partial waves is shown in Fig. **2.2**.

2.1 Speckle Statistics

For polarized monochromatic light, scattered at a surface that is rough on the scale of the optical wavelength (cf. Fig. **2.2**), the amplitude $\mathcal{E}(\boldsymbol{r})$ of the electric field at the observation point $\boldsymbol{r}$ is given by a linear superposition of the amplitudes and phases from N completely uncorrelated elementary scatterers

$$\mathcal{E}(\boldsymbol{r}) = \frac{1}{\sqrt{N}} \sum_{k=1}^{N} |a_k| \, e^{i\varphi_k} \tag{2.1}$$

The sum in equation (2.1) can be regarded as a random walk in the complex plane, which finally leads to the electric field amplitude $\mathcal{E}(\boldsymbol{r}) = \mathrm{Re}[\mathcal{E}(\boldsymbol{r})] + i\mathrm{Im}[\mathcal{E}(\boldsymbol{r})]$. The phases of the elementary scatterers are uniformly distributed over the interval $[0, 2\pi]$. This implies that the real and the imaginary part of the resultant field have zero means and identical variances and are uncorrelated.

2.1.1 Probability Distribution

According to the *central limit theorem* $\mathrm{Re}[\mathcal{E}]$, $\mathrm{Im}[\mathcal{E}]$ and $\mathcal{E}$ itself eventually follow a Gaussian probability distribution, if the number of elementary scattering regions N grows to infinity

$$P(\mathrm{Re}[\mathcal{E}], \mathrm{Im}[\mathcal{E}]) = \frac{1}{2\pi\sigma^2}\ \exp\left[-\frac{\mathrm{Re}^2[\mathcal{E}] + \mathrm{Im}^2[\mathcal{E}]}{2\sigma^2}\right] = \frac{1}{2\pi\sigma^2}\ e^{-|\mathcal{E}|^2/2\sigma^2} \tag{2.2}$$

The joint intensity phase probability distribution function for the intensity[1] $I(\boldsymbol{r}) = |\mathcal{E}(\boldsymbol{r})|^2 = \mathrm{Re}^2[\mathcal{E}(\boldsymbol{r})] + \mathrm{Im}^2[\mathcal{E}(\boldsymbol{r})]$ and the phase $\phi(\boldsymbol{r}) = \arctan(\mathrm{Im}[\mathcal{E}(\boldsymbol{r})]/\mathrm{Re}[\mathcal{E}(\boldsymbol{r})])$ is given by the transformation

$$P(I, \phi) = P(\sqrt{I}\cos\phi, \sqrt{I}\sin\phi)\ |\det(\boldsymbol{J})| = \frac{1}{4\pi\sigma^2}\ e^{-I/2\sigma^2} \tag{2.3}$$

where $\det(\boldsymbol{J}) = \frac{1}{2}$ is the determinant of the corresponding Jacobi matrix. From the joint probability density, the probability density for the intensity or the phase alone is obtained by integrating over I or ϕ, respectively

$$P(I) = \int_0^{2\pi} \mathrm{d}\phi\ P(I, \phi) = \frac{1}{2\sigma^2}\ e^{-I/2\sigma^2} \tag{2.4a}$$

$$P(\phi) = \int_0^{\infty} \mathrm{d}I\ P(I, \phi) = \frac{1}{2\pi} \tag{2.4b}$$

One finds again a uniform distribution for the phase. The intensity follows a negative exponential or Rayleigh distribution. The nth moment of the intensity is given by

$$\overline{I^n} = \int_0^{\infty} \mathrm{d}I\ P(I)\ I^n = n!\,\overline{I}^n \tag{2.5}$$

In particular, the mean value of the intensity is given by $\overline{I} = 2\sigma^2$, and the standard deviation $\Delta I = \sqrt{\overline{I^2} - \overline{I}^2} = \overline{I}$ is equal to the mean intensity itself. The probability that the intensity exceeds a certain value I_0 amounts to the negative exponential function

$$P_0(I_0) = \int_{I_0}^{\infty} \mathrm{d}I\ P(I) = e^{-I_0/\overline{I}} \tag{2.6}$$

2.1.2 Correlation Functions

Random Gaussian variables have the remarkable property that all higher-order correlations among them are expressible in terms of second-order correlations between pairs. This is known as the *Gaussian moment theorem* [68]. For the intensity-intensity correlation function

[1] The actual intensity is given by $I(\boldsymbol{r}) = \frac{1}{2}\, c\, \epsilon_0\, |\mathcal{E}(\boldsymbol{r})|^2$, where c is the speed of light and ϵ_0 is the permittivity of free space. In this chapter, we only consider the reduced intensity for $\frac{1}{2}\, c\, \epsilon_0 = 1$.

$\overline{I(\boldsymbol{r})I(\boldsymbol{r}')} = \overline{|\mathcal{E}(\boldsymbol{r})|^2\,|\mathcal{E}(\boldsymbol{r}')|^2}$ we find

$$\begin{aligned}\overline{I(\boldsymbol{r})I(\boldsymbol{r}')} &= \overline{|\mathcal{E}(\boldsymbol{r})|^2}\;\overline{|\mathcal{E}(\boldsymbol{r}')|^2} + \overline{\mathcal{E}^*(\boldsymbol{r})\mathcal{E}(\boldsymbol{r}')}\;\overline{\mathcal{E}^*(\boldsymbol{r}')\mathcal{E}(\boldsymbol{r})} \\ &= \overline{I}^{\,2}\left(1 + \left|\gamma(\boldsymbol{r}-\boldsymbol{r}')\right|^2\right)\end{aligned} \tag{2.7}$$

since the mean value of the intensity $\overline{I} = \overline{I(\boldsymbol{r})} = \overline{|\mathcal{E}(\boldsymbol{r})|^2}$ is constant. The function $\gamma(\boldsymbol{r})$ defines the complex degree of coherence

$$\gamma(\boldsymbol{r}) = \frac{\overline{\mathcal{E}^*(\boldsymbol{r}+\boldsymbol{r}')\mathcal{E}(\boldsymbol{r}')}}{\overline{|\mathcal{E}(\boldsymbol{r})|^2}} \tag{2.8}$$

Second-order correlations between fluctuations of the intensity are calculated in the same way. If we write $I(\boldsymbol{r}) = \overline{I} + J(\boldsymbol{r})$, where $J(\boldsymbol{r})$ are fluctuations with zero mean $\overline{J(\boldsymbol{r})} = 0$ around the constant mean value $\overline{I}$, the two-point intensity correlation function can be expressed as

$$\overline{I(\boldsymbol{r})I(\boldsymbol{r}')} = \overline{I}^{\,2} + \overline{J(\boldsymbol{r})J(\boldsymbol{r}')} \tag{2.9}$$

The correlation function of the intensity fluctuations is then given by

$$\overline{J(\boldsymbol{r})J(\boldsymbol{r}')} = \overline{I}^{\,2}\left|\gamma(\boldsymbol{r}-\boldsymbol{r}')\right|^2 \tag{2.10}$$

For an infinite medium, the spatial correlation function of the fluctuations $J(\boldsymbol{r})$ is translation invariant. It only depends on the relative distance vector $\boldsymbol{\rho} = \boldsymbol{r} - \boldsymbol{r}'$. According to the *Wiener-Khintchine theorem* [68], the correlation function $\mathcal{P}_J(\boldsymbol{\rho}) = \overline{J(\boldsymbol{r})J(\boldsymbol{r}')}$ of a stationary random process and the spectral density (or the power spectrum) of the process $\mathcal{P}_J(\boldsymbol{q})$ form a Fourier transform pair: $\mathcal{P}_J(\boldsymbol{q}) = \mathcal{F}_d[\mathcal{P}_J(\boldsymbol{\rho})]$. The d-dimensional Fourier transform $\mathcal{F}_d[f(\boldsymbol{\rho})]$ is defined in appendix C. $\mathcal{P}_J(\boldsymbol{q})$ and $\mathcal{P}_J(\boldsymbol{\rho})$ are given by[2]

$$\mathcal{P}_J(\boldsymbol{q}) = \int \mathrm{d}\boldsymbol{\rho}\;\mathcal{P}_J(\boldsymbol{\rho})\,e^{-i\boldsymbol{q}\cdot\boldsymbol{\rho}} \qquad\qquad \mathcal{P}_J(\boldsymbol{\rho}) = \int \frac{\mathrm{d}\boldsymbol{q}}{(2\pi)^d}\;\mathcal{P}_J(\boldsymbol{q})\,e^{i\boldsymbol{q}\cdot\boldsymbol{\rho}} \tag{2.11}$$

Equivalently, the Fourier transform of $J(\boldsymbol{r})$ can be defined as

$$J(\boldsymbol{q}) = \int \mathrm{d}\boldsymbol{r}\;J(\boldsymbol{r})\,e^{-i\boldsymbol{q}\cdot\boldsymbol{r}} \qquad\qquad J(\boldsymbol{r}) = \int \frac{\mathrm{d}\boldsymbol{q}}{(2\pi)^d}\;J(\boldsymbol{q})\,e^{i\boldsymbol{q}\cdot\boldsymbol{r}} \tag{2.12}$$

With (2.11) and (2.12) the correlation function for the intensity fluctuation in Fourier space

[2] Throughout this work the Fourier transform is defined in this way. The factor $(2\pi)^{-d}$ is always attributed to the integral over $\mathrm{d}\boldsymbol{k}$. The Fourier transform and the function itself are denoted by the same symbol although they are of course different functions. Both functions are distinguished by their respective argument. The d-dimensional integration element $\mathrm{d}^d\rho$ is written as $\mathrm{d}\boldsymbol{\rho}$.

can be expressed as

$$\begin{aligned}\overline{J(\boldsymbol{q})J(\boldsymbol{q}')} &= \iint \mathrm{d}\boldsymbol{r}\,\mathrm{d}\boldsymbol{r}'\;\overline{J(\boldsymbol{r})J(\boldsymbol{r}')}\,e^{-i\boldsymbol{q}'\cdot\boldsymbol{r}'}\,e^{-i\boldsymbol{q}\cdot\boldsymbol{r}} \\ &= \int \mathrm{d}\boldsymbol{r}'\;e^{-i(\boldsymbol{q}'+\boldsymbol{q})\cdot\boldsymbol{r}'}\int \mathrm{d}\boldsymbol{\rho}\;\mathcal{P}_J(\boldsymbol{\rho})\,e^{-i\boldsymbol{q}\cdot\boldsymbol{\rho}} = (2\pi)^d\delta(\boldsymbol{q}+\boldsymbol{q}')\,\mathcal{P}_J(\boldsymbol{q}) \end{aligned} \tag{2.13}$$

In order to calculate higher-order correlation functions, one can resort to the *Gaussian moment theorem*. Each correlation function of order n can be expressed as a sum of $n!$ pair correlation functions. In terms of the average intensity $\overline{I} = \overline{I_i} = \overline{\mathcal{E}^*(\boldsymbol{r}_i)\mathcal{E}(\boldsymbol{r}_i)}$ and the complex degree of coherence $\gamma_{ij} = \overline{\mathcal{E}^*(\boldsymbol{r}_i)\mathcal{E}(\boldsymbol{r}_j)}/\overline{I}$ (cf. (2.8)), the third-order correlation function reads

$$\begin{aligned}\overline{I_1 I_2 I_3} &= \overline{I}^{\,3}\left(\gamma_{11}\gamma_{22}\gamma_{33} + \gamma_{11}\gamma_{23}\gamma_{32} + \gamma_{22}\gamma_{13}\gamma_{31} + \gamma_{33}\gamma_{12}\gamma_{21} + \gamma_{12}\gamma_{23}\gamma_{31} + \gamma_{13}\gamma_{21}\gamma_{32}\right) \\ &= \overline{I}^{\,3}\left(1 + |\gamma_{12}|^2 + |\gamma_{23}|^2 + |\gamma_{31}|^2 + 2\,\mathrm{Re}[\gamma_{12}\gamma_{23}\gamma_{31}]\right) \end{aligned} \tag{2.14}$$

On the other hand, the third-order correlation function can be expressed in terms of the fluctuations J_i. Since $I_i = \overline{I} + J_i$ and $\overline{J_i} = 0$, we have

$$\overline{I_1 I_2 I_3} = \overline{I}^{\,3} + \overline{I}\left(\overline{J_1 J_2} + \overline{J_2 J_3} + \overline{J_3 J_1}\right) + \overline{J_1 J_2 J_3} \tag{2.15}$$

The comparison between (2.15) and (2.14) yields the third-order correlation function of the intensity fluctuations

$$\overline{J(\boldsymbol{r})J(\boldsymbol{r}')J(\boldsymbol{r}'')} = 2\overline{I}^{\,3}\,\mathrm{Re}\big[\gamma(\boldsymbol{r}-\boldsymbol{r}')\,\gamma(\boldsymbol{r}'-\boldsymbol{r}'')\,\gamma(\boldsymbol{r}-\boldsymbol{r}'')\big] \tag{2.16}$$

2.1.3 2D Speckle

A two-dimensional speckle can be produced by reflection of a laser from a rough surface (cf. Fig. **2.2**) or by transmission through a random phase mask (diffusor) as shown schematically in Fig. **2.3**.

In the far field from the diffusor the speckle interference pattern can be regarded as quasi two-dimensional, since the speckle grains are very elongated in the z-direction, orthogonal to the optical axis. According to the Huygens-Fresnel principle [69], the electric field at the far field observation plane (x, y) is uniquely determined by the impulse response function $h(x, y, \eta, \xi)$ and the aperture function $\mathcal{A}(\eta, \xi)$

$$\mathcal{E}(x, y) = \iint_{-\infty}^{\infty} \mathrm{d}\eta\,\mathrm{d}\xi\;h(x, y, \eta, \xi)\mathcal{A}(\eta, \xi) \tag{2.17}$$

where $\mathcal{A}(\eta, \xi)$ decreases to zero outside the aperture region in accordance with the Kirchhoff boundary conditions. The Huygens-Fresnel principle states that the field at the observation plane originates from the superposition of an infinitely large number of fictitious point sources

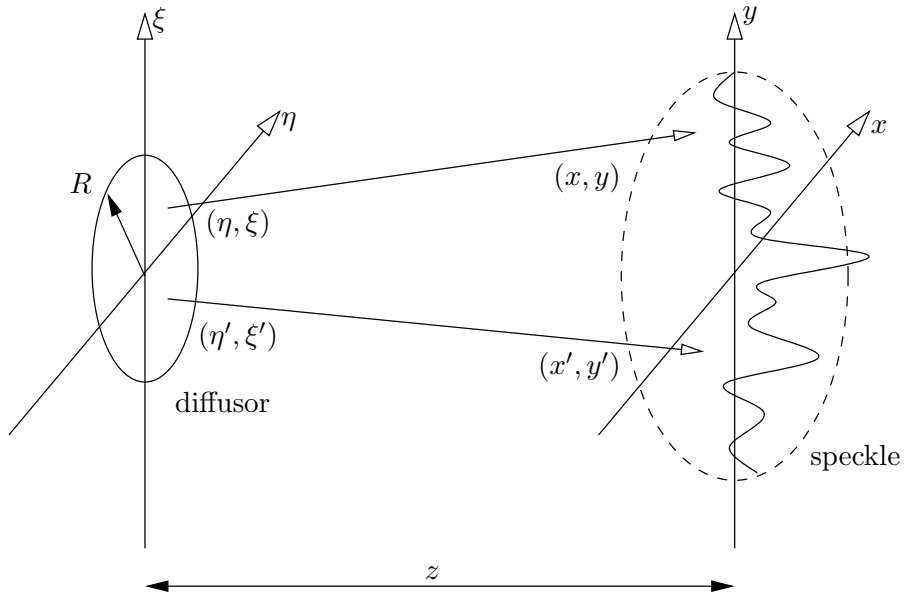

Figure 2.3:
Two-dimensional speckle geometry. The speckle pattern is produced by transmission of a coherent monochromatic laser beam through a circular diffusor of radius R in the (η, ξ)-plane. The speckle interference pattern is observed in the (x, y)-plane located at the distance z from the diffusor.

inside the aperture region. If the distance between the aperture and the observation plane is larger than the extension of the aperture itself ($z \gg R$), the impulse response function can be approximated by

$$h(x, y, \eta, \xi) \approx \frac{1}{i\lambda z} \exp\left[ik_{\mathrm{L}}\sqrt{z^2 + (x-\eta)^2 + (y-\xi)^2}\right] \tag{2.18}$$

As a further simplification, for $z \gg \{(x-\eta),\ (y-\xi)\}$, one may resort to the Fresnel approximation, which consists in a binomial expansion of the exponent

$$h(x, y, \eta, \xi) \approx \frac{e^{ik_{\mathrm{L}}z}}{i\lambda z} \exp\left[\frac{ik_{\mathrm{L}}}{2z}\big((x-\eta)^2 + (y-\xi)^2\big)\right] \tag{2.19}$$

or, for even larger distances z, to the stronger Fraunhofer approximation, which in addition allows to neglect the quadratic exponents η^2 and ξ^2 resulting in

$$h(x, y, \eta, \xi) \approx \frac{e^{ik_{\mathrm{L}}z}}{i\lambda z} \exp\left[\frac{ik_{\mathrm{L}}}{2z}\big((x^2 + y^2) - 2(x\eta + y\xi)\big)\right] \tag{2.20}$$

Reinserting the Fraunhofer approximation for the impulse response function into (2.17), the electric field can be expressed as

$$\mathcal{E}(x, y) = \frac{e^{ik_{\mathrm{L}}z}}{i\lambda z} \exp\left[\frac{ik_{\mathrm{L}}}{2z}(x^2 + y^2)\right] \iint\limits_{-\infty}^{\infty} \mathrm{d}\eta\, \mathrm{d}\xi\ \exp\left[-\frac{ik_{\mathrm{L}}}{z}(x\eta + y\xi)\right] \mathcal{A}(\eta, \xi) \tag{2.21}$$

Apart from the multiplicative amplitude and phase factor the electric field is thus found as a Fourier transform of the aperture function $\mathcal{A}(\eta,\xi)$. Inserting equation (2.21) into the second-order field correlation function $\overline{\mathcal{E}^*(x,y)\,\mathcal{E}(x',y')}$, one obtains

$$\overline{\mathcal{E}^*(x,y)\,\mathcal{E}(x',y')} = \frac{1}{\lambda^2 z^2}\,\exp\left[\frac{-ik_\mathrm{L}}{2z}\left((x^2-x'^2)+(y^2-y'^2)\right)\right] \iiiint\limits_{-\infty}^{\infty} \mathrm{d}\eta\,\mathrm{d}\eta'\,\mathrm{d}\xi\,\mathrm{d}\xi'\;\overline{\mathcal{A}^*(\eta,\xi)\,\mathcal{A}(\eta',\xi')}\;\exp\left[\frac{ik_\mathrm{L}}{z}(x\eta+y\xi-x'\eta'-y'\xi')\right] \tag{2.22}$$

Furthermore, if one assumes that the microstructure of the surface or the diffusor is so fine as to be unresolvable by a lens of the size of the observation region, the electric field at the diffusor appears uncorrelated [3], i. e.

$$\overline{\mathcal{A}^*(\eta,\xi)\,\mathcal{A}(\eta',\xi')} \propto I(\eta,\xi)\,\delta(\eta-\eta')\,\delta(\xi-\xi') \tag{2.23}$$

where $I(\eta,\xi)$ is the intensity right at the aperture. Making use of (2.22) and (2.23) the previously defined expression for the complex degree of coherence (2.8) reads

$$\gamma(x-x',y-y') = \frac{e^{-ik_\mathrm{L}\psi}\iint\limits_{-\infty}^{\infty}\mathrm{d}\eta\,\mathrm{d}\xi\;I(\eta,\xi)\;\exp\left[\frac{ik_\mathrm{L}}{z}\left((x-x')\eta+(y-y')\xi\right)\right]}{\iint\limits_{-\infty}^{\infty}\mathrm{d}\eta\,\mathrm{d}\xi\;I(\eta,\xi)} \tag{2.24}$$

with $\psi = \left((x^2-x'^2)+(y^2-y'^2)\right)/2z$. The phase factor $\exp[-ik_\mathrm{L}\psi]$ becomes obsolete if only the modulus of the complex degree of coherence is required.

Complex Degree of Coherence

Let us assume a circular diffusor of radius R that is uniformly illuminated by coherent light from a laser such that the intensity $I(\eta,\xi)$ can be regarded as constant over the whole range of the diffusor and zero otherwise. Up to the phase factor the complex degree of coherence is then given by

$$\begin{aligned}\gamma(x-x',y-y') &= \frac{1}{\pi R^2}\int_0^{2\pi}\mathrm{d}\varphi\int_0^R \mathrm{d}\omega\;\omega\;\exp\left[\frac{i\omega k_\mathrm{L}\rho}{z}\cos\varphi\right]\\ &= \frac{2}{R^2}\int_0^R \mathrm{d}\omega\;\omega\;\mathcal{J}_0(k_\mathrm{L}\omega\rho/z)\end{aligned} \tag{2.25}$$

with $\rho = \sqrt{(x-x')^2 + (y-y')^2}$ and $\omega = \sqrt{\eta^2 + \xi^2}$. At this stage one can make use of the following recurrence relation for Bessel functions

$$\frac{d}{dx}\left(x^{n+1}\mathcal{J}_{n+1}(x)\right) = x^{n+1}\mathcal{J}_n(x) \tag{2.26}$$

which for $n = 0$ upon integration gives

$$\int_0^x \mathrm{d}x'\; x'\mathcal{J}_0(x') = x\mathcal{J}_1(x) \tag{2.27}$$

Omitting the phase factor, the complex degree of coherence for the circular diffusor is thus given by [3]

$$\gamma(\boldsymbol{\rho}) = 2\,\frac{\mathcal{J}_1(\rho/\zeta)}{\rho/\zeta} \tag{2.28}$$

with $\zeta = z/(k_\mathrm{L}R)$ and $\boldsymbol{\rho} = \boldsymbol{r} - \boldsymbol{r}'$. This result obtained by Goodman corresponds to the *van Cittert-Zernike theorem* [70], which states that the complex degree of coherence for scattered light can be compared to the diffraction pattern of a spherical wave by an aperture of the same size and shape as the diffusor. For a circular diffusor the complex degree of coherence is identical to the Airy diffraction pattern.

The complex degree of coherence defines the characteristic length scale $\zeta = 1/(\alpha k_\mathrm{L})$, where the coefficient $\alpha = R/z$ denotes the numerical aperture. This characteristic length can be identified with the correlation length of the intensity fluctuations in the observation plane. In principle, the definition of the correlation length is not unique. A possible alternative definition is given by the first zero of the complex degree of coherence $\gamma(\zeta_0) = 0$ leading to $\zeta_0 = 3.83\,\zeta$.

The Bessel function $\mathcal{J}_1(x)$ in (2.28) for $|x| \to \infty$ decreases asymptotically with the envelope function $f(x) = \sqrt{2/(\pi x)}$ [71]. For large arguments, i. e. $x = \rho/\zeta \gg 1$, the complex degree of coherence, $\gamma(x)$ thus decreases algebraically with the envelope function $g(x) = \sqrt{8/\pi}\,x^{-3/2}$, while the correlation function of the intensity fluctuations (2.10) $\mathcal{P}_J(x) \propto |\gamma(x)|^2$ is asymptotically bound by $g^2(x) = (8/\pi)x^{-3}$.

Power Spectrum

The power spectrum can be obtained via the two-dimensional Fourier transform (C.1) of the complex degree of coherence $\gamma(\boldsymbol{k}) = \mathcal{F}_2[\gamma(\boldsymbol{\rho})]$ by means of the convolution

$$\mathcal{P}_J(\boldsymbol{q}) = \overline{I}^2 \int \frac{\mathrm{d}\boldsymbol{k}}{(2\pi)^d}\,\gamma(\boldsymbol{k})\gamma(\boldsymbol{q}-\boldsymbol{k}) \tag{2.29}$$

As we have seen, the complex degree of coherence resembles the diffraction pattern of a circular aperture. Since $\gamma(\boldsymbol{\rho})$ is in fact an isotropic function, its Fourier transform given by

(C.1) is also isotropic. It has the form of a disk

$$\gamma(\boldsymbol{k}) = 2\pi \int_0^\infty \mathrm{d}\rho\, \rho\, \gamma(\boldsymbol{\rho})\, \mathcal{J}_0(k\rho) = \frac{4\pi}{k_\zeta^2}\Theta(k_\zeta - k) \tag{2.30}$$

Here, k_ζ denotes the characteristic wavenumber of the correlation defined as $k_\zeta = 1/\zeta$. $\Theta(x)$ is the Heaviside function. The power spectrum can thus be obtained as the intersection area of two identical disks of the form (2.30)

$$\mathcal{P}_J(\boldsymbol{q}) = \frac{8\overline{I}^2}{k_\zeta^2}\left[\arccos\frac{q}{2k_\zeta} - \frac{q}{2k_\zeta}\sqrt{1-\left(\frac{q}{2k_\zeta}\right)^2}\right]\Theta\left(1-\frac{q}{2k_\zeta}\right) \tag{2.31}$$

2.1.4 3D Speckle

To produce a three-dimensional disordered configuration, the speckle grains are obtained as the interference pattern of many wavevectors spanning the largest possible angular aperture. Ideally, this situation corresponds to the interference pattern obtained inside an optical cavity, for example an integrating sphere. The complex degree of coherence is then given by [72]

$$\gamma(\boldsymbol{\rho}) = \frac{\sin(k_\mathrm{L}\rho)}{k_\mathrm{L}\rho} \tag{2.32}$$

where the correlation length is now $\zeta = 1/k_\mathrm{L}$, corresponding to a numerical aperture $\alpha \to 1$. The three-dimensional Fourier transform (C.3) of (2.32), $\gamma(\boldsymbol{k}) = \mathcal{F}_3[\gamma(\boldsymbol{\rho})]$, yields a spherical shell with radius k_L

$$\gamma(\boldsymbol{k}) = \frac{2\pi^2}{k_\mathrm{L}^2}\,\delta(k - k_\mathrm{L}) \tag{2.33}$$

Since the Fourier transform of the product of two functions can be expressed as the convolution of their individual Fourier transforms, the power spectrum of (2.32) can be described as a convolution of two identical spherical shells

$$\mathcal{P}_J(\boldsymbol{q}) = \frac{\overline{I}^2\pi}{2k_\mathrm{L}^4}\int_0^{2\pi}\mathrm{d}\varphi\int_0^\pi \mathrm{d}\vartheta\int_0^\infty \mathrm{d}k\, k^2 \sin\vartheta\, \delta(\left|\boldsymbol{k}-\tfrac{\boldsymbol{q}}{2}\right| - k_\mathrm{L})\,\delta(\left|\boldsymbol{k}+\tfrac{\boldsymbol{q}}{2}\right| - k_\mathrm{L}) \tag{2.34}$$

Evaluating this integral, the power spectrum takes the form

$$\mathcal{P}_J(\boldsymbol{q}) = \frac{\overline{I}^2\pi^2}{k_\mathrm{L}^2 q}\,\Theta(2k_\mathrm{L} - q) \tag{2.35}$$

2.2 Numerical Implementation of a Speckle Pattern

As demonstrated by J. M. Huntley [73] and P. Horak et al. [74], a 2D speckle potential can be implemented numerically in the following way. First, since the real part and the imaginary part of the electric field are Gaussian random variables according to the general speckle property (2.2), two arrays of $L \times L$ elements are filled with random numbers, drawn from a

Gaussian probability distribution with a standard deviation of 1. This creates a completely uncorrelated spatially random electric field $\mathcal{E}'(u_1, u_2)$, where the indices u_1 and u_2 indicate the sites of the $L \times L$ lattice. In a real setup, the spatial correlation of the intensity is obtained as the result of the finite extension of the diffusor. This can be reproduced numerically in a second step by multiplying the Fourier transform of the electric field with a cut-off function $\mathcal{X}(m_1, m_2)$ reflecting the size and the shape of the diffusor. The indices m_i $(i = 1, 2)$ run from 0 to $L - 1$ indicating the lattice sites of the respective $L \times L$ lattice in Fourier space.

For a circular diffusor the numerical aperture function can be described by the two-dimensional Fourier transform

$$\mathcal{A}(m_1, m_2) \propto \frac{1}{L^2} \sum_{u_1=0}^{L-1} \sum_{u_2=0}^{L-1} \mathcal{E}'(u_1, u_2) \exp\left[\frac{2\pi i}{L}(u_1 m_1 + u_2 m_2)\right] \mathcal{X}(m_1, m_2) \tag{2.36}$$

with the cut-off function

$$\mathcal{X}(m_1, m_2) = \Theta\Big(M - \sqrt{\big((L-1)/2 - m_1\big)^2 + \big((L-1)/2 - m_2\big)^2}\Big) \tag{2.37}$$

Here, M is the radius of the circular aperture. The distance between the centre of the lattice and the lattice site (m_1, m_2) is given by $\rho = \sqrt{x^2 + y^2}$ with $x = ((L-1)/2 - m_1)$ and $y = ((L-1)/2 - m_2)$. If this distance is smaller than the aperture radius M, the cut-off function is 1, otherwise it is 0.

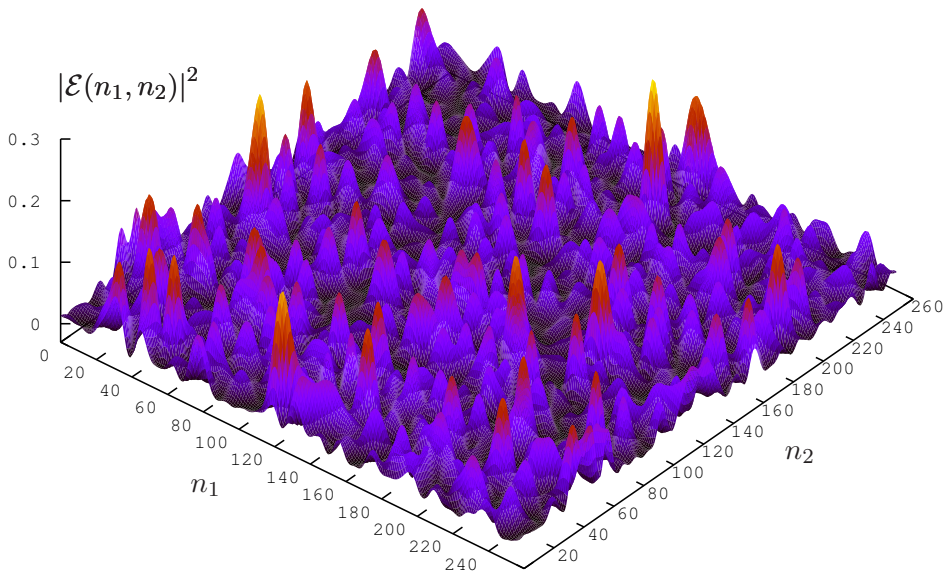

Figure 2.4:
Two-dimensional speckle pattern on a lattice with $N = 256 \times 256$ created with an aperture radius of $M = 16$ sites. The same speckle pattern is given as a contour plot in Fig. **2.1**. Obviously the average height of the speckle peaks is larger than the average depth of the speckle valleys. This characteristic feature of the speckle potential is a consequence of the Rayleigh intensity distribution (2.6). The characteristic length ζ, defined by the 2D speckle correlation function, corresponds to $\zeta/a = \sqrt{N}/(2\pi M) \approx 2.55$ where a is the lattice constant (cf. Fig. **2.6(a)**).

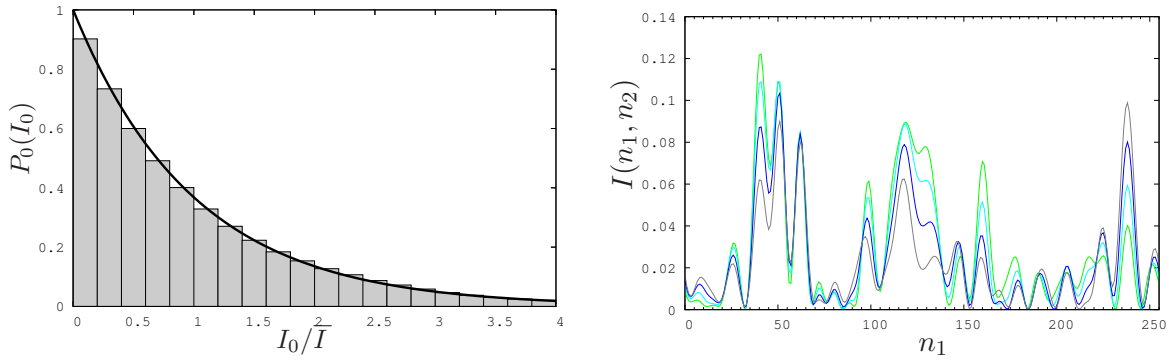

(a) Intensity distribution (b) 1D cut through the potential

Figure 2.5:
(a) Histogram of the intensity of the numerically generated speckle pattern in Fig. **2.4**. The solid curve is given by the function $f(x) = e^{-x}$ with $x = I_0/\overline{I}$ as predicted by (2.6). (b) One-dimensional cut of the numerical speckle pattern in Fig. **2.4** as a function of n_1 for $L = 256$, $M = 16$, and $n_2 \in \{1, 0, L, L-1\}$ (green, light blue, blue, grey). The speckle pattern is periodic in both directions n_1 and n_2.

The final speckle pattern $\mathcal{E}(n_1, n_2)$ is obtained as the inverse Fourier transform of the aperture function (2.36)

$$\mathcal{E}(n_1, n_2) \propto \sum_{m_1=0}^{L-1} \sum_{m_2=0}^{L-1} A(m_1, m_2) \exp\left[-\frac{2\pi i}{L}(n_1 m_1 + n_2 m_2)\right] \tag{2.38}$$

Intensity Distribution

The speckle intensity $I(n_1, n_2)$ at the observation plane (n_1, n_2) is calculated as $I(n_1, n_2) = |\mathcal{E}(n_1, n_2)|^2$. An example for a numerical speckle pattern generated in this way is plotted in Fig. **2.4**. In this example the aperture radius covers $M = 16$ sites. The full speckle pattern is shown as a contour plot in Fig. **2.1**. The numerical speckle nicely confirms the expected Rayleigh distribution (2.6). Indeed one finds a negative exponential decay of the probability $P_0(I_0)$ as a function of $I_0/\overline{I}$ as shown in Fig. **2.5(a)**.

The numerical speckle pattern obtained in the described way is periodic. This can be seen by looking at a one-dimensional cut through the speckle pattern as displayed in Fig. **2.5(b)**, where the first two lines and the last two lines of the lattice are plotted together. The transition from one end of the lattice to the other remains continuous. Any cut through the two-dimensional speckle pattern provides a one-dimensional speckle pattern with the same correlation function.

Correlation Function

In our current numerical implementation we calculate the square of the complex degree of coherence according to (2.7)

$$|\gamma(n_1, n_2)|^2 = \overline{I_0\, I(n_1, n_2)}/\overline{I}_0 - 1 \tag{2.39}$$

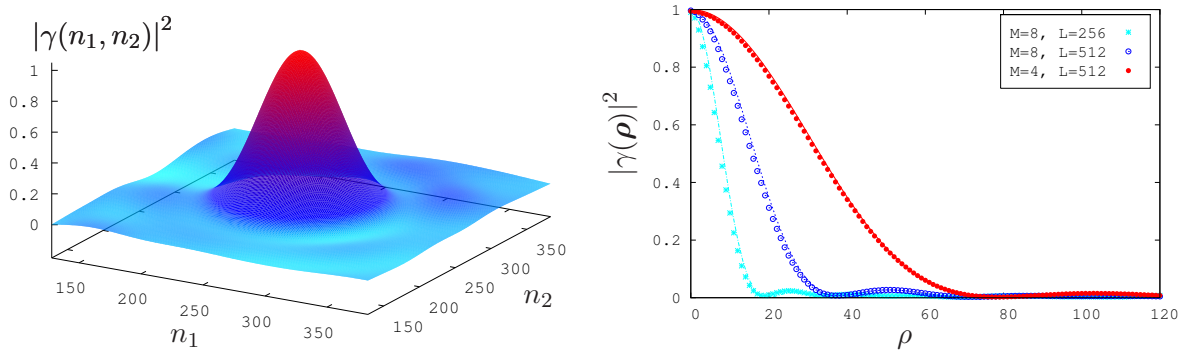

(a) Numerical correlation function

(b) Averaged numerical correlation function

Figure 2.6:
(a) Plot of the numerical correlation function $|\gamma(n_1, n_2)|^2$ for a speckle pattern with $N = 512 \times 512$ sites, 10000 realizations of disorder, and an aperture radius of $M = 4$ sites. (b) Comparison between the numerical and the analytical correlation function for the parameter pairs $(M, L) \in \{(4, 512), (8, 512), (8, 256)\}$ and 10000 realizations of disorder. The numerical correlation function has been averaged over annuli of the width of one lattice site. The correlation length is given by $\zeta = L/(2\pi M)$. The dotted curves represent the numerical result for the correlation function on a lattice with $L \times L$ sites for an aperture of M sites. The solid curves represent the analytical result (2.40).

where I_0 is the speckle intensity at the centre of the lattice, $I(n_1, n_2)$ is the intensity at each lattice point, and $\overline{I}_0$ is the average intensity of the speckle pattern at the center. The average in this case is done over a large number of realizations of the speckle potential. The result of (2.39) is stored in a new array of $L \times L$ sites. A three-dimensional plot of this array for $L = 512$ sites, 10000 realizations of the speckle potential, and the aperture radius $M = 4$ is shown in Fig. **2.6(a)**. The resulting correlation function corresponds closely to the analytical result (cf. (2.28))

$$|\gamma(\boldsymbol{\rho})|^2 = \left|2\frac{\mathcal{J}_1(\rho/\zeta)}{\rho/\zeta}\right|^2 \tag{2.40}$$

Here, the distance to the centre is given by $\rho = \sqrt{x^2 + y^2}$. The position $x = ((L-1)/2 - m_1)$ and $y = ((L-1)/2 - m_2)$ relative to the centre, as well as the correlation length ζ, are measured in units of the lattice constant $a = 1$. In order to determine the exact correlation length, the resulting array for $|\gamma(n_1, n_2)|^2$ is averaged further over annuli of the width of one lattice site. The result can be compared to the function (2.40) as shown in Fig. **2.6(b)** for different lattices and different apertures. The characteristic length ζ in (2.40) can be identified with the correlation length $\zeta = L/(2\pi M)$. Apart from minor deviations due to finite size effects the numerical correlation function corresponds closely to the analytical result. The best result is obtained for the smallest ratio M/L.

2.3 Summary

In this chapter, we have introduced some of the basic aspects of speckle statistics. As a fundamental result we have determined the correlation functions for the intensity fluctuations

of a speckle pattern in two and three dimensions (cf. (2.28) and (2.32)). In addition, we have determined the corresponding power spectra (cf. (2.31) and (2.35)), which are going to be a main ingredient for the calculation of the average transport parameters in chapters 4 to 6. Furthermore, we have verified the correlation function and the intensity distribution for a numerically created two-dimensional speckle potential. Following the work of B. Damski et al. [48] on the numerical solution of the one-dimensional Anderson model in the presence of a speckle potential, our numerical implementation of the speckle pattern can be used as an example for correlated disordered on-site energies in the 1D and the 2D Anderson model. This is described in the following chapter.

Chapter 3

Numerical Study of the Anderson Model

The current chapter is focussed on the Anderson or tight-binding model, which constitutes a simple model for electron transport in disordered systems, and is one of the best ways to illustrate the localization phenomenon. The Anderson model can provide immediate numerical evidence for localization and allows to calculate numerically the localization length in discrete multidimensional systems. Since the first seminal paper by P. W. Anderson [1] to whom the Anderson model owes its name, it has been the basis of one of the most intensively studied fields in condensed matter physics (cf. for example [6, 29, 75–77]).

The one-dimensional Anderson model can be reformulated in terms of a transfer matrix equation, a technique that was originally introduced by F. J. Dyson [78] and H. Schmidt [79] for the vibrations of a disordered harmonic chain. Only for a limited number of cases, for example for the Lloyd model or in the case of a binary disorder distribution [80], this transfer matrix description allows for an exact analytical solution of the Anderson model. For weak disorder, within the one-dimensional transfer matrix description, it is possible to obtain approximative expressions [80] for the integrated density of states and indirectly, via the Lyapunov exponent, for the localization length. In most cases, however, and in particular for higher dimensions, the Anderson model can only be solved numerically. With the development of modern computational resources rapid progress has been made regarding the numerical solution of the underlying eigenvalue problem [81, 82].

This chapter is intended to give a short introduction on the numerical solution of the tight-binding model. In contrast to most studies concerned with localization phenomena in the framework of the Anderson model, which rely on an uncorrelated uniform distribution of the on-site energies (cf. for example [75]), we are also going to use the numerically generated speckle potential introduced in the previous chapter as an example for correlated on-site energies. First results on the numerical solution of the one-dimensional tight-binding model making use of a speckle potential have been published recently by B. Damski et al. [48]. In this case, the tight-binding model can be regarded as the special case of an interaction-free Bose-Hubbard model for atoms in a disordered optical potential.

3.1 The Tight-Binding Model

The one-dimensional tight-binding model is described by the Hamiltonian [80]

$$(\mathcal{H}\psi)_n = t_{n,n+1}\,\psi_{n+1} + t_{n,n-1}\,\psi_{n-1} + v_n\psi_n = \varepsilon\psi_n \tag{3.1}$$

with nearest neighbour hopping (or tunnelling) rates t and on-site energies v_n. The index runs over all lattice sites, i. e. $n = 1, \ldots, N$, for a lattice of N sites.

Disorder can be introduced in (3.1) either through the on-site energies or through the hopping rate. One speaks also of diagonal and non-diagonal disorder referring to the matrix representation of the Hamiltonian, where the on-site energies are the diagonal entries, whereas the hopping elements appear as non-diagonal elements. Of course, both kinds of disorder may also coexist. The physical effect, however, of both kinds of disorder is very similar. For this reason, it is sufficient to consider only diagonal disorder with a constant hopping rate $t = -1$ and random on-site energies v_n.

The tight-binding model can then be seen as a discrete one-dimensional Schrödinger equation, where the lattice site number n replaces the continuum variable x. The discrete Laplace operator is given by

$$\nabla^2\psi_n = \frac{1}{a^2}[\psi_{n+1} - 2\psi_n + \psi_{n-1}] \tag{3.2}$$

where a denotes the lattice constant. The potential and the energy in (3.1) are given in units of the characteristic energy $E_a = \hbar^2/2ma^2$ and the hopping rate is $t = -1$. The middle term in (3.2) and the average value $\overline{U}$ of the potential $U_n = \overline{U} + V_n$ are absorbed in the energy such that $\varepsilon = E/E_a - \overline{U}/E_a - 2$, if E is the actual energy of the system. The fluctuations of the potential $v_n = V_n/E_a$ then yield the on-site energies in (3.1).

Alternatively, the wavefunction of a particle $|\psi\rangle = \sum_n^N \psi_n\,|n\rangle$ can be written as a superposition of the on-site states $|n\rangle$ with the coefficients ψ_n, in which case the Schrödinger equation $\mathcal{H}\,|\psi\rangle = \varepsilon\,|\psi\rangle$ emerges as the matrix equation $\sum_{n=1}^N \psi_n\,\langle n|\,\mathcal{H}\,|n\rangle = \varepsilon\psi_n$. The on-site energies are then given by $\langle n|\,\mathcal{H}\,|n\rangle = v_n$ and the hopping elements by $\langle n|\,\mathcal{H}\,|n \pm 1\rangle = t$. The resulting matrix equation can be written as

$$\begin{pmatrix} v_1 & 1 & 0 & \cdots & b \\ t & v_2 & t & & \vdots \\ 0 & \ddots & \ddots & \ddots & 0 \\ \vdots & & t & v_{n-1} & t \\ b & \cdots & 0 & t & v_n \end{pmatrix} \begin{pmatrix} \psi_1 \\ \psi_2 \\ \vdots \\ \psi_{n-1} \\ \psi_n \end{pmatrix} = \varepsilon \begin{pmatrix} \psi_1 \\ \psi_2 \\ \vdots \\ \psi_{n-1} \\ \psi_n \end{pmatrix} \tag{3.3}$$

Boundary conditions can be implemented through the variation of the matrix element b. Free boundary conditions correspond to $b = 0$, periodic boundary conditions to $b = t$ and

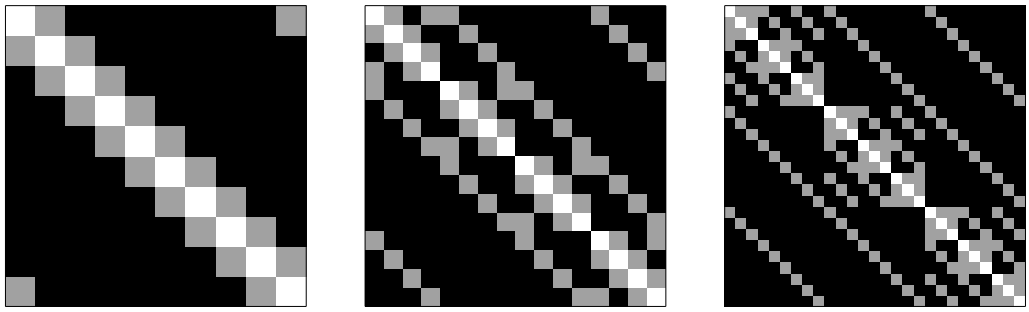

(a) 1D (b) 2D (c) 3D

Figure 3.1:
Anderson matrix in 1D, 2D and 3D for periodic boundary conditions. The white pixels represent the random on-site energies, which are always found on the diagonal. The grey pixels represent the hopping matrix elements. The number of pixels in each line corresponds to the number of nearest neighbours of each site, i. e. two nearest neighbours in 1D (a), four nearest neighbours in 2D (b), and six nearest neighbours in 3D (c).

antiperiodic boundary conditions to $b = -t$.

For d-dimensional systems the discrete Laplace operator can be generalized to

$$\nabla^2\psi(\boldsymbol{n}) = \frac{1}{a^2}\Big[-2d\,\psi(\boldsymbol{n}) + \sum_{\boldsymbol{m}}\psi(\boldsymbol{n}+\boldsymbol{m})\Big] \tag{3.4}$$

The sum in (3.4) runs over all nearest neighbours $\boldsymbol{m} = (ae_1, -ae_1, \ldots, \pm ae_d)$, where the e_α are unit vectors in orthogonal directions. The lattice vector $\boldsymbol{n}$ has the components $\boldsymbol{n} = (n_1, \ldots, n_d)$ with $n_\alpha = 0, \ldots, N_\alpha - 1$, $\alpha = 1, \ldots, d$ and $N_\alpha = L^\alpha$ for a hypercube of length L. The eigenfunctions of the discrete Laplace operator have the same form as the continuum eigenfunctions $\psi(\boldsymbol{n}) = \exp[i\boldsymbol{k}\cdot\boldsymbol{n}]$. Since $\sum_{\boldsymbol{m}}\psi(\boldsymbol{n}+\boldsymbol{m}) = \sum_\alpha 2\cos(k_\alpha a)\,\psi(\boldsymbol{n})$, the discrete dispersion relation for the free particle can be defined as

$$e(\boldsymbol{k}) = \frac{\hbar^2}{ma^2}\sum_{\alpha=1}^{d}\big(1-\cos(k_\alpha a)\big) \tag{3.5}$$

As the cosine in (3.5) is restricted to the range between -1 and 1, the discrete spectrum is confined between $e_{\min} = 0$ and $e_{\max} = 2d\hbar^2/ma^2$. In the long-wavelength limit, i. e. $k_\alpha a \to 0$ and $(1-\cos(k_\alpha a)) \to k_\alpha^2 a^2/2$, the discrete dispersion relation tends towards the continuous dispersion relation of the free particle

$$\lim_{k_\alpha\to 0} e(\boldsymbol{k}) = \sum_{\alpha=1}^{d}\frac{\hbar^2 k_\alpha^2}{2m} = \frac{\hbar^2 k^2}{2m} \tag{3.6}$$

The discrete Schrödinger equation for a hypercube of length L in more than one dimension can still be written in the form of a matrix equation $A\psi = \varepsilon\psi$, where the index j runs from 1 to N, i. e. over the total number of lattice points. The energy ε in this matrix equation is

related to the original energy E in the Schrödinger equation through $\varepsilon = E/E_a - \overline{U}/E_a - 2d$. The matrix M is an $N \times N$-matrix of the form depicted in Fig. **3.1**, which corresponds to a lexicographic order of the indices j [83].

3.1.1 Exact Diagonalization

Since the Anderson matrix for diagonal disorder is symmetric, it can be diagonalized using the similarity transform $\tilde{A} = T^T A T$, where the columns of the orthogonal matrix T are constructed from the eigenvectors ψ_i, and the diagonal elements of the diagonalized matrix $\tilde{A}$ are the eigenvalues ε_i. The index i runs from 1 to N since the Anderson Hamiltonian has exactly N eigenvalues and N eigenvectors.

An exact diagonalization of the Anderson matrix thus provides the energy spectrum and the eigenvectors for any realization of disorder on a finite number of sites. In our numerical implementation we first fill an array of $N \times N$ sites with the hopping matrix elements according to Fig. **3.1**. The diagonal elements are then filled by random on site energies from a uniform distribution of width w. The resulting matrix can be diagonalized using a standard LAPACK diagonalization routine. For small systems ($N \approx 1000$) all eigenvalues and eigenvectors of the Anderson matrix can be calculated in this way.

In the presence of disorder, the eigenvectors in 1D and 2D form localized states as displayed in Fig. **3.2(a)** and Fig. **3.2(b)**. In the absence of disorder, i. e. for zero on-site energies $v_n = 0$, Bloch's theory applies. The energy spectrum for the eigenvalues ε_i in this case is restricted to the interval $[-2d, +2d]$.

The eigenvalue distribution of the Anderson Hamiltonian can be calculated indirectly via the average density of states per unit volume or directly by dividing the total spectrum into several subintervals, and adding up the number of eigenvalues for each interval.

A second quantity of interest apart form the average density of states per unit volume is the inverse participation number, which indicates the order of magnitude of the localization length. If all eigenvectors are known, the inverse participation number can be obtained for the full spectrum.

Density of States

For the unperturbed system with $v_n = 0$ the density of states per unit volume is given by

$$\rho(\varepsilon) = \int \frac{\mathrm{d}\boldsymbol{\kappa}}{(2\pi)^d}\, \delta\Big(\varepsilon - 2\sum_{\alpha=1}^{d} \cos\kappa_\alpha\Big) \tag{3.7}$$

where the integral over $\boldsymbol{\kappa}$ extends over the first Brillouin zone, i. e. from $-\pi$ to π. Here, $\boldsymbol{\kappa} = \boldsymbol{k}a$ and $\varepsilon = E/E_a - \overline{U}/E_a - 2d$ are dimensionless. Using the representation

$$\delta(x) = \int \frac{\mathrm{d}y}{2\pi}\, e^{ixy} \tag{3.8}$$

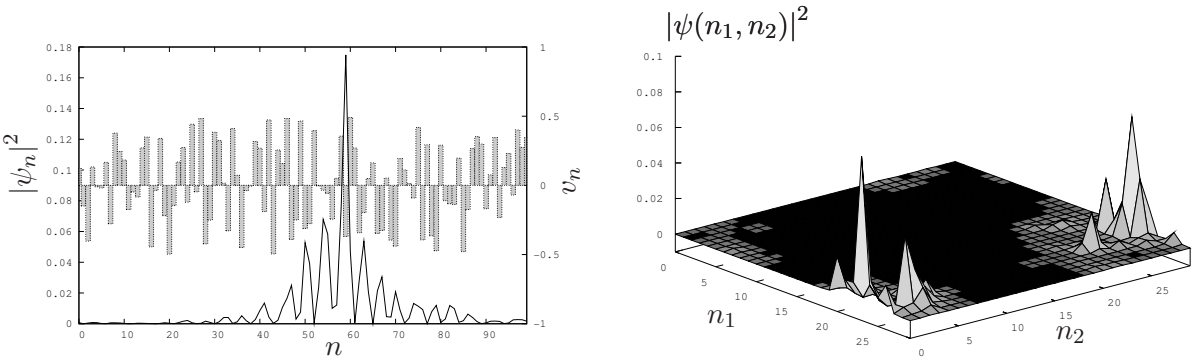

(a) 1D: Localized state

(b) 2D: Localized state

Figure 3.2:
(a) Snapshot of a localized state in 1D plotted together with the corresponding disordered potential (v_n-axis on the right) for a system with $N = 100$ sites. The localized state corresponds to the eigenvalue $\varepsilon = -1.55$. The random potential is distributed uniformly between -0.5 and 0.5. The full width of the disorder distribution is $w = 1$. (b) Snapshot of a localized state in 2D for a system with $N = 30 \times 30 = 900$ sites. The localized state corresponds to the eigenvalue $\varepsilon = -0.95$. The full width of the disorder distribution is $w = 12$.

and the integral representation of the Bessel function [71]

$$\mathcal{J}_0(z) = \frac{1}{\pi} \int_0^\pi \mathrm{d}\kappa \; e^{-iz\cos\kappa} = \frac{1}{\pi} \int_0^\pi \mathrm{d}\kappa \; e^{iz\cos\kappa} \tag{3.9}$$

the density of states per unit volume is evaluated as

$$\rho(\varepsilon) = \frac{1}{\pi} \int_0^\infty \mathrm{d}y \; \big[\mathcal{J}_0(2y)\big]^d \cos(\varepsilon y) \tag{3.10}$$

In one dimension $\rho(\varepsilon)$ can be obtained directly by integrating (3.7) [80]

$$\rho(\varepsilon) = \frac{1}{\pi\sqrt{4-\varepsilon^2}} \, \Theta(2 - |\varepsilon|) \tag{3.11}$$

The same result is obtained using (3.10) and the integral (6.671.8) from [84]. This means that the density of states diverges at the band edge for $\varepsilon = \pm 2$. These divergences are known as van Hove singularities [80]. In two dimensions, making use of (3.10) and the integral (6.672.2) from [84] we obtain

$$\rho(\varepsilon) = \frac{1}{4\pi} \, P_{-1/2}\Big(\frac{\varepsilon^2}{8} - 1\Big) \, \Theta(4 - |\varepsilon|) = \frac{1}{2\pi^2} \, K\Big(1 - \frac{\varepsilon^2}{16}\Big) \, \Theta(4 - |\varepsilon|) \tag{3.12}$$

where $P_\ell(x)$ is the Legendre polynomial and $K(m)$ denotes the complete elliptic integral of the first kind as defined in [71]

$$K(m) = \int_0^{\pi/2} \mathrm{d}\theta \; \frac{1}{\sqrt{1 - m \, \sin^2\theta}} \tag{3.13}$$

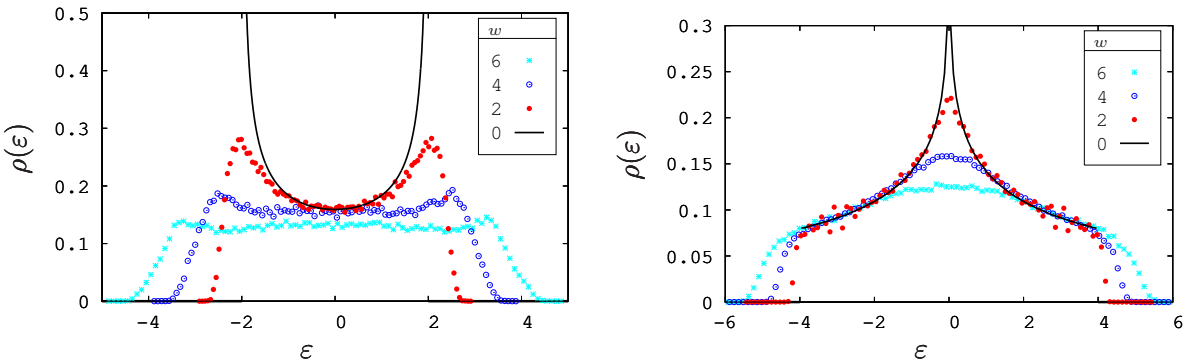

(a) 1D: Average density of states

(b) 2D: Average density of states

Figure 3.3:
Average density of states per unit volume as a function of the energy in 1D and 2D for different widths of the disorder distribution, i. e. different magnitudes of disorder. The on-site energies are chosen at random from a uniform distribution of full width w. The solid black curve is given by the analytical results (3.11) and (3.12) respectively. The dotted curves are obtained using the eigenvalues obtained via an exact numerical diagonalization of the Anderson Hamiltonian. (a) 1D (1000 sites, 100 realizations): The spectrum for the ordered crystal lives on the interval $[-2, +2]$. The density of states diverges at the band edge and is zero outside. (b) 2D (30×30 sites, 100 realizations): The ordered spectrum is confined to $[-4, +4]$. The density of states diverges at the band centre. As for the 1D case this effect is smoothed out in the presence of disorder.

Using the expressions of the Legendre polynomial (8.820.1 from [84]) and the complete elliptic integral $K(m)$ (8.113.1 from [84][1]) in terms of the hypergeometric function, it can be shown that both expressions in (3.12) are identical.

The density of states for the ordered and the average density of stages for the disordered lattice in d dimensions are plotted in Fig. **3.3**. While for small disorder the density of states approaches the exact solution for the perfect lattice ((3.10), (3.11) and (3.12) respectively) it acquires a different shape for higher disorder, similar to the one displayed in the schematic picture in Fig. **1.2** and extends beyond the boundaries of the ordered spectrum. The van Hove singularities are smoothed out. Alongside this behaviour of the density of states, the localization length ξ_{loc} inside the spectrum, which is infinite for the perfect crystal, acquires a finite value in the presence of disorder. To see this we need to study the so-called inverse participation number.

Inverse Participation Number

The energy dependence of the localization length can be observed indirectly by looking at the participation number $p(\varepsilon)$ defined as [85]

$$p^{-1}(\varepsilon) = \sum_{j}^{N} |\psi_j(\varepsilon)|^4 \propto \left(\frac{\xi_{\text{loc}}(\varepsilon)}{a}\right)^{-d} \tag{3.14}$$

[1] [84] uses a different notation for the complete elliptic integral, where $m = k^2$.

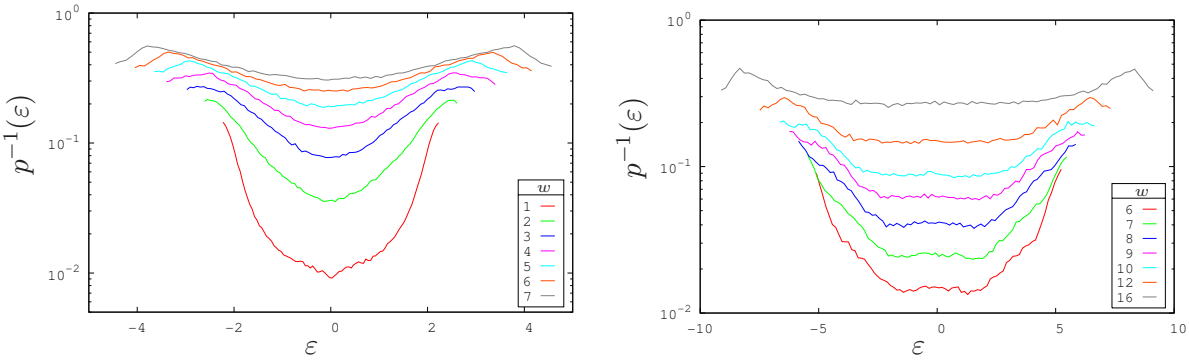

(a) 1D: Inverse participation number

(b) 2D: Inverse participation number

Figure 3.4:

Logarithmic plot of the inverse participation number (3.14) as a function of the energy for a uniform distribution of the on-site energies with different total widths w. The inverse participation number is higher (and hence localization is stronger) at the band edges than at the centre of the band. Even for a very small amount of disorder the participation number is smaller than the number of sites in one lattice direction. (a) 1D (1000 sites, 100 realizations). (b) 2D (30×30 sites, 100 realizations). The participation number decreases (localization increases) for higher disorder. The curves have been obtained from an exact diagonalization of the Anderson Hamiltonian using a standard LAPACK diagonalization routine. The IPN values have been averaged over intervals of the size $(|\varepsilon_{\min}| + |\varepsilon_{\max}|)/100$, where $\varepsilon_{\min} = -2.0 - (0.5\,w)$ and $\varepsilon_{\max} = 2.0 + (0.5\,w)$ in 1D and $\varepsilon_{\min} = -5.0 - (0.3\,w)$ and $\varepsilon_{\max} = 5.0 + (0.3\,w)$ in 2D.

The index j runs over all components of the eigenvector ψ. The participation number is accessible once the eigenvalue spectrum and the corresponding eigenvectors of the Anderson Hamiltonian are known. It measures the average number of sites covered by the wavefunction ψ. In this sense it gives a measure of the dimensionless localization length $\xi_{\text{loc}}(\varepsilon)/a$ at the energy ε.

The inverse participation number (IPN) is plotted in Fig. **3.4** for a disordered 1D and 2D Anderson lattice. The solid curves have been obtained using a standard LAPACK diagonalization routine for the Anderson Hamiltonian, where the on-site energies are drawn at random from a uniform distribution of the full width w. The final IPN values have been averaged over energy intervals of the size $(|\varepsilon_{\min}| + |\varepsilon_{\max}|)/100$, where $\varepsilon_{\min}$ and $\varepsilon_{\max}$ vary with the strength of the disorder. All curves have been checked for consistency with the un-averaged inverse participation number taking into account all sites. The inverse participation number is higher at the band edges than at the centre of the band. This is equivalent to the statement that the states at the band edges are confined to a smaller region (they cover a smaller amount of sites). Hence, localization at the band edges is stronger than at the centre.

When looking at the states in Fig. **3.2(a)** and Fig. **3.2(b)**, it is a priori not clear whether these states remain truly localized, when the size of the system is increased. To be able to identify truly localized states, we need to study the inverse participation number as a function of the size of the system. Only if the IPN value stays constant, i. e. if the localized

state does not change its shape with an increasing system size, the state is truly localized. For this purpose however, larger Anderson matrices have to be considered. This is possible using a refined Lanczos Algorithm, which is briefly discussed in the next section.

3.1.2 The Lanczos Algorithm

For the small systems studied in Fig. **3.3** and Fig. **3.4** an exact diagonalization is still possible, but one soon reaches the limits of standard computers as far as storage and processing speed for large-scale matrices are concerned. One possible way that allows to obtain the eigenvalues and eigenvectors of large-scale matrices is the Lanczos recursion method, which has been originally introduced by C. Lanczos in 1950 [86].

The basic idea of the Lanczos algorithm is to transform the matrix A to a tridiagonal Lanczos matrix, where the elements are only found on the diagonal and the neighbouring sub- and superdiagonals. The Lanczos recursion method can be seen as a modified Gram Schmidt orthonormalization method generating orthonormal basis vectors for the Krylov subspace $K_j = \{\boldsymbol{r}_0, A\boldsymbol{r}_0, A^2\boldsymbol{r}_0, \ldots, A^{j-1}\boldsymbol{r}_0\}$. Here, A is a $N \times N$ real symmetric matrix and $\boldsymbol{r}_0$ is a randomly chosen starting vector. One possible Lanczos recursion for $j \geq 1$ starting from $\beta_0 = |\boldsymbol{r}_0|$ and $\boldsymbol{q}_0 = 0$ is given by [87][2]

$$\begin{aligned}
\boldsymbol{q}_j &= \boldsymbol{r}_{j-1}/\beta_{j-1} \\
\boldsymbol{u}_j &= A\boldsymbol{q}_j - \beta_{j-1}\,\boldsymbol{q}_{j-1} \\
\alpha_j &= \boldsymbol{q}_j^T\boldsymbol{u}_j \\
\boldsymbol{r}_j &= \boldsymbol{u}_j - \alpha_j\boldsymbol{q}_j \\
\boldsymbol{\beta}_j &= |\boldsymbol{r}_j|
\end{aligned} \tag{3.15}$$

The normalized orthogonal vectors $\boldsymbol{q}_j$ are called Lanczos vectors. Assembling the Lanczos vectors in the columns of the $N \times j$ matrix $Q_j = (\boldsymbol{q}_1, \ldots, \boldsymbol{q}_j)$ and defining the tridiagonal Lanczos matrix

$$T_j = \begin{pmatrix} \alpha_1 & \beta_1 & 0 & \cdots & 0 \\ \beta_1 & \alpha_2 & \beta_2 & & \vdots \\ 0 & \beta_2 & \ddots & \ddots & 0 \\ \vdots & & \ddots & \alpha_{j-1} & \beta_{j-1} \\ 0 & \cdots & 0 & \beta_{j-1} & \alpha_j \end{pmatrix} = Q_j^T A Q_j \tag{3.16}$$

it can be shown [87] that for each j, T_j is the projection of the matrix A onto the Krylov subspace K_j spanned by the orthonormal Lanczos vectors $\{\boldsymbol{q}_1, \ldots, \boldsymbol{q}_j\}$. The eigenvalues of the Lanczos matrix T_j are the eigenvalues of the matrix A restricted to the Krylov subspace

[2] There are three alternative implementations of the Lanczos algorithm which use slightly different definitions for the coefficients α_j and β_{j-1} [87].

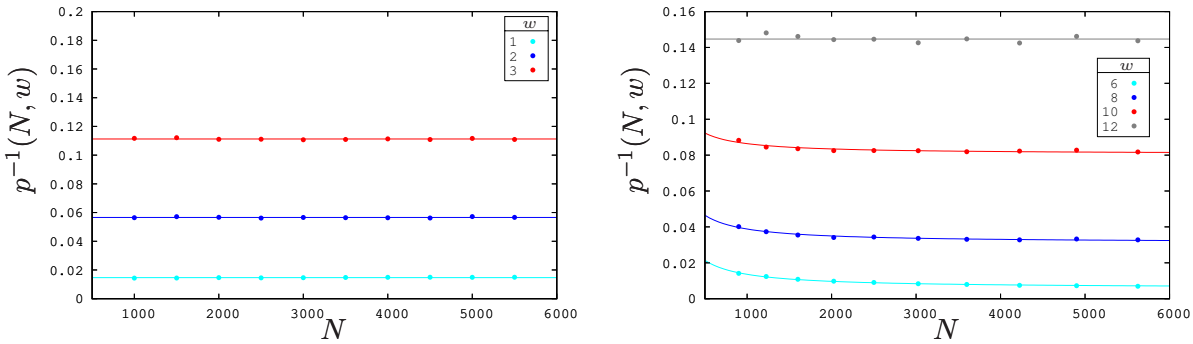

(a) 1D: Size dependence of the IPN

(b) 2D: Size dependence of the IPN

Figure 3.5:
Plot of the inverse participation number at the energy $\varepsilon = -1$ as a function of the system size N for different widths w of the uniform disorder distribution. The IPN value has been averaged over an interval of the width $\Delta\varepsilon = 0.1$ and over 100 realizations of disorder. (a) In 1D, the inverse participation number for different system sizes remains constant over the whole range of the plot. (b) In 2D, the IPN values, as a function of $N = L \times L$, where L is the linear size of the 2D system, have been fitted with the function $f(N) = a + b/N$. For small system sizes and small widths of the disorder distribution the inverse participation number decreases with $1/N$, whereas for larger systems it soon approaches a constant asymptotic value.

K_j. For $j = N$ the eigenvalues of T_j are the eigenvalues of the matrix A.

The basic Lanczos algorithm works as follows: After $m \ll N$ steps of the Lanczos recursion, the first eigenvalues of the Lanczos matrix T_m, which have converged to the largest eigenvalues of the original matrix A are selected. In order to obtain the corresponding original eigenvectors of the matrix A one first computes the corresponding eigenvector φ_i of T_m. The original eigenvector ψ_i is then obtained as the Ritz vector $\psi_i = Q_m \varphi_i$.

The main advantage of the Lanczos algorithm compared to a direct diagonalization of the matrix A is the minimum amount of storage required for large sparse matrices. This makes the algorithm particularly attractive for the eigenvalue problem associated with the tight-binding model. The matrix A enters the Lanczos recursion only through the product $A\boldsymbol{q}_j$ and is not modified during the whole process. Therefore, if a subroutine is provided that computes the product $A\boldsymbol{q}_j$, no extra storage is required for the matrix A itself. The Lanczos algorithm is particularly powerful, if only a small number of eigenvalues and the corresponding eigenvectors are needed, since the tridiagonal Lanczos matrix can then be much smaller than the tridiagonal matrix, which appears in a standard diagonalization routine.

In general, the described Lanczos recursion converges first to the largest eigenvalues of the matrix A. To be able to access any part of the eigenvalue spectrum we used a refined Lanczos algorithm written by D. Delande [88], which maps the eigenvalue spectrum onto Chebyshev-type polynomials (cf. appendix A), similar to the ones used for the polynomial convergence acceleration method described in [81]. The modified Lanczos algorithm converges first to the energy eigenvalues close to the maximum of the respective polynomial.

As an example, in order to verify the dependence of the inverse participation number on

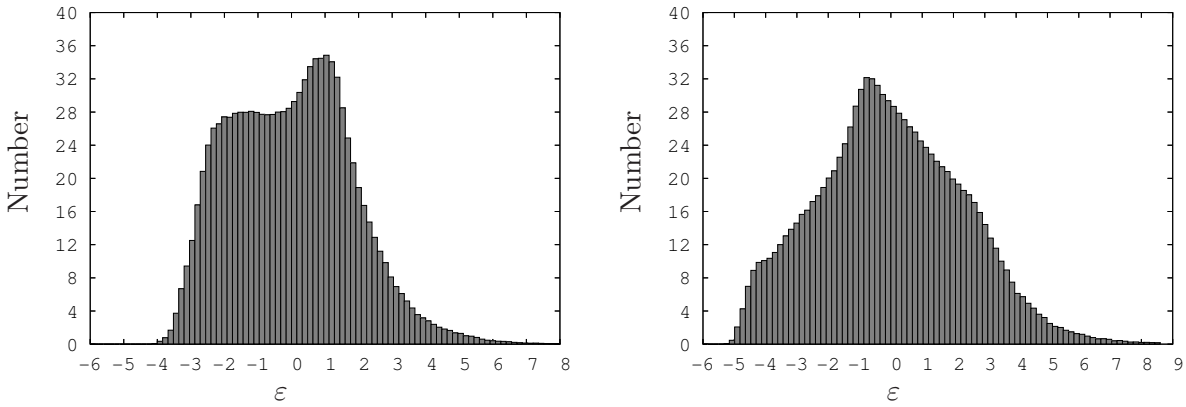

(a) 1D: Speckle eigenvalue histogram (b) 2D: Speckle eigenvalue histogram

Figure 3.6:
Histogram of the number of energy eigenvalues in subintervals of the size $(|\varepsilon_{\min}|+|\varepsilon_{\max}|)/100$ for the Anderson Hamiltonian with correlated on-site potential energies. (a) 1D: 1024 sites, 100 realizations, correlation length $\zeta/a = 40.74$, $\varepsilon_{\min} = -2.0 - (0.5\,z)$, and $\varepsilon_{\max} = 2.0 + (0.5\,z)$. (b) 2D: 32×32 sites, 100 realizations, correlation length $\zeta/a = 1.27$, $\varepsilon_{\min} = -5.0 - (0.3\,z)$, and $\varepsilon_{\max} = 5.0 + (0.3\,z)$. The on-site energies for each realization are centred around zero. They are scaled by a constant factor z, i. e. $v_j = z(I_j - \overline{I})$. For the histograms in (a) and (b) the scaling factor is $z = 12$.

the size of the system, we choose a Chebyshev-type polynomial, which reaches its maximum within the energy range $\varepsilon \in [-1.1, -0.9]$. Making use of the Lanczos algorithm we can then calculate either all eigenvalues or a given subset of eigenvalues inside this interval. A subset of eigenvalues is obtained, if the Lanczos algorithm is stopped after $m \ll N$ steps before all Lanczos eigenvalues have converged. For each converged eigenvalue we can calculate the corresponding eigenvector, which is then used to determine the inverse participation number. The program is optimized to yield a given number of eigenvalues inside the predefined interval for the lowest degree n of the polynomial $D_n(\varepsilon)$ (cf. appendix A) and the lowest number of Lanczos steps m. The final IPN value is obtained as an average over the whole interval and over a given number of realizations of the random on-site energies. The result for different system sizes is plotted in Fig. **3.5(a)** for a 1D system and in Fig. **3.5(b)** for a 2D system.

In 1D, the inverse participation number remains indeed constant as expected, even for relatively small systems of $N = 1000$ sites, while in 2D the behaviour for small systems still depends on the width of the disorder distribution. For small disorder $w \leq 10$ the inverse participation number decreases like $1/N$ for small N, whereas for large disorder $w \geq 12$, the inverse participation number remains constant whatever the size of the system. Therefore, the 2D localized state in Fig. **3.2(b)** for $w = 12$ is indeed a truly localized state, just like the 1D localized state in Fig. **3.2(a)**.

3.1.3 Correlated On-Site Energies

Instead of a uniform distribution of the on-site energies v_j, we can also use the numerically generated speckle pattern from the previous chapter to obtain an Anderson Hamiltonian

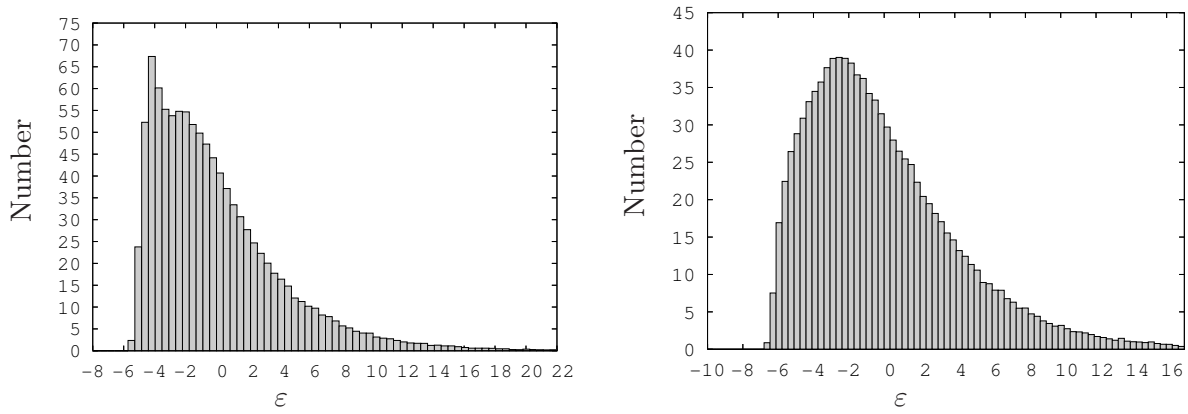

(a) 1D: Rayleigh eigenvalue histogram (b) 2D: Rayleigh eigenvalue histogram

Figure 3.7:
Histogram of the number of eigenvalues in subintervals of the size $(|\varepsilon_{\min}| + |\varepsilon_{\max}|)/100$ for the on-site energies $v_j = z(I_j - w)$, where the I_j are drawn from the negative exponential distribution (3.17) of width w. z is a constant scaling factor, which has been set to $z = 0.1$ for both histograms. (a) 1D: 1024 sites, 100 realizations, $\varepsilon_{\min} = -2.0 - (0.5\,w)$, and $\varepsilon_{\max} = 2.0 + (0.5\,w)$. (b) 2D: 32×32 sites, 100 realizations, $\varepsilon_{\min} = -5.0 - (0.3\,w)$, and $\varepsilon_{\max} = 5.0 + (0.3\,w)$.

with correlated on-site energies. In our program, the on-site energies are chosen according to $v_j = z(I_j - \overline{I})$, where I_j is the intensity of the speckle pattern (in lexicographic order), $\overline{I}$ is the spatially averaged intensity of the speckle pattern and z is a scaling factor. The speckle pattern is correlated over the average correlation length $\zeta = L/(2\pi M)$, where L is the linear size of the speckle pattern and M is the radius of the aperture, which appears in the cut-off function (2.37). In 1D, the on-site energies are given by a one-dimensional cut through the 2D speckle pattern with the same periodicity and the same correlation length.

A histogram of the corresponding spectrum in 1D and in 2D is plotted in Fig. **3.6(a)** and

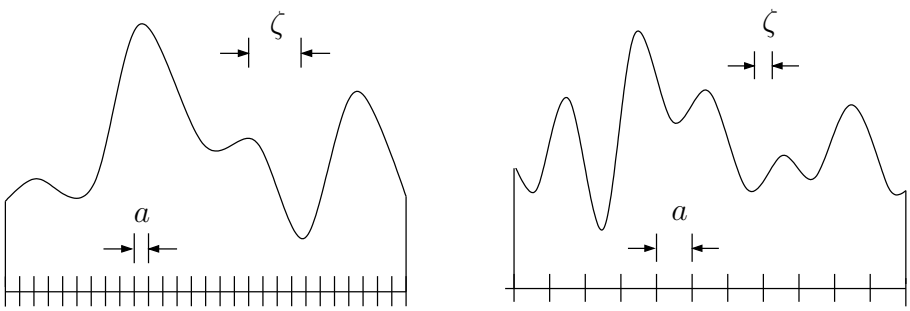

(a) Correlated potential (b) Effectively uncorrelated potential

Figure 3.8:
Schematic view of a correlated random potential on a one-dimensional lattice. In (a) the correlation length ζ is larger than the lattice spacing, whereas in (b) the lattice spacing is larger than the correlation length ζ. In this case, although the potential fluctuations follow the same distribution as in (a), the correlation of the potential fluctuations cannot be resolved by the lattice and the potential appears uncorrelated.

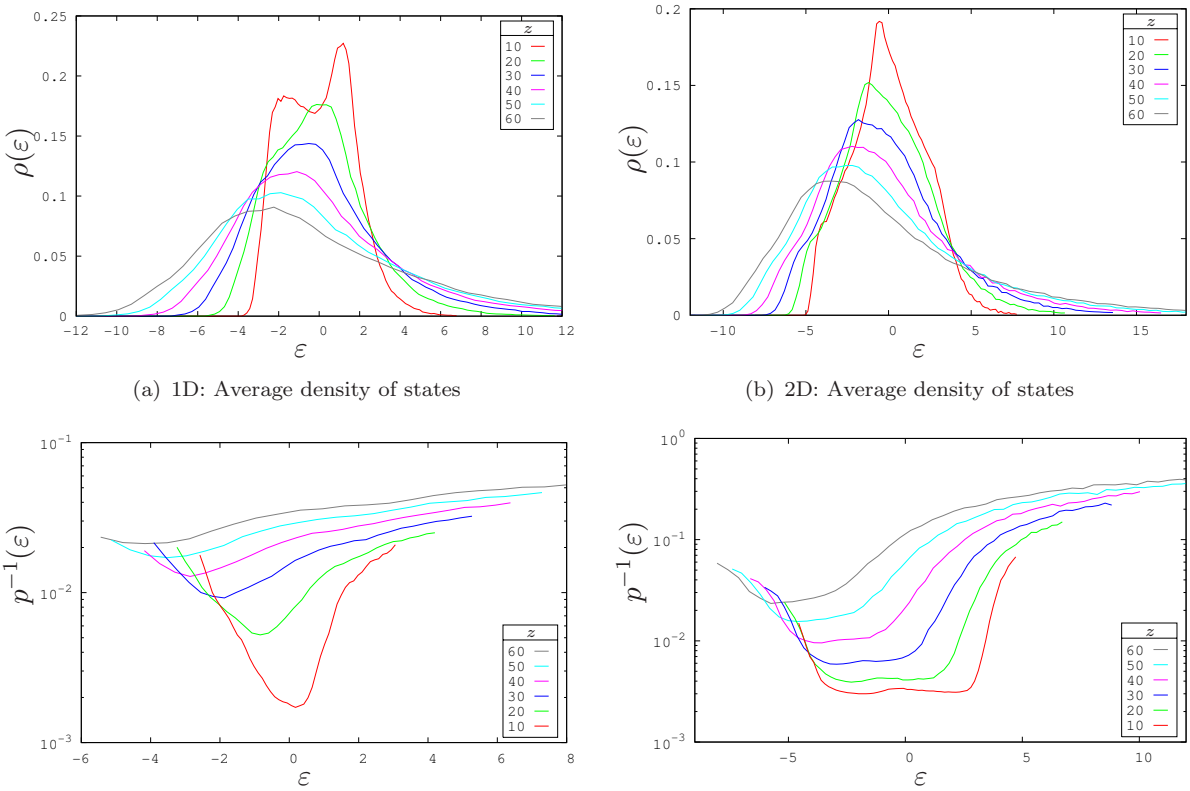

(a) 1D: Average density of states

(b) 2D: Average density of states

(c) 1D: Inverse participation number

(d) 2D: Inverse participation number

Figure 3.9:
Above: Average density of states as a function of the energy for different scaling factors z. (a) 1D: 1024 sites, 100 realizations, correlation length $\zeta/a = 40.74$. (b) 2D: 32×32 sites, 100 realizations, correlation length $\zeta/a = 1.27$. Below: Inverse participation number for different scaling factors z. (c) 1D: 1024 sites, 100 realizations, correlation length $\zeta/a = 40.74$. (d) 2D: 32×32 sites, 100 realizations, correlation length $\zeta/a = 1.27$.

Fig. **3.6(b)**. Since we have subtracted the mean intensity, the spectrum is centred around zero. It is asymmetric and displays a long high-energy tail. This feature is a direct consequence of the Rayleigh distribution of the speckle intensities (2.6) as displayed in Fig. **2.5(a)**. Indeed the spectrum of the Anderson Hamiltonian for uncorrelated on-site energies drawn from a negative exponential distribution of width w

$$P(I_j) = \frac{1}{w} \exp[-I_j/w] \tag{3.17}$$

reveals the same high-energy tail. This is shown in Fig. **3.7(a)** and Fig. **3.7(b)**. For these plots the on-site energies are chosen according to $v_j = z(I_j - w)$ with a constant scaling factor z. We have subtracted the width w, such that the spectrum is centred around zero to allow for a better comparison with Fig. **3.6(a)** and Fig. **3.6(b)**.

The case of the correlated speckle potential applies to the situation depicted schematically in Fig. **3.8(a)**, where the lattice constant a is smaller than the speckle correlation length ζ,

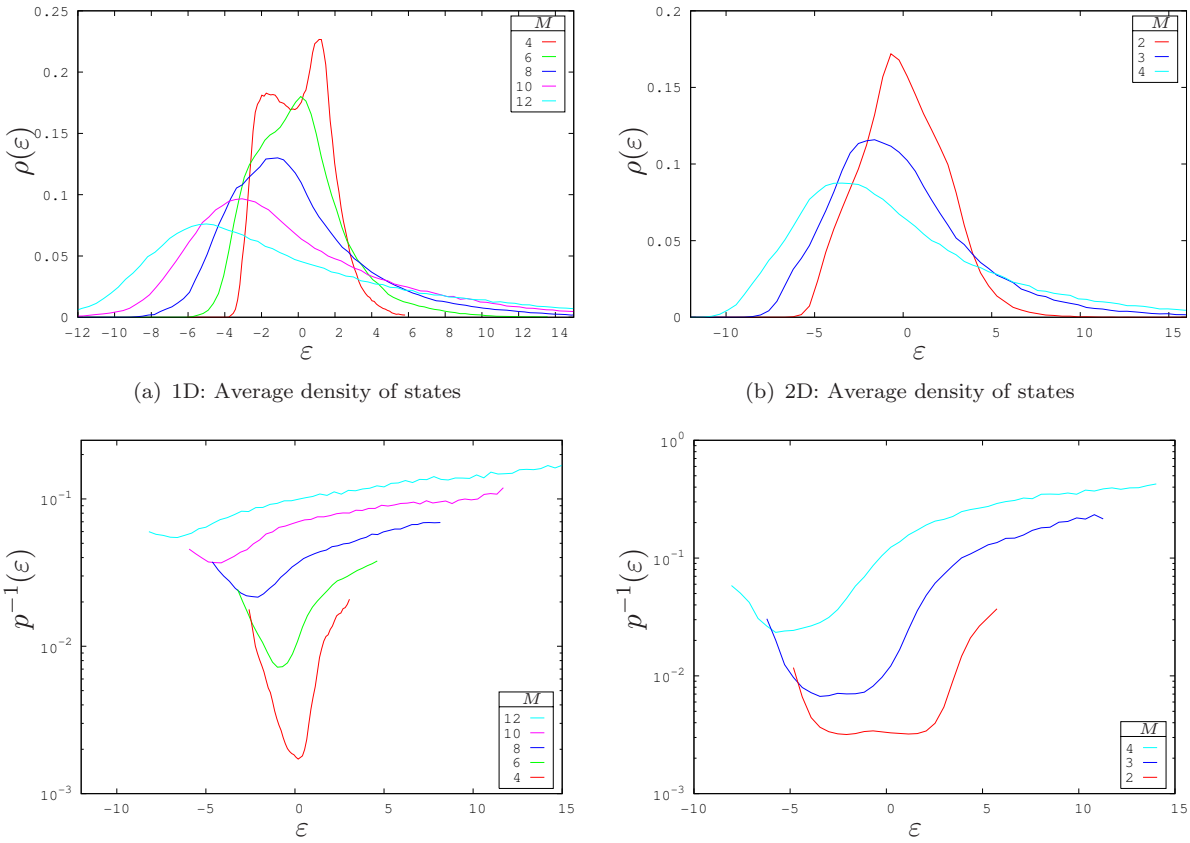

(a) 1D: Average density of states

(b) 2D: Average density of states

(c) 1D: Inverse participation number

(d) 2D: Inverse participation number

Figure 3.10:
Above: Average density of states for different correlation lengths $\zeta = L/(2\pi M)$ of the speckle pattern. (a) 1D: $L = 1024$ sites, 100 realizations, scaling factor $z = 10$. (b) 2D: $L = 32$ sites, 100 realizations, scaling factor $z = 60$. Below: Inverse participation number for different correlation lengths $\zeta = L/(2\pi M)$ of the speckle pattern. (c) 1D: $L = 1024$ sites, 100 realizations, scaling factor $z = 10$. (d) 2D: $L = 32$ sites, 100 realizations, scaling factor $z = 60$.

whereas the second case of uncorrelated on-site energies drawn from a Rayleigh distribution applies to the inverse situation where $\zeta < a$ as shown in Fig. **3.8(b)**.

As in the case of uniform on-site energies (cf. Fig. **3.3**) the shape of the spectrum essentially depends on the width w of the distribution and on the scaling factor z. Rather than plotting a histogram for different z for the correlated on-site energies, we can compare the corresponding shape of the density of states per unit-volume as shown in Fig. **3.9(a)** and Fig. **3.9(b)**. For small scaling factors one can still distinguish the remnants of the van Hove singularities in 1D and in 2D (cf. Fig. **3.3(a)** and Fig. **3.3(b)**). For larger values of z the singularities are suppressed, while the spectrum clearly reveals its anisotropic nature with a long high-energy tail. This anisotropy for high energies is also observed when looking at the inverse participation number as shown in Fig. **3.10(c)** and Fig. **3.10(d)**.

On the other hand, the average density of states per unit volume and the inverse participation number may be studied for a fixed scaling factor and for different correlation lengths ζ,

i. e. for different radii M of the aperture function (2.37). In Fig. **3.10** we have chosen the scaling factor $z = 10$ in 1D and $z = 60$ in 2D. Qualitatively, an increase of the aperture radius, i. e. a decreasing correlation length, has the same effect as an increasing scaling factor: The van Hove singularities in Fig. **3.10(a)** and Fig. **3.10(b)** are smoothed out and the spectrum develops a long high-energy tail. This is accompanied by an increase of the inverse participation number, i. e. a reduced localization length as shown in Fig. **3.10(c)** and Fig. **3.10(d)**. In other words, reducing the spatial correlations of the random potential amplifies localization and vice versa. Hence, the spatial correlations favour delocalization.

3.2 Summary

This chapter was devoted to the Anderson or tight-binding model, as one of the most fundamental models where localization can be observed. We have performed an exact diagonalization of the 1D and the 2D Anderson matrix for standard uncorrelated uniform random on-site energies as well as for the numerically generated speckle pattern from section 2.2 as an example for correlated potential fluctuations. In both cases we have studied the average density of states per unit volume, and the inverse participation number, which can be related to the localization length. We have compared our results for the average density of states of the standard Anderson model to the analytical result ((3.10), (3.11) and (3.12) respectively) in the absence of disorder to check the accuracy of our program and we have studied the dependence of the inverse participation number on the size of the system, using a refined Lanczos algorithm. New results have been presented in the form of the spectrum and the IPN, as a function of the energy, for the correlated two-dimensional speckle potential. In both cases we have studied the impact of a change of the scaling factor, i. e. the magnitude of disorder, and a change of the characteristic correlation length of the speckle potential. In particular, we have seen that the eigenvalue spectrum reflects the intensity distribution of the speckle and that the introduction of spatial correlations in the Anderson model entails delocalization in the form of an increasing participation number of sites, which contribute to a localized state.

Chapter 4

Matter Waves in Disordered Optical Potentials

In the present chapter the basic model for the description of matter-wave transport in disordered optical potentials is introduced. This model relies on a few important simplifications. Most importantly we are going to neglect the atom-atom interaction such that the behaviour of the system is essentially captured by a single-particle description. We consider a two-level atom in the dipole approximation interacting with the spatially disordered electric field of a speckle potential. The saturation parameter is assumed small enough to allow for an independent treatment of the interaction of the atom with the vacuum fluctuation reservoir. The coupling between the polarization of the light field and the internal degrees of freedom of the atoms does not play a role, if transitions between different Zeeman sublevels can be ruled out by an appropriate choice of the atoms, or via the application of an external magnetic field. In this case the light field can be regarded as a scalar electric field.

Under these assumptions the atomic evolution is purely Hamiltonian on a time scale determined by the inverse inelastic scattering rate Γ_ϕ before dissipation sets in. In our case the inelastic scattering rate Γ_ϕ defines the phase-breaking time τ_ϕ, which has already been mentioned in section 1.1.

4.1 Atomic Hamiltonian Dynamics

As a model for the internal atomic structure we consider a two-level atom with the ground state $|g\rangle$ and the excited state $|e\rangle$. The excited state is a metastable state with a finite lifetime $\tau_e = 1/\Gamma_e$, where Γ_e denotes the natural linewidth of the excited state. The characteristic energy of the transition $|e\rangle \to |g\rangle$ is given by $\hbar\omega_\mathrm{A}$.

This two-level description applies to atoms like Strontium [89] with a non-degenerate electronic ground state or atoms like Rubidium, whose ground-state degeneracy is lifted by a strong magnetic field [90]. The Hamiltonian for such a two-level atom of mass m interacting with the electric field of a monochromatic laser beam with wavenumber k_L, wavelength $\lambda_\mathrm{L} = 2\pi/k_\mathrm{L}$ and angular frequency $\omega_\mathrm{L} = c\,k_\mathrm{L}$ can be written as [67]

$$H = H_\mathrm{kin} + H_\mathrm{A} - \boldsymbol{D}\cdot\boldsymbol{\mathcal{E}}(\boldsymbol{r},t) + H_\mathrm{R} - \boldsymbol{D}\cdot\boldsymbol{\mathcal{E}}_\mathrm{R}(\boldsymbol{r}) \tag{4.1}$$

where $H_\mathrm{kin} = \boldsymbol{p}^2/2m$ describes the kinetic energy of the centre-of-mass motion and $H_\mathrm{A} = \hbar\omega_\mathrm{A}\,|e\rangle\langle e|$ takes account of the internal energy of the atom.

The term $-\boldsymbol{D}\cdot\boldsymbol{\mathcal{E}}(\boldsymbol{r},t)$ describes the interaction energy between the atom and the external electric field of the laser

$$\boldsymbol{\mathcal{E}}(\boldsymbol{r},t)=\frac{1}{2}\left[\boldsymbol{u}(\boldsymbol{r})\mathcal{E}(\boldsymbol{r})\,e^{-i\omega_{\mathrm{L}}t}+\boldsymbol{u}^*(\boldsymbol{r})\mathcal{E}^*(\boldsymbol{r})\,e^{i\omega_{\mathrm{L}}t}\right] \tag{4.2}$$

$\mathcal{E}(\boldsymbol{r})$ denotes the amplitude of the electric field and $\boldsymbol{u}(\boldsymbol{r})$ its unit polarization vector. We assume that the external electric field $\boldsymbol{\mathcal{E}}(\boldsymbol{r},t)$ is not modified by the interaction with the atom.

The description of the incident light by a classical external field can be achieved by a unitary transformation, if the initial state $|\Psi(0)\rangle=|\{\alpha_j\}\rangle$ is a coherent state [67]. This unitary transformation is given by $T(t)=\Pi_j\exp\left[\alpha_j^*e^{i\omega_j t}a_j-\alpha_j e^{-i\omega_j t}a_j^\dagger\right]$, where $a_j^\dagger$ and a_j are the creation and annihilation operators and α_j is the eigenvalue to the eigenstate $|\alpha_j\rangle$ of the annihilation operator. For $t=0$, $T^\dagger(0)$ creates the coherent state $|\{\alpha_j\}\rangle=T^\dagger(0)\,|0\rangle$ from the vacuum. The same unitary transformation $T(t)$ transforms the original Hamiltonian, $H_1=\frac{1}{2m}[\boldsymbol{p}-q\boldsymbol{A}(\boldsymbol{r})]^2+H_R$, where H_R is given by $H_R=\sum_j\hbar\omega_j(a_j^\dagger a_j+\frac{1}{2})$, into the new Hamiltonian $H_1'=T(t)H_1T^\dagger(t)=\frac{1}{2m}[\boldsymbol{p}-q\boldsymbol{A}(\boldsymbol{r})-q\boldsymbol{A}_{\mathrm{cl.}}(\boldsymbol{r})]^2+H_R$. This new Hamiltonian describes a particle interacting with the quantum vector potential $\boldsymbol{A}(\boldsymbol{r})$ and the classical vector potential $\boldsymbol{A}_{\mathrm{cl.}}(\boldsymbol{r})$, which only depends on the eigenvalues α_j of the annihilation operator. The transformed initial state $\Psi'(0)=T(0)\,|\{\alpha_j\}\rangle=|0\rangle$ is then the vacuum state.

The electric dipole operator $\boldsymbol{D}$ is a vector operator with odd parity. It only contains non-diagonal contributions in the basis $\{|g\rangle\,,|e\rangle\}$

$$\boldsymbol{D}=\boldsymbol{d}\,|e\rangle\langle g|+\boldsymbol{d}^*\,|g\rangle\langle e| \tag{4.3}$$

The electric dipole moment $\boldsymbol{d}=\langle e|\,\boldsymbol{D}\,|g\rangle$ is a characteristic quantity of the atom used in the experiment. The coupling strength between the atom and the electric field is described by the Rabi frequency

$$\hbar\Omega(\boldsymbol{r})=-(\boldsymbol{d}\cdot\boldsymbol{u}(\boldsymbol{r}))\,\mathcal{E}(\boldsymbol{r}) \tag{4.4}$$

The remaining terms in equation (4.1) incorporate the interaction between the atom and the vacuum fluctuation reservoir $-\boldsymbol{D}\cdot\boldsymbol{\mathcal{E}}_{\mathrm{R}}(\boldsymbol{r})$ and the internal energy of the reservoir H_{R}. They can be neglected compared to the first part of the Hamiltonian, if the detuning is large compared to the Rabi frequency ($|\delta_{\mathrm{L}}|\gg|\Omega|$), and large compared to the spontaneous emission rate ($|\delta_{\mathrm{L}}|\gg\Gamma_e$). In this case the saturation parameter (cf. (B.5))

$$s=\frac{|\Omega|^2/2}{\delta_{\mathrm{L}}^2+\Gamma_e^2/4} \tag{4.5}$$

is small ($s\ll 1$) and the system can be regarded as quasi non-dissipative.

The treatment of the atomic Hamiltonian $H_0=H_{\mathrm{kin}}+H_{\mathrm{A}}-\boldsymbol{D}\cdot\boldsymbol{\mathcal{E}}(\boldsymbol{r},t)$ simplifies in the rotating wave approximation, where non-resonant terms of the form $|e\rangle\langle g|\exp[i\omega_{\mathrm{L}}t]$ and

$|g\rangle\langle e| \exp[-i\omega_{\mathrm{L}} t]$ can be neglected. H_0 then takes the form

$$H_0 = \frac{\boldsymbol{p}^2}{2m} \left(|e\rangle\langle e| + |g\rangle\langle g|\right) + \hbar\omega_{\mathrm{A}} |e\rangle\langle e| + \frac{\hbar\Omega(\boldsymbol{r})}{2} e^{-i\omega_{\mathrm{L}} t} |e\rangle\langle g| + \frac{\hbar\Omega^*(\boldsymbol{r})}{2} e^{i\omega_{\mathrm{L}} t} |g\rangle\langle e| \tag{4.6}$$

The time-dependent Schrödinger equation $i\hbar\,\partial_t |\Psi\rangle = H_0 |\Psi\rangle$ for the total atomic state $|\Psi\rangle$, which can be expanded as $|\Psi\rangle = \psi_g |g\rangle + \psi_e \exp[-i\omega_{\mathrm{L}} t] |e\rangle$, provides us with a system of coupled amplitude equations [91]

$$i\hbar\,\partial_t\,\psi_g = -\frac{\hbar^2}{2m}\nabla^2\psi_g + \frac{\hbar\Omega^*(\boldsymbol{r})}{2}\,\psi_e \tag{4.7a}$$

$$i\hbar\,\partial_t\,\psi_e = -\frac{\hbar^2}{2m}\nabla^2\psi_e + \frac{\hbar\Omega(\boldsymbol{r})}{2}\,\psi_g - \hbar\delta_{\mathrm{L}}\psi_e \tag{4.7b}$$

Far off resonance, i. e. for a large detuning $|\delta_{\mathrm{L}}| \gg |\Omega|$, one can furthermore assume that the atoms, which are initially prepared in their ground state, mostly remain in their ground state during the time evolution. In this case, the spatial and temporal derivatives of the excited state amplitude in equation (4.7b) can be neglected, and ψ_e can be approximated as $\psi_e \approx \Omega(\boldsymbol{r})/(2\delta_{\mathrm{L}})\,\psi_g$.

Under the previously described approximations, inserting (4.7b) into (4.7a), the ground-state amplitude obeys an effective Schrödinger equation with the Hamiltonian

$$H_g = \frac{\boldsymbol{p}^2}{2m} + \frac{\hbar\,|\Omega(\boldsymbol{r})|^2}{4\delta_{\mathrm{L}}} \tag{4.8}$$

which describes the atomic motion in an effective optical potential $U(\boldsymbol{r})$. Reinserting the definition of the Rabi frequency (4.4), the optical dipole potential reads

$$U(\boldsymbol{r}) = \frac{\hbar\,|\Omega(\boldsymbol{r})|^2}{4\delta_{\mathrm{L}}} = \frac{\hbar\Gamma_e}{8}\,\frac{\Gamma_e}{\delta_{\mathrm{L}}}\,\frac{I(\boldsymbol{r})}{I_{\mathrm{s}}} \tag{4.9}$$

where the intensity of the laser field is given by

$$I(\boldsymbol{r}) = \frac{1}{2}\,c\,\epsilon_0\,|\mathcal{E}(\boldsymbol{r})|^2 \tag{4.10}$$

and the saturation intensity I_{s} is defined as

$$I_{\mathrm{s}} = \frac{c\,\epsilon_0\hbar^2\,\Gamma_e^2}{4\,|\boldsymbol{u}\cdot\boldsymbol{d}|^2} \tag{4.11}$$

Due to the coupling to the vacuum fluctuation reservoir, the atomic evolution is purely Hamiltonian only up to the inelastic scattering time τ_ϕ when spontaneous emission occurs. The average inelastic scattering rate for such a dissipative process can be derived from the

optical Bloch equations [67]. It is given by (cf. (B.6))

$$\Gamma_\phi = \frac{1}{\tau_\phi} \approx \frac{\Gamma_e}{\delta_\mathrm{L}} \frac{\overline{U}}{\hbar} \tag{4.12}$$

where $\overline{U} = \overline{U(\boldsymbol{r})}$ is the average value of the optical dipole potential (4.9).

4.2 Effective Medium

The scattered waves in a disordered medium are different from one realization of disorder to another. Therefore, only expectation values obtained by averaging over many realizations may provide a useful characterization of the transport processes. In the language of atom optics, averaging over many speckle realizations introduces an effective medium for the expanding matter wave. The main concern of the present chapter will be to determine the scattering mean free path ℓ_s in the effective medium. To this aim, the average retarded and the average advanced propagators are introduced. They are shown to verify the Dyson equation, which defines the self-energy operator. In the weak-scattering regime, which is determined by the small perturbation parameter that governs the series expansion of the self-energy, the elastic scattering rate γ_s can be calculated exactly in terms of the imaginary part of the self-energy. This defines the elastic scattering time τ_s and the scattering mean free path ℓ_s, which is studied in detail for the 2D and the 3D speckle pattern.

4.2.1 Retarded and Advanced Propagator

The single-particle dynamics for an atom inside the disordered optical potential can be described by the effective Hamiltonian (4.8). Writing the optical potential (4.9) as $U(\boldsymbol{r}) = \overline{U} + V(\boldsymbol{r})$ with the mean value $\overline{U}$ and the potential fluctuations $V(\boldsymbol{r})$, and incorporating the constant mean value into the energy, allows to write the stationary Schrödinger equation for the atomic matter wave as[1]

$$\Big[-\frac{\hbar^2}{2m}\nabla^2 + V(\boldsymbol{r}) \Big] \psi(\boldsymbol{r}) = E\psi(\boldsymbol{r}) \tag{4.13}$$

With the free-particle wavevector $k^2 = 2mE/\hbar^2$ the Fourier transform of (4.13) naturally reads $\left[\nabla^2 + k^2 - \frac{2m}{\hbar^2} V(\boldsymbol{r})\right] \psi(\boldsymbol{r}) = 0$, which differs only slightly from the Helmholtz equation for classical waves, where the potential term is replaced by fluctuations of the dielectric constant [7]. However, due to the fact that the fluctuations of the optical potential do not depend on the energy, the treatment for matter waves is simpler than for classical waves, where this energy dependence results in significant corrections to the transport speed of light [92].

[1] It is also possible to introduce a dimensionless Schrödinger equation, defining all quantities in terms of the speckle correlation length ζ. This approach has been chosen in [28].

Feynman Propagators

In the following, we denote the Hamiltonian for the effective Schrödinger equation (4.13) by H and the free-particle Hamiltonian in the absence of any potential fluctuations by H_0. The time evolution of the atom inside the disordered potential is determined through the time-evolution operator $U(t,t') = \exp\left[-\frac{i}{\hbar}H(t-t')\right]$, which follows the time-dependent Schrödinger equation $i\hbar\,\partial_t\,U(t,t') = (H_0+V)\,U(t,t')$ with the integral solution

$$U(t,t') = U_0(t,t') - \frac{i}{\hbar}\int_{t'}^{t} \mathrm{d}t_1\; U_0(t,t_1)\,V\,U(t_1,t') \tag{4.14}$$

where $U_0(t,t') = \exp\left[-\frac{i}{\hbar}H_0(t-t')\right]$ is the time-evolution operator of the unperturbed Hamiltonian H_0. It is possible to define the time-dependent retarded and advanced Feynman propagators as [67]

$$\begin{aligned} K^R(t,t') &= U(t,t')\Theta(t-t') & K^A(t,t') &= -U(t,t')\Theta(t'-t) \\ K_0^R(t,t') &= U_0(t,t')\Theta(t-t') & K_0^A(t,t') &= -U_0(t,t')\Theta(t'-t) \end{aligned} \tag{4.15}$$

$K^R(t,t')$ is called the retarded propagator, because it is zero for $t < t'$. K^A is called the advanced propagator since it is zero for $t > t'$. Both propagators are Green functions in the time domain. As such they both solve the equation

$$(i\hbar\,\partial_t - H)K^{R,A}(t,t') = i\hbar\,\delta(t-t') \tag{4.16}$$

Here, $K^{R,A}(t,t')$ represents either the retarded or the advanced Feynman propagator. Multiplying equation (4.14) by $\Theta(t-t')$ leads to an equivalent integral equation for the retarded Feynman propagator

$$K^R(t,t') = K_0^R(t,t') - \frac{i}{\hbar}\int_{-\infty}^{\infty} \mathrm{d}t_1\; K_0^R(t,t_1)\,V\,K^R(t_1,t') \tag{4.17}$$

Born Series

Taking the Fourier transform of equation (4.17) and applying the convolution theorem reveals upon iteration the usual Born series for the retarded Green operator (or resolvent) in the energy domain

$$G^R(E) = G_0^R(E) + G_0^R(E)\,V\,G^R(E) \tag{4.18}$$

Here, $G^R(E)$ is defined as the Fourier transform of the retarded Feynman propagator [67]

$$G^R(E) = -\frac{i}{\hbar}\int_{-\infty}^{\infty} \mathrm{d}\tau\; e^{i\,E\tau/\hbar}K^R(\tau) \tag{4.19a}$$

$$K^R(\tau) = \frac{i}{2\pi}\int_{-\infty}^{\infty} \mathrm{d}E\; e^{-i\,E\tau/\hbar}G^R(E) \tag{4.19b}$$

where $\tau = t - t'$. Using the definition (4.15), $G^R(E)$ can be written as

$$G^R(E) = -\frac{i}{\hbar} \lim_{\eta \to 0_+} \int_0^\infty \mathrm{d}\tau \, e^{i\,(E-H+i\eta)\tau/\hbar} = \lim_{\eta \to 0_+} \frac{1}{E - H + i\eta} \tag{4.20}$$

The same calculation for the advanced Green function leads to the propagator

$$G^A(E) = \lim_{\eta \to 0_+} \frac{1}{E - H - i\eta} \tag{4.21}$$

For zero potential fluctuations equations (4.20) and (4.21) yield the free-particle propagators $G_0^R(E)$ and $G_0^A(E)$.

The definition of the Fourier transform adopted for this work (cf. (2.11), (2.12) and appendix C) implies that the identity is resolved by $1 = \int \mathrm{d}\boldsymbol{r} \; |\boldsymbol{r}\rangle\langle\boldsymbol{r}|$ and $1 = \int \mathrm{d}\boldsymbol{k}/(2\pi)^d \; |\boldsymbol{k}\rangle\langle\boldsymbol{k}|$, while the wavefunctions $\psi_{\boldsymbol{k}}(\boldsymbol{r}) = \langle\boldsymbol{r}|\boldsymbol{k}\rangle$ and $\psi_{\boldsymbol{r}}(\boldsymbol{k}) = \langle\boldsymbol{k}|\boldsymbol{r}\rangle$ are given by $\langle\boldsymbol{r}|\boldsymbol{k}\rangle = e^{i\boldsymbol{k}\cdot\boldsymbol{r}}$ and $\langle\boldsymbol{k}|\boldsymbol{r}\rangle = e^{-i\boldsymbol{k}\cdot\boldsymbol{r}}$, for the wavevector $|\boldsymbol{k}\rangle = \hbar^{-1}\,|\boldsymbol{p}\rangle$. The wavevector matrix elements of the free-particle propagators are then determined as

$$\langle\boldsymbol{k}'|\, G_0^{R,A}(E)\, |\boldsymbol{k}\rangle = (2\pi)^d \delta(\boldsymbol{k} - \boldsymbol{k}')\, G_0^{R,A}(k, E) = \lim_{\eta \to 0_+} \frac{(2\pi)^d\, \delta(\boldsymbol{k} - \boldsymbol{k}')}{E - \hbar^2 k^2/2m \pm i\eta} \tag{4.22}$$

Due to the isotropy of space, the free-particle Green function $G^{R,A}(k, E)$ only depends on the modulus $k = |\boldsymbol{k}|$. With $z = E + i\eta$, $A = z - H$ and $B = z - H_0$ and expression (4.20) for the retarded and (4.21) for the advanced propagator, the operator identity [67]

$$A^{-1} = B^{-1} + B^{-1}(B - A)A^{-1} \tag{4.23}$$

recovers the Born series (4.18).

Configuration Average

Taking the configuration average of the Born series for the retarded and advanced propagators (4.20) and (4.21), one obtains[2]

$$\overline{G} = G_0 + G_0\, \overline{V G_0 V}\, G_0 + G_0\, \overline{V G_0 V G_0 V}\, G_0 + \ldots \tag{4.24}$$

where $\overline{G} = \overline{G^{R,A}}(E)$ and $G_0 = G_0^{R,A}(E)$ represent either the retarded or the advanced propagator. The linear term vanishes since we have chosen the origin of the energy such that $\overline{V} = 0$.

The calculation of the average resolvent thus requires the calculation of all higher-order correlation functions of the potential fluctuations V. It is possible, however, to reorganize

[2] The energy dependence has been omitted for clarity.

the Born series in the following form, known as the Dyson equation [93]

$$\overline{G} = G_0 + G_0\,\Sigma\,\overline{G} \tag{4.25}$$

where the retarded or advanced self-energy operator $\Sigma = \Sigma^{R,A}(E)$ contains all irreducible correlation functions, i. e. correlations that cannot be split into products of independent factors by suppressing a single propagator G_0 [93]. Upon iteration the Dyson equation (4.25) reveals a geometric series that is formally solved as

$$\begin{aligned}\overline{G} &= G_0 + G_0\,\Sigma\,[G_0 + G_0\,\Sigma\,[G_0 + G_0\,\Sigma\,[\ldots]]] \\ &= G_0 \sum_{n=0}^{\infty} [\Sigma\, G_0]^n = \frac{1}{{G_0}^{-1} - \Sigma} = \lim_{\eta\to 0_+} \frac{1}{E - H_0 - \Sigma \pm i\eta}\end{aligned} \tag{4.26}$$

Taking the average over many realizations of disorder restores the translational invariance. Consequently, just like the free-space propagator (4.22), $\overline{G^{R,A}}(E)$ is diagonal in wavevector space. Its matrix elements are given by

$$\begin{aligned}\langle \boldsymbol{k}'|\,\overline{G^{R,A}}(E)\,|\boldsymbol{k}\rangle &= (2\pi)^d \delta(\boldsymbol{k}-\boldsymbol{k}')\,\overline{G^{R,A}}(k,E) \\ &= \lim_{\eta\to 0_+} \frac{(2\pi)^d\,\delta(\boldsymbol{k}-\boldsymbol{k}')}{E - \hbar^2k^2/2m - \Sigma^{R,A}(k,E) \pm i\eta}\end{aligned} \tag{4.27}$$

Since the disordered potential preserves space isotropy on average, the function $\overline{G^{R,A}}(k,E)$ again only depends on the modulus $k = |\boldsymbol{k}|$. The same conclusion holds for the self-energy $\Sigma^{R,A}(k,E)$. As we will see in the following section, the imaginary part of the average Green function $\overline{G^{R,A}}$ is of special importance.

4.3 Spectral Function and Density of States

All information about the relative weight, the energy, and the lifetime of excitations dressed by the disordered medium is contained in the spectral function [94]

$$\begin{aligned}A(k,E) &= -2\,\mathrm{Im}[\overline{G^R}(k,E)] = i\Big[\overline{G^R}(k,E) - \overline{G^A}(k,E)\Big] \\ &= \frac{-2\,\mathrm{Im}[\Sigma^R(k,E)]}{(E - \hbar^2k^2/2m - \mathrm{Re}[\Sigma^R(k,E)])^2 + \mathrm{Im}^2[\Sigma^R(k,E)]}\end{aligned} \tag{4.28}$$

The spectral function is positive ($A(k,E) \geq 0$) because the retarded self-energy has a negative imaginary part, and it is normalized to unity: $\int \mathrm{d}E/(2\pi)\,A(k,E) = 1$. It can thus be regarded as the probability density for excitations with wavenumbers k to have an energy E. The normalization condition follows directly from the Fourier transform of the average propagator. Since

$$\Theta(t)\overline{U}(t) = \pm i \int_{-\infty}^{\infty} \frac{\mathrm{d}E}{2\pi}\; e^{\mp iEt/\hbar}\,\overline{G^{R,A}}(E) \tag{4.29}$$

one can replace the average propagator in the normalization integral by the average time-evolution operator at time $t = 0$. Then

$$\int_{-\infty}^{\infty} \frac{\mathrm{d}E}{2\pi}\, A(k,E) = i\int_{-\infty}^{\infty} \frac{\mathrm{d}E}{2\pi}\, \left[\overline{G^R}(k,E) - \overline{G^A}(k,E)\right] = \frac{\overline{U}(0)}{2} + \frac{\overline{U}(0)}{2} = 1 \tag{4.30}$$

as $\overline{U}(0) = 1$ and $\Theta(0) = \frac{1}{2}$. The integration over $\mathrm{d}\boldsymbol{k}$ of the spectral function (4.28) yields the average density of states $N(E)$

$$\int \frac{\mathrm{d}\boldsymbol{k}}{(2\pi)^d}\, A(k,E) = -2\int \frac{\mathrm{d}\boldsymbol{k}}{(2\pi)^d}\, \mathrm{Im}[\overline{G^R}(k,E)] = 2\pi N(E) \tag{4.31}$$

On-shell Approximation for Weak Disorder

The wavevector k_E, corresponding to a given energy E, can be determined as the solution to the complex dispersion relation $E - \hbar^2 k_E^2/2m - \Sigma^R(k_E, E) = 0$. This is the standard approach in atom optics [95]. The wavenumber inside the effective medium is then characterized by $k_E = n(E)\sqrt{2mE}/\hbar$ with the complex refractive index

$$n(E) = \sqrt{1 - \frac{\Sigma^R(k_E,E)}{E}} \tag{4.32}$$

For weak disorder ($\left|\Sigma^R(k_E,E)\right| \ll E$), the potential fluctuations modify only slightly the free dispersion relation. The refractive index of the effective medium can then be approximated by

$$n(E) \approx 1 - \frac{\mathrm{Re}[\Sigma^R(k_E,E)]}{2E} - i\,\frac{\mathrm{Im}[\Sigma^R(k_E,E)]}{2E} \tag{4.33}$$

where the imaginary part $\mathrm{Im}[n(E)]$ accounts for the depletion of the initial modes due to scattering. Unlike for true absorption, where one encounters energy dissipation, the energy in our case is only distributed over scattering modes, and remains conserved during the scattering process. In analogy to real absorption the elastic scattering rate for weak disorder can be defined as

$$\hbar\gamma_s(k_E) = 4E\mathrm{Im}[n(E)] = -2\mathrm{Im}[\Sigma^R(k_E)] \tag{4.34}$$

where $\Sigma^R(k_E) = \Sigma^R(k_E, E)$ denotes the projection of the self-energy onto the energy shell, and $k_E = \sqrt{2mE}/\hbar$ describes the free-particle dispersion relation. For weak disorder, since $\mathrm{Re}[\Sigma^R(k_E)] = \mathrm{Re}[\Sigma^R(k_E,E)] \ll E$, the real part of the self-energy in the denominator of the spectral function (4.28) can be neglected compared to the Energy E, such that the spectral function may be written in the form

$$A(k,E) \approx \frac{\hbar\gamma_s(k_E)}{(E - \hbar^2k^2/2m)^2 + \hbar^2\gamma_s^2(k_E)/4} \tag{4.35}$$

In the same way as for the spectral function, the retarded and the advanced Green functions for weak disorder can be written as [7]

$$\overline{G^{R,A}}(k,E) \approx \frac{1}{E - \hbar^2 k^2/2m \pm i\hbar\gamma_s(k_E)/2} \tag{4.36}$$

Within the weak disorder approximation, the average density of states to zeroth order in the small disorder parameter $\hbar\gamma_s(k_E)/(2E) \ll 1$, is given by

$$N(E) = N_0(E)\Big(1 + \mathcal{O}\Big(\frac{\hbar\gamma_s(k_E)}{2E}\Big)\Big) \tag{4.37}$$

where $N_0(E)$ denotes the free particle density of states

$$N_0(E) = \int \frac{\mathrm{d}\boldsymbol{k}}{(2\pi)^d}\, \delta\big(\tfrac{\hbar^2 k^2}{2m} - E\big) = \frac{\Omega_d}{(2\pi)^d}\, \frac{m^{d/2}}{\hbar^d}\, (2E)^{d/2-1} \tag{4.38}$$

Here, $\Omega_d = \int \mathrm{d}\Omega_d = 2\pi^{d/2}/\Gamma(d/2)$ denotes the surface of the unit sphere. $\Gamma(x)$ is the Euler gamma function. This corresponds to the replacement of the spectral function $A(k,E)$ in (4.31) by the on-shell projector $A_0(k,E) = 2\pi\delta(E - \hbar^2 k^2/2m)$.

Short-Range Correlation Function

The real-space matrix elements of the average propagator $\overline{G^{R,A}}(E)$ are given by the Fourier transform

$$\langle \boldsymbol{r}'|\, \overline{G^{R,A}}(E)\, |\boldsymbol{r}\rangle = \overline{G^{R,A}}(\boldsymbol{r},\boldsymbol{r}',E) = \int \frac{\mathrm{d}\boldsymbol{k}}{(2\pi)^d}\, \overline{G^{R,A}}(k,E)\, e^{i\boldsymbol{k}\cdot(\boldsymbol{r}-\boldsymbol{r}')} \tag{4.39}$$

where $\overline{G^{R,A}}(\boldsymbol{r},\boldsymbol{r}',E)$ has the following form in 2D and in 3D [7]

$$\text{2D:} \qquad \overline{G^{R,A}}(\boldsymbol{r},\boldsymbol{r}',E) = -i\pi N_0\, \mathcal{H}_0^{(1)}\big(\pm k_E\, |\boldsymbol{r}-\boldsymbol{r}'|\big)\, e^{-|\boldsymbol{r}-\boldsymbol{r}'|/2\ell_s(k_E)} \tag{4.40a}$$

$$\text{3D:} \qquad \overline{G^{R,A}}(\boldsymbol{r},\boldsymbol{r}',E) = -\pi N_0\, \frac{e^{\pm i k_E|\boldsymbol{r}-\boldsymbol{r}'|}}{k_E\, |\boldsymbol{r}-\boldsymbol{r}'|}\, e^{-|\boldsymbol{r}-\boldsymbol{r}'|/2\ell_s(k_E)} \tag{4.40b}$$

$\mathcal{H}_0^{(1)}(\pm x) = \pm\mathcal{J}_0(x) + i\mathcal{Y}_0(x)$ is the Hankel function. $\mathcal{J}_0(x)$ is the zeroth-order Bessel function and $\mathcal{Y}_0(x)$ is the zeroth-order von Neumann function.

With the help of the spatial representation of the spectral function it is possible to define the non-local density of states $N(\boldsymbol{r},\boldsymbol{r}',E)$ according to

$$2\pi N(\boldsymbol{r},\boldsymbol{r}',E) = A(\boldsymbol{r},\boldsymbol{r}',E) = -2\mathrm{Im}[\overline{G^R}(\boldsymbol{r},\boldsymbol{r}',E)] = 2\pi N_0\, g\big(|\boldsymbol{r}-\boldsymbol{r}'|, E\big) \tag{4.41}$$

The square of the newly defined function $g(R,E)$ is known as the short-range correlation function $a_A(R,E) = g^2(R,E)$. In 2D and in 3D one encounters the following expressions for

$g(R, E)$ [7]

$$\text{2D:} \qquad g(R,E) = \mathcal{J}_0(k_E R)\, e^{-R/2\ell_s(k_E)} \tag{4.42a}$$

$$\text{3D:} \qquad g(R,E) = \frac{\sin(k_E R)}{k_E R}\, e^{-R/2\ell_s(k_E)} \tag{4.42b}$$

In principle, if the wavevector matrix elements of the self-energy operator can be determined, we now have all necessary information about the average propagators and the average density of states in the effective medium.

4.4 Diagrammatic Representation of the Self-Energy

The self-energy operator in the Dyson equation (4.25) embodies an asymptotic series [96] that is constructed out of an infinite number of terms like $\overline{VG_0V}$, $\overline{VG_0VG_0V}$, etc. Each term of order n in the fluctuation strength $\overline{U}$ consists of the product of $n-1$ propagators G_0 and 1 correlation function of order n of the potential fluctuations V. Up to the factor $(\overline{U}/\overline{I})^n$ these correlation functions are exactly identical to the correlation functions of the speckle-intensity fluctuations. The real-space matrix element of the second-order correlation function is given by

$$\overline{V(\boldsymbol{r})\,V(\boldsymbol{r}')} = \overline{U}^2 \left|\gamma(\boldsymbol{r}-\boldsymbol{r}')\right|^2 \tag{4.43}$$

just like in (2.10). $\overline{U} = \overline{U(\boldsymbol{r})}$ denotes the average height of the optical potential and $\gamma(\boldsymbol{r})$ is the complex degree of coherence. The real-space matrix element of the third-order correlation function is given by (cf. (2.16))

$$\overline{V(\boldsymbol{r})\,V(\boldsymbol{r}')\,V(\boldsymbol{r}'')} = 2\overline{U}^3\,\mathrm{Re}[\gamma(\boldsymbol{r}-\boldsymbol{r}')\,\gamma(\boldsymbol{r}'-\boldsymbol{r}'')\,\gamma(\boldsymbol{r}-\boldsymbol{r}'')] \tag{4.44}$$

The self-energy terms can be assembled according to powers of the average speckle fluctuation strength $\overline{U}^n$, such that

$$\Sigma = \sum_{n\geq 2} \Sigma_n \tag{4.45}$$

where the first terms can be represented in diagrammatic form as

$\Sigma_2 =$ (4.46a)

$\Sigma_3 =$ (4.46b)

$\Sigma_4 =$ 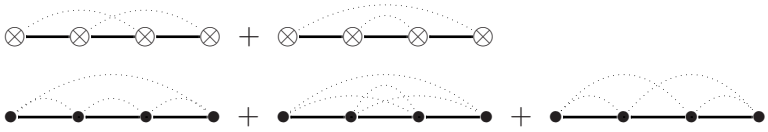 (4.46c)

$\Sigma_5 =$ $+\ldots$ (4.46d)

In these diagrams, every straight line represents the free propagator G_0. The diagrams are irreducible in the sense that by cutting any such single propagator line, they do not split into independent parts. A dotted line connecting two black dots like $\bullet \overset{\frown}{} \bullet = \overline{U}\gamma$ represents a field correlation function, whereas a dotted line connecting two potential fluctuation operators $\otimes = V$, like $\otimes \overset{\frown}{} \otimes = \overline{U}^2\gamma^2$, represents a potential correlation function (4.43). The appearance of odd terms Σ_{2q+1} in the formal series (4.45) reflects the non-Gaussian character of the potential fluctuations.

To evaluate a diagram, its expression in terms of correlation functions and propagators has to be integrated over all free internal variables. Since the potential fluctuation operator $\otimes = V$ is diagonal in real space and therefore translation invariant in Fourier space, the wavevector representation of Σ_2 is given by

$$\langle \boldsymbol{k}' | \otimes \overset{\frown}{\text{——}} \otimes | \boldsymbol{k} \rangle = \int \frac{\mathrm{d}\boldsymbol{k}_1}{(2\pi)^d} \, \overline{V(\boldsymbol{k}_1 - \boldsymbol{k}')\, V(\boldsymbol{k} - \boldsymbol{k}_1)} \, G_0^{R,A}(k_1, E) \tag{4.47}$$

Inserting the correlation function of the potential fluctuations

$$\overline{V(\boldsymbol{k})\, V(\boldsymbol{k}')} = (2\pi)^d \, \delta(\boldsymbol{k} + \boldsymbol{k}') \; \mathcal{P}_V(\boldsymbol{k}) \tag{4.48}$$

where $\mathcal{P}_V(\boldsymbol{k})$ is the Fourier transform of $\mathcal{P}_V(\boldsymbol{r} - \boldsymbol{r}') = \overline{V(\boldsymbol{r})\, V(\boldsymbol{r}')}$, we find

$$\langle \boldsymbol{k}' | \otimes \overset{\frown}{\text{——}} \otimes | \boldsymbol{k} \rangle = (2\pi)^d \, \delta(\boldsymbol{k} - \boldsymbol{k}') \, \Sigma_2^{R,A}(k, E) \tag{4.49}$$

Here, the subscript for the correlation function $\mathcal{P}_V$ indicates that we are dealing with potential fluctuations V instead of intensity fluctuations J as in (2.11). However, the difference only lies in the prefactor $\overline{U}$. As expected, the self-energy operator is diagonal in wavevector space and isotropic. The matrix elements of the self-energy operator Σ_2 are thus given by the convolution of the power spectrum $\mathcal{P}_V$ with the free Green function G_0

$$\Sigma_2^{R,A}(k, E) = \int \frac{\mathrm{d}\boldsymbol{k}_1}{(2\pi)^d} \, \mathcal{P}_V(\boldsymbol{k} - \boldsymbol{k}_1) \, G_0^{R,A}(k_1, E) \tag{4.50}$$

In principle, all diagrams in the self-energy series have to be calculated in this way and summed up to give the self-energy contribution in (4.27).

4.5 Identification of the Perturbation Parameter

The identification of the perturbation parameter is best achieved in dimensionless units as described in [28]. We therefore define the dimensionless wavenumber $\kappa = k/k_\zeta$ and the dimensionless energy $\varepsilon = E/E_\zeta$ in units of the inverse correlation length $k_\zeta = 1/\zeta$ and the correlation energy $E_\zeta = \hbar^2 k_\zeta^2/m$. The high-energy case $\kappa = \sqrt{2\varepsilon} \gg 1$ and the low-energy case $\kappa \ll 1$ are discussed separately.

High-Energy Limit ($\boldsymbol{\kappa} \gg 1$)

In the high-energy limit, it is possible to determine the dependence of Σ_n on the ultraviolet wavevector $\kappa \gg 1$ by simple power counting. Each irreducible diagram contributing to Σ_n contains $n-1$ internal propagators G_0, p field correlation functions ($0 \leq p \leq n$), and $(n-p)/2$ potential correlation functions. Taking into account all momentum conservation laws, this leaves exactly $(n+p)/2$ independent variables $\boldsymbol{\kappa}_i$, which can be chosen to be the arguments of the correlation functions. Because of the strict momentum cut-off, these correlation functions constrain the norms $\kappa_i = |\boldsymbol{\kappa}_i|$ to remain of order unity or smaller. The only dependence on κ comes from the Green functions that are evaluated at momenta $\boldsymbol{\kappa}_j = \boldsymbol{\kappa} - \sum_i \alpha_i \boldsymbol{\kappa}_i$ with topology-dependent coefficients $\alpha_i \in \{0, \pm 1\}$.

Linearizing around the on-shell value $\varepsilon = \kappa^2/2$ for $\kappa \gg \kappa_i$, each Green function contributes a power κ^{-1}. Additionally, each field correlation function is weighted by a factor $\overline{U}$, and each potential correlation function contributes a factor $\overline{U}^2$. The on-shell self-energy matrix element of order n has the form

$$\Sigma_n^{R,A}(k) \propto \overline{U}^n \kappa^{1-n} E_\zeta^{1-n}\, a_n \tag{4.51}$$

where a_n is related to the number of n-point irreducible diagrams. If we further define the dimensionless disorder parameter

$$\eta = \frac{\overline{U}}{E_\zeta} \tag{4.52}$$

the ratio $\Sigma^{R,A}(k)/E$ for $\kappa \gg 1$ can be rewritten as $\Sigma^{R,A}(k)/E \propto \sum_{n\geq 2} (a_n/\kappa)\, g^n$. This reveals the effective expansion parameter

$$g = \frac{\eta}{\kappa} = \frac{\overline{U}}{\sqrt{2EE_\zeta}} \tag{4.53}$$

Low-Energy Limit ($\boldsymbol{\kappa} \ll 1$)

2D: The low-energy limit $\kappa \ll 1$ in the 2D geometry allows for a similar analysis. Each of the $(n+p)/2$ correlation functions in Σ_n tends towards its isotropic limit and becomes a constant. Together with the contribution κ^{n+p} from the $(n+p)/2$ integration measures, and κ^{2-2n} from the $n-1$ Green functions, this yields a scaling κ^{2-n+p} for Σ_n. If n is even, Σ_n is therefore dominated by the diagrams with $p = 0$, containing only potential correlation functions and diverging like κ^{2-n}.

If n is odd, the dominant contribution comes from the diagrams with the smallest number of field correlations, $p = 3$, that appear first in Σ_3 and reappear subsequently in higher non-Gaussian terms Σ_{2q+1}. One can then rewrite the dominant contributions to (4.45) for $\kappa \ll 1$

in a 2D system in the form

$$\Sigma^{R,A}(k)/E \propto \sum_{q\geq 1} \left(a_{2q}\, g^{2q} + \kappa^3 a_{2q+1}\, g^{2q+1}\right) \tag{4.54}$$

Remarkably, g as defined in (4.53) is still the expansion parameter, and remains small, if $\overline{U}/E_\zeta \ll \kappa \ll 1$.

Terms that are negligible compared to both their neighbours in the series can be omitted. This applies to all odd terms when $\kappa^3 g^{2q+1} \ll g^{2q+2}$, i. e. $\kappa^3 \ll g$ at fixed g. In this regime, the self-energy does no longer depend on the field correlation functions, and only the Gaussian terms without explicit κ dependence survive

$$\Sigma^{R,A}(k)/E = \sum_{q\geq 1} a_{2q}\, g^{2q} \tag{4.55}$$

We thus recover an effective δ-correlated Gaussian-distributed potential with the same small perturbation parameter as before. This result is quite natural: because of its large coherence length, the matter wave is not sensitive to phenomena occurring at the scale of ζ.

3D: The 3D case requires a separate discussion. As far as the pure intensity correlations ($p = 0$) are concerned, actually the same reasoning as for 2D holds, because the low-κ divergence of the potential correlation $\propto \kappa^{-1}$ is compensated by a supplementary factor from the integration measure.

However, the pure 3D field correlation functions $\gamma(\kappa) \propto \delta(1-\kappa)$ cannot tend to a constant as $\kappa \to 0$, but project all integration momenta onto the modulus unit sphere. Consequently, a small-κ contribution of the integration measure and the correlation functions can only come from the $(n-p)/2$ variables in the potential correlation functions: it is of the form κ^{n-p}. The contribution of a propagator is either κ^{-2} (as in the 2D case), if it does not depend on a field-correlation momentum, or independent of κ in the limit $\kappa \to 0$, because field-correlation momenta of order unity remain present. Thus, the diagrams depending only on the field correlations ($n = p$) behave like κ^0. At fixed n and p, the dominant diagrams, mixing field correlation functions and potential correlation functions, are those with the largest number of propagator lines independent of the p field-correlation variables. This happens when field correlations can be written as products of the largest number of independent field-correlation subdiagrams that never cross the potential correlation lines.

An example for such a diagram is the first contribution to Σ_5 shown in (4.46d), which displays a Σ_3-type field correlation inside a Σ_2 potential correlation. In all dominant cases, the field sub-diagrams contain at most 3, 4 or 5 vertices (as those shown in Σ_3, Σ_4, and Σ_5), because higher-order field correlations can be factorized into these elementary ones, thus yielding an additional independent propagator. Writing $p = 3n_1 + 4n_2 + 5n_3$, where the n_i are non-negative integers, the largest possible number of subdiagrams is obtained by

maximizing the sum $n_1 + n_2 + n_3$. The number of propagator lines giving a κ^{-2} contribution to the diagram is then $n - p + n_1 + n_2 + n_3 - 1$, and the total contribution of the diagram is $\kappa^{2-n+n_1+2n_2+3n_3}$.

It turns out that, when n is even, the dominant contribution κ^{2-n} to Σ_n comes from the potential-correlation diagrams ($p = 0$). When n is odd, the main contribution κ^{3-n} is due to the diagrams with $n_1 = 1$, i. e. $p = 3$. Similarly to the 2D case, the dominant contribution to the self-energy (4.45) is

$$\Sigma^{R,A}(k)/E = \sum_{q\geq 1} \left(a_{2q}\, g^{2q} + \kappa a_{2q+1}\, g^{2q+1}\right) \tag{4.56}$$

As in the 2D case, g as defined in (4.53) is the expansion parameter. Again, terms which are negligible compared to both their neighbours can be omitted. This applies to the odd terms when $\kappa^2 \ll \eta \ll \kappa \ll 1$ at fixed g, i. e. in the quantum regime discussed at the end of section 4.6. In this regime, an effective δ-correlated Gaussian potential is recovered.

4.6 Weak-Scattering Approximation

The ratio of two consecutive terms Σ_n and Σ_{n+1} in the momentum representation of the self-energy series is proportional to the effective scattering parameter $g = \eta/\kappa$, where $\kappa = k/k_\zeta$ is the reduced incident wave vector and $\eta = \overline{U}/E_\zeta$ is the reduced disorder parameter. Since the number of diagrams a_n grows factorially with n, we face the well-known troublesome fact that, even if the global weak-scattering condition, $g \ll 1$, covering both the high-energy and low-energy regime, is fulfilled, the series (4.45) formally diverges.

However, the self-energy series can be understood as an asymptotic series [96], which can be accurately approximated by just the first few terms. When the effective coupling constant g is sufficiently small, a truncation to the first term already gives a good approximation of the self-energy. For $g \ll 1$, or equivalently for $\eta \ll \kappa$, the self-energy operator can then be approximated by

$$\Sigma^{R,A}(k) \approx \Sigma_2^{R,A}(k), \qquad g \ll 1 \tag{4.57}$$

This is known as the weak-scattering or Born approximation.

4.6.1 Weak-Scattering Parameter

In terms of the atomic kinetic energy, the weak-scattering condition reads $\varepsilon = E/E_\zeta = \kappa^2/2 \gg \eta^2$ or

$$\Delta = \frac{\eta^2}{\varepsilon} = \frac{\overline{U}^2}{EE_\zeta} \ll 1 \tag{4.58}$$

This condition determines the range of validity for the diagrammatic perturbation theory.

Random Phase Kicks

The correlation length ζ of the potential fluctuations defines the characteristic time $\tau_\zeta = \zeta/v$, which is the time during which an atom, propagating with the velocity $v = \hbar k/m$, experiences correlations of the potential fluctuations. In a semiclassical picture the multiple scattering process in the effective medium can be described as a series of scattering events of time τ_ζ during which the atom receives a random phase-kick. In-between two consecutive scattering events the atom travels on a straight path of length ℓ_s, which is the decay length of the average amplitude in the effective medium. Along a path with length ζ, the typical accumulated phase is $\overline{U}\tau_\zeta/\hbar$, which is equivalent to the small parameter g defined in 4.53. The weak-scattering condition $g \ll 1$ or $\Delta \ll 1$ (cf. (4.57) and (4.58)) is thus equivalent to the fact that the accumulated phase is small. This is the condition of applicability of the thin phase grating approximation [97]. If the effect of the potential fluctuations is weak, the atomic wave is only slightly distorted and scattered after travelling a distance ζ.

Quantum Reflection Probability

The same condition (4.58) is obtained if we consider the quantum reflection probability for a particle that is scattered by a 1D potential barrier with height $\overline{U}$ and linear size ζ (cf. Fig. **4.1**).

Classical Regime ($E > \overline{U}$): In this case the atom flies well above the potential fluctuations, which corresponds to the regime of classical atomic motion. For $E > \overline{U}$ or $\varepsilon > \eta$ the standard quantum reflection coefficient in the reduced units $\varepsilon = E/E_\zeta$ and $\eta = \overline{U}/E_\zeta$ can be written as [98]

$$R^{-1} = 1 + \frac{x^2}{\Delta \sin^2 x} \tag{4.59}$$

with $x = \sqrt{2(\varepsilon - \eta)}$. Since the oscillating term $\sin x/x \leq 1$ is always bounded by 1, a small quantum reflection coefficient is achieved for $\Delta \ll 1$, which corresponds precisely to the weak-scattering condition (4.58). If the fluctuation strength is smaller than the correlation energy $\overline{U} < E_\zeta$, the weak-scattering condition requires an atom with an energy that is larger than the correlation energy $E > E_\zeta$. If on the other hand $\overline{U} > E_\zeta$, the weak-scattering condition can still be fulfilled with a sufficiently high atomic energy $E \gg E_\zeta$.

Quantum Regime ($E < \overline{U}$): In the quantum regime, where $E < \overline{U}$ or $\varepsilon < \eta$ the quantum reflection coefficient becomes

$$R^{-1} = 1 + \frac{x^2}{\Delta \sinh^2 x} \tag{4.60}$$

with $x = \sqrt{2(\eta - \varepsilon)}$. In this case, the weak-scattering regime is realized if $E < \overline{U} \ll E_\zeta$, i. e. for a correlation energy that is much larger than the potential fluctuations. This corresponds to a Taylor expansion for small x in (4.60). Hence $R^{-1} \approx 1 + 1/\Delta \gg 1$ for

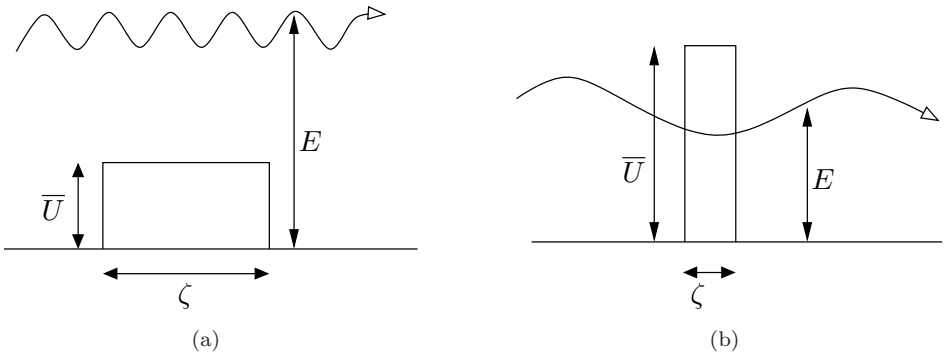

Figure 4.1:
Classical Regime (a) vs. Quantum Regime (b) for a particle scattered at a potential barrier with height $\overline{U}$ and linear size ζ.

$\Delta \ll 1$, which again corresponds to the weak-scattering condition (4.58).

4.6.2 Weak-Scattering Energy

Equivalently, the weak-scattering condition (4.57) can be written as $E \gg E_\Delta$ with the weak-scattering energy

$$E_\Delta = \overline{U}^2/E_\zeta \tag{4.61}$$

In the 3D case (for $k\zeta < 1$), this energy scale coincides up to a numerical factor with the mobility edge E_m, which separates extended states with $E > E_m$ from localized states with $E < E_m$. When $\overline{U} < E_\zeta$, the energy of a localized state would be $E < E_m < \overline{U}$, which means that such an atom is simply trapped in deep local potential wells. When $\overline{U} > E_\zeta$, then $E_m > \overline{U}$, which means that strong localization can in principle be achieved for $E > \overline{U}$. Classically, the atoms would fly above the potential fluctuations and could diffuse to arbitrarily remote spatial regions. However, because of interference, the corresponding atomic state is in fact localized. In both cases, however, the mobility edge is very close to the validity limit of the perturbation theory.

4.7 Scattering Mean Free Path

Using the expression (4.34) for the elastic scattering rate for weak disorder, together with the imaginary part of the self-energy in the Born approximation (4.50), the average elastic scattering time $\tau_s(k) = 1/\gamma_s(k)$ is obtained as

$$\tau_s^{-1}(k) = \frac{2\pi N_0}{\hbar} \int \frac{\mathrm{d}\Omega_d}{\Omega_d}\, \mathcal{P}_V(k\hat{\boldsymbol{k}} - k\hat{\boldsymbol{k}}') = \frac{2\pi N_0}{\hbar}\, \langle \mathcal{P}_V(k,\theta)\rangle \tag{4.62}$$

where $\hat{\boldsymbol{k}}$ and $\hat{\boldsymbol{k}}'$ are unit vectors pointing in the direction of $\boldsymbol{k}$ and $\boldsymbol{k}'$ and θ is the angle between $\boldsymbol{k}$ and $\boldsymbol{k}'$. $\langle \ldots \rangle$ denotes the angular average and $\mathcal{P}_V(k\hat{\boldsymbol{k}} - k\hat{\boldsymbol{k}}') = \mathcal{P}_V(k,\theta)$ is the power spectrum.

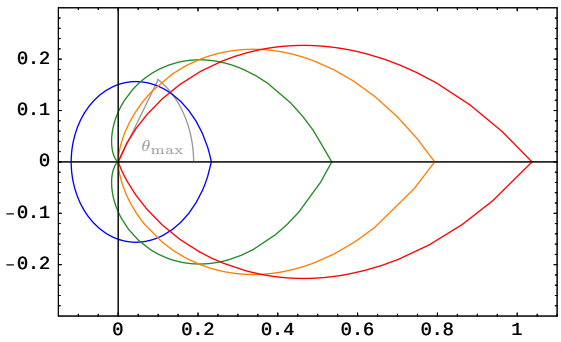

Figure 4.2:
2D: Polar plot of the phase function $f_2(k,\theta)$ in (4.68) for different atomic wavenumbers $k\zeta = 0.4, 1.0, 1.4, 1.8$ (from left to right: blue, green, orange, red) in units of the inverse speckle correlation length $\zeta^{-1} = \alpha k_{\mathrm{L}}$. The phase function represents the differential single-scattering cross-section. It is nearly isotropic for slow atoms $k\zeta \ll 1$, whereas for fast atoms, $k\zeta \gg 1$, it is strongly peaked in the forward direction with a maximal scattering angle: $\theta_{\max} \approx 2/k\zeta$.

The elastic scattering rate defines the elastic scattering mean free path $\ell_s = \hbar k/(m\gamma_s)$ for a quasi-monochromatic wave packet centred around the wavevector $\boldsymbol{k}$. Under the Born approximation this simplifies to

$$\frac{1}{k\ell_s(k)} = -\frac{\mathrm{Im}[\Sigma_2^R(k)]}{E} \tag{4.63}$$

The scattering mean free path describes the distance over which a particle travels on average without being scattered. Consistently with the weak-disorder condition $\mathrm{Im}[\Sigma_2^R(k)] \ll E$, we have $\hbar\gamma_s/2 \ll E$ and equivalently

$$k\ell_s \gg 1 \tag{4.64}$$

Taking the imaginary part of equation (4.50) with the help of

$$\mathrm{Im}[G_0^R(k,E)] = -\pi\,\delta\big(\tfrac{\hbar^2k^2}{2m} - E\big) \tag{4.65}$$

gives the inverse scattering mean free path (4.63) in the form

$$\frac{1}{k\ell_s(k)} = -\frac{2m\,\mathrm{Im}[\Sigma_2^R(k)]}{\hbar^2k^2} = \frac{m^2}{\hbar^4}\,\frac{k^{d-4}}{(2\pi)^{d-1}}\int \mathrm{d}\Omega_d\,\mathcal{P}_V(k,\theta) \tag{4.66}$$

Here, $\mathcal{P}_V(k,\theta)$ denotes the angular correlation function as a function of the scattering angle θ between $\boldsymbol{k}$ and $\boldsymbol{k}_1$ at fixed on-shell momenta $k = k_1$. The d-dimensional angular integration measure $\mathrm{d}\Omega_d$ is given by $\mathrm{d}\Omega_2 = \mathrm{d}\theta$ (integration range from 0 to 2π) and $\mathrm{d}\Omega_3 = 2\pi\sin\theta\,\mathrm{d}\theta$ (integration range from 0 to π).

Since $\mathcal{P}_V(k,\theta)$ is proportional to the square of the optical potential $\overline{U}^2$ (cf. (4.43)), and hence proportional to δ_{L}^2, the scattering mean free path does not depend on the sign of the laser detuning.

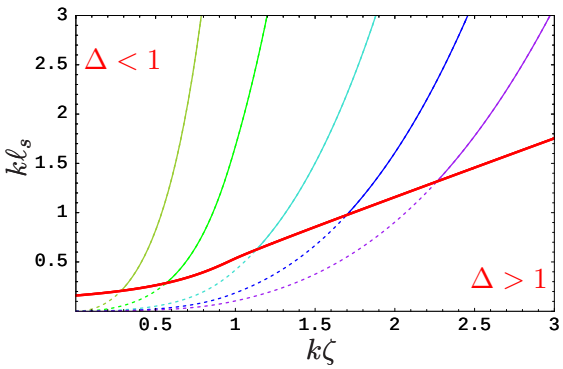

Figure 4.3:
2D: Plot of $k\ell_s$ as a function of the reduced atomic wavenumber $k\zeta$ for different values of the disorder strength (thin curves from left to right) $\eta = 0.2, 0.4, 0.8, 1.2, 1.6$. The thick red line connects all points of $k\ell_s$ where $\Delta = 1$, i. e. $k\zeta = \sqrt{2}\,\eta$, indicates the weak-scattering limit. The perturbative approach clearly is only valid in the weak-scattering regime, where $\Delta < 1$ (solid curves). The dotted curves only indicate an extrapolation into the strong scattering regime, which is not covered by the perturbative theory.

4.7.1 2D Speckle

The 2D angular correlation function of the potential fluctuations for $0 < \theta < 2\pi$ reads (cf. (2.31))

$$\mathcal{P}_V(k,\theta) = \frac{8\overline{U}^2}{k_\zeta^2}\Big[\arccos(\kappa\sin\tfrac{\theta}{2}) - (\kappa\sin\tfrac{\theta}{2})\sqrt{1-(\kappa\sin\tfrac{\theta}{2})^2}\Big]\Theta(1-\kappa\sin\tfrac{\theta}{2}) \tag{4.67}$$

with $\kappa = k/k_\zeta = k\zeta$. The Heaviside function $\Theta(1-\kappa\sin\frac{\theta}{2})$ restricts the scattering angle to $\sin\frac{\theta}{2} < 1/\kappa$. When $\kappa \leq 1$, this condition is always fulfilled, and all angles are accessible. When $\kappa > 1$, the scattering direction is restricted to a maximum scattering angle $|\theta| \leq \theta_{\max} = 2\arcsin(1/\kappa)$. This is illustrated in Fig. **4.2** by a polar plot of the 2D phase function[3]

$$f_2(k,\theta) = \frac{\mathcal{P}_V(k,\theta)}{\displaystyle\int \mathrm{d}\Omega_2\, \mathcal{P}_V(k,\theta)} \tag{4.68}$$

For fast atoms, $\kappa \gg 1$, the differential scattering cross-section is strongly peaked in the forward direction, which clearly reveals the anisotropic nature of the scattering process. In this case, $\theta_{\max} \approx 2/\kappa \ll 1$. For slow atoms, $\kappa \ll 1$, the differential scattering cross-section becomes isotropic. In this case, the correlation function $\mathcal{P}_V(\boldsymbol{\rho})$ can be approximated by a delta function such that its Fourier transform is constant: $\mathcal{P}_V(\boldsymbol{q}) \approx 4\pi$. Hence, the angular dependence is lost for $\kappa \ll 1$. Already the first scattering event randomizes the direction of scattering. Inserting the angular correlation function (4.67) into (4.66), it is possible to calculate the scattering mean free path. For $\kappa = 1$ the integral can be solved exactly

$$k\ell_s = \frac{\pi}{2(\pi^2-4)\eta^2} \qquad k\zeta = 1 \tag{4.69}$$

[3]The name "phase function" has its origins in astronomy, where it refers to lunar phases [99]

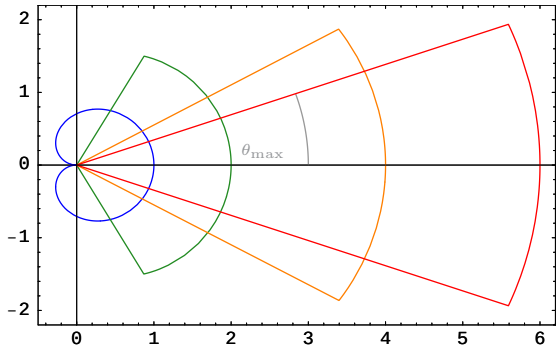

Figure 4.4:
3D: Polar plot of the effective phase function $f_3'(k,\theta)$, (4.72), for different atomic wavenumbers $k\zeta = 1.0, 2.0, 4.0, 6.0$ (from left to right). All plots with $k\zeta \leq 1$ are identical. If $k\zeta \gg 1$, the phase function is strongly anisotropic and displays the maximum scattering angle $\theta_{\max} \approx 2/k\zeta$.

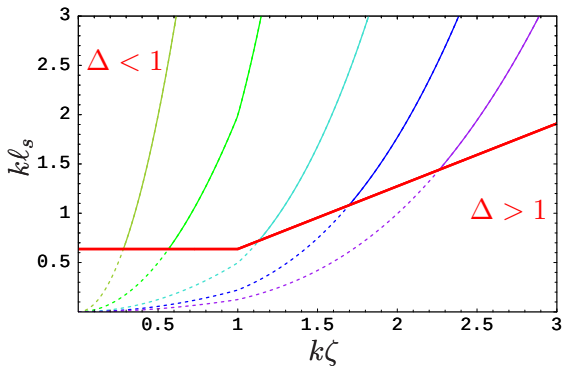

Figure 4.5:
3D: Plot of $k\ell_s$ as a function of the reduced atomic wavenumber $k\zeta$ for different values of the disorder strength (thin curves from left to right) $\eta = 0.2, 0.4, 0.8, 1.2, 1.6$. The thick red line connects all points of $k\ell_s$ where $\Delta = 1$, i. e. $k\zeta = \sqrt{2}\,\eta$, indicating the weak-scattering limit.

It is also possible to obtain analytic results in the limiting cases $\kappa \gg 1$ and $\kappa \ll 1$, where the respective approximations $\sin x \approx x$ and $\arccos x - x\sqrt{1-x^2} \approx \frac{\pi}{2}$ can be used

$$k\ell_s \approx \frac{(k\zeta)^2}{4\pi\eta^2} \qquad k\zeta \ll 1 \tag{4.70a}$$

$$k\ell_s \approx \frac{3\pi(k\zeta)^3}{32\eta^2} \qquad k\zeta \gg 1 \tag{4.70b}$$

The condition $\Delta \leq 1$ implies the boundary $k\ell_s \geq \frac{1}{2\pi}$, such that weak scattering $\Delta \ll 1$ indeed describes weak disorder $k\ell_s \gg 1$, even at very low momenta. At higher momenta (cf. (4.70b)), weak scattering $\Delta \leq 1$ implies the boundary $\ell_s \geq \frac{3\pi}{16}\zeta$, which agrees with the intuitive expectation that the scattering mean free path cannot be considerably shorter than the 2D speckle correlation length ζ itself. Fig. **4.3** shows a plot of $k\ell_s$ as a function of $k\zeta$ obtained by numerical integration of (4.66). The boundary $\Delta = 1$ indicates the limit of validity of the weak-scattering approximation.

4.7.2 3D Speckle

In three dimensions the angular correlation function of the potential fluctuations for $0 < \theta < \pi$ is given by (cf. (2.35))

$$\mathcal{P}_V(k,\theta) = \frac{\overline{U}^2\pi^2}{k_\zeta^3}\,\frac{\Theta(1-\kappa\sin\frac{\theta}{2})}{2\kappa\sin\frac{\theta}{2}} \tag{4.71}$$

with $\kappa = k/k_\zeta = k\zeta$ and $k_\zeta = k_\mathrm{L}$. Since in 3D $\mathcal{P}_V(k,\theta) = \mathcal{P}_V(2k\sin\frac{\theta}{2})$ diverges in the forward direction $\theta \to 0$, we plot in Fig. **4.4** the effective phase function including the angular Jacobian

$$f_3'(k,\theta) = \sin\theta f_3(k,\theta) = \frac{\sin\theta\,\mathcal{P}_V(k,\theta)}{\displaystyle\int \mathrm{d}\Omega_3\,\mathcal{P}_3(k,\theta)} \tag{4.72}$$

As for the 2D case, the plot shows bounded scattering $|\theta| \leq \theta_\mathrm{max}$ for fast atoms $\kappa > 1$ and unrestricted scattering for slow atoms $\kappa \leq 1$. Exact backscattering $\theta = \pi$ appears suppressed due to the angular Jacobian. The inverse elastic scattering mean free path (4.66) is given by

$$\frac{1}{k\ell_s} = \pi\eta^2\left[\frac{\Theta(k\zeta-1)}{(k\zeta)^3} + \frac{\Theta(1-k\zeta)}{(k\zeta)^2}\right] \tag{4.73}$$

in terms of the correlation length $\zeta = k_\mathrm{L}^{-1}$ and the speckle strength $\eta = \overline{U}/E_\zeta$.

The condition $\Delta \leq 1$ implies the boundary $k\ell_s \geq \frac{2}{\pi}$, such that weak scattering $\Delta \ll 1$ indeed describes weak disorder $k\ell_s \gg 1$, even at low momenta. At high momenta, weak scattering $\Delta \leq 1$ implies that $k\ell_s \geq \frac{2}{\pi}k\zeta$, i. e. the lowest achievable scattering mean free path is of the order of the 3D speckle correlation length ζ itself. Fig. **4.5** shows a plot of $k\ell_s$ as a function of $k\zeta$ as obtained by (4.73).

4.8 Summary

In this chapter we have studied the physical model, which, in the following, is going to be the basis for the theoretical description of matter-wave transport in disordered optical potentials. We have derived the spatially varying optical dipole potential (4.9) that plays the role of the disordered potential for our atoms and we have identified the phase-breaking time τ_ϕ, during which a Hamiltonian evolution of the atomic matter waves is expected (cf. (4.12)). In the remaining part of the current chapter we have derived the elastic scattering mean free path in the effective medium for the 2D and the 3D speckle pattern (cf. (4.66)). In contrast to isotropic scattering, where the scatterers are assumed to be uncorrelated singularities, the speckle potential exhibits non-local correlations. This is the reason for the anisotropic nature of the differential single-scattering cross-section, which is revealed in the polar plots of the effective 2D and 3D phase functions. Moreover, due to the fact that only the electric field but not the intensity is a true Gaussian random variable, additional field-correlation diagrams appear in the self-energy representation. These field-correlation diagrams have to be considered in addition to the common potential fluctuation diagrams, in order to determine the small perturbation parameter g (cf. (4.53)). We have seen that the self-energy embodies an asymptotic series governed by the small perturbation parameter, which can be approximated by the first diagram in the series for $g \ll 1$. This determines the weak-scattering regime and gives the limit of validity of the diagrammatic perturbation theory.

Chapter 5

Diffusive Transport

In the present chapter we derive a general expression for the average probability density to find an atom at the point $\boldsymbol{r}$ inside the disordered optical potential at the time t for any initial phase-space configuration of the atoms. We also establish the general continuity equation between the average probability density and the average current density. Both quantities can be determined in terms of the intensity kernel that combines the average retarded and advanced propagator. The intensity kernel is shown to verify a Bethe-Salpeter equation. In the wavevector representation, this Bethe-Salpeter equation results in the quantum kinetic equation, which can be solved in the long-time, large-distance limit following mainly the original derivation by Vollhardt and Wölfle. This provides a closed expression for the intensity kernel, which is shown to obey a diffusion equation. In the remaining part of this chapter we calculate the diffusion constant in the Boltzmann approximation, which characterizes the classical contribution to the diffusive matter-wave transport. This approximation is shown to be consistent with the weak-scattering approximation introduced in the previous chapter, via the Ward identity. The Boltzmann diffusion constant defines the Boltzmann transport mean free path as the typical length scale over which the matter wave loses all memory of its initial direction. This quantity is calculated for the 2D and the 3D speckle pattern and compared to the scattering mean free path.

5.1 Probability Transport

In the course of its propagation in a disordered potential, an initial matter wave is rapidly turned into a diffuse matter wave invading the entire scattering region. The dynamics of this process is described by the disorder-averaged probability density $p(\boldsymbol{r},t)$, which can be obtained as the expectation value of the projection operator $\hat{n}(\boldsymbol{r}) = |\boldsymbol{r}\rangle\langle\boldsymbol{r}|$ for the time $t > 0$

$$\begin{aligned} p(\boldsymbol{r},t) &= \Theta(t)\mathrm{Tr}[\overline{\varrho}(t)\hat{n}(\boldsymbol{r})] = \langle\boldsymbol{r}|\,\Theta(t)\overline{\varrho}(t)\,|\boldsymbol{r}\rangle \\ &= \int\frac{\mathrm{d}\boldsymbol{k}}{(2\pi)^d}\int\frac{\mathrm{d}\boldsymbol{q}}{(2\pi)^d}\,e^{i\boldsymbol{q}\cdot\boldsymbol{r}}\,\langle\boldsymbol{k}+\tfrac{\boldsymbol{q}}{2}|\,\Theta(t)\overline{\varrho}(t)\,|\boldsymbol{k}-\tfrac{\boldsymbol{q}}{2}\rangle = \int\frac{\mathrm{d}\boldsymbol{k}}{(2\pi)^d}\,\overline{W}(\boldsymbol{k},\boldsymbol{r},t) \end{aligned} \tag{5.1}$$

where $\overline{\varrho}(t)$ is the average atomic density operator and $\overline{W}(\boldsymbol{k},\boldsymbol{r},t)$ is the Wigner function at $t \geq 0$ defined as

$$\overline{W}(\boldsymbol{k},\boldsymbol{r},t) = \int \frac{\mathrm{d}\boldsymbol{q}}{(2\pi)^d}\, e^{i\boldsymbol{q}\cdot\boldsymbol{r}}\, \langle \boldsymbol{k}_+|\, \Theta(t)\overline{\varrho}(t)\, |\boldsymbol{k}_-\rangle = \int \mathrm{d}\boldsymbol{R}\, e^{-i\boldsymbol{k}\cdot\boldsymbol{R}}\, \langle \boldsymbol{r}_+|\, \Theta(t)\overline{\varrho}(t)\, |\boldsymbol{r}_-\rangle \tag{5.2a}$$

$$\overline{\varrho}(\boldsymbol{k},\boldsymbol{q},t) = \langle \boldsymbol{k}_+|\, \Theta(t)\overline{\varrho}(t)\, |\boldsymbol{k}_-\rangle = \int \mathrm{d}\boldsymbol{r}\, e^{-i\boldsymbol{q}\cdot\boldsymbol{r}}\, \overline{W}(\boldsymbol{k},\boldsymbol{r},t) \tag{5.2b}$$

with $\boldsymbol{r}_\pm = \boldsymbol{r} \pm \boldsymbol{R}/2$ and $\boldsymbol{k}_\pm = \boldsymbol{k} \pm \boldsymbol{q}/2$. $p(\boldsymbol{r},t)$ is normalized such that $\int \mathrm{d}\boldsymbol{r}\, p(\boldsymbol{r},t) = 1$.

The current density operator is defined as [4] $\hat{\boldsymbol{j}}(\boldsymbol{r}) = \hbar/(2m)\,\{\hat{n}(\boldsymbol{r}), \hat{\boldsymbol{k}}\}$ with the anti-commutator $\{\hat{A},\hat{B}\} = \hat{A}\hat{B} + \hat{B}\hat{A}$. The current density at time $t \geq 0$ at the point $\boldsymbol{r}$ is then given by the expectation value

$$\begin{aligned} \boldsymbol{j}(\boldsymbol{r},t) &= \Theta(t)\mathrm{Tr}[\overline{\varrho}(t)\hat{\boldsymbol{j}}(\boldsymbol{r})] = \frac{\hbar}{2m}\, \langle \boldsymbol{r}|\, \big\{\Theta(t)\overline{\varrho}(t), \hat{\boldsymbol{k}}\big\}\, |\boldsymbol{r}\rangle \\ &= \frac{\hbar}{m} \int \frac{\mathrm{d}\boldsymbol{k}}{(2\pi)^d} \int \frac{\mathrm{d}\boldsymbol{q}}{(2\pi)^d}\, e^{i\boldsymbol{q}\cdot\boldsymbol{r}}\, \boldsymbol{k}\, \overline{\varrho}(\boldsymbol{k},\boldsymbol{q},t) = \frac{\hbar}{m} \int \frac{\mathrm{d}\boldsymbol{k}}{(2\pi)^d}\, \boldsymbol{k}\, \overline{W}(\boldsymbol{k},\boldsymbol{r},t) \end{aligned} \tag{5.3}$$

The probability density (5.1) at $t \geq 0$ and the current density (5.3) at $t \geq 0$ are coupled through the continuity equation

$$\partial_t\, p(\boldsymbol{r},t) + \nabla \cdot \boldsymbol{j}(\boldsymbol{r},t) = \delta(t) p(\boldsymbol{r},0) \tag{5.4}$$

The source term on the right-hand side is given by the initial probability density $p(\boldsymbol{r},0)$ at the time $t = 0$.

Time Evolution

The time evolution of the density operator is given by $\overline{\varrho}(t) = \overline{U(t)\, \varrho_0\, U^\dagger(t)}$, where ϱ_0 denotes the initial atomic density operator and $U(t)$ is the time-evolution operator. Making use of the retarded Green operator (4.19a) and its hermitian conjugate, together with the definition (4.15), the density matrix element $\overline{\varrho}(\boldsymbol{k},\boldsymbol{q},t)$ at $t \geq 0$ can be written as

$$\overline{\varrho}(\boldsymbol{k},\boldsymbol{q},t) = \int \frac{\mathrm{d}E}{2\pi} \int \frac{\mathrm{d}\epsilon}{2\pi} \int \frac{\mathrm{d}\boldsymbol{k}'}{(2\pi)^d}\, e^{-i\epsilon t/\hbar}\, \varrho_0(\boldsymbol{k}',\boldsymbol{q})\, \Phi(\boldsymbol{k},\boldsymbol{k}',\boldsymbol{q},E,\epsilon) \tag{5.5}$$

The matrix element of the intensity kernel operator $\Phi = \overline{G^A \otimes G^R}$ is given by

$$\Phi(\boldsymbol{k},\boldsymbol{k}',\boldsymbol{q},E,\epsilon) = \overline{\langle \boldsymbol{k}'_-|\, G^A(E_+)\, |\boldsymbol{k}_-\rangle\, \langle \boldsymbol{k}_+|\, G^R(E_-)\, |\boldsymbol{k}'_+\rangle} \tag{5.6}$$

with the energy entries $E_+ = E + \epsilon/2$ and $E_- = E - \epsilon/2$ and the wavevector entries $\boldsymbol{k}_\pm = \boldsymbol{k} \pm \boldsymbol{q}/2$ and $\boldsymbol{k}'_\pm = \boldsymbol{k}' \pm \boldsymbol{q}'/2$. Due to the conservation of the total momentum (i. e. the sum of the incoming wavevectors equals the sum of the outgoing wavevectors), the transfer vectors are equal, $\boldsymbol{q} = \boldsymbol{q}'$. The ensemble average is done after taking the product of the Green functions, which means that all correlations between different amplitudes are included. In

the diagrammatic representation this corresponds to the four-point diagram

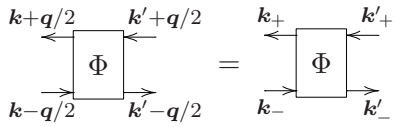

(5.7)

where the upper entries refer to the retarded Green function and the lower entries refer to the advanced Green function. The incoming vectors are $\boldsymbol{k}'+\boldsymbol{q}/2$ for the retarded and $\boldsymbol{k}-\boldsymbol{q}/2$ for the advanced Green function.

Replacing the initial density matrix $\varrho_0(\boldsymbol{k}',\boldsymbol{q})$ in (5.5) by the Fourier transform of the initial Wigner function $W_0(\boldsymbol{k}',\boldsymbol{r}')$

$$\varrho_0(\boldsymbol{k}',\boldsymbol{q}) = \int \mathrm{d}\boldsymbol{r}'\; e^{-i\boldsymbol{q}\cdot\boldsymbol{r}'}\, W_0(\boldsymbol{k}',\boldsymbol{r}') \tag{5.8}$$

the probability density (5.1) can be written as

$$p(\boldsymbol{r},t) = \int \frac{\mathrm{d}\boldsymbol{k}'}{(2\pi)^d} \int \mathrm{d}\boldsymbol{r}'\; \mathcal{F}(\boldsymbol{k}',\boldsymbol{r}-\boldsymbol{r}',t)\, W_0(\boldsymbol{k}',\boldsymbol{r}') \tag{5.9}$$

Here, $\mathcal{F}(\boldsymbol{k}',\boldsymbol{r}-\boldsymbol{r}',t)$ is the intensity relaxation kernel, which will be specified in the following subsection.

Intensity Relaxation Kernel

The intensity relaxation kernel $\mathcal{F}(\boldsymbol{k}',\boldsymbol{r}-\boldsymbol{r}',t)$ in (5.9) describes the evolution of the Wigner function $W_0(\boldsymbol{k}',\boldsymbol{r}')$ in phase space. It is given by the Fourier transform

$$\mathcal{F}(\boldsymbol{k}',\boldsymbol{R},t) = \int \frac{\mathrm{d}\epsilon}{2\pi} \int \frac{\mathrm{d}\boldsymbol{q}}{(2\pi)^d}\; e^{i\boldsymbol{q}\cdot\boldsymbol{R}}\, e^{-i\epsilon t/\hbar}\, \mathcal{F}(\boldsymbol{k}',\boldsymbol{q},\epsilon) \tag{5.10}$$

where $\boldsymbol{R}=\boldsymbol{r}-\boldsymbol{r}'$. The new kernel function $\mathcal{F}(\boldsymbol{k}',\boldsymbol{q},\epsilon)$ itself is given by

$$\mathcal{F}(\boldsymbol{k}',\boldsymbol{q},\epsilon) = \int \frac{\mathrm{d}E}{2\pi} \int \frac{\mathrm{d}\boldsymbol{k}}{(2\pi)^d}\; \Phi(\boldsymbol{k},\boldsymbol{k}',\boldsymbol{q},E,\epsilon) \tag{5.11}$$

The Fourier transform of the probability density and the Fourier transform of the current density then read

$$p(\boldsymbol{q},\epsilon) = \int \frac{\mathrm{d}\boldsymbol{k}'}{(2\pi)^d}\; \varrho_0(\boldsymbol{k}',\boldsymbol{q})\, \mathcal{F}(\boldsymbol{k}',\boldsymbol{q},\epsilon) \tag{5.12a}$$

$$\boldsymbol{j}(\boldsymbol{q},\epsilon) = \int \frac{\mathrm{d}\boldsymbol{k}'}{(2\pi)^d}\; \varrho_0(\boldsymbol{k}',\boldsymbol{q})\, \boldsymbol{J}(\boldsymbol{k}',\boldsymbol{q},\epsilon) \tag{5.12b}$$

with $\mathcal{F}(\boldsymbol{k}', \boldsymbol{q}, \epsilon)$ as defined in (5.11) and

$$\boldsymbol{J}(\boldsymbol{k}', \boldsymbol{q}, \epsilon) = \frac{\hbar}{m} \int \frac{\mathrm{d}E}{2\pi} \int \frac{\mathrm{d}\boldsymbol{k}}{(2\pi)^d}\, \boldsymbol{k}\, \Phi(\boldsymbol{k}, \boldsymbol{k}', \boldsymbol{q}, E, \epsilon) \tag{5.13}$$

The continuity equation (5.4) then leads to an additional continuity equation for the newly defined kernel functions (5.11) and (5.13) of the form

$$-i\epsilon\, \mathcal{F}(\boldsymbol{k}', \boldsymbol{q}, \epsilon) + i\hbar\, \boldsymbol{q} \cdot \boldsymbol{J}(\boldsymbol{k}', \boldsymbol{q}, \epsilon) = 1 \tag{5.14}$$

Bethe-Salpeter Equation

The dynamics of the atomic probability density is essentially governed by the intensity kernel operator $\Phi(E_-, E_+) = \overline{G^A(E_-) \otimes G^R(E_+)}$, a four-point operator, whose matrix elements in wavevector representation are the integrand of (5.11). In its operator form, the intensity kernel $\Phi(E_-, E_+)$ obeys a Bethe-Salpeter equation[1]

$$\Phi = [\overline{G^A} \otimes \overline{G^R}] + [\overline{G^A} \otimes \overline{G^R}]\, U\, \Phi \tag{5.15}$$

The first term on the right-hand side represents the ballistic propagation in the effective medium with uncorrelated average propagators (4.26). All correlated scattering events are described by the irreducible scattering vertex U. In fact, the Bethe-Salpeter equation actually defines U, in the same way as the Dyson equation (4.25) defines the self-energy Σ.

5.2 Quantum Kinetic Equation

The Bethe-Salpeter equation (5.15) for the intensity propagation kernel $\Phi(E_-, E_+)$ can be reformulated in wavevector space as a quantum kinetic equation [4]. The matrix elements of the scattering operator U and the operator $[\overline{G^A} \otimes \overline{G^R}]$ are given by

$$\langle \boldsymbol{k}'_-, \boldsymbol{k}_+ |\, U(E_-, E_+)\, | \boldsymbol{k}_-, \boldsymbol{k}'_+ \rangle = U(\boldsymbol{k}, \boldsymbol{k}', \boldsymbol{q}, E, \epsilon) \tag{5.16a}$$

$$\langle \boldsymbol{k}'_-, \boldsymbol{k}_+ |\, \overline{G^A}(E_-) \otimes \overline{G^R}(E_+)\, | \boldsymbol{k}_-, \boldsymbol{k}'_+ \rangle = (2\pi)^d \delta(\boldsymbol{k} - \boldsymbol{k}')\, \overline{G^A}(\boldsymbol{k}, \boldsymbol{q}, E, \epsilon) \overline{G^R}(\boldsymbol{k}, \boldsymbol{q}, E, \epsilon) \tag{5.16b}$$

with the wavevector entries $\boldsymbol{k}_\pm = \boldsymbol{k} \pm \boldsymbol{q}/2$ and $\boldsymbol{k}'_\pm = \boldsymbol{k}' \pm \boldsymbol{q}/2$ and the energy entries $E = (E_+ + E_-)/2$ and $\epsilon = E_+ - E_-$ as before. In this notation, the incoming wavevector entries appear on the right-hand side in the $|\ldots\rangle$ vectors.

Using the identity $ab = [a - b]/[b^{-1} - a^{-1}]$, for the numbers a and b, the product $\overline{G^A}\, \overline{G^R}$ in (5.16b) can be written as

$$\overline{G^A}(\boldsymbol{k}, \boldsymbol{q}, E, \epsilon) \overline{G^R}(\boldsymbol{k}, \boldsymbol{q}, E, \epsilon) = \frac{-\Delta G(\boldsymbol{k}, \boldsymbol{q}, E, \epsilon)}{\epsilon - \frac{\hbar^2}{m} \boldsymbol{k} \cdot \boldsymbol{q} - \Delta\Sigma(\boldsymbol{k}, \boldsymbol{q}, E, \epsilon)} \tag{5.17}$$

[1] The energy arguments have been suppressed for clarity.

where the functions $\Delta G(\boldsymbol{k}, \boldsymbol{q}, E, \epsilon)$ and $\Delta\Sigma(\boldsymbol{k}, \boldsymbol{q}, E, \epsilon)$ denote the differences of the retarded and advanced Green functions and self energies, respectively, according to

$$\Delta G(\boldsymbol{k}, \boldsymbol{q}, E, \epsilon) = \overline{G^R}(\boldsymbol{k}_+, E_+) - \overline{G^A}(\boldsymbol{k}_-, E_-) \tag{5.18a}$$

$$\Delta\Sigma(\boldsymbol{k}, \boldsymbol{q}, E, \epsilon) = \Sigma^R(\boldsymbol{k}_+, E_+) - \Sigma^A(\boldsymbol{k}_-, E_-) \tag{5.18b}$$

Multiplying by the denominator of (5.17) and integrating over the free variables, the quantum kinetic equation then reads

$$\left[\epsilon - \frac{\hbar^2}{m}\,\boldsymbol{k}\cdot\boldsymbol{q} - \Delta\Sigma(\boldsymbol{k}, \boldsymbol{q}, E, \epsilon)\right]\Phi(\boldsymbol{k}, \boldsymbol{k}', \boldsymbol{q}, E, \epsilon) = -\Delta G(\boldsymbol{k}, \boldsymbol{q}, E, \epsilon) \times \left[(2\pi)^d\delta(\boldsymbol{k}-\boldsymbol{k}') + \int \frac{\mathrm{d}\boldsymbol{k}''}{(2\pi)^d}\, U(\boldsymbol{k}, \boldsymbol{k}'', \boldsymbol{q}, E, \epsilon)\,\Phi(\boldsymbol{k}'', \boldsymbol{k}', \boldsymbol{q}, E, \epsilon)\right] \tag{5.19}$$

Ward Identity

As shown by Vollhardt and Wölfle [5], the irreducible vertex function $U(\boldsymbol{k}, \boldsymbol{k}'', \boldsymbol{q}, E, \epsilon)$ is linked to the self-energy $\Sigma(\boldsymbol{k}, \boldsymbol{q}, E, \epsilon)$ through the Ward identity[2]

$$\Delta\Sigma(\boldsymbol{k}, \boldsymbol{q}, E, \epsilon) = \int \frac{\mathrm{d}\boldsymbol{k}''}{(2\pi)^d}\; \Delta G(\boldsymbol{k}'', \boldsymbol{q}, E, \epsilon)\, U(\boldsymbol{k}'', \boldsymbol{k}, \boldsymbol{q}, E, \epsilon) \tag{5.20}$$

This identity is valid for all $\boldsymbol{q}$ and ϵ [5]. It can be shown that each diagram (also the non-Gaussian diagrams) in the series expansion of the self-energy (4.45) independently verifies (5.20). The Ward identity thus applies to the whole self-energy series, even if the potential is not δ-correlated.

Bringing the self-energy term to the right-hand side of (5.19) and making use of the Ward identity (5.20), the quantum kinetic equation (5.19) can also be written as

$$\left[\epsilon - \frac{\hbar^2}{m}\,\boldsymbol{k}\cdot\boldsymbol{q}\right]\Phi(\boldsymbol{k}, \boldsymbol{k}', \boldsymbol{q}, E, \epsilon) = -(2\pi)^d\delta(\boldsymbol{k}-\boldsymbol{k}')\Delta G(\boldsymbol{k}, \boldsymbol{q}, E, \epsilon) + C[\Phi] \tag{5.21}$$

Here, $C[\Phi]$ denotes the linear collision functional given by

$$C[\Phi] = \int \frac{\mathrm{d}\boldsymbol{k}''}{(2\pi)^d}\, U(\boldsymbol{k}'', \boldsymbol{k}, \boldsymbol{q}, E, \epsilon)\left[\Delta G(\boldsymbol{k}'', \boldsymbol{q}, E, \epsilon)\,\Phi(\boldsymbol{k}, \boldsymbol{k}', \boldsymbol{q}, E, \epsilon) - \Delta G(\boldsymbol{k}, \boldsymbol{q}, E, \epsilon)\,\Phi(\boldsymbol{k}'', \boldsymbol{k}', \boldsymbol{q}, E, \epsilon)\right] \tag{5.22}$$

where we have used the fact that $U(\boldsymbol{k}'', \boldsymbol{k}, \boldsymbol{q}, E, \epsilon) = U(\boldsymbol{k}, \boldsymbol{k}'', \boldsymbol{q}, E, \epsilon)$ since the scattering vertex depends only on the absolute value $|\boldsymbol{k}-\boldsymbol{k}''|$.

If (5.21) is integrated over $\mathrm{d}\boldsymbol{k}$, the collision functional disappears. Integrating again over

[2]The Ward identity is a generalization of the *optical theorem*, which establishes a relation between the total scattering cross-section and the imaginary part of the scattering amplitude in the forward direction and essentially expresses the conservation of energy.

$\mathrm{d}E$ and making use of the normalization of the spectral function

$$\int \frac{\mathrm{d}E}{2\pi}\, A(\boldsymbol{k},\boldsymbol{q},E,\epsilon) = i\int \frac{\mathrm{d}E}{2\pi}\, \Delta G(\boldsymbol{k},\boldsymbol{q},E,\epsilon) = 1 \tag{5.23}$$

one recovers the continuity equation (5.4). The Ward identity (5.20) and the continuity equation (5.4) encode the conservation of the probability density.

Approximation of the Collision Functional

The quantum kinetic equation can be solved in the long-time and large-distance (or Kubo) limit, i. e. for $\epsilon \to 0$ and $\boldsymbol{q} \to 0$ along the lines given in [4–6][3]. In the Kubo limit the vertex function $U(\boldsymbol{k},\boldsymbol{k}'',\boldsymbol{q},E,\epsilon)$ and the spectral functions $i\Delta G(\boldsymbol{k}'',\boldsymbol{q},E,\epsilon)$ and $i\Delta G(\boldsymbol{k},\boldsymbol{q},E,\epsilon)$ inside the linear collision functional can approximated by the leading order of a Taylor expansion in $\boldsymbol{q}$ and in ϵ.

For the average retarded and advanced Green functions a Taylor expansion to zeroth order in ϵ and to first order in $\boldsymbol{q}$ but for a constant, i. e. $\boldsymbol{q}$- and ϵ-independent self-energy $\Sigma(\boldsymbol{k},\boldsymbol{q},E,\epsilon) \approx \Sigma(k,E)$ yields

$$\begin{aligned}\overline{G^{R,A}}(\boldsymbol{k},\boldsymbol{q},E) &\approx \overline{G^{R,A}}(k,E) + \boldsymbol{q}\cdot\nabla_{\boldsymbol{q}}\,\overline{G^{R,A}}(\boldsymbol{k},\boldsymbol{q},E)\Big|_{\boldsymbol{q}=0} \\ &= \overline{G^{R,A}}(k,E) \pm \frac{\hbar^2}{2m}\,[\overline{G^{R,A}}(k,E)]^2\,\boldsymbol{k}\cdot\boldsymbol{q}\end{aligned} \tag{5.24}$$

while the difference and the product of Green functions can be approximated by

$$\Delta G(\boldsymbol{k},\boldsymbol{q},E) \approx \Delta G(k,E) + \frac{\hbar^2}{2m}\Big[[\overline{G^R}(k,E)]^2 + [\overline{G^A}(k,E)]^2\Big]\,\boldsymbol{k}\cdot\boldsymbol{q} \tag{5.25a}$$

$$\overline{G^R}(\boldsymbol{k},\boldsymbol{q},E)\,\overline{G^A}(\boldsymbol{k},\boldsymbol{q},E) \approx \overline{G^R}(k,E)\,\overline{G^A}(k,E)\Big[1 + \frac{\hbar^2}{2m}\,\Delta G(k,E)\,\boldsymbol{k}\cdot\boldsymbol{q}\Big] \tag{5.25b}$$

5.2.1 Diffusion Approximation

The dependence of $\Phi(\boldsymbol{k},\boldsymbol{k}',\boldsymbol{q},E,\epsilon)$ on $\boldsymbol{k}$ (or on $\boldsymbol{k}'$ since $\Phi(\boldsymbol{k},\boldsymbol{k}',\boldsymbol{q},E,\epsilon)$ is totally symmetric in $\boldsymbol{k}$ and $\boldsymbol{k}'$) is dominated by the peaked structure of $\Delta G(\boldsymbol{k},\boldsymbol{q},E,\epsilon) = -iA(\boldsymbol{k},\boldsymbol{q},E,\epsilon)$ (cf. (4.28)) as a function of $\boldsymbol{k}$ for a fixed energy E around the absolute value $k = k_E$. We can therefore expand $\Phi(\boldsymbol{k},\boldsymbol{k}',\boldsymbol{q},E,\epsilon)$ as [4–6]

$$\Phi(\boldsymbol{k},\boldsymbol{k}',\boldsymbol{q},E,\epsilon) \approx \frac{A(k,E)}{2\pi N(E)}\Big[\Phi_0 + \Phi_1\,\boldsymbol{k}\cdot\boldsymbol{q}\Big] \tag{5.26}$$

The effect of disorder is expected to eventually level all angular dependences. The angular expansion of $\Phi(\boldsymbol{k},\boldsymbol{k}',\boldsymbol{q},E,\epsilon)$ on $\boldsymbol{k}$ is therefore truncated after the first two moments. This is

[3] In [28] we present a different way to solve the quantum kinetic equation, which involves the kernel functions defined in (5.11) and (5.13).

known as the *diffusion approximation*. Applying the definitions

$$\mathcal{K}(\boldsymbol{k}', \boldsymbol{q}, E, \epsilon) = \int \frac{\mathrm{d}\boldsymbol{k}}{(2\pi)^d}\, \Phi(\boldsymbol{k}, \boldsymbol{k}', \boldsymbol{q}, E, \epsilon) \tag{5.27a}$$

$$\mathcal{J}(\boldsymbol{k}', \boldsymbol{q}, E, \epsilon) = \frac{\hbar}{m} \int \frac{\mathrm{d}\boldsymbol{k}}{(2\pi)^d}\, \boldsymbol{k}\, \Phi(\boldsymbol{k}, \boldsymbol{k}', \boldsymbol{q}, E, \epsilon) \tag{5.27b}$$

we find $\Phi_0 = \mathcal{K}(\boldsymbol{k}', \boldsymbol{q}, E, \epsilon)$ and $\Phi_1 = md/(\hbar q^2 \langle k^2 \rangle_E)\, \boldsymbol{q} \cdot \boldsymbol{\mathcal{J}}(\boldsymbol{k}', \boldsymbol{q}, E, \epsilon)$ where $\langle \ldots \rangle_E$ denotes the average with respect to the normalized spectral function

$$\langle k^2 \rangle_E = \int \frac{\mathrm{d}\boldsymbol{k}}{(2\pi)^d}\, \frac{A(k, E)}{2\pi N(E)}\, k^2 \tag{5.28}$$

and d is the dimension of the system. The diffusion approximation now reads

$$\Phi(\boldsymbol{k}, \boldsymbol{k}', \boldsymbol{q}, E, \epsilon) \approx \frac{A(k, E)}{2\pi N(E)} \left[\mathcal{K}(\boldsymbol{k}', \boldsymbol{q}, E, \epsilon) + \frac{md}{\hbar \langle k^2 \rangle_E}\, (\boldsymbol{k} \cdot \hat{\boldsymbol{q}})\, \hat{\boldsymbol{q}} \cdot \boldsymbol{\mathcal{J}}(\boldsymbol{k}', \boldsymbol{q}, E, \epsilon) \right] \tag{5.29}$$

where $\hat{\boldsymbol{q}}$ is the unit vector pointing in the direction of $\boldsymbol{q}$.

Inserting the diffusion approximation (5.29) into (5.21), multiplying by the scalar product $\boldsymbol{q} \cdot \boldsymbol{k}$ and integrating over $\mathrm{d}\boldsymbol{k}$, leaves us with

$$\boldsymbol{q} \cdot \boldsymbol{\mathcal{J}}(\boldsymbol{k}', \boldsymbol{q}, E, \epsilon) \left[1 - i\tilde{\tau}\, \frac{\epsilon}{\hbar} \right] = -i\, \frac{\hbar^2 \langle k^2 \rangle_E\, \tilde{\tau}\, q^2}{m^2\, d}\, \mathcal{K}(\boldsymbol{k}', \boldsymbol{q}, E, \epsilon) + i\tilde{\tau}\, \frac{\boldsymbol{k}' \cdot \boldsymbol{q}}{m}\, \Delta G(\boldsymbol{k}', \boldsymbol{q}, E, \epsilon) \tag{5.30}$$

where we have defined the transport time $\tilde{\tau}(E)$ as

$$\frac{\hbar}{\tilde{\tau}(E)} = \iint \frac{\mathrm{d}\boldsymbol{k}}{(2\pi)^d}\, \frac{\mathrm{d}\boldsymbol{k}''}{(2\pi)^d}\, \frac{d\big[(\boldsymbol{k} \cdot \hat{\boldsymbol{q}})^2 - (\boldsymbol{k} \cdot \hat{\boldsymbol{q}})(\boldsymbol{k}'' \cdot \hat{\boldsymbol{q}})\big]}{\langle k^2 \rangle_E}\, \frac{A(k, E) A(k'', E)}{2\pi N(E)}\, U(\boldsymbol{k}, \boldsymbol{k}'', E) \tag{5.31}$$

Since the vertex function $U(\boldsymbol{k}, \boldsymbol{k}'', E)$ is only a function of $\hat{\boldsymbol{k}} \cdot \hat{\boldsymbol{k}}''$, the transport time must be independent of $\hat{\boldsymbol{q}}$. Relabelling $\boldsymbol{k}'' \to \boldsymbol{k}'$, one can also write (5.31) as

$$\frac{\hbar}{\tilde{\tau}(E)} = \frac{\hbar}{\tilde{\tau}_s(E)} - \iint \frac{\mathrm{d}\boldsymbol{k}}{(2\pi)^d}\, \frac{\mathrm{d}\boldsymbol{k}'}{(2\pi)^d}\, \frac{(\boldsymbol{k} \cdot \boldsymbol{k}')}{\langle k^2 \rangle_E}\, \frac{A(k, E) A(k', E)}{2\pi N(E)}\, U(\boldsymbol{k}, \boldsymbol{k}', E) \tag{5.32}$$

where the average scattering time $\tilde{\tau}_s(E)$ has been extracted according to the Ward identity

$$\frac{\hbar}{\tilde{\tau}_s(E)} = \frac{1}{2\pi N(E)} \iint \frac{\mathrm{d}\boldsymbol{k}}{(2\pi)^d}\, \frac{\mathrm{d}\boldsymbol{k}'}{(2\pi)^d}\, A(k, E) A(k', E)\, U(\boldsymbol{k}, \boldsymbol{k}', E) \tag{5.33}$$

This scattering time generally contains the full scattering vertex U. It is therefore applicable to all scattering processes. The same is true for the average transport time (5.31) and (5.32). In particular, any approximation on the average scattering time $\tilde{\tau}_s(E)$ requires via the Ward identity (5.33) a consistent approximation on the vertex function $U(\boldsymbol{k}, \boldsymbol{k}', E)$ and vice versa.

On the other hand, inserting the diffusion approximation (5.29) into (5.21) and integrating

over $\mathrm{d}\boldsymbol{k}$ yields

$$-i\epsilon\,\mathcal{K}(\boldsymbol{k}',\boldsymbol{q},E,\epsilon)+i\hbar\,\boldsymbol{q}\cdot\boldsymbol{\mathcal{J}}(\boldsymbol{k}',\boldsymbol{q},E,\epsilon)=i\Delta G(\boldsymbol{k}',\boldsymbol{q},E,\epsilon) \tag{5.34}$$

which resembles a continuity equation with an energy-dependent source term on the right-hand side. Integrating this equation over $\mathrm{d}E$ recovers the continuity equation (5.4) for the probability density (5.1) and the current density (5.3) as before. The continuity equation (5.34) and equation (5.30), which corresponds to Fick's law, provide a closed set of equations for the intensity kernel $\mathcal{K}(\boldsymbol{k}',\boldsymbol{q},E,\epsilon)$ and the current kernel $\boldsymbol{\mathcal{J}}(\boldsymbol{k}',\boldsymbol{q},E,\epsilon)$ which is solved by

$$\mathcal{K}(\boldsymbol{k}',\boldsymbol{q},E,\epsilon)=\frac{i\Delta G(\boldsymbol{k}',\boldsymbol{q},E,\epsilon)}{-i\epsilon[1-i\tilde{\tau}(E)\,\epsilon/\hbar]+\hbar\tilde{D}(E)q^2}\left(1-i\tilde{\tau}(E)\,\epsilon/\hbar-i\tilde{\tau}(E)\,\frac{\hbar\,\boldsymbol{k}'\cdot\boldsymbol{q}}{m}\right) \tag{5.35a}$$

$$\boldsymbol{q}\cdot\boldsymbol{\mathcal{J}}(\boldsymbol{k}',\boldsymbol{q},E,\epsilon)=\frac{i\Delta G(\boldsymbol{k}',\boldsymbol{q},E,\epsilon)}{-i\epsilon[1-i\tilde{\tau}(E)\,\epsilon/\hbar]+\hbar\tilde{D}(E)q^2}\left(-i\tilde{D}(E)q^2-i\tilde{\tau}(E)\,\frac{\epsilon\,\boldsymbol{k}'\cdot\boldsymbol{q}}{m}\right) \tag{5.35b}$$

where we have introduced the diffusion constant

$$\tilde{D}(E)=\frac{\hbar^2\langle k^2\rangle_E}{m^2 d}\,\tilde{\tau}(E) \tag{5.36}$$

Here, $\tilde{\tau}(E)$ is the average transport time (5.31). This solution of the quantum kinetic equation is valid for all kinds of disorder. In particular, it is valid independently of the Boltzmann approximation to transport because it still contains the general scattering vertex function $U(\boldsymbol{k},\boldsymbol{k}',E)$.

5.2.2 Solution in the Kubo Limit and for Weak Disorder

We now study the previous results in the Kubo limit and for weak disorder. In the Kubo limit $i\Delta G(\boldsymbol{k}',\boldsymbol{q},E,\epsilon)$ can be replaced by the spectral function $A(k',E)$. For weak disorder the spectral function simplifies further to $A(k',E)\approx A_0(k',E)=2\pi\delta(E-\hbar^2k'^2/2m)$ and the density of states can be developed to zeroth order in the small disorder parameter $\hbar/(2E\tau_s)$ (cf. (4.37)). $N(E)$ can therefore be replaced by the free-particle density of states $N_0(E)$. The average with respect to the normalized spectral function (5.28) then reduces to

$$\langle k^2\rangle_E\approx\int\frac{\mathrm{d}\boldsymbol{k}}{(2\pi)^d}\,\frac{A_0(k,E)}{2\pi N_0}\,k^2=k_E^2 \tag{5.37}$$

In this case, we can redefine the transport time as a function of the on-shell wavenumber k_E

$$\frac{\hbar}{\tau(k_E)}=\frac{1}{2\pi N(E)}\iint\frac{\mathrm{d}\boldsymbol{k}}{(2\pi)^d}\,\frac{\mathrm{d}\boldsymbol{k}'}{(2\pi)^d}\,(1-\hat{\boldsymbol{k}}\cdot\hat{\boldsymbol{k}}')\,A(k,E)A(k',E)\,U(\boldsymbol{k},\boldsymbol{k}',E) \tag{5.38}$$

Furthermore, in the Kubo limit, we have $\epsilon\tau/\hbar\ll 1$. Therefore, the second term on the right-hand side in (5.35a) and the second term on the right-hand side in (5.35b) as well as the term $i\epsilon\tau/\hbar$ in the denominator in (5.35a) and (5.35b) can be neglected. Under this

approximation, (5.29) can be written as

$$\Phi(\boldsymbol{k},\boldsymbol{k}',\boldsymbol{q},E,\epsilon) \approx \frac{A_0(k,E)}{2\pi N_0}\,\frac{A_0(k',E)}{2\pi N_0} \times \Big[\mathcal{K}_0(\boldsymbol{q},E,\epsilon) + \mathcal{K}_1(\boldsymbol{q},E,\epsilon)\,\boldsymbol{k}\cdot\boldsymbol{q} + \mathcal{K}_2(\boldsymbol{q},E,\epsilon)\,\boldsymbol{k}'\cdot\boldsymbol{q}\Big] \tag{5.39}$$

with $|\boldsymbol{k}| = |\boldsymbol{k}'| = k_E$, $D(k_E) = (\hbar^2 k_E^2/m^2 d)\,\tau(k_E)$ and

$$\mathcal{K}_0(\boldsymbol{q},E,\epsilon) = \frac{2\pi N_0}{-i\epsilon + \hbar D(k_E) q^2} \tag{5.40a}$$

$$\mathcal{K}_1(\boldsymbol{q},E,\epsilon) = \mathcal{K}_2(\boldsymbol{q},E,\epsilon) = -\frac{i\hbar\tau(k_E)}{m}\,\mathcal{K}_0(\boldsymbol{q},E,\epsilon) \tag{5.40b}$$

This expression is needed in section 5.4 in order to calculate the diffuson.

Diffusive Intensity Relaxation Kernel

Our final goal is to determine the probability density (5.9) or its Fourier transform (5.12a). Therefore, we need to calculate the function (5.11), which can be obtained as the integral over $\mathrm{d}E$ of the intensity kernel $\mathcal{K}(\boldsymbol{k}',\boldsymbol{q},E,\epsilon)$ derived in (5.35a). In the long-time limit, for $\epsilon\tau/\hbar \ll 1$, the second term on the right-hand side and in the denominator of (5.35a) can be neglected as before. Furthermore, in the large-distance limit, for $\hbar\tau(k)kq/m = \ell(k)q \ll 1$, it is possible to neglect also the third term on the right-hand side in (5.35a) (here $\ell(k)$ denotes the general transport mean free path $\ell(k) = \hbar k\tau(k)/m$), which results in

$$\mathcal{K}(\boldsymbol{k}',\boldsymbol{q},E,\epsilon) \approx \frac{A_0(k',E)}{-i\epsilon + \hbar D(k_E) q^2} \tag{5.41}$$

Integrating over $\mathrm{d}E$, one finally obtains the intensity kernel

$$\mathcal{F}(\boldsymbol{k}',\boldsymbol{q},\epsilon) = \int \frac{\mathrm{d}E}{2\pi}\,\mathcal{K}(\boldsymbol{k}',\boldsymbol{q},E,\epsilon) = \frac{1}{-i\epsilon + \hbar D(k') q^2} \tag{5.42}$$

with the diffusion constant $D(k) = (\hbar^2 k^2/m^2 d)\,\tau(k) = (\hbar k/md)\,\ell(k) = \ell^2(k)/(\tau(k)d)$ and the transport time $\tau(k)$ defined by (5.38). Equation (5.42) provides the required kernel function, which allows to calculate the average probability density (5.9) or (5.12a). The importance of this result lies in the diffusive pole of (5.42). The Fourier transform back to the time domain for $t \geq 0$

$$\mathcal{F}(\boldsymbol{k}',\boldsymbol{q},t) = \int \frac{\mathrm{d}\epsilon}{2\pi}\,\Phi(\boldsymbol{k}',\boldsymbol{q},\epsilon)\,e^{-i\epsilon t/\hbar} = \exp\big[-q^2 D(k')t\big] \tag{5.43}$$

and further into position space reveals that the intensity relaxation kernel

$$\mathcal{F}(\boldsymbol{k}',\boldsymbol{R},t) = \frac{1}{(4\pi D(k')t)^{d/2}}\,\exp\Big[-\frac{|R|^2}{4D(k')t}\Big] \tag{5.44}$$

obeys the diffusion equation: $\partial_t \mathcal{F}(\boldsymbol{k}', \boldsymbol{R}, t) - D(k')\,\Delta\,\mathcal{F}(\boldsymbol{k}', \boldsymbol{R}, t) = \delta(\boldsymbol{R})\delta(t)$, where $\boldsymbol{R} = \boldsymbol{r} - \boldsymbol{r}'$.

Essentially, we have found diffusive dynamics, as expected for particles in a conservative random potential. It is, however, not the average probability density $p(\boldsymbol{r}, t)$ itself that obeys a diffusion equation, but the intensity relaxation kernel $\mathcal{F}(\boldsymbol{k}', \boldsymbol{R}, t)$. The average probability density $p(\boldsymbol{r}, t)$ is finally obtained according to (5.9) by a further convolution of the kernel function with the initial Wigner function $W_0(\boldsymbol{k}', \boldsymbol{r}')$ and by integrating over all initial wavevectors $\boldsymbol{k}'$.

5.3 Diagrammatic Representation of the Scattering Vertex

The irreducible vertex operator U introduced in (5.15) describes the average scattering of the local probability density. Just like the self-energy, the scattering vertex U can be expanded in a power series

$$U = \sum_{n \geq 2} U_n \tag{5.45}$$

where U_n contains the speckle strength $\eta = \overline{U}/E_\zeta$ (cf. (4.52)) to the power n, and all irreducible contributions with n field correlations. The first terms of the power series $U = \sum_{n\geq 2} U_n$ for the irreducible intensity vertex can be represented by the following diagrams:

$U_2 =$ (5.46a)

$U_3 =$ 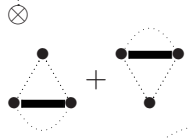 (5.46b)

$U_4 =$ 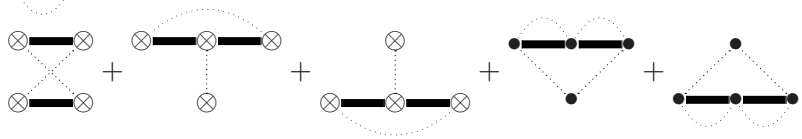 $+\ldots$ (5.46c)

As before, "irreducible" means that these diagrams do not fall apart into independent sub-diagrams, if a single propagator line is removed. In these diagrams the thick lines represent the averaged propagators $\overline{G^R}$ (upper entries) and $\overline{G^A}$ (lower entries). Dotted lines connecting two $\otimes$ (or $\bullet$) represent an intensity (or field) correlation function. In addition to the familiar potential correlations as in U_2 and in the displayed contributions to U_4, we find field-correlation diagrams as in U_3 and all higher orders. This stems from the fact that the potential fluctuations do not obey Gaussian statistics.

Through the Ward identity (5.20) every self-consistent diagram in the expansion of the self-energy corresponds to a set of diagrams in the expansion of U. For example, the diagram (5.46a) is linked to the self-consistent diagram . The next two diagrams (5.46b) are linked to the field-correlation , defining Σ_3, and the first three diagrams in (5.46c) correspond to .

5.4 Boltzmann Transport

Generally, the irreducible vertex function $U(\boldsymbol{k}, \boldsymbol{k}', E)$, which enters (5.38) cannot be calculated exactly, since correlations of arbitrarily high order are involved, and one has to resort to an approximation. In the Boltzmann approximation (also known as the independent scattering approximation) the infinite series is truncated after the lowest-order contribution, similar to the weak-scattering approximation for the self-energy series

$$U \approx U_B =$$ (5.47)

The irreducible vertex function is then given by

$$U_B(\boldsymbol{k}, \boldsymbol{k}', E) = \mathcal{P}_V(\boldsymbol{k} - \boldsymbol{k}') \tag{5.48}$$

The irreducible vertex in the Boltzmann approximation does not depend on the transfer vector $\boldsymbol{q}$. As it consists only of one single correlation function, it neither depends explicitly on the energy E nor on the energy transfer ϵ.

The Bethe-Salpeter equation (5.15) can be formally recast into the form

$$\Phi = [\overline{G^A} \otimes \overline{G^R}] + [\overline{G^A} \otimes \overline{G^R}]\, R\, [\overline{G^A} \otimes \overline{G^R}] \tag{5.49}$$

where the reducible vertex R is related to the irreducible vertex U according to

$$R = U + U\, [\overline{G^A} \otimes \overline{G^R}]\, R \tag{5.50}$$

In the Boltzmann approximation, the reducible vertex is obtained as

$$R \approx R_B =$$ $+ L$ (5.51)

Here, L denotes the so-called diffuson. The letter L refers to the ladder structure of the diagrams

$L =$ 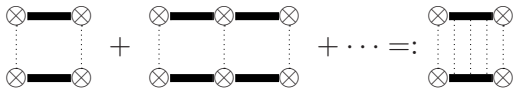 (5.52)

The diffuson describes multiple scattering as a sequence of average intensity propagation between scattering events, where both the retarded and the advanced amplitude travel along the same path. In other words, the Boltzmann approximation retains only the propagation of the intensity, a classical quantity, and discards all interference corrections. While in this picture there are no correlations between successive scattering events, the local speckle correlations are fully taken into account. Equation (5.52) provides a microscopic justification of the Boltzmann-Lorentz transport theory for non-interacting particles in the presence of quenched disorder, which has been successfully applied to a large number of physical systems,

ranging from the Drude transport theory of electrons in metals [33] to the radiative transfer equation in optics [99, 100].

5.4.1 The Diffuson

To find an analytical expression in the diffusive regime, the idea is to start from the geometric series for Φ_B in the Boltzmann approximation. Going to the wavevector representation, we can then compare the expansion for $\Phi_B(\boldsymbol{k}, \boldsymbol{k}', \boldsymbol{q}, E, \epsilon)$, which we have obtained in the diffusive and weak-scattering regime in section 5.2, with the corresponding expansion for the diffuson vertex $L(\boldsymbol{k}, \boldsymbol{k}', \boldsymbol{q}, E, \epsilon)$. The full series for Φ_B reads

$\Phi_B =$ 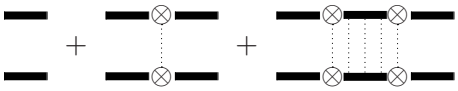 (5.53)

The first term in (5.53) describes ballistic propagation, whereas the second term describes single scattering in the effective medium. The third term finally contains the sum of all multiple scattering terms. The diagrammatic representation of the diffuson vertex is analogous to the representation of Φ (cf. (5.7))

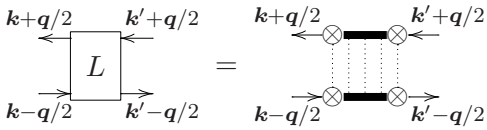

(5.54)

Its wavevector-space matrix element is defined as

$$L(\boldsymbol{k}, \boldsymbol{k}', \boldsymbol{q}, E, \epsilon) = \langle \boldsymbol{k}'_-, \boldsymbol{k}_+ | \, L(E_-, E_+) \, | \boldsymbol{k}_-, \boldsymbol{k}'_+ \rangle \tag{5.55}$$

In order to evaluate (5.53), we recall the diffusion approximation (5.39) for $\Phi(\boldsymbol{k}, \boldsymbol{k}', \boldsymbol{q}, E, \epsilon)$ in the Kubo limit for which we already know the result. In order to obtain $\Phi_B(\boldsymbol{k}, \boldsymbol{k}', \boldsymbol{q}, E, \epsilon)$ instead of $\Phi(\boldsymbol{k}, \boldsymbol{k}', \boldsymbol{q}, E, \epsilon)$ we have to replace the diffusion constant $D(k)$ by the Boltzmann diffusion constant $D_B(k)$. A similar expansion in moments of $\boldsymbol{k} \cdot \boldsymbol{q}$ and $\boldsymbol{k}' \cdot \boldsymbol{q}$ as in (5.39) can be performed for the diffuson vertex

$$L(\boldsymbol{k}, \boldsymbol{k}', \boldsymbol{q}, E, \epsilon) = L_0(\boldsymbol{q}, E, \epsilon) + L_1(\boldsymbol{q}, E, \epsilon) \, \boldsymbol{k} \cdot \boldsymbol{q} + L_2(\boldsymbol{q}, E, \epsilon) \, \boldsymbol{k}' \cdot \boldsymbol{q} \tag{5.56}$$

Inserting (5.39) and (5.56) into the wavevector representation of (5.53), expressing the propagator product in the Kubo limit as $\overline{G^A}(k, E) \, \overline{G^R}(k, E) = \tau_s / \hbar \, A(k, E)$ according to (5.17), and replacing the spectral function $A(k, E)$ by the on-shell projector $A(k, E) \approx$

$A_0(k,E)$, one obtains the equation

$$\begin{aligned} &A_0(k,E)A_0(k',E)\Big[\mathcal{K}_0(\boldsymbol{q},E,\epsilon)+\mathcal{K}_1(\boldsymbol{q},E,\epsilon)\,\boldsymbol{k}\cdot\boldsymbol{q}+\mathcal{K}_2(\boldsymbol{q},E,\epsilon)\,\boldsymbol{k}'\cdot\boldsymbol{q}\Big] \\ &\quad = A_0(k,E)(2\pi)^d\delta(\boldsymbol{k}-\boldsymbol{k}')\,\frac{(2\pi N_0)^2\tau_s}{\hbar}+A_0(k,E)A_0(k',E)\,\frac{(2\pi N_0\tau_s)^2}{\hbar^2}\mathcal{P}_V(\boldsymbol{k}-\boldsymbol{k}') \\ &+A_0(k,E)A_0(k',E)\,\frac{(2\pi N_0\tau_s)^2}{\hbar^2}\Big[L_0(\boldsymbol{q},E,\epsilon)+L_1(\boldsymbol{q},E,\epsilon)\,\boldsymbol{k}\cdot\boldsymbol{q}+L_2(\boldsymbol{q},E,\epsilon)\,\boldsymbol{k}'\cdot\boldsymbol{q}\Big] \end{aligned} \tag{5.57}$$

The coefficients $L_0(\boldsymbol{q},E,\epsilon)$, $L_1(\boldsymbol{q},E,\epsilon)$ and $L_2(\boldsymbol{q},E,\epsilon)$ can then be obtained by integrating (5.57) over $\mathrm{d}\boldsymbol{k}$ and $\mathrm{d}\boldsymbol{k}'$ in the case of $L_0(\boldsymbol{q},E,\epsilon)$ or by multiplying first by $\boldsymbol{k}\cdot\boldsymbol{q}$ or $\boldsymbol{k}'\cdot\boldsymbol{q}$ and then integrating over $\mathrm{d}\boldsymbol{k}$ and $\mathrm{d}\boldsymbol{k}'$ in the case of $L_1(\boldsymbol{q},E,\epsilon)$ and $L_2(\boldsymbol{q},E,\epsilon)$. The equation for $L_0(\boldsymbol{q},E,\epsilon)$ is given by

$$\mathcal{K}_0(\boldsymbol{q},E,\epsilon)=\frac{4\pi N_0\tau_s}{\hbar}+\frac{(2\pi N_0\tau_s)^2}{\hbar^2}L_0(\boldsymbol{q},E,\epsilon) \tag{5.58}$$

The first term $4\pi N_0\tau_s/\hbar$ on the right-hand side in (5.58) originates from the first and the second term on the right-hand side in (5.57), which both yield the same contribution. This can be shown using equation (4.62). In the Kubo limit, this contribution can be neglected compared to $\mathcal{K}_0(\boldsymbol{q},E,\epsilon)$. Altogether, replacing $\mathcal{K}_0(\boldsymbol{q},E,\epsilon)$ from (5.40a), and $\mathcal{K}_1(\boldsymbol{q},E,\epsilon)$ and $\mathcal{K}_2(\boldsymbol{q},E,\epsilon)$ from (5.40b) one finally obtains

$$L_0(\boldsymbol{q},E,\epsilon)=\frac{\hbar^2}{2\pi N_0\tau_s^2(k_E)}\,\frac{1}{-i\epsilon+\hbar D_B(k_E)q^2} \tag{5.59a}$$

$$L_1(\boldsymbol{q},E,\epsilon)=L_2(\boldsymbol{q},E,\epsilon)=-\frac{i\hbar\tau_s(k_E)}{m}\,L_0(\boldsymbol{q},E,\epsilon) \tag{5.59b}$$

The fact that the coefficients L_1 and L_2 are identical reflects the symmetric nature of the quantum kinetic equation. This result is needed for the calculation of the cooperon vertex in section 6.1, where weak-localization corrections to the Boltzmann approximation are taken into account.

5.5 Comparison to Isotropic Scattering

The main complication with regard to the solution of the diffuson series (5.52) arises from the fact that the scattering of matter waves in the speckle potential is not isotropic. In our case the correlations of the potential fluctuations prevent a simple solution without going to the Kubo limit. For isotropic scattering, however, the diffuson can be solved exactly. To this aim, the diffuson (5.52) can be formally rewritten as a geometric series

$L =$ 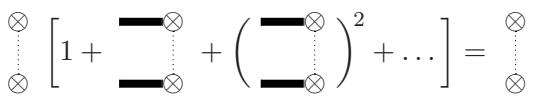 $= \dfrac{1}{1-\Upsilon}$ (5.60)

The wavevector matrix elements of the ladder insertion operator Υ are defined as

$$\Upsilon(\boldsymbol{k}, \boldsymbol{k}', \boldsymbol{q}, E, \epsilon) = \langle \boldsymbol{k}'_-, \boldsymbol{k}_+ | \, \Upsilon(E_-, E_+) \, | \boldsymbol{k}_-, \boldsymbol{k}'_+ \rangle \tag{5.61}$$

The main difference for isotropic scattering, as compared to the previous derivation of the diffuson for anisotropic scattering, is that the single-scattering vertex function does not depend on the angle between the wavevectors $\boldsymbol{k}$ and $\boldsymbol{k}'$. For this reason, the isotropic ladder insertion function and the diffuson also remain independent of the direction of $\boldsymbol{k}$ and $\boldsymbol{k}'$. The isotropic ladder insertion function can then be calculated as the integral

$$\Upsilon_{\text{iso}}(\boldsymbol{q}, E, \epsilon) = \frac{\hbar}{2\pi N_0 \tau_s} \int \frac{\mathrm{d}\boldsymbol{k}}{(2\pi)^d} \, \overline{G^R}(\boldsymbol{k} + \tfrac{\boldsymbol{q}}{2}, E + \tfrac{\epsilon}{2}) \, \overline{G^A}(\boldsymbol{k} - \tfrac{\boldsymbol{q}}{2}, E - \tfrac{\epsilon}{2}) \tag{5.62}$$

where the single-scattering vertex function only contributes the constant prefactor $U_B = \hbar/(2\pi N_0 \tau_s)$. In 3D (5.62) yields [4]

$$\Upsilon_{\text{iso}}(\boldsymbol{q}, E, \epsilon) = \frac{i}{2q\ell_s} \ln\left(\frac{i + \epsilon\tau_s/\hbar + q\ell_s}{i + \epsilon\tau_s/\hbar - q\ell_s}\right) \tag{5.63}$$

In the stationary case ($\epsilon = 0$), we find the well-known expression $\Upsilon_{\text{iso}} = \arctan(q\ell_s)/(q\ell_s)$. In 2D a similar calculation leads to

$$\Upsilon_{\text{iso}}(\boldsymbol{q}, E, \epsilon) = \frac{1}{\sqrt{(1 - i\epsilon\tau_s/\hbar)^2 + q^2\ell_s^2}} \tag{5.64}$$

In the Kubo limit, where $\epsilon\tau_s/\hbar \ll 1$ and $q\ell_s \ll 1$, (5.63) and (5.64) a Taylor expansion to leading order in $\epsilon\tau_s/\hbar$ and in $q\ell_s$ yields

$$\Upsilon_{\text{iso}}(\boldsymbol{q}, E, \epsilon) \approx 1 + \frac{i\epsilon\tau_s}{\hbar} - \frac{1}{d} q^2\ell_s^2 \tag{5.65}$$

with $d = 2$ in 2D and $d = 3$ in 3D. This approximation for the isotropic ladder insertion function is equivalent to the diffusion approximation. Inserting (5.65) and the single-scattering vertex $U_B = \hbar/(2\pi N_0 \tau_s)$ into (5.60) in the wavevector representation, finally recovers the diffuson

$$L_{\text{iso}}(\boldsymbol{q}, E, \epsilon) = \frac{\hbar^2}{2\pi N_0 \tau_s^2(k_E)} \frac{1}{-i\epsilon + \hbar D(k_E) q^2} \tag{5.66}$$

where the diffusion constant is defined as $D(k) = \ell_s^2(k)/(\tau_s(k)d) = (\hbar k/md)\ell_s(k)$, since for isotropic scattering $\ell_s = \ell_B$. Hence, in the isotropic case, the diffuson $L_{\text{iso}}(\boldsymbol{q}, E, \epsilon)$ in the Kubo limit is identical with the first moment $L_0(\boldsymbol{q}, E, \epsilon)$ (cf. (5.59a)) in the expansion (5.56) of the anisotropic diffuson vertex $L(\boldsymbol{k}, \boldsymbol{k}', \boldsymbol{q}, E, \epsilon)$.

5.6 Transport Mean Free Path

The respective approximations for the self-energy Σ and for the scattering vertex U are not independent from each other. If probability conservation is imposed as a fundamental constraint, both approximations (4.57) and (5.47) must verify the Ward identity (5.20). In the diffusive regime and under the Boltzmann approximation, the Ward identity reduces to (cf. (4.62))

$$\frac{\hbar}{\tau_s(k_E)} = \int \frac{\mathrm{d}\boldsymbol{k}}{(2\pi)^d}\, A_0(k,E)\, \mathcal{P}_V(\boldsymbol{k}-\boldsymbol{k}') = 2\pi N_0 \int \frac{\mathrm{d}\Omega_d}{\Omega_d}\, \mathcal{P}_V(k_E,\theta) \tag{5.67}$$

where $\mathcal{P}_V(k_E,\theta) = \mathcal{P}_V(k_E\hat{\boldsymbol{k}} - k_E\hat{\boldsymbol{k}}') = \mathcal{P}_V(2k_E \sin\frac{\theta}{2})$ is the angular potential correlation function, $\theta \in [0, 2\pi]$ being the angle between $\boldsymbol{k}$ and $\boldsymbol{k}'$ at the on-shell momenta $k_E = |\boldsymbol{k}| = |\boldsymbol{k}'|$. The Boltzmann transport time is then given by

$$\begin{aligned}\frac{\hbar}{\tau_B(k_E)} &= \frac{\hbar}{\tau_s(k_E)} - \frac{1}{2\pi N_0} \iint \frac{\mathrm{d}\boldsymbol{k}}{(2\pi)^d}\, \frac{\mathrm{d}\boldsymbol{k}'}{(2\pi)^d}\, A_0(k,E) A_0(k',E)\, \mathcal{P}_V(\boldsymbol{k}-\boldsymbol{k}')\, \hat{\boldsymbol{k}}\cdot\hat{\boldsymbol{k}}' \\ &= 2\pi N_0 \int \frac{\mathrm{d}\Omega_d}{\Omega_d}\, (1 - \hat{\boldsymbol{k}}\cdot\hat{\boldsymbol{k}}')\, \mathcal{P}_V(k_E,\theta)\end{aligned} \tag{5.68}$$

This transport time also defines the Boltzmann diffusion constant $D_B(k)$ and the Boltzmann transport mean free path $\ell_B(k)$ according to

$$D_B(k) = \frac{1}{d}\frac{\hbar^2 k^2}{m^2}\, \tau_B(k) = \frac{1}{d}\frac{\hbar k}{m}\, \ell_B(k) \tag{5.69}$$

The transport mean free path is the average distance required to completely erase the memory of the initial direction of propagation. It is related to the scattering mean free path (4.66) through

$$\frac{\ell_s}{\ell_B} = 1 - \langle\cos\theta\rangle_f = 1 - \int \mathrm{d}\Omega_d\, \cos\theta\, f_d(k,\theta) \tag{5.70}$$

where the cosine of the scattering angle is averaged over the phase function (4.68) in 2D or (4.72) in 3D. The term $\langle\cos\theta\rangle_f$ is known as the *anisotropy function* of the scattering process. For fully isotropic scattering it is zero, and $\ell_B = \ell_s$. For strongly anisotropic scattering, however, $\langle\cos\theta\rangle_f$ can take a value close to 1. In this case the transport mean free path is much larger than the scattering mean free path ($\ell_B \gg \ell_s$).

5.6.1 2D Speckle

In general, the 2D transport mean free path has to be calculated numerically. Only for $\kappa = k\zeta = 1$ (cf. (4.69)) and in the asymptotic cases $\kappa \ll 1$ and $\kappa \gg 1$ analytical expressions can be found. For $\kappa \ll 1$, making use of (5.70), the transport mean free path is given by

$$\ell_B = \frac{\pi^2 - 4}{\pi^2 - 8}\, \ell_s \qquad k\zeta = 1 \tag{5.71}$$

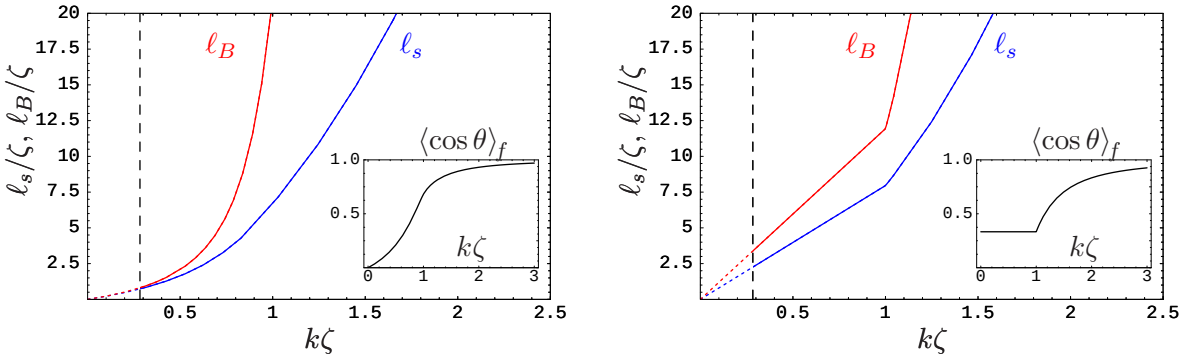

(a) 2D: ℓ_s and ℓ_B & anisotropy function

(b) 3D: ℓ_s and ℓ_B & anisotropy function

Figure 5.1:
Plot of ℓ_s and ℓ_B as a function of the reduced atomic wavenumber $k\zeta$ for $\eta = \overline{U}/E_\zeta = 0.2$ in 2D (a) and in 3D (b). The dashed lines indicate the weak-scattering limit. The insets show the respective anisotropy function $\langle\cos\theta\rangle_f$ as a function of the reduced atomic wavenumber $k\zeta$.

whereas the asymptotic expressions for ℓ_B are given by

$$\ell_B \approx \ell_s \qquad k\zeta \ll 1 \tag{5.72a}$$

$$\ell_B \approx \frac{15}{4}\,(k\zeta)^2\,\ell_s \qquad k\zeta \gg 1 \tag{5.72b}$$

A comparison between the 2D transport mean free path and the 2D scattering mean free path is shown in Fig. **5.1(a)** for $\eta = \overline{U}/E_\zeta = 0.2$. The inset shows a plot of the 2D anisotropy function $\langle\cos\theta\rangle_f$ as a function of $k\zeta$. For small wavenumbers $k\zeta \to 0$ one has $\langle\cos\theta\rangle_f \to 0$ and $\ell_B \to \ell_s$. In this limit the scattering is isotropic. When $k\zeta \gg 1$, the ratio ℓ_B/ℓ_s scales as $(k\zeta)^2$. This can be easily understood because the phase function limits the angular integration to $|\theta| \leq \theta_{\max} \sim 1/k\zeta$ such that $1 - \langle\cos\theta\rangle_f \approx \frac{1}{2}\,\langle\theta\rangle_f \propto \theta_{\max}^2$. Thus, roughly $(k\zeta)^2$ independent scattering events are needed to fully erase the memory of the initial direction. In other words, the correlated speckle potential can only weakly deviate atoms with large wavenumbers $k \gg \alpha k_{\mathrm{L}}$.

5.6.2 3D Speckle

In the 3D case (5.70) yields the exact result

$$\frac{1}{k\ell_B} = \frac{2\pi}{3}\,\eta^2\left[\frac{\Theta(k\zeta-1)}{(k\zeta)^5} + \frac{\Theta(1-k\zeta)}{(k\zeta)^2}\right] \tag{5.73}$$

In terms of the scattering mean free path (4.73) we have

$$\ell_B = \frac{3\ell_s}{2}\,\left[(k\zeta)^2\,\Theta(k\zeta-1) + \Theta(1-k\zeta)\right] \tag{5.74}$$

As one can see in Fig. **5.1(b)**, a slight anisotropy $\ell_B = \frac{3}{2}\ell_s$ remains for all $k\zeta \leq 1$, implying $\langle\cos\theta\rangle_f = \frac{1}{3}$. This feature has already been evidenced by the anisotropic phase function

plotted in Fig. **4.4**. The residual anisotropy in 3D is due to the divergence of $\mathcal{P}_V(\boldsymbol{\kappa})$ (cf. (2.35)) near $\kappa = 0$. At higher momenta, $k\zeta \geq 1$, the ratio ℓ_B/ℓ_s scales as $(k\zeta)^2$ for the same reason as in 2D.

5.7 Summary

In the present chapter we have set the foundations for the calculation of intensity (or probability) transport in the effective medium. A detailed discussion of the quantum kinetic equation has been presented making use of a slightly modified approach to the one used by Vollhardt and Wölfle. An approximation in the long-time, large-distance limit (Kubo limit) of the collision functional in (5.22) together with the diffusion approximation allows to derive a general expression for the average transport time (5.31) that is valid even beyond the Boltzmann approximation to transport. In the Kubo limit and for weak disorder the quantum kinetic equation can be solved for the intensity relaxation kernel, which is needed to calculate the average probability density (5.9).

Using the Boltzmann approximation for the scattering vertex we have determined the diffuson vertex, which describes the classical diffusive propagation of matter waves in the presence of a disordered potential. As a net result we have seen that a correlated disordered potential generally leads to anisotropic multiple scattering with a Boltzmann transport mean free path that is larger than the scattering mean free path. This relation is encoded in the anisotropy function for the 2D and the 3D speckle pattern. Nearly isotropic scattering is only encountered for very cold atoms with a de Broglie wavelength that is much larger than the correlation length of the speckle fluctuations. In this case, the matter wave cannot resolve the local correlation of the speckle pattern and the disordered potential appears to be δ-correlated white noise. For larger wavenumbers, however, one encounters strongly anisotropic scattering. Nevertheless, we have seen that in the long-time and large-distance limit one still encounters a diffusive process just like for isotropic scattering.

Among others, three results of the present chapter are of particular importance in the following. The general expression (5.9) for the average probability density, which has formed the point of origin of the present chapter is used in section 6.6 to calculate the variance of an expanding cloud of cold atoms as one of the most important experimental observables to determine the diffusion constant and possible localization effects in the disordered potential. In the following chapter, the general expression for the transport time (5.38) is evaluated beyond the Boltzmann approximation. And finally, in the same context, the diffuson vertex (5.52), which has presently been identified with Boltzmann transport, reappears under time reversal symmetry as the cooperon vertex describing quantum corrections to the classical diffusion process.

Chapter 6

Coherent Multiple Scattering

This chapter contains the theoretical description of the coherent interference effects that can occur when a matter wave is multiply scattered by a random potential. One of the basic questions we were interested in, was whether localization of matter waves could be observed experimentally, and, if this is the case, whether it could be described by the diagrammatic perturbation theory, within the range of validity that we have established in chapter 4. It turned out that the answer to both questions can indeed be affirmative under certain conditions, most importantly, if the initial momentum and the initial momentum dispersion of the atoms is sufficiently small.

The experimental observability of localization of course depends on a number of factors that are not treated in the present work. By setting up a simple model for non-interacting atoms in a scalar electric field, we have made several simplifications compared to the situation in a real experiment. We have also only regarded a bulk system and not particular geometries. However, some of these restrictions can be overcome. For example the atom-atom interaction can be tuned via Feshbach resonances [25, 26] making use of the magnetic field dependence of the scattering length. In the absence of other phase-breaking mechanisms apart from the interaction of the atoms with the vacuum fluctuation reservoir, the phase coherence length is only determined by the spontaneous emission rate, which can be controlled through the variation of the detuning and the intensity of the laser light, that creates the optical potential. This guarantees phase-coherent elastic multiple scattering as one of the main prerequisites for the observation of localization effects.

A crucial question that is addressed in the present chapter is the effect of the finite spatial distribution and the finite momentum distribution of the atoms. As in some of the recent experimental investigations of matter waves in disordered potentials (cf. for example [19, 51]), we consider the temporal evaluation of the position variance of an atomic cloud.

As in the previous chapters, the basis for the presented results is Vollhardt's and Wölfle's self-consistent diagrammatic perturbation theory [5, 6, 38]. To be able to adapt this theory to matter-wave transport, a few important modifications were necessary, mainly due to the fact that the disordered optical potential exhibits spatial correlations in contrast to the general picture of Gaussian white noise, which is used for the description of coherent multiple scattering of electrons. We derive in detail the weak-localization correction to the diffusion constant and comment on the self-consistent approach by Vollhardt and Wölfle, which al-

lows to obtain some insight about what happens when the strong-localization threshold is approached. Within the self-consistent theory it is possible to obtain an expression for the localization length and to derive the critical exponents for the localization length and the diffusion constant.

With regard to the anisotropic nature of matter-wave scattering in disordered optical potentials, the basic picture of two-wave interference within quantum loops has to be extended, including scattering effects of the same order in the weak-disorder parameter, which can be described by additional vertex functions known as Hikami boxes [101]. By reason of fundamental arguments based on Einstein's relation and the Ward identity these additional contributions cannot be discarded contrary to the case of isotropic scattering.

6.1 Weak-Localization Correction

Within the Boltzmann approximation to transport discussed in section 5.4, all quantum interference effects are discarded. At first sight this may seem reasonable because any such effects are expected to be suppressed by the ensemble average over all possible realizations of the random potential. This means that the effect of the disorder average is to single out products of amplitudes and conjugate amplitudes travelling along the same paths in the same direction, where no phase differences are present. As they are insensitive to dephasing processes these contributions describe classical propagation.

It was realized, however, that this argument is too simplistic [35] for well isolated systems, where phase-coherent interference between different scattering paths can occur. This can be understood by considering the return probability to a given point. In this case the scattering paths are closed loops. Two waves propagating in opposite directions around any such loop interfere constructively as they do not pick up any phase difference (unless a magnetic field for charged particles is applied, or dephasing processes are at work). This constructive two-wave interference enhances the return probability to twice the classically expected value. The enhancement of the return probability in turn decreases the diffusion constant for the onward propagation.

6.1.1 The Cooperon

In diagrammatic terms, the quantum corrections, which have to be introduced in (5.15), in addition to the Boltzmann scattering vertex defined in (5.47), are described by wavevector diagrams with counter-propagating amplitudes. The simplest replacement of the irreducible scattering vertex U in (5.15) that can account for the described interference effect is [75]

$$U \to U_B + C_A \tag{6.1}$$

Here, C_A is the sum of all maximally crossed diagrams

$C_A =$ 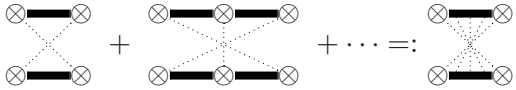 (6.2)

This series is also known as the cooperon.

The sum of all maximally crossed diagrams C_A can be calculated making use of time reversal symmetry. This allows to flip the cooperon diagram according to

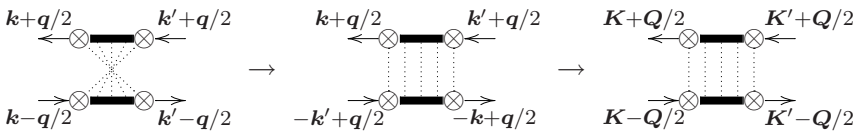

(6.3)

The entry vectors have been relabelled by a change of variables according to

$$\boldsymbol{K} = \frac{\boldsymbol{k}-\boldsymbol{k}'}{2} + \frac{\boldsymbol{q}}{2} \qquad \boldsymbol{K}' = \frac{\boldsymbol{k}'-\boldsymbol{k}}{2} + \frac{\boldsymbol{q}}{2} \qquad \boldsymbol{Q} = \boldsymbol{k}+\boldsymbol{k}' \tag{6.4}$$

Hence, under time reversal symmetry, we obtain

$$C_A(\boldsymbol{k},\boldsymbol{k}',\boldsymbol{q},E,\epsilon) = L(\boldsymbol{K},\boldsymbol{K}',\boldsymbol{Q},E,\epsilon) \tag{6.5}$$

It is therefore possible to express the cooperon in terms of the diffuson which we have already studied in section 5.4 (cf. (5.56)). Performing the replacement $U \to U_B + C_A$, the transport time (5.38) becomes

$$\frac{\tau_B}{\tau_A^*} = 1 + \frac{\tau_B}{2\pi N(E)\hbar} \iint \frac{\mathrm{d}\boldsymbol{k}}{(2\pi)^d}\,\frac{\mathrm{d}\boldsymbol{k}'}{(2\pi)^d}\; A(k,E)A(k',E)\,(1-\hat{\boldsymbol{k}}\cdot\hat{\boldsymbol{k}}')\,L(\boldsymbol{K}_0,-\boldsymbol{K}_0,\boldsymbol{Q},E,\epsilon) \tag{6.6}$$

In the Kubo limit, $\boldsymbol{q} \to 0$, we have $\boldsymbol{K}_0 = (\boldsymbol{k}-\boldsymbol{k}')/2$ and $\boldsymbol{K}_0' = -\boldsymbol{K}_0$. In this special case the second and the third term in the expansion (5.56) of $L(\boldsymbol{K}_0,-\boldsymbol{K}_0,\boldsymbol{Q},E,\epsilon)$ cancel out each other, since $L_1(\boldsymbol{Q},E,\epsilon) = L_2(\boldsymbol{Q},E,\epsilon)$. Therefore, we can directly replace $L(\boldsymbol{K}_0,-\boldsymbol{K}_0,\boldsymbol{Q},E,\epsilon)$ by $L_0(\boldsymbol{Q},E,\epsilon)$.

In (6.6) appears the factor $(1-\hat{\boldsymbol{k}}\cdot\hat{\boldsymbol{k}}')$ instead of $-\boldsymbol{k}\cdot\boldsymbol{k}'$, which is often found in the literature (cf. for example [4]). This factor $(1-\hat{\boldsymbol{k}}\cdot\hat{\boldsymbol{k}}')$ stems from the fact that, beyond the Boltzmann approximation for the scattering vertex U, the scattering time τ_s in (5.68) has to be corrected as well. According to the Ward identity (5.20) we have (cf. (5.33))

$$\frac{\tau_s}{\tau_s^A} = 1 + \frac{\tau_s}{2\pi N(E)\hbar} \iint \frac{\mathrm{d}\boldsymbol{k}}{(2\pi)^d}\,\frac{\mathrm{d}\boldsymbol{k}'}{(2\pi)^d}\; A(k,E)A(k',E)\,L_0(\boldsymbol{Q},E,\epsilon) \tag{6.7}$$

Due to the diffusive pole of $L_0(\boldsymbol{Q},E,\epsilon)$ (cf. (5.59a)) the dominant contribution to this integral arises from the neighbourhood of $\boldsymbol{Q}=0$, i. e. around $\boldsymbol{k}=-\boldsymbol{k}'$. Changing the integration variables from $\boldsymbol{k}$ and $\boldsymbol{k}'$ to $\boldsymbol{k}$ and $\boldsymbol{Q}=\boldsymbol{k}+\boldsymbol{k}'$, we can then set $\boldsymbol{Q}=0$ in the spectral functions.

Using $A(-k,E) = A(k,E)$, one obtains

$$\frac{\tau_s}{\tau_s^A} = 1 + \frac{\tau_s}{2\pi N(E)\hbar} \int \frac{\mathrm{d}\boldsymbol{k}}{(2\pi)^d}\, A^2(k,E) \int \frac{\mathrm{d}\boldsymbol{Q}}{(2\pi)^d}\, L_0(\boldsymbol{Q},E,\epsilon) \tag{6.8}$$

The replacement $U \to U_B + C_A$ that leads to (6.8) is not entirely consistent with the Ward identity. I will come back to this point in section 6.2, where I will discuss an alternative but consistent approximation on the scattering vertex.

The integral for the transport time (6.6) can be solved along the same lines, except that the factor $(1 - \hat{\boldsymbol{k}} \cdot \hat{\boldsymbol{k}}')$ for $\boldsymbol{k} = -\boldsymbol{k}'$ introduces an additional factor 2 to the correction term

$$\frac{\tau_B}{\tau_A^*} = 1 + \frac{\tau_B}{\pi N(E)\hbar} \int \frac{\mathrm{d}\boldsymbol{k}}{(2\pi)^d}\, A^2(k,E) \int \frac{\mathrm{d}\boldsymbol{Q}}{(2\pi)^d}\, L_0(\boldsymbol{Q},E,\epsilon) \tag{6.9}$$

One way to treat the integral over $\mathrm{d}\boldsymbol{k}$ in (6.8) and (6.9) is to replace the square of the spectral function by

$$\begin{aligned} A^2(k,E) = [i\,(\overline{G^R}(k,E) - \overline{G^A}(k,E))]^2 = 2\overline{G^R}(k,E)\overline{G^A}(k,E) \\ - ([\overline{G^R}(k,E)]^2 + [\overline{G^A}(k,E)]^2) \end{aligned} \tag{6.10}$$

where we have used the definition of the spectral function $A(k,E) = -2\mathrm{Im}[G^R(k,E)] = i\Delta G(k,E)$ (cf. (4.28)). Performing the integral over $\mathrm{d}\boldsymbol{k}$ of the square of the Green functions $-([\overline{G^R}(k,E)]^2 + [\overline{G^A}(k,E)]^2)$ yields a contribution of the order $\mathcal{O}(N_0/E)$, both in 2D and in 3D. For weak disorder, where $\hbar/(2\tau_s E) \ll 1$, this contribution can be neglected compared to the contribution of the product of the retarded and the advanced propagator $2\overline{G^R}(k,E)\overline{G^A}(k,E)$, which amounts to $4\pi N_0 \tau_s/\hbar$. Furthermore, we can make use of (5.17) to re-express the product $\overline{G^R}(k,E)\overline{G^A}(k,E)$ in terms of the spectral function

$$\overline{G^R}(k,E)\overline{G^A}(k,E) = -\frac{iA(k,E)}{\Delta\Sigma(k,E)} \approx \frac{\tau_s}{\hbar} A(k,E) \tag{6.11}$$

The last approximation holds for weak scattering, where the self-energy can be taken on-shell such that, using (4.63), $\Delta\Sigma(k,E)$ can be expressed by $\Delta\Sigma(k) = 2i\mathrm{Im}[\Sigma^R(k)] = -i\hbar/\tau_s$. Up to the factor $2\tau_s/\hbar$, the integral over $\mathrm{d}\boldsymbol{k}$ of $A^2(k,E)$ in (6.9) thus reduces to the integral over $\mathrm{d}\boldsymbol{k}$ of the spectral function alone, which yields the average density of states (cf. (4.31)) $\int \mathrm{d}\boldsymbol{k}/(2\pi)^d\; A(k,E) = 2\pi N(E)$. One finally obtains the following approximation for the transport time corrected by the cooperon contribution to the scattering vertex (6.9)

$$\frac{\tau_B}{\tau_A^*} = 1 + \frac{4\tau_B\tau_s}{\hbar^2} \int \frac{\mathrm{d}\boldsymbol{Q}}{(2\pi)^d}\, L_0(\boldsymbol{Q},E,\epsilon) = 1 + \left[\frac{2\tau_B}{\tau_s}\right] \frac{\Omega_d}{\pi N_0 \hbar} \int \frac{\mathrm{d}Q}{(2\pi)^d}\, \frac{Q^{d-1}}{-i\omega + D_B Q^2} \tag{6.12}$$

where we have replaced $L_0(\boldsymbol{Q},E,\epsilon)$ from (5.59a) and ϵ by $\hbar\omega$. The integral over $\mathrm{d}Q$ in (6.12) in 2D and in 3D diverges. However, this divergence only stems from the fact that we have set $\boldsymbol{Q} = 0$ in the spectral functions in (6.6). Before I am going to discuss the result (6.12)

further, I would like to present two different approaches to calculate the integral over the spectral functions in (6.6).

Generalization for Arbitrary Exponents

The integral over the spectral functions can be generalized for arbitrary exponents. For this purpose let us consider the general integral

$$\mathcal{I} = \int \frac{\mathrm{d}\boldsymbol{k}}{(2\pi)^d}\, [\overline{G^R}(k,E)]^m [\overline{G^A}(k,E)]^n\, g(k,\hat{\boldsymbol{k}}) \tag{6.13}$$

with some function $g(k,\hat{\boldsymbol{k}})$, which may depend on the direction $\hat{\boldsymbol{k}}$. We then have to solve

$$\mathcal{I} = \int_0^\infty \mathrm{d}\eta\, N_0(\eta)\, (E-\eta+i\hbar/2\tau_s)^{-m}(E-\eta-i\hbar/2\tau_s)^{-n} \int \frac{\mathrm{d}\Omega_d}{\Omega_d}\, g(k_\eta,\hat{\boldsymbol{k}}) \tag{6.14}$$

Since the Green functions are peaked around $\eta = E$, the density of states and the function $g(k_\eta,\hat{\boldsymbol{k}})$ can be evaluated at $N_0(\eta) = N_0(E)$ and $g(k_E,\hat{\boldsymbol{k}})$, respectively, if they are smoothly varying functions of η at this point. Furthermore, the lower integration range can be extended to $-\infty$. This procedure introduces an error of the order $\mathcal{O}(\hbar/2\tau_s E)$, which can be neglected for weak disorder. For consistency, the average density of states $N(E)$ in (6.9) has to be replaced by the free-particle density of sates $N_0(E)$ in this case. The integral can then be solved by the residue theorem

$$\mathcal{I} = \int \frac{\mathrm{d}\boldsymbol{k}}{(2\pi)^d}\, [\overline{G^R}(k,E)]^m [\overline{G^A}(k,E)]^n\, g(k,\hat{\boldsymbol{k}}) \approx f^{n,m}(\tau_s) \int \frac{\mathrm{d}\Omega_d}{\Omega_d}\, g(k_E,\hat{\boldsymbol{k}}) \tag{6.15}$$

where we have defined the function [7]

$$\begin{aligned} f^{n,m}(\tau_s) &= \frac{2\pi i N_0}{(m-1)!} \lim_{\eta\to(E+i\hbar/2\tau_s)} \left[\frac{d}{d\eta}\right]^{m-1} \left[\frac{(-1)^m(-1)^n}{(\eta-E+i\hbar/2\tau_s)^n}\right] \\ &= 2\pi N_0\, i^{n-m}\, \frac{(n+m-2)!}{(m-1)!(n-1)!} \left(\frac{\tau_s}{\hbar}\right)^{n+m-1} \end{aligned} \tag{6.16}$$

Using (6.11) together with (6.13) and (6.16) for $m = n = 2$ one finds

$$\int \frac{\mathrm{d}\boldsymbol{k}}{(2\pi)^d}\, A^2(k,E) = \frac{\hbar^2}{\tau_s^2} \int \frac{\mathrm{d}\boldsymbol{k}}{(2\pi)^d}\, [\overline{G^R}(k,E)]^2 [\overline{G^A}(k,E)]^2 = \frac{\hbar^2}{\tau_s^2}\, f^{2,2}(\tau_s) \tag{6.17}$$

with $f^{2,2}(\tau_s) = 4\pi N_0 \tau_s^3/\hbar^3$. Making use of (6.17) to calculate the integral over the spectral functions in (6.9) yields again the result (6.12).

Hikami Function

Alternatively, (6.6) can be solved without putting $\boldsymbol{Q} \to 0$ in the spectral functions. Keeping the approximation $\boldsymbol{k} = -\boldsymbol{k}'$ in (6.6), but leaving the spectral functions unchanged, the

transport time can then be specified more accurately as

$$\frac{\tau_B}{\tau_A^*} = 1 + \frac{4\pi N_0 \tau_B}{\hbar} \iint \mathrm{d}\boldsymbol{R}\,\mathrm{d}\boldsymbol{R}' \iint \frac{\mathrm{d}\boldsymbol{k}}{(2\pi)^d} \frac{\mathrm{d}\boldsymbol{Q}}{(2\pi)^d}\, e^{-i\boldsymbol{k}\cdot\boldsymbol{R}}\, e^{-i(\boldsymbol{Q}-\boldsymbol{k})\cdot\boldsymbol{R}'} \times g(R,E) g(R',E)\, L_0(\boldsymbol{Q},E,\epsilon) \quad (6.18)$$

Here, we have used the real-space representation of the spectral function (4.41): $A(R,E) = -2\mathrm{Im}[\overline{G^R}(R,E)] = 2\pi N_0 g(R,E)$, where $\boldsymbol{R} = \boldsymbol{r} - \boldsymbol{r}'$, and we have replaced the average density of states $N(E)$ in (6.6) by the free-particle density of states $N_0(E)$, which is possible for weak scattering. Performing the integration over $\mathrm{d}\boldsymbol{k}$ and $\mathrm{d}\boldsymbol{R}'$, (6.18) simplifies further to

$$\begin{aligned}\frac{\tau_B}{\tau_A^*} &= 1 + \frac{4\pi N_0 \tau_B}{\hbar} \int \mathrm{d}\boldsymbol{R} \int \frac{\mathrm{d}\boldsymbol{Q}}{(2\pi)^d}\, e^{-i\boldsymbol{Q}\cdot\boldsymbol{R}}\, g^2(R,E)\, \frac{\hbar^2/2\pi N_0 \tau_s^2}{-i\epsilon + \hbar D_B Q^2} \\ &= 1 + \left[\frac{2\tau_B}{\tau_s}\right] \int \frac{\mathrm{d}\boldsymbol{Q}}{(2\pi)^d}\, a_A(Q,E)\, \frac{\hbar/\tau_s}{-i\epsilon + \hbar D_B Q^2} \end{aligned} \quad (6.19)$$

Here, we have defined the Hikami function $a_A(Q,E)$ as the Fourier transform of the short-range correlation function $a_A(R,E) = g^2(R,E)$

$$a_A(Q,E) = \int \mathrm{d}\boldsymbol{R}\, e^{-i\boldsymbol{Q}\cdot\boldsymbol{R}}\, g^2(R,E) \quad (6.20)$$

The function $g(R,E)$ is given explicitly in 2D and in 3D in (4.42). The comparison of (6.19) with (6.12) shows that the previous approximations on the spectral functions correspond to the following approximation on the Hikami function

$$a_A(Q,E) \approx a_A(0,E) = \int \mathrm{d}\boldsymbol{R}\, g^2(R,E) = \frac{\tau_s}{\pi N_0 \hbar} \quad (6.21)$$

$a_A(0,E)$ is proportional to the volume $\lambda^{d-1}\ell_s$. This volume can be interpreted as the tube of length ℓ_s and surface λ^{d-1}, which describes the volume of the crossing region of the cooperon [7]. The Hikami function (6.20) can also be obtained directly from the Hikami vertex associated to this crossing region. For this reason, the Hikami vertex is discussed briefly in the following section.

6.1.2 Discussion of the Cooperon and the Hikami Function

The wavevector diagram (6.2) for the maximally crossed series corresponds to the sum over all possible real-space diagrams of the form described in Fig. **6.1(a)** (cf. Fig. **1.1(a)**). To see this equivalence, it is helpful to assume uncorrelated isotropic scatterers. Having at hand the general formalism of Green functions and the diagrammatic representation of the scattering vertex derived in sections 4.2.1 and 5.4, we can identify the solid line in Fig. **6.1(a)** as a series of averaged retarded Green functions and the dotted line as a series of averaged advanced Green functions.

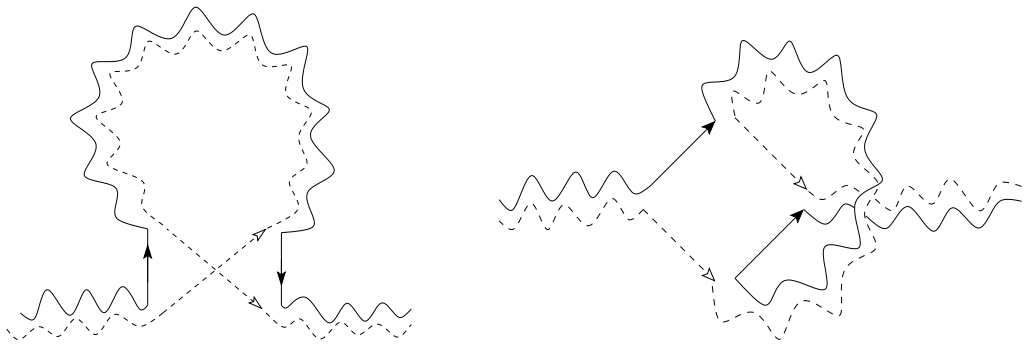

(a) cooperon diagram (b) 1st Hikami box H_A

Figure 6.1:
Cooperon vs. Hikami diagram in position space. The Hikami diagram (b) is topologically identical with the corresponding real-space diagram (a). The notion Hikami box refers to the actual vertex confined by the two highlighted retarded and advanced propagators.

At every wriggle in the diffusive path a scattering event takes place, which is described by the single-scattering vertex (5.46a). If the scattering events inside the loop are numbered in the same order in which they occur (the order is different for the conjugated amplitude, which travels around the loop in the opposite direction) and neighbouring scattering events are connected by an average retarded propagator for the upper elements in the wavevector diagram and by an average advanced propagator for the lower part, the wavevector diagram corresponding to the loop in Fig. **6.1(a)** is obtained, if all scattering events with the same number are connected by a correlation line. The full cooperon is then obtained by the sum over all possible loops.

The real-space diagram in Fig. **6.1(a)** consists of three long-range contributions and one short-range contribution. The short-range contribution arises from the crossing region. Before and after the crossing as well as during the loop we encounter a diffusive behaviour of the matter wave, which is essentially a long-range phenomenon. While the characteristic length scale of the short-range contribution is ℓ_s, the long-range contribution determines the length scale ℓ_B.

The crossing region can be regarded as a vertex of its own. This becomes obvious, if the diagram is written in a slightly different way, shown in Fig. **6.1(b)**. The only difference is that the crossing in Fig. **6.1(a)** has been disentangled. The crossing region now defines a box confined by two retarded and two advanced Green functions. The linear size of this so-called Hikami box is determined by the decay length ℓ_s of the Green functions.

The Hikami box is a real function of the four corner points $H(\{\boldsymbol{r}_i\}) = H(\boldsymbol{r}_1, \boldsymbol{r}_2, \boldsymbol{r}_3, \boldsymbol{r}_4)$ [7]. Integrating over two of its arguments, one obtains the function

$$H(\boldsymbol{r} - \boldsymbol{r}') = \iint \mathrm{d}\boldsymbol{r}_2\, \mathrm{d}\boldsymbol{r}_4\; H(\boldsymbol{r}, \boldsymbol{r}_2, \boldsymbol{r}', \boldsymbol{r}_4) \tag{6.22}$$

The first Hikami box shown in Fig. **6.1(b)** is given by

$$H_A(\boldsymbol{Q}) = \int \frac{\mathrm{d}\boldsymbol{k}}{(2\pi)^d}\, \overline{G^R}(\boldsymbol{k})\, \overline{G^A}(\boldsymbol{k})\, \overline{G^R}(\boldsymbol{k}-\boldsymbol{Q})\, \overline{G^A}(\boldsymbol{k}-\boldsymbol{Q}) = \frac{(2\pi N_0 \tau_s)^2}{\hbar^2}\, a_A(Q,E) \tag{6.23a}$$

$$H_A(\boldsymbol{R}) = \int \frac{\mathrm{d}\boldsymbol{Q}}{(2\pi)^d}\, e^{i\boldsymbol{Q}\cdot\boldsymbol{R}}\, H_A(\boldsymbol{Q}) = \frac{(2\pi N_0 \tau_s)^2}{\hbar^2}\, g^2(R,E) \tag{6.23b}$$

The Hikami function $a_A(Q,E)$ in three dimensions is given by

$$a_A(Q,E) = \frac{\pi}{k_E^2 Q}\Big[\arctan\big((2k_E - Q)\ell_s\big) + 2\arctan\big(Q\ell_s\big) - \arctan\big((2k_E + Q)\ell_s\big)\Big] \tag{6.24}$$

For weak disorder ($k_E \ell_s(k_E) \gg 1$) and for small Q ($Q \ll k_E$), only the term in the middle survives, such that

$$a_A(Q,E) \approx \frac{2\pi}{k_E^2 Q}\arctan\big(Q\ell_s\big) = \frac{\tau_s}{\pi N_0 \hbar}\,\frac{\arctan\big(Q\ell_s\big)}{Q\ell_s} \tag{6.25}$$

Here, we have used the 3D density of states $N_0(k_E) = mk_E/(2\pi^2\hbar^2)$. Furthermore, in the large-distance limit ($Q\ell_s \ll 1$), one recovers the approximation (6.21). In two dimensions, there seems to be no simple analytical expression for $a_A(Q,E)$. However, the same approximation for $Q\ell_s \ll 1$ holds in 2D and in 3D such that

$$a_A(Q,E) \approx \frac{\tau_s}{\pi N_0 \hbar}\Big(1 - \frac{Q^2\ell_s^2}{d}\Big) = a_A(0,E) + \mathcal{O}(Q^2) \tag{6.26}$$

for $d = 2, 3$. This result for the Hikami function can also be directly obtained from (6.23a) using a Taylor expansion for small $\boldsymbol{Q}$ similar to (5.24).

6.1.3 Comparison to the Kubo Theory

From the Kubo theory for electron scattering in disordered semiconductors we know that the classical conductivity σ_B is reduced by the coherent contribution [7]

$$\delta\sigma = \frac{se^2 D_B}{\pi\hbar}\int \frac{\mathrm{d}\boldsymbol{Q}}{(2\pi)^d}\,\mathrm{Re}\Big[\frac{1}{-i\omega + D_B Q^2}\Big] \tag{6.27}$$

where s is the spin degeneracy factor and e is the elementary charge of the electrons. The classical conductivity satisfies Einstein's relation. In terms of the transport time, Einstein's relation reads

$$\sigma_B = se^2 N_0 D_B = \frac{se^2 N_0}{d}\,\frac{\hbar^2 k^2}{m^2}\,\tau_B \tag{6.28}$$

In the stationary case, where $\omega = 0$, this relation exists not only between D_B and σ_B, but also between $\delta\sigma$ and δD and hence between $\sigma = \sigma_B - \delta\sigma$ and $D^* = D_B - \delta D$. The

weak-localization correction to the transport time should therefore be given by

$$\frac{\tau_B}{\tau^*} = \left[1 - \frac{1}{\pi N_0 \hbar} \int \frac{\mathrm{d}\boldsymbol{Q}}{(2\pi)^d} \frac{1}{D_B Q^2}\right]^{-1} \approx 1 + \frac{1}{\pi N_0 \hbar} \int \frac{\mathrm{d}\boldsymbol{Q}}{(2\pi)^d} \frac{1}{D_B Q^2} \tag{6.29}$$

for $\delta\tau \ll \tau_B$. The weak-localization correction to the conductivity (6.27) is derived using similar diagrammatic techniques to the ones used in chapter 5 and in the current chapter. Therefore, (6.29) should be equal to our result (6.12). However, a direct comparison reveals that (6.12) differs from (6.29) by the factor $[2\tau_B/\tau_s]$. The reason for this discrepancy is twofold:

The factor $[\tau_B/\tau_s]$ in (6.12) is a signature of anisotropic scattering. For isotropic scattering, as in the case of (6.27) and (6.29), this factor is equal to 1, since $\tau_B = \tau_s$.

The additional factor 2 in (6.12) originates from the required renormalization of the scattering time as a result of the Ward identity (cf. (6.8)). It does not appear, if τ_s is directly assumed to be constant, as it is sometimes done in the literature. In our previous description in section 6.1.1, where only the C_A diagram is incorporated in the scattering vertex U, this factor 2 does not disappear even for isotropic scattering. In order to obtain the correct result (6.29) we therefore have to perform a different approximation of the scattering vertex including other diagrams in addition to the C_A diagram.

This alleged discrepancy between the diagrammatic perturbation theory for τ^* and the diagrammatic perturbation theory for the conductivity σ^*, which becomes manifest via Einstein's relation, deserves a special investigation in the next section.

6.2 Anisotropic Hikami Contributions

The simple substitution $U \to U_B + C_A$ introduced in (6.1) is not compatible with probability density conservation in the strict sense that only a small fraction of all intensity diagrams required by the Ward identity (5.20) is included in the irreducible scattering vertex.

For electron transport in highly anisotropic systems P. Wölfle and R. N. Bhatt [102] have performed the calculation for the conductivity tensor. In this calculation two additional conductivity diagrams corresponding to dressed Hikami boxes [7] are taken into account. The calculation for the anisotropic conductivity tensor is similar to the calculation of the weak-localization correction to the diffusion constant that we wish to perform. We therefore need to include the same additional Hikami diagrams C_B and C_C adapted to our case. We will see in (6.37) and (6.40) that these diagrams yield a contribution of the same order as the cooperon C_A to the general general scattering time (cf. (5.33)) and the general transport time (cf. (5.38)). The complete vertex to be added to the Boltzmann term is

$$C = C_A + C_B + C_C \tag{6.30}$$

6.2.1 Correlated Hikami Diagrams

The wavevector diagrams corresponding to (6.30) are given by

$C =$ 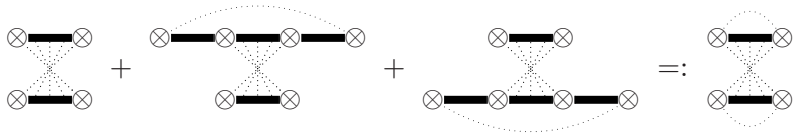 (6.31)

The matrix elements of the two additional diagrams in (6.31) are

$$\langle \boldsymbol{k}'_-, \boldsymbol{k}_+ | \, C_{B,C}(E_-, E_+) \, | \boldsymbol{k}_-, \boldsymbol{k}_+ \rangle = C_{B,C}(\boldsymbol{k}, \boldsymbol{k}', \boldsymbol{q}, E, \epsilon) \tag{6.32}$$

with the wavevector entries $\boldsymbol{k}_\pm = \boldsymbol{k} \pm \boldsymbol{q}/2$ and $\boldsymbol{k}_\pm = \boldsymbol{k} \pm \boldsymbol{q}/2$ and the energy entries $E_\pm = E \pm \epsilon$. The function $C_{B,C}(\boldsymbol{k}, \boldsymbol{k}', \boldsymbol{q}, E, \epsilon)$ is explicitly calculated as (cf. [102])

$$\begin{aligned} C_{B,C}(\boldsymbol{k}, \boldsymbol{k}', \boldsymbol{q}, E, \epsilon) = \int \frac{\mathrm{d}\boldsymbol{Q}}{(2\pi)^d} \, \mathcal{P}_V(\boldsymbol{k} + \boldsymbol{k}' - \boldsymbol{Q}) \, L_0(\boldsymbol{Q}, E, \epsilon) \\ \times G^{R,A}(\boldsymbol{k} \mp \tfrac{\boldsymbol{q}}{2} - \boldsymbol{Q}, E) G^{R,A}(\boldsymbol{k}' \mp \tfrac{\boldsymbol{q}}{2} - \boldsymbol{Q}, E) \end{aligned} \tag{6.33}$$

The total weak-localization correction (5.38) with the new replacement $U \to U_B + C$, the vertex $C = C_A + C_B + C_C$, and the matrix elements (6.5) and (6.33), respectively, takes the form

$$\begin{aligned} \frac{\tau_B}{\tau^*} = 1 + \frac{\hbar \tau_B}{2\pi N(E) \tau_s^2} \iint \frac{\mathrm{d}\boldsymbol{k}}{(2\pi)^d} \frac{\mathrm{d}\boldsymbol{k}'}{(2\pi)^d} \, \overline{G^R}(k, E) \overline{G^A}(k, E) \, \overline{G^R}(k', E) \overline{G^A}(k', E) \\ \times \Big[C_A(\boldsymbol{k}, \boldsymbol{k}', \boldsymbol{q}, E, \epsilon) + C_B(\boldsymbol{k}, \boldsymbol{k}', \boldsymbol{q}, E, \epsilon) + C_C(\boldsymbol{k}, \boldsymbol{k}', \boldsymbol{q}, E, \epsilon) \Big] \, (1 - \hat{\boldsymbol{k}} \cdot \hat{\boldsymbol{k}}') \end{aligned} \tag{6.34}$$

Here we have used the identity (6.11) in order to express the spectral functions $A(k, E)$ and $A(k', E)$ in (5.38) in terms of the averaged retarded and advanced Green functions. Counting only contributions with $\boldsymbol{Q} \to 0$ due to the divergence of the diffuson $L_0(\boldsymbol{Q}, E, \epsilon)$, which appears in all three matrix elements, and performing the replacement $\boldsymbol{k}' \to -\boldsymbol{k}'$ for the contribution C_B and C_C, which are both evaluated to zeroth order in $\boldsymbol{q}$, (6.34) simplifies to[1]

$$\begin{aligned} \frac{\tau_B}{\tau^*} = \frac{\tau_B}{\tau_A^*} + \frac{\hbar \tau_B}{2\pi N(E) \tau_s^2} \iint \frac{\mathrm{d}\boldsymbol{k}}{(2\pi)^d} \frac{\mathrm{d}\boldsymbol{k}'}{(2\pi)^d} \, \Big[[\overline{G^R}(k)]^2 \overline{G^A}(k) \, [\overline{G^R}(k')]^2 \overline{G^A}(k') \\ + \overline{G^R}(k) [\overline{G^A}(k)]^2 \, \overline{G^R}(k') [\overline{G^A}(k')]^2 \Big] \, (1 + \hat{\boldsymbol{k}} \cdot \hat{\boldsymbol{k}}') \, \mathcal{P}_V(\boldsymbol{k} - \boldsymbol{k}') \int \frac{\mathrm{d}\boldsymbol{Q}}{(2\pi)^d} \, L_0(\boldsymbol{Q}, E, \epsilon) \end{aligned} \tag{6.35}$$

Making use of our previous result (6.15), the total weak-localization correction can then be

[1] The energy dependence of the Green function has been left out for better visibility.

written in the form

$$\frac{\tau_B}{\tau^*} = 1 + \frac{\hbar\tau_B}{2\pi N_0 \tau_s^2}\left[2\,[f^{2,2}] + \int \frac{\mathrm{d}\Omega_d}{\Omega_d}\,(1+\hat{\boldsymbol{k}}\cdot\hat{\boldsymbol{k}}')\,\mathcal{P}_V(k_E,\theta)\left[[f^{2,1}]^2 + [f^{1,2}]^2\right]\right] \times \int \frac{\mathrm{d}\boldsymbol{Q}}{(2\pi)^d}\,L_0(\boldsymbol{Q},E,\epsilon) \quad (6.36)$$

For consistency with the result (6.15), the average density of states $N(E)$ in (6.35) has been replaced by the free-particle density of states $N_0(E)$ in (6.36). The function $f^{n,m}(\tau_s)$ is defined by (6.16).

Hikami Correction for the Scattering Mean Free Path

At this stage it is instructive to look at the scattering mean free path τ_s. Under the Ward identity (5.20) it is renormalized according to (cf. (5.33))

$$\frac{\tau_s}{\tau_s^*} = 1 + \frac{\hbar}{2\pi N_0 \tau_s}\left[[f^{2,2}] + \int \frac{\mathrm{d}\Omega_d}{\Omega_d}\,\mathcal{P}_V(k_E,\theta)\left[[f^{2,1}]^2 + [f^{1,2}]^2\right]\right]\int \frac{\mathrm{d}\boldsymbol{Q}}{(2\pi)^d}\,L_0(\boldsymbol{Q},E,\epsilon) \quad (6.37)$$

as compared to (6.7) without the additional Hikami contributions. The form of this equation is very similar to (6.36) except for the absence of the factor $(1+\hat{\boldsymbol{k}}\cdot\hat{\boldsymbol{k}}')$. A very interesting consequence of this fact becomes obvious when the functions $f^{n,m}(\tau_s)$ are replaced by their actual values according to the definition (6.16)

$$f^{2,2}(\tau_s) = \frac{4\pi N_0 \tau_s^3}{\hbar^3} \quad (6.38a)$$

$$f^{2,1}(\tau_s) = -f^{1,2} = \frac{2\pi i N_0 \tau_s^2}{\hbar^2} \quad (6.38b)$$

Hence, $[f^{2,1}]^2 + [f^{1,2}]^2 = -2\pi N_0 \tau_s/\hbar\,[f^{2,2}]$. Making use of (4.62), we have

$$[f^{2,1}]^2 + [f^{1,2}]^2 = -[f^{2,2}]\left[\int \frac{\mathrm{d}\Omega_d}{\Omega_d}\,\mathcal{P}_V(k_E,\theta)\right]^{-1} \quad (6.39)$$

Thus, for the scattering time τ_s^* the contribution of the Hikami diagrams C_B and C_C cancels out completely the contribution of the first cooperon diagram C_A in (6.37) This means that, to zeroth order in the small disorder parameter $\hbar/(2E\tau_s) = 1/(k\ell_s)$, the scattering time is not influenced by interference effects and can safely be replaced by the scattering time in the Boltzmann approximation $\tau_s^* = \tau_s$.

Hikami Correction for the Transport Mean Free Path

Equivalently, the renormalized transport time (6.36) can be written as

$$\frac{\tau_B}{\tau^*} = 1 + \frac{\tau_s^2}{\hbar^2}\left[\frac{2\tau_B}{\tau_s}\right](1 - \langle\cos\theta\rangle_f)\int \frac{\mathrm{d}\boldsymbol{Q}}{(2\pi)^d}\,L_0(\boldsymbol{Q},E,\epsilon) \quad (6.40)$$

where

$$(1-\langle\cos\theta\rangle_f) = 1 - \frac{\displaystyle\int \frac{\mathrm{d}\Omega_d}{\Omega_d}\, \mathcal{P}_V(k_E,\theta)(\hat{\boldsymbol{k}}\cdot\hat{\boldsymbol{k}}')}{\displaystyle\int \frac{\mathrm{d}\Omega_d}{\Omega_d}\, \mathcal{P}_V(k_E,\theta)} = \left[\frac{\ell_s}{\ell_B}\right] = \left[\frac{\tau_s}{\tau_B}\right] \tag{6.41}$$

The replacement $U \to U_B + C$, taking into consideration the additional Hikami diagrams C_B and C_C in (5.38), thus corresponds to the replacement

$$U \to U_B + \frac{1-\langle\cos\theta\rangle_f}{2}\, C_A \tag{6.42}$$

The additional factor $(1-\langle\cos\theta\rangle_f) = [\tau_s/\tau_B]$ cancels out the factor $[\tau_B/\tau_s]$, which appeared as a signature of anisotropic scattering in our first result (6.12) in section 6.1, where only the simple substitution $U \to U_B + C_A$ (6.1) was used. The additional factor $\frac{1}{2}$ cancels out the factor 2 which had to be introduced in (6.12) to account for the renormalization of the elastic scattering time, if only C_A is considered.

With the present approximation for the scattering vertex $U \to U_B + C_A + C_B + C_C$, i. e. when all Hikami diagrams are included, both Einstein's relation (6.28) and the Ward identity (5.20) are always fulfilled, for isotropic as well as for anisotropic scattering.

As in section 6.1.2, the diagrams C_A, C_B and C_C in (6.31) can be compared to the corresponding real-space diagrams and to the respective Hikami loops. C_A is represented by the real-space diagram in Fig. **6.1(a)** as before, whereas C_B and C_C are represented by the diagrams in Fig. **6.2(a)** and Fig. **6.2(c)** or by the dressed Hikami boxes in Fig. **6.2(b)** and Fig. **6.2(d)** respectively.

Discussion of the Weak-Localization Correction

As a net result the total weak-localization correction is given by

$$\frac{\tau^*}{\tau_B} = \frac{D^*}{D_B} = \frac{1}{1+\delta D/D_B} \tag{6.43}$$

where we have defined the weak-localization parameter

$$\frac{\delta\tau}{\tau_B} = \frac{\delta D}{D_B} = \frac{1}{\pi N_0}\int \frac{\mathrm{d}\boldsymbol{Q}}{(2\pi)^d}\, \frac{1}{-i\epsilon + \hbar D_B Q^2} \tag{6.44}$$

In general, this integral is divergent. This divergence results from the replacement $\boldsymbol{Q} = 0$ in the spectral functions in (6.33) that was performed to obtain (6.35). Because of this artificial divergence, meaningful results can only be obtained by introducing an ultra-violet cut-off to the $\boldsymbol{Q}$-integral in (6.44). In the stationary case where $\epsilon = 0$, the integral also displays an infra-red divergence, which can be circumvented by a suitable infra-red cut-off. The choice of the ultra-violet and the infra-red cut-off is not unique. The natural choice for the ultra-violet cut-off is $1/\ell_c = 1/\ell_s$, since ℓ_s describes the extension of the crossing region (cf. (6.21)) and

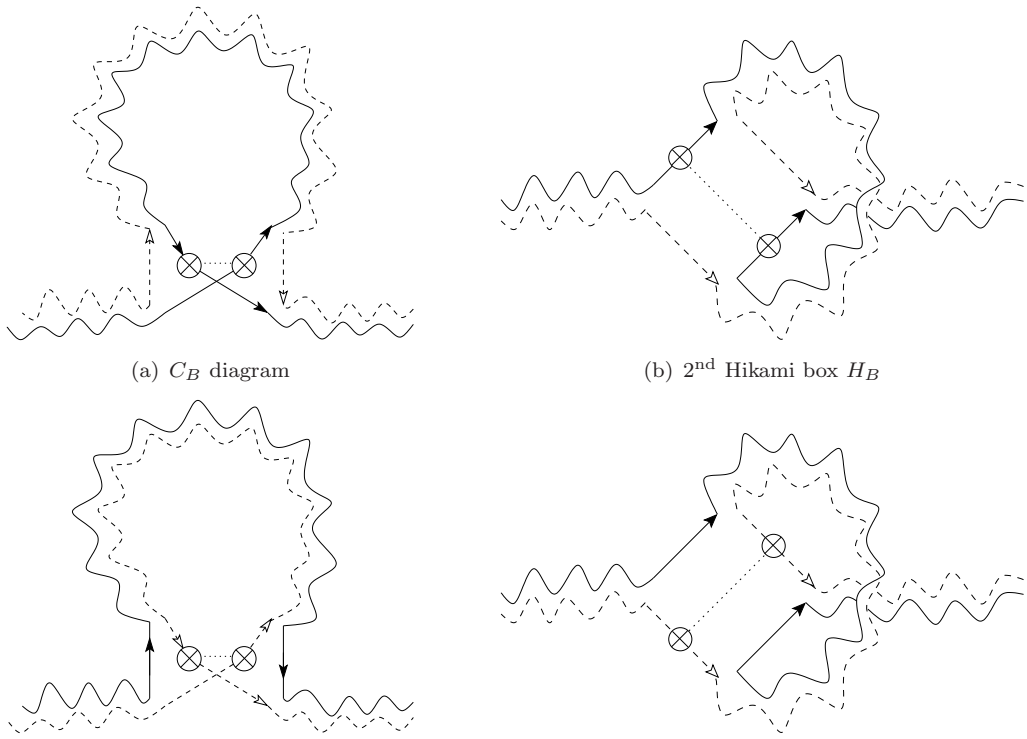

(a) C_B diagram

(b) 2nd Hikami box H_B

(c) C_C diagram

(d) 3rd Hikami box H_C

Figure 6.2:
Cooperon vs. Hikami diagrams. (a) cooperon diagram with an additional correlation line connecting the first and the last scattering event (highlighted by the symbol $\otimes$) of the matter wave in the quantum loop. It turns out that this diagram yields a contribution of the same order as C_A in Fig. **6.1(a)**. (b) Hikami loop that corresponds to the real-space diagram in (a). The Hikami box H_B is the Hikami box H_A from Fig. **6.1(b)** dressed by one correlation line connecting the retarded propagators. (c) cooperon diagram with an additional correlation line connecting the first and the last scattering event of the conjugated wave. (d) Hikami loop that corresponds to the real-space diagram in (c). The Hikami box H_C is the Hikami box H_A dressed by one correlation line connecting the advanced propagators.

as such defines the smallest possible length scale on which interferences effects can take place. This cut-off has been chosen in [27].

For anisotropic scattering, however, $\ell_c = \ell_B > \ell_s$ provides a more severe constraint. Since equation (6.43) has been obtained in the diffusion approximation, the Q-integral strictly is only meaningful for $Q \leq 1/\ell_B$. This feature does not persist for isotropic scattering where $\ell_s = \ell_B$.

The inverse infra-red cut-off is generally identified with the overall size of the system L, or, in the presence of strong phase-breaking mechanisms, with the phase coherence length L_ϕ, beyond which phase-breaking mechanisms are bound to destroy the coherence of the counter-propagating amplitudes. This distance is given by $L_\phi = \sqrt{D_B \tau_\phi}$, where τ_ϕ is the characteristic time between two such phase-breaking events. Choosing $\ell_c = \ell_B$ as UV cut-off

and $L_0 = \min[L, L_\phi]$ as IR cut-off, (6.44) for $\epsilon = 0$ becomes

$$\frac{\delta D}{D_B} = \frac{d}{\pi k^{d-1} \ell_B} \int_{1/L_0}^{1/\ell_c} \mathrm{d}Q \, \frac{Q^{d-1}}{Q^2} \tag{6.45}$$

which is solved by

$$\text{2D:} \qquad \frac{\delta D}{D_B} = \frac{2}{\pi k \ell_B} \ln \frac{L_0}{\ell_c} \tag{6.46a}$$

$$\text{3D:} \qquad \frac{\delta D}{D_B} = \frac{3}{\pi k^2 \ell_B \ell_c} \Big[1 - \frac{\ell_c}{L_0}\Big] \tag{6.46b}$$

Alternatively, the weak-localization parameter in the presence of phase-breaking mechanisms can be calculated as the integral

$$\frac{\delta D}{D_B} = \frac{d}{\pi k^{d-1} \ell_B} \int_0^{1/\ell_c} \mathrm{d}Q \, \frac{Q^{d-1}}{Q^2 + 1/L_0^2} \tag{6.47}$$

where the IR regularization of the divergent integral is performed through the additional term $1/L_0^2$ in the denominator. This leads to

$$\text{2D:} \qquad \frac{\delta D}{D_B} = \frac{1}{\pi k \ell_B} \ln\Big[1 + \frac{L_0^2}{\ell_c^2}\Big] \tag{6.48a}$$

$$\text{3D:} \qquad \frac{\delta D}{D_B} = \frac{3}{\pi k^2 \ell_B L_0} \Big[\frac{L_0}{\ell_c} - \arctan \frac{L_0}{\ell_c}\Big] \tag{6.48b}$$

As outlined above, ℓ_c can be identified with the Boltzmann transport mean free path. For $L_0 \gg \ell_c$ (6.48) merges with (6.46). In this limit, both regularization methods for the IR divergence are identical.

The weak-localization parameter (6.44) is always positive. In the weak-disorder regime, $k\ell_B \geq k\ell_s \gg 1$, $\delta D/D_B$ is small compared to one. The corrected transport time τ^* in (6.43) as obtained by the diagrammatic perturbation theory so far always remains finite (the lowest possible value for τ^*/τ_B is $\frac{1}{2}$) and therefore cannot describe the transition to the strong-localization regime. However, as we will see in the following, it is possible to reach the strong-localization threshold via a self-consistent treatment of the diffusion constant in the denominator of (6.43).

6.3 Self-Consistent Renormalization of the Scattering Vertex

The physical picture described by the replacement $U \to U_B + C$ becomes obvious when the reducible vertex R (cf. (5.50)) is examined, this time taking into account also the additional Hikami contributions

$R =$ 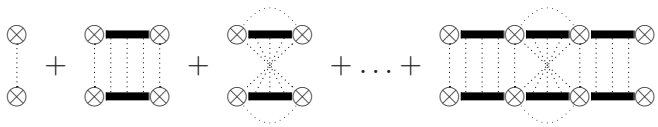 (6.49)

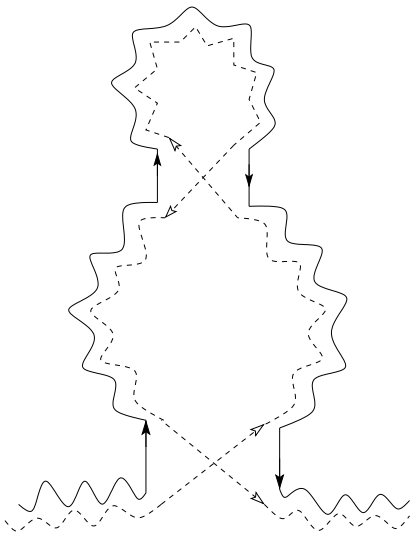

Figure 6.3: Nested loop diagram

As before, the first term describes single scattering, the second term describes classical diffusion, and all subsequent terms account for quantum corrections to the classical diffusion process. These terms actually correspond to a series of loops in the diffusive path of the particle in the effective medium. However, in expanding the reducible vertex in this way, an important contribution is left out.

Obviously, each diagram in the series (6.49) has its time reversal counterpart. Therefore, we also have to include all flipped diagrams corresponding to the intermediate quantum correction diagrams in (6.49)

$R =$ 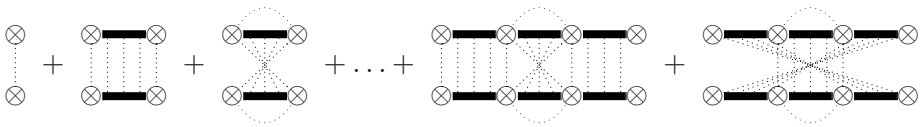 $+ \ldots$ (6.50)

The additional flipped diagrams in (6.50) correspond to nested loop diagrams in real space of the form depicted in Fig. **6.3**.

For isotropic scattering and without taking into account the Hikami contributions C_B and C_C, Vollhardt and Wölfle have shown [4, 6] that the full self-consistent picture is obtained, if the Boltzmann diffusion constant D_B in (6.44) is replaced by the fully weak-localization corrected diffusion constant D^*. In our case this corresponds to the following replacement for the irreducible scattering vertex in (5.38)

$$U(\boldsymbol{k}, \boldsymbol{k}', \boldsymbol{q}, E, \epsilon) \to U_B(\boldsymbol{k}, \boldsymbol{k}', E) + \frac{(1 - \langle \cos\theta \rangle_f)}{2} \frac{\hbar^2}{(2\pi N_0 \tau_s)^2} \mathcal{K}_0(\boldsymbol{Q}, E, \epsilon) \tag{6.51}$$

The factor $\frac{1}{2}(1 - \langle \cos\theta \rangle_f) = [\tau_s / 2\tau_B]$ is the same as in (6.42). It has to be included, in order to account for anisotropic scattering and the renormalization of the scattering time.

Along the same lines as before, one then obtains the self-consistent transport time as

$$\frac{\tau_B}{\tau^*(\omega)} = \frac{D_B}{D^*(\omega)} = 1 + \frac{\Omega_d}{\pi N_0 \hbar} \int \frac{\mathrm{d}Q}{(2\pi)^d} \frac{Q^{d-1}}{-i\omega + D^*(\omega)Q^2} \tag{6.52}$$

where the diffusion constant in the denominator of the integrant is now given by the full renormalized diffusion constant instead of its Boltzmann approximation. Apart form the replacement of D_B by D^*, (6.52) is identical with (6.44). Solving (6.52) for D^* yields

$$\frac{D^*}{D_B} = 1 - \frac{\delta D}{D_B} \tag{6.53}$$

where the weak-localization parameter for $\omega \to 0$ is now redefined as

$$\frac{\delta\tau}{\tau_B} = \frac{\delta D}{D_B} = \frac{1}{\pi N_0 \hbar D_B} \int \frac{\mathrm{d}\boldsymbol{Q}}{(2\pi)^d} \frac{1}{1/L_*^2 + Q^2} \tag{6.54}$$

with the diffusion constant $D_B(k) = \hbar k \ell_B(k)/md$, the free-particle density of states $N_0 = (m/\hbar^2)\,(\Omega_d/(2\pi)^d)\,k^{d-2}$ and $L_* = \lim_{\omega\to 0}\sqrt{iD^*(\omega)/\omega}$. The characteristic limit L_* for $\omega \to 0$ is a real quantity with the dimension of a length. It ensures the infra-red convergence of the integral over $\mathrm{d}\boldsymbol{Q}$ in (6.54). In general, the characteristic limit encapsulates three different lengths, each of which determines the weak-localization correction in a certain regime: the linear system size L, the phase coherence length L_ϕ and the localization length ξ_{loc}. All three effects can be included in the following discussion on a general ground, if we define the characteristic length L_* as

$$\frac{1}{L_*^2} = \frac{1}{L^2} + \frac{1}{L_\phi^2} + \frac{1}{\xi_{\mathrm{loc}}^2} \tag{6.55}$$

This length has been found to monitor correctly the behaviour of the diffusion constant in bulk media ($L \to \infty$) in the presence of phase-breaking mechanisms close to the strong-localization threshold [103]. Two asymptotic regimes may be distinguished: In the weak-localization regime all states sill extend to infinity such that $\xi_{\mathrm{loc}} \to \infty$. The characteristic IR regularization length is then determined by the interplay of the system size and the phase coherence length : $\frac{1}{L_*^2} = \frac{1}{L^2} + \frac{1}{L_\phi^2}$. The interference of the counterpropagating waves is essentially limited by the smaller of the two quantities. In the bulk this is the phase coherence length L_ϕ, whereas in a completely phase coherent sample the interference is only destroyed for quantum loops, which extend beyond the size of the system. Equivalently, in the weak-localization regime the IR cut-off could also be determined by the minimum $L_0 = \min[L, L_\phi]$. On the other hand, in the strong-localization regime, the localization length ξ_{loc}, which describes the average extension of the localized states, remains finite. For $\xi_{\mathrm{loc}} \ll L$ and $\xi_{\mathrm{loc}} \ll L_\phi$, the characteristic IR regularization length L_* is then given by the localization length alone: $L_* = \xi_{\mathrm{loc}}$.

Furthermore, we have to introduce an ultra-violet cut-off $1/\ell_c$ to the Q-integral to prevent its divergence in 2D and in 3D. The weak-localization parameter takes the same form as in

(6.48) where L_0 is replaced by L_*. Together with (6.53) this leads to the following weak-localization correction for the diffusion constant

$$\text{2D:} \qquad D^* = D_B\left[1 - \frac{1}{\pi k \ell_B} \ln\left[1 + \frac{L_*^2}{\ell_c^2}\right]\right] \tag{6.56a}$$

$$\text{3D:} \qquad D^* = D_B\left[1 - \frac{3}{\pi k^2 \ell_B L_*}\left[\frac{L_*}{\ell_c} - \arctan\frac{L_*}{\ell_c}\right]\right] \tag{6.56b}$$

The self-consistent theory thus provides an explanation for the occurrence of a phase transition between the weakly localized regime, where D^* remains finite, and the strongly localized regime, where D^* is zero. Definitely, the weak-localization interference effect contributes to the strong-localization phenomenon. However, different physical processes, which might be described by other than the cooperon diagram and the dressed Hikami boxes, could also yield a contribution for strong disorder. With the current theory this possibility cannot be ruled out completely. However, in the following, we assume that the dominant contribution to strong localization of matter waves stems from the same interference effect that is responsible for the weak-localization phenomenon.

6.4 Localization Length and Critical Exponents

The self-consistent theory allows to calculate the localization length in 2D and the critical exponents for the localization length and the diffusion constant at the mobility edge in 3D (cf. (1.9) in section 1.1). The idea is to solve the conditional equation $D^* = 0$ for the characteristic length L_*. The localization length can then be obtained making use of the definition (6.55).

Localization Length

2D: In 2D the strong-localization condition $D^* = 0$ in (6.56a) yields

$$\frac{L_*}{\ell_c} = (\exp[\pi k \ell_B] - 1)^{1/2} \approx \exp\left[\frac{\pi}{2} k \ell_B\right] \tag{6.57}$$

where the last approximation is valid for $k\ell_B \geq k\ell_s \gg 1$. Together with the definition of the characteristic length (6.55), (6.57) determines the 2D localization length.

3D: In 3D we obtain the transcendental equation

$$\frac{L_*}{\ell_c}\left[1 - \left(\frac{\gamma_0}{\gamma}\right)^2\right] = \arctan\frac{L_*}{\ell_c} \tag{6.58}$$

where we have defined the critical disorder parameter γ and the constant γ_0 according to

$$\gamma = \frac{1}{k\ell_c}\left(\frac{\ell_c}{\ell_B}\right)^{1/2} \qquad \gamma_0 = \left(\frac{\pi}{3}\right)^{1/2} \tag{6.59}$$

Three cases can be distinguished: (1) In the metallic regime, where $\gamma < \gamma_0$, i. e. when $k^2\ell_c\ell_B > 3/\pi$, (6.58) has no solution apart from $L_* = 0$. (2) Precisely at the threshold, γ is equal to the critical disorder parameter γ_0. This equality determines the Ioffe-Regel criterion. (3) In the localized regime $\gamma > \gamma_0$, but close to the threshold, L_* still tends to infinity. Therefore, we can solve (6.58) for L_* in the limit $\lim_{L_*\to\infty} \arctan(L_*/\ell_c) = \pi/2$. This can be seen by a graphical analysis of (6.58), if the function $f(z) = \arctan(z)$ is plotted together with the function $g(z) = az$, where $z = L_*/\ell_c$ and $a = [1 - (\gamma_0/\gamma)^2]$ is the slope of the linear function $g(z)$. For $\gamma < \gamma_0$ the slope is negative and the two curves cross only at the origin. For $\gamma > \gamma_0$ the two curves cross at infinity where $f(z) = \pi/2$.

Critical Exponent: The critical exponent that determines the behaviour of L_* close to the transition can be directly derived from the conditional equation (6.58) in the localized regime, where $\lim_{L_*\to\infty} \arctan(L_*/\ell_c) = \pi/2$, if (6.58) is rewritten as

$$\frac{L_*}{\ell_c} = \frac{\pi}{2}\, C\Big(\frac{\gamma}{\gamma_0}\Big)\, \Big[\Big(\frac{\gamma}{\gamma_0}\Big) - 1\Big]^{-1} \tag{6.60}$$

with $C(x) = x^2/(1+x)$. For $\gamma \to \gamma_0$, L_*/ℓ_c diverges like $|(\gamma/\gamma_0) - 1|^{-\nu}$ with the critical exponent $\nu = 1$. The prefactor $C(\gamma/\gamma_0)$ remains always finite and tends towards 1 for $\gamma \to \gamma_0$. Therefore, it does not contribute to the critical exponent ν. The critical exponent is independent of the cut-off ℓ_c. This result is expected since usually the critical exponents are universal in the sense that they do not depend on the detailed form and magnitude of the interactions or in our case on the strength of disorder. This universality of the critical exponent stands in contrast to the disorder parameter itself (6.59), which does depend on the choice of the cut-off.

Cut-off: The parameter γ simplifies considerably, if we identify the cut-off length ℓ_c with the Boltzmann transport mean free path. In this case γ is independent of the dimension of the system and has the simple form $\gamma = 1/(k\ell_B)$. For isotropic scattering, where $k\ell_B = k\ell_s$, γ becomes identical to the well-known disorder parameter $1/(k\ell_s)$. Replacing γ and γ_0 in (6.58) and ℓ_c by ℓ_B yields

$$\frac{L_*}{\ell_B} = \frac{3/2}{3/\pi - k^2\ell_B^2} \tag{6.61}$$

This expression determines L_* in the localized regime close to the Anderson threshold in terms of the Boltzmann transport mean free path. If ℓ_c is identified with the Boltzmann transport mean free path, the Ioffe-Regel criterion reads

$$k\ell_B = \sqrt{\frac{3}{\pi}} \tag{6.62}$$

Mobility Edge: Often the critical behaviour of L_* is stated as a function of the energy. For $k\zeta \geq 1$, and $\ell_c = \ell_B$, the Ioffe-Regel criterion $\gamma = \gamma_0$ leads to the expression $\Delta = \sqrt{3/\pi}\,(k\zeta)^3$

for the weak-scattering parameter Δ defined in (4.58). However, for $k\zeta \gg 1$ one finds $\Delta \gg 1$, which lies out of the range of validity of the diagrammatic perturbation theory. In 3D, for large wavenumbers $k\zeta \gg 1$, we therefore cannot describe the Anderson transition within the limit of the diagrammatic perturbation theory.

On the other hand, for small wavenumbers $k\zeta \leq 1$, making use of (4.61) and (5.73), the disorder parameter can be expressed in terms of the energy according to

$$\frac{\gamma}{\gamma_0} = \sqrt{\frac{\pi}{3}}\,\Delta = \sqrt{\frac{\pi}{3}}\,\frac{E_\Delta}{E} = \frac{E_m}{E} \tag{6.63}$$

where E_m denotes the mobility edge, i. e. the critical energy for the Anderson transition (cf. (1.9)). Here, E_Δ denotes the weak-scattering energy defined in (4.61) and Δ is the weak-scattering parameter defined in (4.58). Making use of (6.60) one thus finds the critical behaviour

$$L_* \propto (E_m - E)^{-1} \tag{6.64}$$

This general behaviour has already been highlighted in the introductory section 1.1 as one of the main predictions of the scaling theory. In (1.9a) the critical behaviour has been stated for the localization length ξ_{loc} instead of the characteristic length L_*. According to the definition (6.55), the case $L_* = \xi_{\text{loc}}$ corresponds to a bulk system ($L \to \infty$) in the absence of phase-breaking mechanisms ($L_\phi \to \infty$).

Diffusion Constant

In just the same way as for L_* we can also calculate the critical exponent of the diffusion constant itself. Close to the Anderson threshold where $L_* \to \infty$, the 3D diffusion constant (6.56b) in terms of the critical disorder parameter (6.59) reads

$$\frac{D^*}{D_B} = 1 - \left(\frac{\gamma}{\gamma_0}\right)^2 = H\left(\frac{\gamma}{\gamma_0}\right)\left[1 - \left(\frac{\gamma}{\gamma_0}\right)\right] \tag{6.65}$$

with $H(x) = 1 + x$. We thus find the critical behaviour

$$D^* \propto (\gamma_0 - \gamma)^s \propto (E - E_m)^s \tag{6.66}$$

with the critical exponent $s = 1$. E_m denotes the mobility edge (cf. (6.63)).

Again, this result corresponds to the critical exponent predicted by the scaling theory (cf. (1.9b)). This is particularly remarkable since the diagrammatic perturbation theory is in principle only valid for weak disorder and a priori cannot describe the strong-localization onset. The accurate description of the critical exponents within this theory, however, can be seen as a strong hint that the quantum interference corrections, which are responsible for weak localization, also remain the dominant contribution for strong localization.

6.5 Possible Experimental Observation of Localization

For the observation of weak localization it is necessary that a coherent diffusive process is established inside a large enough scattering region. The absence of quantum corrections can be due to two reasons: (1) The total size of the scattering medium may be too small ($L < \ell_B$), such that the propagation inside the medium can only be ballistic. (2) Or phase-breaking events may occur at a too rapid rate $\Gamma_\phi = 1/\tau_\phi$. In this case the phase coherence length $L_\phi = \sqrt{D_B \tau_\phi}$ comes into play, which measures the average distance over which the matter wave can travel before the coherence of counterpropagating waves inside a quantum loop is destroyed. If $L_\phi < \ell_B$, the propagation remains entirely classical.

For atoms experiencing the light shift (4.9) inside the speckle field, one possible phase-breaking mechanism is inelastic photon scattering, i. e. the spontaneous reemission of a photon into a different field mode, accompanied by a recoil momentum kick for the scattering atom. The average inelastic scattering rate associated to this process is given by $\Gamma_\phi \propto \overline{U}/\delta_\mathrm{L}$ (cf. (4.12)). Its inverse gives the phase coherence time $\tau_\phi = \hbar\delta_\mathrm{L}/(\overline{U}\Gamma_e)$. The phase coherence length is given by $L_\phi = \sqrt{D_B \tau_\phi}$ or in dimensions of the correlation length ζ

$$\frac{L_\phi}{\zeta} = \sqrt{\frac{k\ell_B}{d}\frac{\delta_L}{\Gamma_e}\frac{1}{\eta}} \tag{6.67}$$

The phase coherence effect can be controlled by changing the detuning δ_L at a fixed potential strength $\overline{U} \propto \overline{I}/\delta_\mathrm{L}$, i. e. keeping $\eta = \overline{U}/E_\zeta$ constant.

To ensure that interference corrections can be observed experimentally, one has to satisfy both the diffusive transport condition $L \gg \ell_B$ and the coherent transport condition $L_\phi \gg \ell_B$. Both L and L_ϕ appear in our final expression (6.56) for the weak-localization correction via the IR regularization length L_* defined in (6.55).

Table 6.1: Rubidium ^{87}Rb data ($5^2S_{1/2} \to 5^2P_{3/2}$) transition [104]

atomic mass	m	$1.44 \times 10^{-25}\,\mathrm{kg}$
atomic frequency	ω_A	$2.42 \times 10^{15}\,\mathrm{s}^{-1}$
speckle wavelength (vacuum)	λ_L	$780.24\,\mathrm{nm}$
speckle wavenumber (vacuum)	k_L	$8.05 \times 10^{6}\,\mathrm{m}^{-1}$
lifetime	τ_e	$26.24\,\mathrm{ns}$
linewidth	Γ_e	$3.81 \times 10^{7}\,\mathrm{s}^{-1}$
saturation intensity	I_s	$1.67\,\mathrm{mW/cm}^2$
recoil frequency	ω_R	$2\pi \cdot 3.77\,\mathrm{kHz}$
recoil temperature	T_R	$361.96\,\mathrm{nK}$

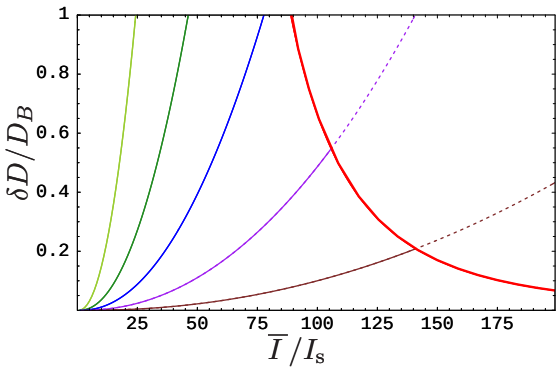

Figure 6.4:
2D: Weak-localization correction δD relative to the Boltzmann diffusion constant D_B as a function of the reduced intensity $\overline{I}/I_s$ (I_s is the saturation intensity of the atom). The curves correspond to different atomic wavenumbers $k\zeta \in \{0.8, 1.0, 1.2, 1.5, 2.0\}$ (from left to right). The speckle field size is $L = 2\,\mathrm{cm}$. The laser detuning is $\delta_L = 10^6\,\Gamma_e$. For each value of $k\zeta$, the weak-scattering condition $\Delta < 1$ is valid to the left of the thick red line (solid curves).

6.5.1 2D Speckle

Weak localization: The 2D weak-localization correction relative to the Boltzmann diffusion constant reads

$$\frac{\delta D}{D_B} = \frac{2}{\pi k \ell_B} \ln \frac{L_*}{\ell_B} \tag{6.68}$$

Here we have used (6.56a) with $\ell_c = \ell_B$ in the limit $L_* \gg \ell_B$. The characteristic length L_* in the weak-localization regime where $\xi_{\mathrm{loc}} \to \infty$ is given by $\frac{1}{L_*^2} = \frac{1}{L^2} + \frac{1}{L_\phi^2}$.

The interference correction to the diffusion constant diverges for $L_* \to \infty$, which indicates that a perfectly phase-coherent wave in an infinite disordered 2D system is in fact always localized, as predicted by the single-parameter scaling theory [32]. In the weak-localization regime, (6.68) predicts noticeable corrections especially for strongly disordered realizations, where $k\ell_B$ is close to one.

Three parameters are of particular interest, i. e. the average intensity of the speckle pattern $\overline{I}$, the detuning δ_L and the atomic momentum $\hbar k$. In order to estimate whether the weak-localization threshold can be reached with current experimental techniques, the perturbative results for weak localization can be used to calculate the order of magnitude for these parameters, as long as the fundamental condition $\Delta < 1$ remains fulfilled.

Fig. **6.4** shows the relative weak-localization correction $\delta D/D_B$ as a function of the speckle intensity $\overline{I}$ for different initial atomic velocities. The laser detuning for this plot is fixed at $\delta_L = 10^6\,\Gamma_e$ and the speckle size is $L = 2\,\mathrm{cm}$. At the weak-scattering limit $\Delta = 1$, for $k\zeta = 2.0$, the weak-localization correction δD reaches already 20% of the Boltzmann diffusion constant D_B itself. For a smaller wave number $k\zeta = 1.5$, the value of $\delta D/D_B$ rises to 55%. As a general rule, the colder the atoms, the larger are the interference corrections. Since $\zeta = 1/\alpha k_L \gg 1/k_L$, experimental evidence of weak localization in 2D requires initial temperatures for the atomic sample well below the recoil temperature. In turn, this means that a Bose-Einstein condensate could be a promising candidate for the initial atomic matter wave.

Towards strong localization: The strong-localization threshold is reached for $\delta D/D_B = 1$. At this point the interference corrections are so strong on large scales that the corrected

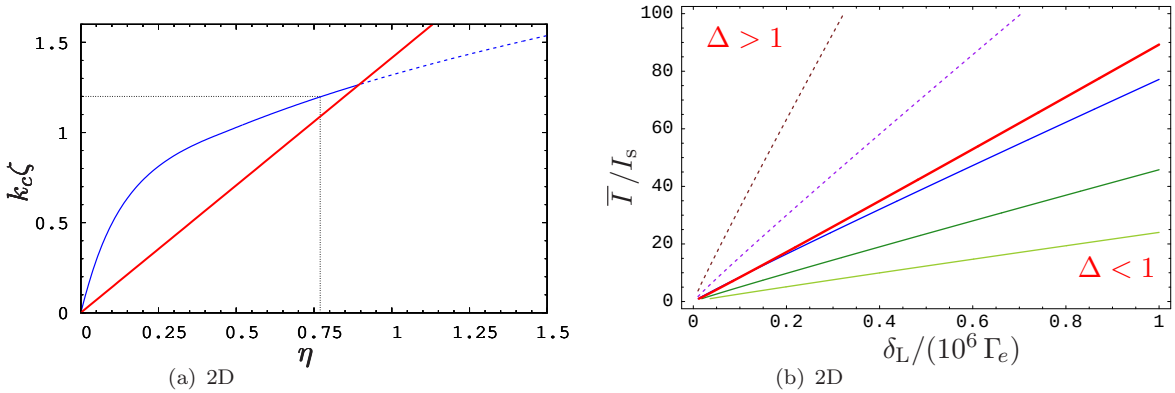

(a) 2D (b) 2D

Figure 6.5:
(a) 2D: Critical wavenumber k_c (in units of $k_\zeta = \alpha k_L$) at the strong-localization onset as a function of $\eta = \overline{U}/E_\zeta$, separating the weak-localization regime above from the strong-localization regime below the blue line. The speckle field size for this plot has been fixed at $L = 2\,\mathrm{cm}$ and the laser detuning is $\delta_\mathrm{L} = 10^6\,\Gamma_e$. The laser detuning enters via the phase breaking length L_ϕ defined in (6.67). The red line indicates the limit $\Delta = 1$. (b) 2D: Strong-localization onset in $(\delta_\mathrm{L}, \overline{I})$ phase space for different atomic wavenumbers $k\zeta \in \{0.8, 1.0, 1.2, 1.5, 2.0\}$ (from right to left). The onset is defined by $\delta D = D_B$. The speckle field size is $L = 2\,\mathrm{cm}$. The strong-localization regime lies above and to the left of each curve $k\zeta = \mathrm{const}$. The thick red line corresponds to the criterion $\Delta = 1$. All solid curves below can reach the strong-localization onset within the weak-scattering regime. The dotted curves only give extrapolated values for the strong-localization onset.

diffusion constant vanishes: $D^* = 0$. Diffusion is only possible as long as the corrected diffusion constant remains positive. This introduces a critical wavenumber k_c defined by the equation $\delta D(k_c) = D_B(k_c)$. Below this value, diffusion is completely suppressed, and all modes are localized. The critical wavenumber $\kappa_c = k_c\zeta = k_c/\alpha k_L$ is shown in Fig. **6.5(a)** as a function of $\eta = \overline{U}/E_\zeta$. The highlighted point in Fig. **6.5(a)** at the critical wavenumber $k_c = 1.2$ corresponds to the point in Fig. **6.4** where the blue curve crosses the upper boundary at $\delta D/D_B = 1$. In the following, we choose this point to calculate the order of magnitude of the transport parameters at the Anderson threshold for ^{87}Rb atoms (cf. Tab. 6.1).

From Fig. **6.4** we can directly obtain the average intensity of the speckle field $\overline{I} = 77\,I_\mathrm{s}$ at the strong-localization onset, whereas Fig. **6.5(a)** provides the value of η at this point. Going to smaller wavenumbers $k\zeta$ the Anderson threshold is reached for lower speckle intensities and for lower values of η at the same detuning δ_L. To monitor also the effect of the detuning we have plotted in Fig. **6.5(b)** the strong-localization onset in the $(\delta_\mathrm{L}, \overline{I})$ parameter plane for different atomic wavenumbers. The curves are very close to straight lines, which is due to the fact that the transport mean free path in the denominator of (6.68) for $\delta D/D_B$ scales as $\eta^2 \propto \overline{U}^2$. As a consequence, $\delta D/D_B$ scales as $(\overline{I}/\delta_\mathrm{L})^2$, and we expect a linear dependence in the $(\delta_\mathrm{L}, \overline{I})$ plane, where the slope is a function of the initial atomic velocity. Small corrections to this behaviour are due to the logarithmic dependence of $\delta D/D_B$ on L_*/ℓ_B. For each point on the curves in Fig. **6.5(b)**, one can obtain the corresponding values for the multiple scattering parameters. Starting from any such point one reaches the strong-localization regime when either the detuning δ_L is decreased or the intensity $\overline{I}$ is increased.

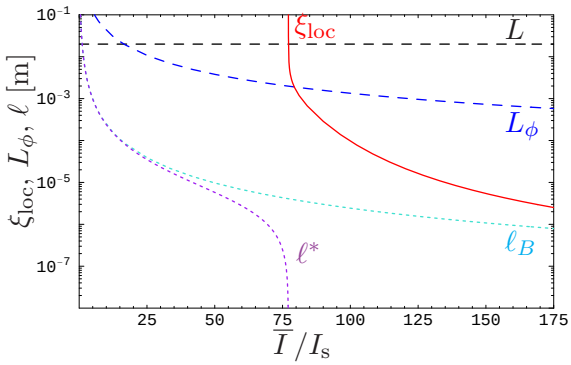

Figure 6.6:
2D: Logarithmic plot of the 2D localization length $\xi_{\rm loc}$ and of the phase coherence length L_ϕ as a function of the speckle intensity $\overline{I}$ in units of the saturation intensity $I_{\rm s}$. The atomic wavenumber is fixed at $k\zeta = 1.2$, the detuning at $\delta_{\rm L} = 10^6\,\Gamma_e$, and the system size at $L = 2\,$cm. $\xi_{\rm loc}$ diverges at the strong-localization threshold, which is reached for $\overline{I} = 77\,I_{\rm s}$, where the corrected transport mean free path $\ell^* = 2mD^*/\hbar k$ vanishes. The strong-localization regime is reached for $\overline{I} > 77\,I_{\rm s}$ where $\xi_{\rm loc} \ll L_\phi$.

When crossing the thick red curve where $\Delta = 1$, one enters the strong scattering regime where the diagrammatic perturbation cannot make safe predictions. The point ($\delta_{\rm L} = 10^6\,\Gamma_e$, $\overline{I} = 77\,I_{\rm s}$) lies on the blue curve for $k\zeta = 1.2$ on the right border of Fig. **6.5(b)**. For this point one obtains the following transport parameter values for ^{87}Rb atoms (cf. Tab. 6.1), for $L = 2\,$cm, and $\alpha = 0.1$:

ℓ_s	ℓ_B	L_*	$k\ell_s$	ζ	η	Δ	$E/\overline{U}$
$0.8\,\mu$m	$4.1\,\mu$m	$2.0\,$mm	0.81	1.2μm	0.77	0.83	0.93

Although the value for ℓ_s is very small, it still lies within the boundary $\ell_s \geq \frac{3\pi}{16}\zeta$ stated in section 4.7.1. The strong-localization threshold is found at $k\ell_s \approx 0.81$. The atoms have an energy of the same order of magnitude as the speckle fluctuations, $E \approx 0.9\,\overline{U}$. These numbers are meant to give an idea of the order of magnitude of the relevant transport parameters. They are obtained by applying the weak-scattering approximation quite close to its limit of validity (at the transition point $\Delta \approx 0.83$), and as such they can only be taken as qualitative results. However, they can give some idea of the parameter range where the transition point could be found. Although we cannot make safe predictions about the strong-localization onset in the regime above the thick red curve in Fig. **6.5(b)**, this does not mean that localization cannot occur in this regime.

Localization Length In the strong-localization regime, the previously extended atomic wavefunctions become exponentially localized as a function of the distance, and the corresponding localization length $\xi_{\rm loc}$ enters as a new length scale. In a bulk system $L \to \infty$ the characteristic length (6.55) then reads $\frac{1}{L_*^2} = \frac{1}{L_\phi^2} + \frac{1}{\xi_{\rm loc}^2}$ [103]. Together with equation (6.57), this determines the 2D localization length $\xi_{\rm loc}$.

Fig. **6.6** shows the characteristic length scales on both sides of the strong-localization threshold as a function of the speckle intensity $\overline{I}$ for $k\zeta = 1.2$, $L = 2\,$cm, $\alpha = 0.1$, and the detuning $\delta_{\rm L} = 10^6\,\Gamma_e$. With increasing speckle intensity, the phase coherence length L_ϕ (blue dashed curve) decreases since the probability of spontaneous photon scattering increases. The Boltzmann transport mean free path ℓ_B (turquoise dashed curve), a purely

local quantity, shows no particular singularity, while the corrected mean-free path ℓ^* (violet dashed line) drops to zero at the threshold value $\overline{I} = 77\, I_s$. The same applies to the corrected diffusion constant $D^* = \hbar k \ell^*/2m$. This threshold value corresponds precisely to the transition point ($\delta_L = 10^6\, \Gamma_e$, $\overline{I} = 77\, I_s$) on the phase boundary for $k\zeta = 1.2$ in Fig. **6.5(b)** and to the corresponding point where $\delta D/D_B = 1$ in Fig. **6.4**. The localization length itself diverges at the threshold and tends towards $\xi_{loc} = \ell_B \exp[(\pi/2)k\ell_B]$ for increasing intensities, where $L_\phi \gg \xi_{loc}$. In the strong-localization regime a further increase of the speckle intensity leads to localized wavefunctions which cover an increasingly narrow region in space.

6.5.2 3D Speckle

Weak localization: In 3D, the weak-localization correction relative to the Boltzmann diffusion constant for $\ell_c = \ell_B$ and $L_* \gg \ell_B$ is given by (cf. (6.56b))

$$\frac{\delta D}{D_B} = \frac{3}{\pi (k\ell_B)^2} \tag{6.69}$$

Contrary to the 2D case, the 3D correction remains finite for $L_* \to \infty$. Therefore, the transition to the strongly localized regime cannot be driven by L_* as in 2D. Instead, the onset of strong localization is determined by the Ioffe-Regel criterion [85]. In the context of isotropic scattering this criterion is given by $k\ell_s \lesssim 1$. In our case the Ioffe-Regel criterion is given by (6.62).

The relative weak-localization correction $\delta D/D_B$ for a given detuning $\delta_L = 10^4\, \Gamma_e$ is shown in Fig. **6.7**. As expected, the largest interference corrections are obtained when $k\zeta \leq 1$, which means that sub-recoil temperatures are needed to observe a strong effect. This indicates that a Bose-Einstein condensate might be required as a source in a possible experiment.

Towards strong localization Extrapolating the self-consistent 3D weak-localization correction (6.69) to the strong-disorder regime, we locate the onset $\delta D/D_B = 1$ at $k\ell_B = \sqrt{3/\pi} \approx 0.95$ (cf. (6.62)). In terms of the atomic energy, the corresponding 3D mobility edge for $k\zeta \leq 1$ lies at $E_c = \sqrt{\pi/3}\, E_\Delta$ (cf. (6.63)). As illustrated in Fig. **6.8(a)**, the condition $\delta D(k_c) = D_B(k_c)$ defines the critical wavenumber k_c, where diffusive transport is suppressed

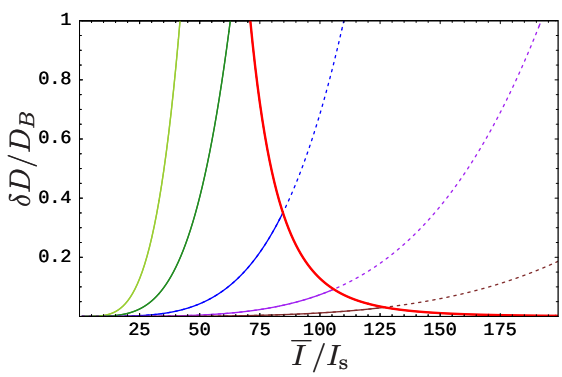

Figure 6.7:
3D: Weak-localization correction $\delta D/D_B$ (for $L_* \to \infty$) as a function of the reduced speckle intensity $\overline{I}/I_s$. The curves correspond to different atomic wavenumbers (from left to right: $k\zeta = 0.6, 0.9, 1.2, 1.5, 1.8$). The detuning is fixed at $\delta_L = 10^4\, \Gamma_e$. For each value of $k\zeta$, the weak-scattering condition $\Delta < 1$ is valid to the left of the thick red line (solid curves).

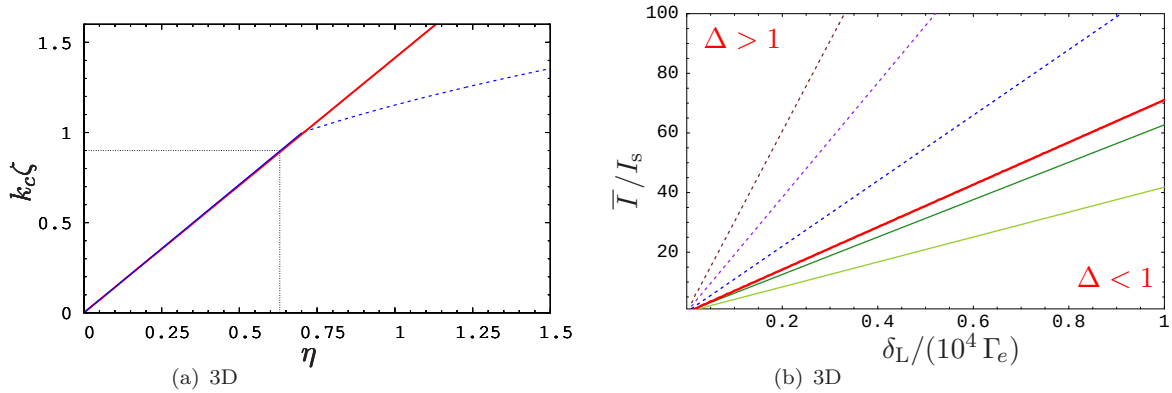

(a) 3D (b) 3D

Figure 6.8:

(a) 3D: Critical wavenumber k_c (in units of $k_\zeta = 1/\zeta = k_L$) at the strong-localization onset as a function of $\eta = \overline{U}/E_\zeta$ (blue line). The red line corresponds to the limit $\Delta = 1$. For $k_c\zeta < 1$ both curves are very close, which corresponds to the fact that the mobility edge $E_m = \sqrt{\pi/3}E_\Delta$ is almost identical to the weak scattering energy. For $k_c\zeta > 1$ the strong-localization threshold no longer lies within the boundary $\Delta = 1$. (b) 3D: Phase diagram of the strong-localization onset defined by $\delta D/D_B = 1$ for different atomic wavenumbers (right to left) $k\zeta \in \{0.6, 0.9, 1.2, 1.5, 1.8\}$. The speckle field size is $L = 2\,\mathrm{cm}$. For each value of $k\zeta$, the strong-localization regime lies on the left side of the corresponding curve. The red line corresponds to the criterion $\Delta = 1$. All solid curves below can reach the strong-localization onset within the weak-scattering regime. The dotted curves only give extrapolated values of (6.69).

by interference. In 3D, for $L_* \to \infty$, we obtain for the critical wavenumber $\kappa_c = k_c\zeta = k_c/\alpha k_L$

$$k_c\zeta = \left(\frac{4\pi}{3}\right)^{1/4} \eta\,\Theta(1-k\zeta) + \left(\frac{4\pi}{3}\right)^{1/10} \eta^{2/5}\,\Theta(k\zeta - 1) \tag{6.70}$$

For a sufficiently large characteristic length $L_* \gg \ell_B$, we have $\delta D/D_B \propto (\overline{I}/\delta_\mathrm{L})^4$. In the $(\delta_\mathrm{L}, \overline{I})$ parameter plane, the strong-localization threshold $\delta D/D_B = 1$ is thus characterized by the simple linear scaling $\overline{I} \propto \delta_\mathrm{L}$. This is illustrated in a phase diagram of the 3D strong-localization onset for different initial atomic velocities in Fig. **6.8(b)**.

For the highlighted point $k\zeta = 0.9$ and $\eta = 0.63$ in Fig. **6.8(a)**, at the realistic detuning $\delta_\mathrm{L} = 10^4\Gamma_e$, we locate the strong-localization threshold for Rubidium atoms (cf. Tab. 6.1) and $\alpha = 1$ at the speckle intensity value $\overline{I} = 63\,I_\mathrm{s}$. At this point one finds the following transport parameter values:

ℓ_s	ℓ_B	L_*	$k\ell_s$	ζ	η	Δ	$E/\overline{U}$
$0.09\,\mu$m	$0.13\,\mu$m	$9\,\mu$m	0.65	0.12μm	0.63	0.99	0.64

The calculated transport parameters are obtained close to the upper bound $\ell_s \geq \frac{2}{\pi}\zeta = 0.08\,\mu$m, given in section 4.7.2 and close to the limit of validity $\Delta = 1$ of the perturbative transport theory. Therefore, they can only give a qualitative prediction of the expected parameter values close to the transition point.

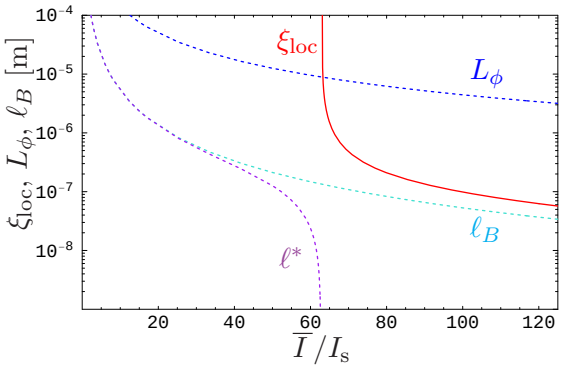

Figure 6.9:
3D: Logarithmic plot of the 3D localization length $\xi_{\rm loc}$ and of the phase coherence length L_ϕ as a function of the speckle intensity $\overline{I}$ in units of the saturation intensity $I_{\rm s}$. The atomic wavenumber is fixed at $k\zeta = 0.9$, and the detuning at $\delta_{\rm L} = 10^4\,\Gamma_e$. This corresponds to the dark green curve in Fig. **6.7** and Fig. **6.8(b)**. At the strong-localization threshold, which is reached for $\overline{I} = 63\,I_{\rm s}$, the corrected transport mean free path $\ell^* = 3m(D_B - \delta D)/\hbar k$ coming from the weak-localization regime drops to zero, whereas the localization length $\xi_{\rm loc}$ diverges.

Localization Length In the localized regime, close to the threshold, the characteristic length L_* is determined by (cf. (6.61)) $L_*/\ell_B = 3/2\,(3/\pi - k^2\ell_B^2)^{-1}$. Together with (6.55) this expression determines the 3D localization length $\xi_{\rm loc}$. A logarithmic plot of the 3D localization length as a function of the intensity $\overline{I}/I_{\rm s}$, for Rubidium atoms (cf. Tab. 6.1) at $k\zeta = 0.9$ and $\delta_{\rm L} = 10^4\,\Gamma_e$, as a function of the intensity $\overline{I}/I_{\rm s}$, is shown in Fig. **6.9** together with the phase coherence length L_ϕ and the classical as well as the corrected transport mean free path. The situation is similar to the 2D scenario. Precisely at the transition point, which is reached for $\overline{I} = 63\,I_{\rm s}$, the corrected transport mean-free path vanishes, $\ell^* = 0$, whereas the localization length $\xi_{\rm loc}$ diverges. For increasing intensities from this point onwards, one enters the strong-localization regime, where $\xi_{\rm loc} \ll \{L, L_\phi\}$. In the 3D case, the plot of $\xi_{\rm loc}$ is nearly indistinguishable from the characteristic length L_*, which also diverges at the threshold, whereas it only grows exponentially in 2D. This is a signature of the fact that the Anderson transition in 3D is indeed a true phase transition.

6.6 Influence of the Initial Wigner Distribution

Having at hand the general expressions for the average probability density distribution (5.9) together with the expression of the diffusion constant in the presence of weak localization (6.52), we can specify our results to particular initial phase-space distributions subjected to a disordered optical potential. This allows to define criteria for the unambiguous observation of localization effects in real experiments.

One possible experimental observable is the variance of the expanding cloud of cold atoms. The variance is defined as: $\Delta\boldsymbol{r}^2 = \langle(\boldsymbol{r} - \langle\boldsymbol{r}\rangle)^2\rangle = \langle\boldsymbol{r}^2\rangle - \langle\boldsymbol{r}\rangle^2$, where $\langle f(\boldsymbol{r})\rangle = \int \mathrm{d}\boldsymbol{r}\; f(\boldsymbol{r})\, p(\boldsymbol{r}, t)$ denotes the average with respect to the probability density distribution (5.9). Inserting the intensity relaxation kernel in the diffusive regime (5.44), we have

$$p(\boldsymbol{r}, t) = \int \frac{\mathrm{d}\boldsymbol{k}'}{(2\pi)^d} \int \mathrm{d}\boldsymbol{r}'\; (4\pi D(k')t)^{-d/2} \exp\Big[-\frac{|\boldsymbol{r} - \boldsymbol{r}'|^2}{4D(k')t}\Big]\, W_0(\boldsymbol{k}', \boldsymbol{r}') \tag{6.71}$$

The atoms are initially prepared in a state characterized by the Wigner function $W_0(\boldsymbol{k}, \boldsymbol{r})$.

From this Wigner distribution one can extract the marginals $p_0(\boldsymbol{r})$ (initial spatial distribution) and $\pi_0(\boldsymbol{k})$ (initial wavevector distribution) according to

$$p_0(\boldsymbol{r}) = \int \frac{\mathrm{d}\boldsymbol{k}}{(2\pi)^d}\, W_0(\boldsymbol{k},\boldsymbol{r}) \qquad \pi_0(\boldsymbol{k}) = \int \mathrm{d}\boldsymbol{r}\, W_0(\boldsymbol{k},\boldsymbol{r}) \tag{6.72}$$

The normalization of these marginals is set by $\int \mathrm{d}\boldsymbol{k}/(2\pi)^d\, \pi_0(\boldsymbol{k}) = \int \mathrm{d}\boldsymbol{r}\, p_0(\boldsymbol{r}) = 1$.

The variance is given by

$$\Delta\boldsymbol{r}^2(t) = \Delta\boldsymbol{r}_0^2 + 2d\mathcal{D}t \tag{6.73}$$

It depends linearly on time with a modified diffusion coefficient $\mathcal{D}$ given by the convolution of the diffusion constant and the marginal $\pi_0(\boldsymbol{k})$ of the initial Wigner function

$$\mathcal{D} = \int \frac{\mathrm{d}\boldsymbol{k}}{(2\pi)^d}\, D(k)\, \pi_0(\boldsymbol{k}) \tag{6.74}$$

The constant term $\Delta\boldsymbol{r}_0^2$ describes the initial variance $\Delta\boldsymbol{r}_0^2 = \langle \boldsymbol{r}^2\rangle_0 - \langle \boldsymbol{r}\rangle_0^2$, where $\langle f(\boldsymbol{r})\rangle_0$ denotes the average with respect to the initial distribution $p_0(\boldsymbol{r})$ in position space.

If the weak-localization correction to the diffusion constant is taken into account, special attention has to be given to the integration range of the integral over $\mathrm{d}\boldsymbol{k}'$. To account for the fact that the diffusion constant is zero for $k < k_c$ in the strong-localization regime it has to be replaced by

$$D(k) = D^*(k)\, \Theta(k - k_c) = (D_B - \delta D)\, \Theta(k - k_c) \tag{6.75}$$

in (6.71) and (6.74) with $\delta D(k)/D_B(k)$ from (6.68) in 2D and (6.69) in 3D. On the other hand, for classical diffusion, $D(k)$ is merely given by the Boltzmann diffusion constant $D_B(k) = \hbar k \ell_B(k)/(md)$.

Inserting (6.75) into (6.71) splits the wavevector integral into two parts describing the localized and the diffusive fraction of the average probability density: $p(\boldsymbol{r},t) = p_{\mathrm{loc}}(\boldsymbol{r}) + p_{\mathrm{diff}}(\boldsymbol{r},t)$, where

$$p_{\mathrm{loc}} = \int \frac{\mathrm{d}\boldsymbol{k}'}{(2\pi)^d}\, \pi_0(\boldsymbol{k}')\, \Theta(k_c - k') \tag{6.76a}$$

$$p_{\mathrm{diff}}(\boldsymbol{r},t) = \int \frac{\mathrm{d}\boldsymbol{k}'}{(2\pi)^d} \int \mathrm{d}\boldsymbol{r}'\, (4\pi D^*(k')t)^{-d/2} \exp\Big[-\frac{|\boldsymbol{r}-\boldsymbol{r}'|^2}{4D^*(k')t}\Big]\, W_0(\boldsymbol{k}',\boldsymbol{r}')\, \Theta(k' - k_c) \tag{6.76b}$$

Separable Initial Wigner Function

In the following, we consider a separable initial Wigner function given by a product of two independent functions in $\boldsymbol{r}$ and $\boldsymbol{k}$, i.e. without any position momentum correlations: $W(\boldsymbol{k},\boldsymbol{r}) = \pi_0(\boldsymbol{k})\, p_0(\boldsymbol{r})$. The simplest possible example is a product of two Gaussian wave

packets

$$W(\boldsymbol{k},\boldsymbol{r}) = \pi_0(\boldsymbol{k})\, p_0(\boldsymbol{r}) \qquad \pi_0(\boldsymbol{k}) = (2\pi)^d \mathcal{G}(\boldsymbol{k},\sigma_k) \qquad p_0(\boldsymbol{r}) = \mathcal{G}(\boldsymbol{r},\sigma_x) \tag{6.77a}$$

$$\mathcal{G}(\boldsymbol{u},\sigma_u) = (2\pi\sigma_u^2)^{-d/2} \exp\Big[\frac{-|\boldsymbol{u}-\boldsymbol{u}_0|^2}{2\sigma_u^2}\Big] \tag{6.77b}$$

A Wigner function of this kind may serve as an approximation for several physical realizations. For example, it can accurately describe the phase-space distribution of an atomic cloud in a magneto-optical trap (MOT). Only the values for σ_x and σ_k have to be adjusted to match with the experimental data. Generally for a MOT, $\sigma_x\sigma_k \gg 1$.

The same initial Wigner function is also found for a single particle in a harmonic oscillator with the oscillator frequency $\omega_{\rm ho}$ and the characteristic oscillator length $a_{\rm ho} = \sqrt{\hbar/m\omega_{\rm ho}}$. In this case one obtains [105]

$$\sigma_x = \frac{a_{\rm ho}}{\sqrt{2\gamma}} \qquad \sigma_k = \frac{1}{a_{\rm ho}\sqrt{2\gamma}} \qquad \gamma = \tanh\frac{\hbar\omega_{\rm ho}}{2k_BT} \tag{6.78}$$

In the high-temperature limit ($T \to \infty$), this amounts to $\sigma_x = \sqrt{k_BT/m\omega_{\rm ho}^2}$ and $\sigma_k = \sqrt{mk_BT/\hbar^2}$. The product of the standard deviations is then given by $\sigma_k\sigma_x = k_BT/\hbar\omega_{\rm ho}$.

The Wigner function (6.77) for $T \to 0$ accurately describes the initial Wigner function of the condensate fraction of an ideal Bose gas in a harmonic trapping potential. For $T \to 0$ one finds $\sigma_x = a_{\rm ho}/\sqrt{2}$ and $\sigma_x\sigma_k = \frac{1}{2}$, which corresponds to the ground state $\varphi_0(\boldsymbol{r}) = (2\pi\sigma_x^2)^{-d/4}\exp\big[|\boldsymbol{r}-\boldsymbol{r}_0|^2/4\sigma_x^2\big]$ of the harmonic potential.

The thermal fraction of an ultra-cold Bose gas below the critical temperature is described by a similar separable Wigner function, except that the function $\mathcal{G}(\boldsymbol{u},\sigma_u)$ is now replaced by $\mathcal{G} = (2\pi\sigma_u^2)^{-d/2}\zeta_R(d)^{-1}\, g_{d/2}(\exp[-|\boldsymbol{u}-\boldsymbol{u}_0|^2/2\sigma_u^2])$. Here, $g_\alpha(z)$ is defined as $g_\alpha(z) = \sum_{n=1}^\infty z^n/n^\alpha$, and $\zeta_R(d) = g_d(1)$ is the Riemann ζ-function which has the numerical value $\zeta_R(2) = \pi^2/6 \approx 1.645$ in 2D and $\zeta_R(3) \approx 1.202$ in 3D. However, qualitatively, the thermal fraction is equally well approximated by the initial Wigner function (6.77) in the high-temperature limit.

Visibility of the Weak-Localization Effect

Without specifying σ_x and σ_k, we can thus treat the previous examples on the same footing. Making use of (6.75) and the marginal $\pi(\boldsymbol{k})$ of a separable Gaussian Wigner function, the diffusion coefficient (6.74) for the initial Wigner function (6.77) including the weak-localization correction to the Boltzmann diffusion constant is then given by

$$\mathcal{D}^* = \int \frac{\mathrm{d}\boldsymbol{k}}{(2\pi\sigma_k^2)^{d/2}}\, D^*(k)\, \exp\Big[-\frac{|\boldsymbol{k}-\boldsymbol{k}_0|^2}{2\sigma_k^2}\Big]\, \Theta(k-k_c) \tag{6.79}$$

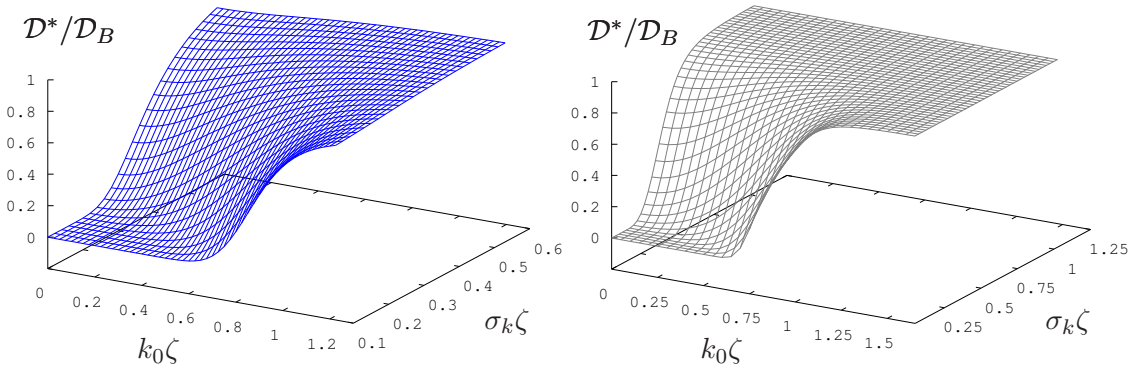

(a) 2D (b) 3D

Figure 6.10:
Ratio of the diffusion coefficient $\mathcal{D}^*$ including the weak-localization correction and the diffusion coefficient $\mathcal{D}_B$ in the Boltzmann approximation as a function of the central wavenumber $k_0\zeta = k_0/(\alpha k_\mathrm{L})$ and the width of the wavevector distribution $\sigma_k\zeta = \sigma_k/(\alpha k_\mathrm{L})$. (a) 2D: $\alpha = 0.1$, $\eta = 0.3$, $k_c\zeta \approx 0.85$. (b) 3D: $\alpha = 1.0$, $\eta = 0.5$, $k_c\zeta \approx 0.72$.

In the absence of weak localization the diffusion coefficient $\mathcal{D}_B(k)$ is given by (6.74), where $D(k)$ is replaced by the Boltzmann diffusion constant.

A plot of the ratio $\mathcal{D}^*/\mathcal{D}_B$ as a function of $k_0/\alpha k_L$ and $\sigma_k/\alpha k_L$ for a fixed value of $\eta = \overline{U}/E_\zeta$ is shown in Fig. **6.10(a)** for the 2D case and in Fig. **6.10(b)** for the 3D case. The integrals have been evaluated numerically. A value of $\mathcal{D}^*/\mathcal{D}_B$ close to 1 means that the weak-localization effect is invisible, whereas weak localization becomes more and more pronounced as this value approaches zero. This is the case for an ultra-cold atomic cloud with vanishing initial momentum $\hbar k_0 \to 0$ and a narrow initial wavevector distribution $\sigma_k \to 0$. When $\mathcal{D}^*/\mathcal{D}_B = 0$, these atoms are localized and the variance (6.73) remains unchanged over time.

There are two special cases of interest, which are depicted in Fig. **6.12**, namely the case where $\sigma_k = 0$ and the case where $k_0 = 0$.

The first case, $\mathcal{D}^*/\mathcal{D}_B$ for $\sigma_k = 0$, is depicted in Fig. **6.11(a)** for the 2D scenario and in Fig. **6.11(b)** for the 3D scenario for different values of $\eta = \overline{U}/E_\zeta$. A zero standard deviation $\sigma_k = 0$, selects the value of the diffusion constant $D^*(k')$ at the central wavenumber k_0 in (6.79). Since the diffusion coefficient (6.79) is zero for $k < k_c$, one only gets a contribution for $k_0 > k_c$. Therefore, the curves touch the k_0-axis exactly at the critical value k_c.

The second case, $\mathcal{D}^*/\mathcal{D}_B$ for $k_0 = 0$, is shown in Fig. **6.12(a)** in 2D and Fig. **6.12(b)** in 3D again for different values of $\eta = \overline{U}/E_\zeta$. In this case non-zero values for $\mathcal{D}^*/\mathcal{D}_B$ are also observed for $\sigma_k < k_c$, since the wings of the Gaussian wave packet centred at the origin extend beyond the critical value k_c.

In view of the desired observation of weak localization for cold atoms in speckle potentials, it is important to create samples with a temperature that is low enough to satisfy the criterion $\sigma_k \lesssim k_c$. Likewise, we need to satisfy $k_0 \lesssim k_c$ in order to be able to observe a visible effect. The criterion for the central wavenumber can be easily fulfilled by looking at an initially immobile atomic cloud. However, the criterion for σ_k remains out of reach for a thermal

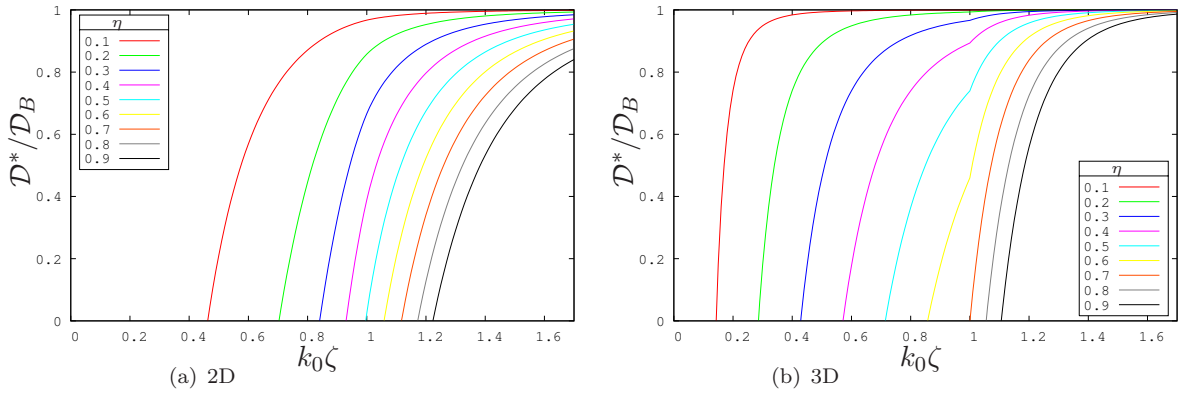

(a) 2D (b) 3D

Figure 6.11:
Ratio of the diffusion coefficient $\mathcal{D}^*$, including the weak-localization correction, and the diffusion coefficient $\mathcal{D}_B$ in the Boltzmann approximation, as a function of the central wavenumber $k_0/(\alpha k_L)$, for different values of $\eta = \overline{U}/E_\zeta$ and for $\sigma_k = 0$. (a) 2D, $\alpha = 0.1$ and (b) 3D, $\alpha = 1$.

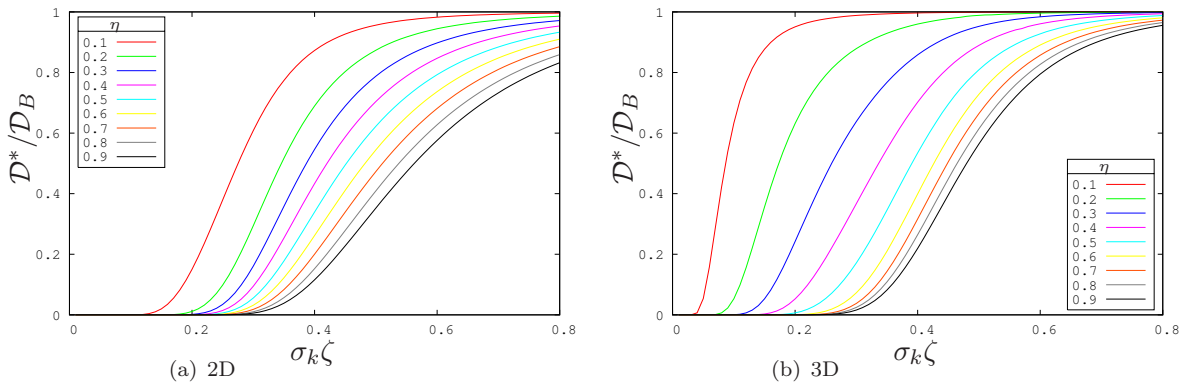

(a) 2D (b) 3D

Figure 6.12:
Ratio $\mathcal{D}^*/\mathcal{D}_B$ as a function of the width of the initial Gaussian wavevector distribution $\sigma_k/(\alpha k_L)$ for $k_0 = 0$ and for different values of $\eta = \overline{U}/E_\zeta$. (a) 2D, $\alpha = 0.1$ and (b) 3D, $\alpha = 1$.

cloud of cold atoms in a MOT, where $\sigma_k = \sqrt{mk_BT/\hbar^2}$. Let us assume $k_c \sim \alpha k_L$, then $\sigma_k \lesssim k_c$ means that the atoms would have to be as cold as

$$T \lesssim \frac{\hbar^2 k_c^2}{mk_B} \sim \alpha^2 T_R \tag{6.80}$$

where $T_R = \hbar^2 k_L^2/(mk_B)$ is the recoil temperature. For Rubidium (cf. Tab. 6.1) we have $T_R = 361\,\mathrm{nK}$. For a thermal cloud in a MOT the recoil temperature determines the lowest possible temperature value. $T \lesssim \alpha^2 T_R$ is therefore only just reachable, if $\alpha = 1$ as in 3D, and remains out of reach, if $k_c < \alpha k_L$. If the atoms are not initially immobile, the same argument applies. However, if the atoms are cooled below the recoil temperature T_R, weak localization does become observable.

The best possible choice for our sample is a Bose-Einstein condensate. Here, σ_k does no longer depend on the temperature. Instead, we have $\sigma_k = \sqrt{m\omega_{\mathrm{ho}}/2\hbar}$, which only depends on ω_{ho}. Thus, the criterion $\sigma_k \lesssim k_c$ actually imposes a condition on the trapping frequency

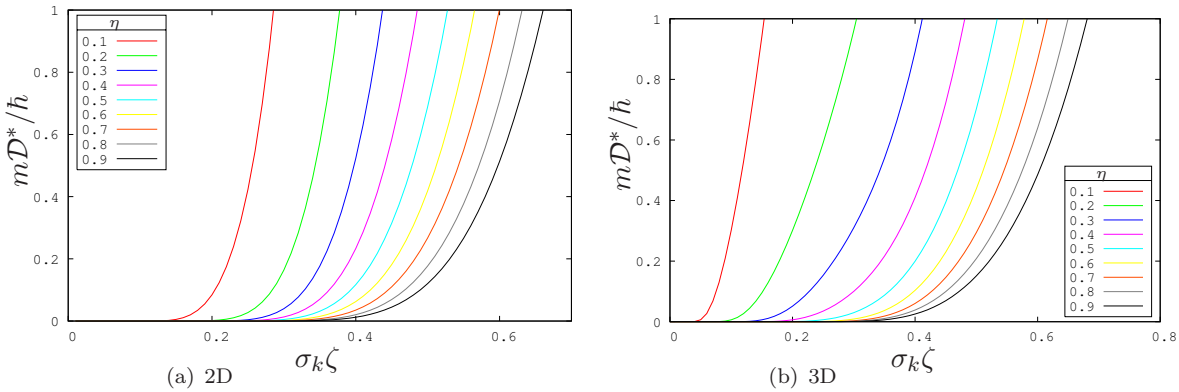

Figure 6.13:
Diffusion coefficient $\mathcal{D}^*$ in units $\hbar/m$ as a function of the width of the initial Gaussian wavevector distribution $\sigma_k/(\alpha k_L)$ for $k_0 = 0$ and for different values of $\eta = \overline{U}/E_\zeta$. (a) 2D, $\alpha = 0.1$ and (b) 3D, $\alpha = 1$.

of the harmonic potential. If we assume $k_c \sim \alpha k_L$, then

$$\omega_{\text{ho}} \lesssim \frac{2\hbar k_c^2}{m} \sim 4\alpha^2 \omega_R \tag{6.81}$$

For Rubidium the recoil frequency is $\omega_R = \hbar k_L^2/(2m) = 2\pi\, 3.77\,\text{kHz}$. According to the criterion (6.81) this requires a trapping frequency of $\omega_{\text{ho}} \lesssim 2\pi\alpha^2\, 15.08\,\text{kHz}$, which is indeed accessible. Thus, for the propagation of a Bose-Einstein condensate that is initially prepared in a suitable harmonic trapping potential, it should be possible to observe a considerable reduced diffusion coefficient due to weak localization.

Typical trapping frequencies are of the order of 10 to 100 Hz [12]. In 2D, for a trapping frequency of $2\pi\, 10\,\text{Hz}$ and $\alpha = 0.1$ one finds $\sigma_k\zeta = 0.26$ and $\sigma_x = 1.94\,\zeta$ for Rubidium atoms (cf. Tab. 6.1). The initial variance $\Delta\boldsymbol{r}_0^2$ for $t = 0$ for the Gaussian Wigner function in our example is given by $\Delta\boldsymbol{r}_0^2 = d\sigma_x^2$ where d is the dimension of the system. In 2D, $\Delta\boldsymbol{r}_0 = 2.75\,\zeta = 3.4\,\mu\text{m}$. For a smaller trapping frequency, the condensate would initially extend over a larger area of the speckle pattern.

For any value $\sigma_k\zeta$, corresponding to an initial trapping frequency ω_{ho}, and for any disorder strength η, we can then obtain the ratio $\mathcal{D}^*/\mathcal{D}_B$ from Fig. **6.12(a)** and the reduced diffusion coefficient from Fig. **6.13(a)**. For the trapping frequency given above and the disorder strength $\eta = 0.5$, the reduced diffusion coefficient $\mathcal{D}^*$ only reaches 1% of the classical diffusion coefficient $\mathcal{D}_B$. This suggests a visible localization effect even for a relatively weak speckle potential. For higher values of η the ratio $\mathcal{D}^*/\mathcal{D}_B$ decreases even further. After an expansion of $t = 100\,\text{ms}$, the rms radius $\Delta\boldsymbol{r}$ (cf. (6.73)) of the condensate in our example classically would have reached $\Delta\boldsymbol{r} = 7.3\,\mu\text{m}$. Quantum interference limits this expansion to $\Delta\boldsymbol{r} = 3.8\,\mu\text{m}$.

In 3D, the criterion for the trapping frequency is less stringent since $\alpha = 1$. Even for a larger trapping frequency of $2\pi\, 500\,\text{Hz}$, i. e. $\sigma_k\zeta = 0.18$, one finds a small ratio $\mathcal{D}^*/\mathcal{D}_B = 0.002$ for the same fixed potential strength $\eta = 0.5$. This corresponds to an initial rms size

$\Delta \boldsymbol{r}_0 = 4.8\,\zeta = 0.6\,\mu$m. After an expansion of 100 ms the 3D condensate classically would inflate to the rms radius $\Delta \boldsymbol{r} = 17\,\mu$m. Quantum interference due to disorder could reduce this expansion to the much lower value $\Delta \boldsymbol{r} = 1.3\,\mu$m during the same expansion time.

Again these values are meant to give an idea of the order of magnitude of the relevant parameters. They only apply to an ideal Bose-Einstein condensate with zero central momentum in a harmonic trapping potential. However, our values give a strong hint that a visible suppression of the variance as compared to the classical behaviour can be expected, if the expansion of an almost ideal Bose-Einstein condensate is studied, where the phase-breaking effect of the interactions can be suppressed.

6.7 Summary

This chapter was concerned with the weak-localization correction to transport. In the first part of the chapter the theoretical foundations for the analytical description of coherent multiple scattering have been reviewed and modified for the description of anisotropic scattering. In particular, we have seen that the simple approximation to the Boltzmann scattering vertex, where just the cooperon diagram is considered, is incomplete, and two additional diagrams have to be considered in order to obtain the full picture for anisotropic scattering. Using a Ward-consistent approximation for the general scattering vertex, we have derived the renormalization of the diffusion constant in (6.52). The self-consistent theory then allows to calculate the 2D and 3D localization length and the critical exponents for the localization length and the diffusion constant close to the strong-localization threshold in 3D.

We have seen that the quantum corrections originate from the constructive interference between matter waves that are propagating in normal and reverse order on loop-like scattering paths in the effective medium. As all interference phenomena they are sensitive to phase-breaking mechanisms such as the spontaneous emission of a photon. However, these spontaneous dissipative processes can be maintained at a very low rate for conveniently chosen values of the experimental parameters. We have shown that in this case the weak-localization correction δD can reach a considerable fraction of the Boltzmann diffusion constant D_B within the weak-scattering regime for atoms at recoil or sub-recoil temperatures.

The magnitude of the weak-localization correction δD, within the limit of validity of the diagrammatic perturbation theory determined in chapter 4, has been compared to the explicit values of D_B derived in chapter 5. We have also given estimates for the parameter range, in which the onset of strong localization could be expected in the experiment, and determined the critical wavenumber attributed to this transition.

The general expression for the probability density derived in the framework of the diagrammatic perturbation theory allows to calculate the variance for any initial phase-space distribution in a disordered environment. This model can be used to describe the configuration-averaged propagation of the condensate fraction of an ideal Bose gas that is released from a harmonic trap into a disordered optical potential, or the configuration-averaged propagation

of a thermal cloud of cold atoms. As a direct application of this model, we have calculated the effect of weak localization for different momentum distributions. Clearly, a significant weak-localization effect is observable for initially slow atoms with a small initial momentum uncertainty.

Chapter 7

Conclusions and Outlook

Only very recently transport experiments with ultra-cold atoms in disordered optical potentials have been performed, which have opened the door to a whole new field of atomic physics. Our aim was to provide a theoretical description of the physical processes relevant to the transport of matter-waves in a disordered optical potential, which could encourage future experiments in this new field.

The basic characteristics of the disordered optical potential have been reviewed in chapter 2. We have calculated the spatial correlation functions of the speckle fluctuations in 2D and in 3D, as well as the corresponding power spectra (cf. (2.31) and (2.35)), and we have verified the intensity distribution and the correlation function for a numerically generated two-dimensional speckle potential. This numerical speckle potential has been used as an example for a correlated potential for the Anderson model in chapter 3. We have studied the density of states per unit volume and the inverse participation number, as a measure for the average extension of localized states, for different strengths of disorder and different degrees of the speckle correlations.

In the remaining part of the thesis we have presented the basic framework for an analytical study of coherent transport of matter waves in a disordered optical potential. To this aim, we have introduced a simple model, which can be solved using standard diagrammatic perturbation techniques, and which allows for a comprehensive study of the physical effects that are linked to the presence of disorder.

One important difference of our model, compared to the standard theory for electrons, stems from the fact that the disordered optical potential exhibits spatial correlations, in contrast to the multiple scattering environment for electrons in condensed matter physics, which generally consists of δ-correlated point-scatterers. This has several important implications for the application of the diagrammatic perturbation theory to our case. A further difference in our model, compared to most model systems, where the diagrammatic perturbation theory is used, is the non-Gaussian character of the speckle potential. Again this constitutes a major difference to the δ-correlated potential, which might be seen as the simplest example of a Gaussian potential (Gaussian white noise).

The optical potential is proportional to the intensity of the generating laser beam at the point where it is probed by an expanding matter wave of cold atoms. The spatial variations of the potential result in a ground state light-shift for the atoms. While the electric field

of the speckle potential is a Gaussian random variable and follows Gaussian statistics, the intensity itself is not a Gaussian random variable. This property of the speckle potential leads to the emergence of field correlation functions, which would be zero for a potential with Gaussian statistics.

These field correlation functions, as well as the usual potential correlation functions, reappear in the series expansion of the self-energy operator, which has been introduced in chapter 4. In principle, the knowledge of the self-energy operator allows to calculate the disorder-averaged amplitude and the elastic scattering mean free path ℓ_s for the multiple scattering process in the effective medium. However, an analytic expression can only be obtained, if the self-energy series is truncated after the first diagram. This is possible in the Born approximation for weak scattering. This approximation essentially leads to a semiclassical description of matter-wave transport in the effective medium.

We have shown, that the weak scattering parameter, which governs the self-energy expansion, in our case differs from the usual weak-disorder parameter $1/k\ell_s$. It is given by $g = \overline{U}/\sqrt{2EE_\zeta}$ (cf. (4.53)). If g is small, a scattered particle receives only a small random phase kick, while it experiences the correlation range of the potential fluctuations. Essentially, the new weak-scattering condition $g \ll 1$ contains the weak-disorder condition, but it furthermore implies that the scattering mean free path is larger than the correlation length ζ. The appearance of the new parameter is thus directly linked to the fact that we have a correlated potential.

Another feature of the correlated potential is that it usually entails anisotropic scattering. This can be demonstrated by a polar plot of the effective phase function of the potential fluctuations, which represents the differential single-scattering cross-section. An important distinction can be made between fast atoms with $k\zeta \gg 1$, for which the scattering is highly anisotropic, and slow atoms with $k\zeta \ll 1$, which are scattered almost isotropically.

In chapter 5 we have derived a general expression for the time dependent average probability density (5.9), which provides the necessary framework for the study of matter waves with a finite initial phase-space distribution as outlined in chapter 6. The calculation of the probability density amounts to the calculation of the intensity relaxation kernel, which requires the solution of a quantum kinetic equation. In particular we have seen that the intensity relaxation kernel follows a diffusion equation, in contrast to the probability density itself. As a result of the standard diagrammatic perturbation theory one obtains a general expression for the transport time τ^* (cf. (5.31)), and thus for the diffusion constant D^*, as a function of the scattering vertex.

In the remaining part of chapter 5 we have studied the Boltzmann approximation for the scattering vertex, corresponding to the Born approximation for the self-energy. This approximation allows to calculate the diffuson, which describes the classical probability transport, and the classical transport mean free path ℓ_B, the average distance over which a scattered particle loses the memory of its initial orientation. The difference between ℓ_B and the scattering mean free path ℓ_s from chapter 4 is again a characteristic of the correlated potential.

For a δ-correlated potential the diffuson can be obtained directly within the Boltzmann approximation. For correlated potentials however, it can only be calculated in the long-time and large-distance limit.

The diffuson is used in chapter 6 to calculate the weak-localization correction of the scattering vertex, which also includes quantum interference effects beyond the Boltzmann approximation. We have shown that the simple substitution $U \to U_B + C_A$, which only takes into account the cooperon diagrams, does not hold for anisotropic scattering. As before, this is a feature of the correlated potential.

Based on previous studies by P. Wölfle and R. N. Bhatt [102] and E. Akkermanns and G. Montambaux [7], who have calculated anisotropic corrections to the conductivity for electron transport, using an additional subset of diagrams, which was first taken into account by S. Hikami [101], we have derived the contribution of the corresponding anisotropic Hikami diagrams C_B and C_C to the diffusion constant (cf. (6.40)). In addition, we have seen that these diagrams are also relevant for the correction of the scattering mean free path (cf. (6.37)) since any correction of the scattering vertex requires, via the Ward identity, a consistent correction of the self-energy. Our final result for the diffusion constant (cf. (6.43)), obtained within the self-consistent theory of Vollhardt and Wölfle [4–6], including the correct weak-localization substitution $U \to U_B + C_A + C_B + C_C$ verifies Einstein's relation. It is valid for isotropic, as well as for anisotropic scattering.

Using this result, we have calculated, within the limit of validity of the perturbative theory, the experimentally relevant transport parameters in the effective medium. In addition, starting form the general definition of the probability density as a function of the initial phase-space distribution, we have calculated the variance of an expanding Gaussian wave packet. This allows to determine criteria for the possible experimental observation of weak-localization for a thermal cloud of cold atoms (cf. (6.80)) and a Bose-Einstein condensate, initially prepared in the ground state of a harmonic trapping potential (cf (6.81)). In conclusion, our model predicts a considerable weak-localization effect for atoms that are initially cooled to very low temperatures, and for the expansion of a Bose-Einstein condensate, which is released from a harmonic trap with a small enough trapping frequency.

The weak-localization effect is susceptible to phase-breaking mechanisms. As an example we have studied the effect of spontaneous emission of a photon by the atom in the disordered optical potential. This effect can be controlled by adjusting the detuning from the atomic resonance frequency of the laser beam, which generates the speckle potential, and at the same time the intensity of the speckle potential, while keeping the ratio between these two quantities fixed.

Further studies of the coherent transport of matter waves in disordered potentials could include atom-atom interactions and the interaction between the optical potential and internal spin degrees of freedom of the atoms. This is expected to introduce additional phase-breaking effects, which would reduce the weak-localization effect (cf. for example [106] for the effect of interactions and [107] for the effect of the internal degeneracy of the atoms, acting as

scatterers for photons, on the coherent backscattering cone). An important extension would be the study of coherent backscattering from a speckle pattern, or the transmission through a speckle pattern of a finite size, where the geometry of the scattering region becomes important.

It could also be very interesting to study the propagation of matter waves in disordered potentials, which exhibit different correlation functions. A promising candidate could be the disordered magnetic potential, which exists above atom chips with a rough surface (cf. [61, 62, 66]). A further extension of this work based on our results presented in chapter 3 could include a quantitative analysis of the localization length as obtained by a direct diagonalization of the Anderson Hamiltonian for the tight-binding model for correlated on-site energies. This would be especially interesting for three-dimensional systems where a true Anderson transition is expected.

Appendix A

Chebyshev Polynomials

Chebyshev polynomials can be defined via the identity

$$T_n(x) = \cos(n \arccos(x)) \tag{A.1}$$

They satisfy the following recurrence relation for $n \geq 1$

$$T_{n+1}(x) = 2xT_n(x) - T_{n-1}(x) \tag{A.2}$$

with $T_0(x) = 1$ and $T_1(x) = x$. The first Chebyshev polynomials, which are plotted in Fig. **A.1(a)** are given by

$$\begin{aligned} T_0(x) &= 1 \\ T_1(x) &= x \\ T_2(x) &= -1 + 2x^2 \\ T_3(x) &= -3x + 4x^3 \\ T_4(x) &= 1 - 8x^2 + 8x^4 \\ T_5(x) &= 5x - 20x^3 + 16x^5 \end{aligned} \tag{A.3}$$

As described in [81], a slightly modified recursion relation

$$\begin{aligned} P_0(x) &= 1 \\ P_1(x) &= a + bx^2 \\ P_{n+1}(x) &= 2(a + bx^2)P_n - P_{n-1} \end{aligned} \tag{A.4}$$

with $a = (x_1^2 + x_2^2)/(x_1^2 - x_2^2)$ and $b = 2/(x_2^2 - x_1^2)$ creates a polynomial $P_n(x)$ with a local maximum at zero, $|P_n(x)| > 1$ for $|x| < x_1$. In the intervals $[x_1, x_2]$ and $[-x_2, -x_1]$ the polynomial is bound between -1 and 1, whereas it grows rapidly for $|x| > x_2$.

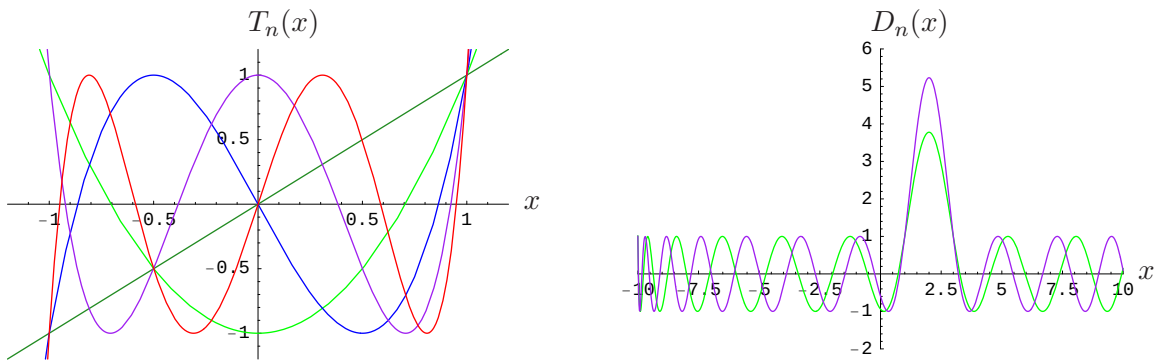

(a) Chebyshev polynomials

(b) Modified Chebyshev polynomials

Figure A.1:
(a) Chebyshev polynomials $T_n(x)$ with $n = 1, 2, 3, 4, 5$ (dark green, green, blue, purple, red). (b) Modified Chebyshev polynomials $D_{12}(x)$ (green) and $D_{14}(x)$ (purple) with $x_{\min} = -10$, $x_{\max} = 10$, $x_1 = 1$, $x_2 = 3$. The height of the maximum depends on the degree of the polynomial and on the size of the intervals $[x_1, x_2]$ and $[x_{\min}, x_{\max}]$.

A polynomial, which acquires the local maximum not at zero but inside a given interval $[x_1, x_2]$, can be created via the recursion relation [88]

$$\begin{aligned} D_0(x) &= 1 \\ D_1(x) &= ax^2 + bx + c \\ D_{n+1}(x) &= 2(ax^2 + bx + c)D_n - D_{n-1} \end{aligned} \tag{A.5}$$

The conditional equations $D_1(x_1) = D_1(x_2) = -1$ and $D_1(x_3) = 1$ for the parabola then yield the coefficients

$$\begin{aligned} a &= 2/n \\ b &= (-2(x_1 + x_2))/n \\ c &= (x_1x_2 + x_3(x_1 + x_2) - x_3^2)/n \\ n &= (x_3 - x_1)(x_3 - x_2) \end{aligned} \tag{A.6}$$

Setting the outer limit x_3, beyond which the polynomials $D_n(x)$ cease to be bound between -1 and 1, to $x_3 = \max[x_{\max}, x_{\min} + x_1 + x_2]$ ensures that the polynomial oscillates between -1 and 1 everywhere in the interval $[x_{\min}, x_1]$ and $[x_2, x_{\max}]$. Between x_1 and x_2 the polynomial reaches a maximum as shown in Fig. **A.1(b)**.

Appendix B

Optical Bloch Equations

The time evolution of the internal atomic density matrix for a two-level atom with the ground state $|g\rangle$ and the excited state $|e\rangle$, in the dipole approximation, interacting with an external electric field of a laser (cf. (4.2) and (4.3)), is described by the Optical Bloch equations [67]. With regard to their different rates of variation, the contribution $\dot{\sigma} = \frac{i}{\hbar}\left[\sigma, H_A - \boldsymbol{D} \cdot \boldsymbol{\mathcal{E}}(\boldsymbol{r}, t)\right]$ due to the coupling to the external field $\boldsymbol{\mathcal{E}}(\boldsymbol{r}, t)$, and the relaxation terms describing spontaneous emission due to the coupling with the vacuum fluctuation reservoir, may be added independently from each other, as though each coupling acted alone [67].

In the basis $\{|e\rangle, |g\rangle\}$, where $H_A = \hbar\omega_A |e\rangle\langle e|$, one then finds the following equations for the density matrix elements (in the following, a *real* Rabi frequency $\Omega(\boldsymbol{r})$ is assumed)

$$\dot{\sigma}_{ee} = \frac{i\Omega(\boldsymbol{r})}{2}\left[\sigma_{eg}\, e^{i\omega_{\mathrm{L}}t} - \sigma_{ge}\, e^{-i\omega_{\mathrm{L}}t}\right] - \Gamma_e \sigma_{ee} \tag{B.1a}$$

$$\dot{\sigma}_{eg} = \frac{i\Omega(\boldsymbol{r})}{2}\left[(\sigma_{ee} - \sigma_{gg})\, e^{-i\omega_{\mathrm{L}}t}\right] - i(\omega_A + \Delta_A)\sigma_{eg} - \frac{\Gamma_e}{2}\,\sigma_{eg} \tag{B.1b}$$

Δ_{A} is the difference of the level-shifts of the two energy levels due to the interaction with the radiation field. It can be incorporated in ω_A by a redefinition of the atomic resonance frequency [67]. The equations for $\dot{\sigma}_{gg}$ and $\dot{\sigma}_{ge}$ are given by $\sigma_{gg} = 1 - \sigma_{ee}$ and $\sigma_{ge} = \sigma_{eg}^*$. Using the abbreviations

$$\begin{aligned} u &= \frac{1}{2}\left[\sigma_{ge}\, e^{-i\omega_{\mathrm{L}}t} + \sigma_{eg}\, e^{i\omega_{\mathrm{L}}t}\right] \\ v &= \frac{1}{2i}\left[\sigma_{ge}\, e^{-i\omega_{\mathrm{L}}t} - \sigma_{eg}\, e^{i\omega_{\mathrm{L}}t}\right] \\ w &= \frac{1}{2}\left(\sigma_{ee} - \sigma_{gg}\right) \end{aligned} \tag{B.2}$$

the Optical Bloch equations can be written in the form

$$\begin{aligned} \dot{u} &= -\frac{\Gamma_e}{2}\, u + \delta_{\mathrm{L}}\, v \\ \dot{v} &= -\delta_{\mathrm{L}}\, u - \frac{\Gamma_e}{2}\, v - \Omega(\boldsymbol{r})\, w \\ \dot{w} &= \Omega(\boldsymbol{r})\, v - \Gamma_e\, w - \frac{\Gamma_e}{2} \end{aligned} \tag{B.3}$$

These equations have the stationary solution

$$u = \frac{\delta_{\mathrm{L}}}{\Omega(\boldsymbol{r})} \frac{s(\boldsymbol{r})}{1+s(\boldsymbol{r})} \qquad v = \frac{\Gamma_e}{2\Omega(\boldsymbol{r})} \frac{s(\boldsymbol{r})}{1+s(\boldsymbol{r})} \qquad w = -\frac{1}{2} \frac{1}{1+s(\boldsymbol{r})} \tag{B.4}$$

where $s(\boldsymbol{r})$ denotes the saturation parameter

$$s(\boldsymbol{r}) = \frac{\Omega^2(\boldsymbol{r})/2}{\delta_{\mathrm{L}}^2 + \Gamma_e^2/4} \tag{B.5}$$

The number of photons spontaneously emitted by the atom per unit time is given by $\Gamma_\phi = \Gamma_e \sigma_{ee}$ (cf. (B.1a)). Using the definition (B.2) for w and $\sigma_{ee} + \sigma_{gg} = 1$ we have $w = \frac{1}{2}(\sigma_{ee} - \sigma_{gg}) = \sigma_{ee} - \frac{1}{2}$ and hence

$$\Gamma_\phi = \Gamma_e \sigma_{ee} = \Gamma_e (w + \tfrac{1}{2}) = \frac{\Gamma_e}{2} \frac{s(\boldsymbol{r})}{1+s(\boldsymbol{r})} \tag{B.6}$$

This gives the inelastic scattering rate associated to the spontaneous emission of photons in terms of the saturation parameter (B.5). For weak saturation, $s \ll 1$, the approximation $\Gamma_\phi \approx s(\boldsymbol{r})\Gamma_e/2$ holds, which is used in (4.12).

Appendix C

Multidimensional Fourier Transform

C.1 2D Fourier Bessel Transform

The Fourier transform of a radially symmetric function in two dimensions is given by

$$\begin{aligned}\mathcal{F}_2[f(r)] = g(k) &= \int \mathrm{d}\boldsymbol{r}\; f(r)\, e^{-i\boldsymbol{k}\cdot\boldsymbol{r}} \\ &= \int_0^{2\pi} \mathrm{d}\varphi \int_0^{\infty} \mathrm{d}r\; r\, f(r)\, e^{-ikr\cos\varphi} \\ &= 2\pi \int_0^{\infty} \mathrm{d}r\; r\, f(r)\, \mathcal{J}_0(kr) \end{aligned} \tag{C.1}$$

$$\begin{aligned}\mathcal{F}_2^{-1}[g(k)] = f(r) &= \int \frac{\mathrm{d}\boldsymbol{k}}{(2\pi)^2}\; g(k)\, e^{i\boldsymbol{k}\cdot\boldsymbol{r}} \\ &= (2\pi)^{-1} \int_0^{\infty} \mathrm{d}k\; k\, g(k)\, \mathcal{J}_0(kr) \end{aligned} \tag{C.2}$$

C.2 3D Fourier Transform

The Fourier transform of a radially symmetric function in three dimensions is given by

$$\begin{aligned}\mathcal{F}_3[f(r)] = g(k) &= \int \mathrm{d}\boldsymbol{r}\; f(r)\, e^{-i\boldsymbol{k}\cdot\boldsymbol{r}} \\ &= \int_0^{2\pi} \mathrm{d}\varphi \int_0^{\pi} \mathrm{d}\vartheta \int_0^{\infty} \mathrm{d}r\; r^2\, \sin\vartheta\, f(r)\, e^{-ikr\cos\vartheta} \\ &= 2\pi \int_0^{\infty} \mathrm{d}r \int_{-1}^{1} \mathrm{d}x\; r^2\, f(r)\, e^{-ikrx} \\ &= 2\pi \int_0^{\infty} \mathrm{d}r\; r^2\, f(r)\, \frac{e^{ikr} - e^{-ikr}}{ikr} \\ &= 4\pi \int_0^{\infty} \mathrm{d}r\; r^2\, f(r)\, \frac{\sin(kr)}{kr} \end{aligned} \tag{C.3}$$

$$\begin{aligned}\mathcal{F}_3^{-1}[g(k)] = f(r) &= \int \frac{\mathrm{d}\boldsymbol{k}}{(2\pi)^3}\; g(k)\, e^{i\boldsymbol{k}\cdot\boldsymbol{r}} \\ &= (2\pi^2)^{-1} \int_0^{\infty} \mathrm{d}k\; k^2\, g(k)\, \frac{\sin(kr)}{kr} \end{aligned} \tag{C.4}$$

Bibliography

[1] P. W. Anderson, *Absence of diffusion in certain random lattices*, Phys. Rev. **109** (1958) p. 1492.

[2] N. F. Mott, *Metal-Insulator Transitions*, Taylor & Francis, London (1990).

[3] J. W. Goodman, *Statistical properties of laser speckle patterns* in J. C. Dainty (editor) *Laser speckle and related phenomena*, Springer-Verlag (1975).

[4] J. Rammer, *Quantum Transport Theory*, Perseus Books, Reading, Mass. (1998).

[5] D. Vollhardt and P. Wölfle, *Diagrammatic, self-consistent treatment of the Anderson localization problem in $d \leq 2$ dimensions*, Phys. Rev. B **22** (1980) p. 4666.

[6] D. Vollhardt and P. Wölfle, *Self-consistent theory of Anderson localization* in W. Hanke and Y. V. Kopaev (editors) *Electronic phase transitions*, Elsevir Science B. V., Amsterdam (1992).

[7] E. Akkermans and G. Montambaux, *Physique mésoscopique des électrons et des photons*, EDP Sciences, CNRS Editions, Paris (2004).

[8] M. R. Andrews, M.-O. Mewes, N. J. van Druten, D. S. Durfee, D. M. Kurn, and W. Ketterle, *Direct, nondestructive observation of a Bose condensate*, Science **273** (1996) p. 84.

[9] M. H. Anderson, J. R. Ensher, M. R. Matthews, C. E. Wieman, and E. A. Cornell, *Observation of Bose-Einstein condensation in a dilute atomic vapor*, Science **269** (1995) p. 198.

[10] B. DeMarco and D. S. Jin, *Onset of Fermi degeneracy in a trapped atomic gas*, Science **285** (1999) p. 1703.

[11] M. Lewenstein, A. Sanpera, V. Ahufinger, B. Damski, A. Sen De, and U. Sen. *Ultracold atomic gases in optical lattices: Mimicking condensed matter physics and beyond* (2006). `http://arXiv.org/abs/cond-mat/0606771`.

[12] F. Dalfovo and S. Giorgini, *Theory of Bose-Einstein condensation in trapped gases*, Rev. Mod. Phys. **71** (1999) p. 463.

[13] A. J. Leggett, *Bose-Einstein condensation in the alkali gases: some fundamental concepts*, Rev. Mod. Phys. **73** (2001) p. 307.

[14] R. Kaiser, C. Westbrook, and F. David, *Les Houches, Session LXXII, Coherent atomic matter waves*, Springer-Verlag, Berlin (2001).

[15] I. Bloch, *Ultracold quantum gases in optical lattices*, Nature Physics **1** (2005) p. 23.

[16] I. Bloch, *Exploring quantum matter with ultracold atoms in optical lattices*, J. Phys. B: At. Mol. Opt. Phys. **38** (2005) p. S629.

[17] L. Sanchez-Palencia and L. Santos, *Bose-Einstein condensates in optical quasicrystal lattices*, Phys. Rev. A **72** (2005) p. 053607.

[18] J. E. Lye, L. Fallani, M. Modugno, D. S. Wiersma, C. Fort, and M. Inguscio, *Bose-Einstein condensate in a random potential*, Phys. Rev. Lett. **95** (2005) p. 070401.

[19] C. Fort, L. Fallani, V. Guarrera, J. E. Lye, M. Modugno, D. S. Wiersma, and M. Inguscio, *Effect of optical disorder and single defects on the expansion of a Bose-Einstein condensate in a one-dimensional waveguide*, Phys. Rev. Lett. **95** (2005) p. 170410.

[20] T. Schulte, S. Denkelforth, J. Kruse, W. Ertmer, J. Arlt, K. Sacha, J. Zakrzewski, and M. Lewenstein, *Routes towards Anderson-like localization of Bose-Einsten condensates in disordered optical lattices*, Phys. Rev. Lett. **95** (2005) p. 170411.

[21] D. Clément, A. F. Varón, J. A. Retter, P. Bouyer, L. Sanchez-Palencia, D. M. Gangardt, G. V. Shlyapnikov, and A. Aspect, *Suppression of transport of an interacting elongated Bose-Einstein condensate in a random potential*, Phys. Rev. Lett. **95** (2005) p. 170409.

[22] J. A. Retter, A. F. Varón, D. Clément, M. Hugbart, P. Bouyer, L. Sanchez-Palencia, D. Gangardt, G. V. Shlyapnikov, and A. Aspect, *Inhibition of transport of a Bose-Einstein condensate in a random potential*, Journal de physique IV **135** (2006) p. 145.

[23] D. Clément, A. F. Varón, J. A. Retter, L. Sanchez-Palencia, A. Aspect, and P. Bouyer, *Experimental study of the transport of coherent interacting matter-waves in a 1D random potential induced by laser speckle*, New Journal of Physics **8** (2006) p. 165.

[24] T. Schulte, S. Denkelforth, J. Kruse, R. Tiemeyer, K. Sacha, J. Zakrzewski, M. Lewenstein, W. Ertmer, and J. J. Arlt, *Analysis of localization phenomena in weakly interacting disordered lattice gases*, New Journal of Physics **8** (2006) p. 230.

[25] R. A. Duine and H. T. C. Stoof, *Atom–molecule coherence in Bose gases*, Phys. Rep. **396** (2004) p. 115.

[26] E. Timmermans, P. Tammasini, M. Hussein, and A. Kerman, *Feshbach resonances in atomic Bose-Einstein condensates*, Phys. Rep. **315** (1999) p. 199.

[27] R. C. Kuhn, C. Miniatura, D. Delande, O. Sigwarth, and C. A. Müller, *Localization of matter waves in two-dimensional disordered optical potentials*, Phys. Rev. Lett. **95** (2005) p. 250403.

[28] R. C. Kuhn, O. Sigwarth, C. Miniatura, D. Delande, and C. A. Müller. *Coherent matter wave transport in speckle potentials* (2007). `http://arXiv.org/abs/cond-mat/0702183`.

[29] B. Kramer and A. MacKinnon, *Localization: theory and experiment*, Rep. Prog. Phys. **56** (1993) p. 1469.

[30] G. Bergmann, *Weak localization in thin films*, Phys. Rep. **107** (1984) p. 1.

[31] P. A. Lee and T. V. Ramakrishnan, *Disordered electronic systems*, Rev. Mod. Phys. **57** (1985) p. 287.

[32] E. Abrahams, P. W. Anderson, D. C. Licciardello, and T. V. Ramakrishnan, *Scaling theory of localization: absence of diffusion in two dimensions*, Phys. Rev. Lett. **42** (1979) p. 673.

[33] N. Ashcroft and D. Mermin, *Solid State Physics*, Saunders College, Philadelphia (1976).

[34] O. Sigwarth, *Localisation faible de la lumière par un gaz d'atomes froids en présence d'un champ magnétique*, PhD thesis, Laboratoire Kastler-Brossel, Université Pierre & Marie Curie, Paris (2004).

[35] J. S. Langer and T. Neal, *Breakdown of the concentration expansion for the impurity resistivity of metals*, Phys. Rev. Lett. **16** (1966) p. 984.

[36] P. E. Wolf and G. Maret, *Weak localization and coherent backscattering of photons in disordered media*, Phys. Rev. Lett. **55** (1985) p. 2696.

[37] M. P. van Albada and A. Lagendijk, *Observation of weak localization of light in a random medium*, Phys. Rev. Lett. **55** (1985) p. 2692.

[38] D. Vollhardt and P. Wölfle, *Scaling equations from a self-consistent theory of Anderson localization*, Phys. Rev. Lett. **48** (1982) p. 699.

[39] L. van den Dries, C. van Haesendonck, and Y. Bruynseraede, *Two-dimensional localization in thin copper films*, Phys. Rev. Lett. **46** (1981) p. 565.

[40] D. Jaksch, C. Bruder, J. I. Cirac, C. W. Gardiner, and P. Zoller, *Cold bosonic atoms in optical lattices*, Phys. Rev. Lett. **81** (1998) p. 3108.

[41] M. Greiner, *Ultracold quantum gases in three-dimensional optical lattice potentials*, PhD thesis, Ludwig-Maximilians-Universität München (2003).

[42] M. Greiner, O. Mandel, T. Esslinger, T. W. Hänsch, and I. Bloch, *Quantum phase transition from a superfluid to a Mott insulator in a gas of ultracold atoms*, Nature **415** (2002) p. 39.

[43] M. P. A. Fisher, P. B. Weichman, G. Grinstein, and D. S. Fisher, *Boson localization and the superfluid-insulator transition*, Phys. Rev. B **40** (1989) p. 546.

[44] K. Góral, L. Santos, and M. Lewenstein, *Quantum phases of dipolar bosons in optical lattices*, Phys. Rev. Lett. **88** (2002) p. 170406.

[45] L. Fallani, J. E. Lye, V. Guarrera, C. Fort, and M. Inguscio. *Towards a Bose-Glass of ultracold atoms in a disordered crystal of light* (2006). `http://arXiv.org/abs/cond-mat/0603655`.

[46] R. Roth and K. Burnett, *Ultracold bosonic atoms in two-color disordered optical superlattices*, J. Opt. B: Quantum Semiclass. Opt. **5** (2003) p. S50.

[47] R. Roth and K. Burnett, *Phase diagram of bosonic atoms in two-color superlattices*, Phys. Rev. A **68** (2003) p. 023604.

[48] B. Damski, J. Zakrzewski, L. Santos, P. Zoller, and M. Lewenstein, *Atomic Bose and Anderson glasses in optical lattices*, Phys. Rev. Lett. **91** (2003) p. 080403.

[49] L. Guidoni, C. Triché, P. Verkerk, and G. Grynberg, *Quasiperiodic Optical Lattices*, Phys. Rev. Lett. **79** (1997) p. 3363.

[50] R. Penrose, *The role of aesthetics in pure and applied mathematical research*, Bull. Inst. Math. Appl. **10** (1974) p. 266.

[51] L. Guidoni, B. Dépret, A. di Stefano, and P. Verkerk, *Atomic diffusion in an optical quasicrystal with five-fold symmetry*, Phys. Rev. A **60** (1999) p. R4233.

[52] M. Modugno, *Collective dynamics and expansion of a Bose-Einstein condensate in a random potential*, Phys. Rev. A **73** (2006) p. 013606.

[53] J. E. Lye, L. Fallani, C. Fort, V. Guarrera, M. Modugno, D. S. Wiersma, and M. Inguscio. *Effect of interactions on the localization of a Bose-Einstein condensate in a quasi-periodic lattice* (2006). `http://arXiv.org/abs/cond-mat/0611146`.

[54] L. Sanchez-Palencia, *Smoothing effect and delocalization of interacting Bose-Einstein condensates in random potentials*, Phys. Rev. A **74** (2006) p. 053625.

[55] H. Perrin, Y. Colombe, B. Mercier, V. Lorent, and C. Henkel, *Diffuse reflection of a Bose-Einstein condensate from a rough evanescent wave mirror*, J. Phys. B: At. Mol. Opt. Phys. **39** (2006) p. 4649.

[56] C. Henkel, K. Mølmer, R. Kaiser, N. Vansteenkiste, C. I. Westbrook, and A. Aspect, *Diffuse atomic reflection at a rough mirror*, Phys. Rev. A **55** (1997) p. 1160.

[57] V. Savalli, D. Stevens, J. Estève, P. Featonby, V. Josse, N. Westbrook, C. I. Westbrook, and A. Aspect, *Specular reflection of matter waves from a rough mirror*, Phys. Rev. Lett. **88** (2002) p. 250404.

[58] U. Gavish and Y. Castin, *Matter-wave localization in disordered cold atom lattices*, Phys. Rev. Lett. **95** (2005) p. 020401.

[59] Pietro Massignan, *Three-dimensional strong localization of matter waves by scattering from atoms in a lattice with a confinement-induced resonance*, Phys. Rev. A (2006) p. 74.

[60] S. Ospelkaus, C. Ospelkaus, O. Wille, M. Succo, P. Ernst, K. Sengstock, and K. Bongs, *Localization of bosonic atoms by fermionic impurities in a 3D optical lattice*, Phys. Rev. Lett. **96** (2006) p. 180403.

[61] D. W. Wang, M. D. Lukin, and E. Demler, *Disordered Bose-Einstein condensates in quasi-one-dimensional magnetic microtraps*, Phys. Rev. Lett. **92** (2004) p. 076802.

[62] R. Folman, P. Krüger, D. Cassettari, B. Hessmo, T. Maier, and J. Schmiedmayer, *Controlling cold atoms using nanofabricated surfaces: atom chips*, Phys. Rev. Lett. **84** (2000) p. 4749.

[63] H. Gimperlein, S. Wessel, J. Schmiedmayer, and L. Santos, *Ultracold atoms in optical lattices with random on-site interactions*, Phys. Rev. Lett. **95** (2005) p. 170401.

[64] V. Ahufinger, L. Sanchez-Palencia, A. Kantian, A. Sanpera, and M. Lewenstein, *Disordered ultracold atomic gases in optical lattices: A case study of Fermi-Bose mixtures*, Phys. Rev. A **72** (2005) p. 063616.

[65] L. Sanchez-Palencia, V. Ahufinger, A. Kantian, J. Zakrzewski, A. Sanpera, and M. Lewenstein, *Strongly correlated Fermi-Bose mixtures in disordered optical lattices*, J. Phys. B: At. Mol. Opt. Phys. **39** (2006) p. S121.

[66] T. Paul, P. Leboeuf, N. Pavloff, K. Richter, and P. Schlagheck, *Nonlinear transport of Bose-Einstein condensates through waveguides with disorder*, Phys. Rev. A **72** (2005) p. 063621.

[67] C. Cohen-Tannoudji, J. Dupont-Roc, and G. Grynberg, *Atom-Photon Interactions: Basic Processes and Applications*, Wiley, New York (1998).

[68] L. Mandel and E. Wolf, *Optical coherence and quantum optics*, Cambridge University Press, Cambridge (1996).

[69] J. W. Goodman, *Introduction to Fourier optics*, McGraw-Hill, New York (1968).

[70] M. Born and E. Wolf, *Principles of Optics*, Cambridge University Press, Cambridge (1998).

[71] M. Abramowitz and I. Stegun, *Handbook of mathematical functions with formulas, graphs, and mathematical table*, Dover Publications, New York (1972).

[72] M. V. Berry, *Regular and irregular semiclassical wavefunctions*, J. Phys. A: Math. Gen. **10** (1977) p. 2083.

[73] J. M. Huntley, *Speckle photography fringe analysis: assessment of current algorithms*, Appl. Opt. **28** (1989) p. 4316.

[74] P. Horak, J-Y. Courtois, and Gilbert Grynberg, *Atom cooling and trapping by disorder*, Phys. Rev. A **58** (1998) p. 3953.

[75] P. Sheng, *Introduction to wave scattering, localization and mesoscopic phenomena*, Academic Press (1995).

[76] J. Kroha, *Diagrammatic self-consistent theory of Anderson localization for the tight-binding model*, Physica A **167** (1990) p. 231.

[77] J. Kroha, T. Kopp, and P. Wölfle, *Self-consistent theory of Anderson localization for the tight-binding model with site-diagonal disorder*, Phys. Rev. B **41** (1990) p. 888.

[78] F. J. Dyson, *The dynamics of a disordered linear chain*, Phys. Rev. **92** (1953) p. 1331.

[79] H. Schmidt, *Disordered one-dimensional crystals*, Phys. Rev. **105** (1957) p. 425.

[80] J.-M. Luck, *Systèmes désordonnés unidimensionnels*, Commissariat à l'Energie Atomique, Gif-sur-Yvette Cedex (1992).

[81] U. Elsner, V. Mehrmann, F. Milde, R. A. Römer, and M. Schreiber, *The Anderson model of localization: a challenge for modern eigenvalue methods*, SIAM J. Sci. Comput. **20** (1999) p. 2089.

[82] G. Schubert, A. Weiße, G. Wellein, and H. Fehske. *Comparative numerical study of Anderson localisation in disordered electron systems* (2005). `http://arXiv.org/abs/cond-mat/0309015`.

[83] G. Schubert, *Numerische Untersuchung ungeordneter Elektronensysteme*, PhD thesis, Universität Bayreuth (2003).

[84] I. S. Gradshteyn and I. M Ryzhik, *Table of integrals series and products*, Academic Press, San Diego (2000).

[85] B. A. van Tiggelen, *Localization of waves* in J.-P. Fouque (editor) *Diffusive waves in complex media*, Kluwer Academic Publishers, NATO Science Series, Dordrecht (1999).

[86] C. Lanczos, *An iterative method for the solution of the eigenvalue problem of linear diffential and integral operators*, J. Res. Nat. Bur. Standards, Sect. B **45** (1950) p. 255.

[87] J. K. Cullum and R. A. Willoughby, *Lanczos algorithms for large symmetric eigenvalue computations Vol. I Theory*, Birkhäuser, Boston (1985).

[88] D. Delande. *Private communication* (2005).

[89] Y. Bidel, B. Klappauf, J. C. Bernard, D. Delande, G. Labeyrie, C. Miniatura, D. Wilkowski, and R. Kaiser, *Coherent light transport in a cold strontium cloud*, Phys. Rev. Lett. **88** (2002) p. 203902.

[90] O. Sigwarth, G. Labeyrie, T. Jonckheere, D. Delande, R. Kaiser, and C. Miniatura, *Magnetic field enhanced coherence length in cold atomic gases*, Phys. Rev. Lett **93** (2004) p. 143906.

[91] A. Mouchet, C. Miniatura, R. Kaiser, B. Gremaud, and D. Delande, *Chaos-assisted tunneling with cold atoms*, Phys. Rev. E **64** (2001) p. 016221.

[92] A. Lagendijk and B. A. van Tiggelen, *Resonant multiple scattering of light*, Phys. Rep. **270** (1996) p. 143.

[93] U. Frisch, *Wave propagation in random media* in A. T. Bharucha-Reid (editor) *Probabilistic methods in applied mathematics*, Academic Press, New York (1968).

[94] G. D. Mahan, *Many Particle Physics*, Springer-Verlag, Berlin (1990).

[95] C. S. Adams, M. Sigel, and J. Mlynek, *Atom Optics*, Phys. Rep. **240** (1994) p. 145.

[96] C. M. Bender and S. A. Orszag, *Advanced Mathematical Methods for Scientists and Engineers*, Springer-Verlag, New York (1999).

[97] C. Henkel, J.-Y. Courtois, and A. Aspect, *Atomic diffraction by a thin phase grating*, J. Phys. II France **4** (1994) p. 1955.

[98] A. Galindo and P. Pascual, *Quantum Mechanics I*, Springer-Verlag, Berlin (1991).

[99] A. Ishimaru, *Wave propagation and scattering in random media*, IEEE Press, New York (1997).

[100] S. Chandrasekhar, *Radiative Transfer*, Dover Publications, New York (1960).

[101] S. Hikami, *Anderson localization in a nonlinear–σ–model representation*, Phys. Rev. B **24** (1981) p. 2671.

[102] P. Wölfle and R. N. Bhatt, *Electron localization in anisotropic systems*, Phys. Rev. B **30** (1984) p. 3542.

[103] G. M. Minkov, A. V. Germanenko, O. E. Rut, A. A. Sherstobitov, and B. N. Zvonkov. *Giant suppression of the Drude conductivity due to quantum interference in disordered two-dimensional systems* (2006). `http://arXiv.org/abs/cond-mat/0606566`.

[104] D. A. Steck. *Rubidium* 87 *D line data* (2001). `http://steck.us/alkalidata`.

[105] B.-G. Englert, *On the operator bases underlying Wigner's, Kirkwood's and Glauber's phase space functions*, J. Phys. A: Math. Gen. **22** (1989) p. 625.

[106] B. L. Altshuler and A. G. Aronov, *Electron-electron interaction in disordered conductors* in A. L. Efros and M. Pollak (editors) *Electron-electron interaction in disordered systems*, North-Holland, Amsterdam (1985).

[107] C. A. Müller, T. Jonckheere, C. Miniatura, and D. Delande, *Weak localization of light by cold atoms: The impact of quantum internal structure*, Phys. Rev. A **64** (2001) p. 053804.

Acknowledgements – Danksagung – Remerciements

A very special thanks to my Doktorvater Prof. Dr. Cord Müller and my French supervisor, Dr. Christian Miniatura, for their continuous guidance and support during my PhD years.

I would like to thank Prof. Dr. Müller for all his help with my work, for having me as his first PhD student and for going through all the trouble so that I could do a binational PhD with the university of Nice and spend part of my PhD abroad in France and in Singapore.

I would like to thank Dr. Miniatura for welcoming me in Nice, where I could be part of the cold atoms group at the INLN. In Nice I spent ten fabulous months of my life. I will never forget this time. Nor will I forget my unique time in Singapore. I definitely will miss our discussions at the Spinelli Cafe which provided the fuel for tackling new problems.

I am particularly indebted to Dr. Dominique Delande at the LKB in Paris who provided me with the Lanczos algorithm and with lots of valuable advise and help on the numerics and on the general concepts of multiple scattering theory. I would like to thank Dr. Delande for making me feel at home at the LKB and for finding me such nice accommodation in Paris. I really enjoyed working at the LKB.

I am also particularly indebted to Prof. Dr. Berthold-Georg Englert for welcoming me at the Quantum Information Technology Group at the National University of Singapore where I spent six very nice months of my PhD. And I would like to thank Dr. Bart van Tiggelen for accepting to become cocorrector for my thesis and for coming to Bayreuth especially for my thesis defense, and Dr. Gilles Montambeaux for very helpful discussions in Aussois and in Paris on technical issues of the diagrammatic perturbation theory.

I would like to thank all members of the Theoretical Physics chair in Bayreuth and especially all members of the QTLM group in Bayreuth: Cord Müller, Olivier Sigwarth, Christopher Gaul, Christian Wickles, Tobias Kerscher and Torsten Scholak. I won't forget our legendary trips to the wine cellars of Alsace and the icy heights of mount Schneekoppe. I guess no other group has those nice Bambergers for their group sessions. "This is a damn fine Bamberger" as special agent Dale Bartholomew Cooper would say ;-).

A very special thanks to my roommates, Juan Pablo Zagorodny, Olivier Sigwarth and Torsten Scholak. Without Olivier's help and his contributions to our publications a large part of my thesis would not have been possible. Merci beaucoup, Olivier. And I would like to thank Juan Pablo for sharing with me such good times and Torsten Scholak for our entanglement discussions and especially for making such a fabulous hat for me! Muchas Gracias Juan. Vielen Dank Torsten.

I would like to thank all members of the INLN in Nice and especially all members of

the cold atoms group: Guillaume Labeyrie, David Wilkowski, Robin Kaiser and Gian-Luca Gattobigio, for their interest in my work and for making me feel at home at the INLN. And I would like to thank all members of the LKB in Paris, in particular Riccardo Sapienza, Martino Trassinelli, Julien Le Bars, Sylvain Gigan, Francesco Intravaia, Benoît Grémaud and Thomas Wellens for making my stay in Paris an unforgettable experience.

A very special thanks to Sigrid Glas, Nathalie Hamel and Monique Bonamie for their help with all administrative issues. I am particularly indepted to the DAAD for financial support for my binational PhD thesis and to Ursula Bazoune for her help with all matters concerning the DAAD fellowship.

I also would like to thank the experimental physicists at Bayreuth university, in particular Albert Voit, Wolfgang Michel, Gerhard Wittko, Pablo Fernandez, Marianne Hartung and Silke Oellerich, who showed me that there is a life outside the office ;-).

Last but not least I would like to thank my parents for their Schnipsel letters and for being always there for me, my sister Anne for proofreading my manuscript and for being the best sister in the world and my girlfriend Silke for her love and her support.

Vielen Dank.